NUMERICAL MODELING OF DENSITY-DRIVEN CHEMICAL OXIDATION OF CHLORINATED SOLVENTS

by

THOMAS HATCHER HENDERSON
B.A., Oberlin College, 1987

A THESIS SUBMITTED IN PARTIAL FULFILLMENT OF
THE REQUIREMENTS FOR THE DEGREE OF
DOCTOR OF PHILOSOPHY

in

THE FACULTY OF GRADUATE STUDIES

(Geological Sciences)

THE UNIVERSITY OF BRITISH COLUMBIA

(Vancouver)

July 2009

ABSTRACT

A popular method for the treatment of aquifers contaminated with chlorinated solvents is chemical oxidation using potassium permanganate ($KMnO_4$). Numerical modeling was employed to investigate permanganate-based remediation under free convection conditions, considering contaminant treatment, and geochemical reactions including the oxidation of naturally occurring organic matter, mineral dissolution and precipitation, and ion exchange reactions. The MIN3P multicomponent reactive transport code was enhanced to simulate the remediation technology. The modified code (MIN3PD) provides a direct coupling between density-dependent fluid flow, solute transport, contaminant treatment, and geochemical reactions. The code was utilized to identify the processes most important to remediation efficiency and the geochemical response to a $KMnO_4$ injection. The investigation was achieved through a sensitivity analysis, the development of a three-dimensional model of a field trial of TCE oxidation, and automated inverse modeling. Investigation results elucidate the important role of density-induced flow and transport on the distribution of the oxidant solution. The soil organic matter content, aquifer hydraulic conductivity and porosity, and the DNAPL dissolution kinetics comprise primary system attributes controlling the geochemical evolution and remediation efficiency. Detailed monitoring data collected during the field trial were used to evaluate the ability of the MIN3PD model to adequately simulate permanganate-based groundwater remediation. The calibrated model reproduced the transient distribution of aqueous species, and supported a quantitative evaluation of remediation efficiency. Automated inverse modeling was employed to systematically evaluate the quality of the model calibration, and identify optimal values of model input parameters. The investigation supported a quantitative evaluation of the conceptual model of the remediation technology, and capabilities and limitations of the numerical model.

TABLE OF CONTENTS

LIST OF TABLES

LIST OF FIGURES

ACKNOWLEDGEMENTS

I wish to thank my wife, Kate, and my parents for the considerable level of support provided during this effort. In particular, Kate facilitated the completion of this research over the critical final year of work. The Montana Department of Environmental Quality provided flexible work scheduling and support. Clare Stewart collected and compiled the field data supporting the mathematical modeling. My advisor, Dr. Ulrich Mayer, provided critical analysis, encouragement, and a positive introduction to Linux-based scientific computing. Finally, I wish to thank the faculty and my colleagues at the Department of Earth and Ocean Sciences for many excellent experiences during my time on campus.

Funding was provided through an NSERC Collaborative Research and Development Grant awarded to Beth L. Parker. Additional funding was provided through the University Consortium for Field-Focused Groundwater Contamination Research and a Thomas and Marguerite MacKay Memorial Scholarship. Simulations were partially conducted using the WestGrid computing resources, which are funded in part by the Canada Foundation for Innovation, Alberta Innovation and Science, BC Advanced Education, and the participating research institutions.

Chapter 1 Introduction

The volatile organic compounds trichloroethylene (TCE) and tetrachloroethylene (PCE), widely used in metal degreasing and dry cleaning applications, have impacted aquifers and motivated the development of groundwater remediation technologies [Pankow and Cherry, 1996; USEPA, 1998; ITRC, 2005]. Both chemicals have been identified at over 50 percent of the 1,430 National Priorities List sites in the United States [ATSDR, 1997a; ATSDR, 1997b] and have impacted urban and rural drinking water wells [Squillance et al., 1999; USEPA, 1999a; Moran et al., 2002]. Remediation is required when these chemicals are present at concentrations above government regulatory thresholds in soils and groundwater. Chemical oxidization provides a mechanism for the destruction of TCE and PCE, and is the subject of the current research.

Potassium permanganate ($KMnO_4$) has historically been employed as a chemical oxidant in the treatment of drinking water [Stewart, 1965; USEPA, 1999b; Siegrist et al., 2001]. The utilization of the permanganate ion (MnO_4^-) to remediate TCE and PCE-contaminated media has been the focus of recent research incorporating laboratory and field-scale investigations [West et al., 1997; Schnarr et al., 1998; Yan and Schwartz, 1999; Nelson et al., 2001; Schroth et al., 2001; Lowe et al., 2002; MacKinnon and Thomson, 2002; Conrad et al., 2002; Lee et al., 2003; Li and Schwartz, 2004a; Li and Schwartz, 2004b; Mumford et al., 2005; Honning et al., 2007]. The delivery of the oxidant solution to the contaminated zones has been identified as a potential limiting factor for in-situ remediation [Li and Schwartz, 2000; Ibaraki and Schwartz, 2001; MacKinnon and Thomson, 2002; Gavaska and Yoon, 2002]. Nelson et al. [2001] and Parker et al. [2002] introduced and field-tested the concept of utilizing the contrast in fluid density between the oxidant and the groundwater as an effective means for oxidant delivery to impacted areas. The current investigation focuses on groundwater remediation using this approach, also known as the inject-and-leave method [Nelson et al., 2001; Stewart, 2002], which consists of the injection and distribution of a dense permanganate treatment solution that is subsequently left in the subsurface to destroy the contaminants. The transport and reaction processes associated with this technology are coupled and complex due to the interdependence of the movement of fluids, the transport of dissolved compounds, and chemical reactions.

1.1 Problem Definition

Chemical oxidation technologies applied at field sites are affected by a multitude of processes, which makes it difficult to design the remedial action and evaluate its effectiveness [ITRC, 2005; Huling and Pivetz, 2006]. In the case of permanganate-based remediation, the movement of the injected oxidant solution and displaced groundwater exhibits temporal and spatial variability in flow velocities and directions, and the three-dimensional distributions of dissolved aqueous species are simultaneously affected by transport and reaction processes [Nelson et al., 2001; Stewart, 2002]. The chemical reactions driven by the introduction of the oxidant solution are complicated by the presence of multiple phases and dissolved species, which are distributed heterogeneously in space and change over time [Conrad et al., 2002; MacKinnon and Thomson, 2002; Lee et al., 2003]. Interpretive tools are required to integrate the monitoring data to assess the three-dimensional distribution of dissolved species, and estimate the effectiveness of the remediation.

Primary issues in the current investigation of this technology include the remediation effectiveness, and the processes and site attributes most important to the fate of the oxidant. Multicomponent reactive transport modeling provides a quantitative approach to consider multiple processes that are coupled in a non-linear fashion [Steefel and Lasaga, 1994; Mayer et al., 2001a; Mayer et al., 2001b; Freedman and Ibaraki, 2002; Essaid et al., 2003; Jurjovec et al., 2004; Colombani et al., 2009] and can therefore be used effectively to simulate and assess this remediation technology. Reactive transport modeling is based on the integration of a defined reaction network with mass-conservative continuum equations describing the movement of fluids and chemicals [Clement et al., 1998; Mayer et al., 2002; Prommer et al., 2003; Xu et al., 2004]. This approach allows simultaneous processes to be simulated, and provides a mechanism to evaluate the sensitivity of treatment efficiency to the physical and chemical attributes [Gandhi at al., 2002].

However, the complex and site-specific nature of permanganate-based aquifer remediation presents obstacles to the application of common numerical modeling methods. A generalized formulation is required to represent the processes of interest. In the current study, the fundamental requirement is the capability for simulating fully coupled fluid flow, chemical transport, and a variable set of chemical reactions in porous media. Although coupled process simulators have been developed in the hydrogeological sciences [Voss, 1984; Kipp, 1986; Steefel and Lasaga, 1994; Ackerer et al., 1999; Frolkovic, 1999; Oltean and Buès, 2001; Diersch, 2002; Graf and Therrien, 2007], the consideration of all three processes represents a developing field of research [Freedman

and Ibaraki, 2002; Xu at al., 2004; Mao et al., 2006] and has only been applied very sparsely in the field of groundwater contamination [Zhang and Schwartz, 1995]. A model for the simulation of permanganate-based groundwater remediation that includes the movement of variable density fluids, the relevant geochemical reactions, and changes in media porosity and permeability has not been developed to date.

Simulation of permanganate-based remediation requires an appropriate model formulation and model parameterization. Model calibration at the field site scale is complicated by the existence of many degrees of freedom [Zheng and Bennett, 2002]. In the case of permanganate-based remediation, the mathematical model incorporates the physical scale of the problem and the complexity inherent to chemical reactions involving multiple phases. These considerations emphasize the importance of an objective and systematic process in the estimation of model parameters and the evaluation of model performance.

1.2 Research Objectives and Scope

The primary objective of this research is to elucidate the characteristics of permanganate-based remediation focusing on the coupling between processes, and develop a mechanism to relate the measured geochemical response to a permanganate injection to an assessment of the efficiency of the remediation. The research objective was pursued using numerical modeling methods. A computer code with a generalized formulation capable of representing the processes defined by the conceptual model of the coupled reactive system was required. The MIN3PD code developed for this work integrates capabilities developed in the field of variable density flow [Frind, 1982; Huyakorn et al., 1987; Oldenburg and Pruess, 1995; Langevin and Guo, 2006] and reactive chemical transport [Clement et al., 1998; Mayer et al., 2002; Prommer et al., 2003] to develop a generalized computer program.

While the program is a development of the existing MIN3P reactive transport code [Mayer et al., 2002], significant modifications were required in order represent the bi-directional coupling between the movement of variable density fluids and the reactive transport of aqueous species. The primary elements of this work were the implementation of a mass-conservative fluid continuum equation, and the numerical methods to facilitate the solution of the coupled sets of equations. In the

current formulation, fluid density is computed as a function of dissolved aqueous species concentrations under assumed isothermal conditions.

Permanganate-based remediation is investigated in a hydrological regime isolated from the regional hydraulic gradient, which is not manipulated by introduction or extraction of fluids other than the introduction of the oxidant solution. The characteristics of the coupled reactive system are elucidated through the numerical investigation of two defined problems. In the first case, an idealized representation of a remediation site is developed in which heterogeneity is absent. For the defined hydrologic regime, this model provides a general case in which the processes of fluid flow, chemical transport, chemical reactions, and contaminant destruction can be characterized, and strength of coupling can be evaluated. Sensitivity analysis is conducted to relate overall responses to model parameters [Essaid et al., 2003; Sanz and Voss, 2006; Hill and Tiedeman, 2007] using transient distributions of aqueous components, and mass balance results quantifying the fate of the injected oxidant.

The hypothetical evaluation is complimented by a site-specific investigation of a permanganate remediation trial performed in North Haven, Connecticut, USA [Stewart, 2002]. The three-dimensional MIN3PD model is developed representing the discontinuous distribution of TCE DNAPL, and the irregular topography of the contact between the aquifer and aquitard at the facility. The reactive system is represented using ten aqueous components, two mineral phases, TCE (dissolved, adsorbed, and NAPL), reactive organic matter, and simulates ion exchange reactions. The calibrated MIN3PD model is employed to evaluate the characteristics of permanganate-based remediation in a heterogeneous natural system, and relate the measured geochemical evolution to the remediation efficiency.

Automated inverse modeling is employed to compliment the three-dimensional modeling by addressing the uncertainty in model parameters and model predictions. A two-dimensional representation of the field trial utilizing a radial grid geometry is developed for the investigation, and benchmarked against the three-dimensional model. The systematic approach in identifying model parameters and measuring the quality of the calibration facilitates the evaluation of model errors, and limitations present in employing numerical models in investigating permanganate remediation in heterogeneous field scale systems.

1.3 Organization of Thesis

The conceptual model of permanganate-based remediation of aquifers contaminated with chlorinated solvents is developed in Chapter 2. This chapter introduces key elements of the remediation method from the literature and based on observations from the North Haven field site. The coupled processes of variable density flow and chemical transport that occur as a result of the injection of the oxidant solution are described. A chemical reaction network is defined, describing targeted and non-targeted chemical oxidation reactions, mass transfer processes between phases, and changes in geochemistry resulting from a permanganate injection. The processes that contribute to potential changes in the permeability of the porous media are identified. The chapter concludes with a description of the key elements of the conceptual model for permanganate-based groundwater remediation to be represented in the numerical model formulation.

Chapter 3 describes the development of the MIN3PD computer code. The numerical implementation is documented, including the mass conservation and constitutive equations employed and the methods and sequence of solution. Additional developments required to simulate specific features of the permanganate remediation problem are summarized. The methods employed to represent residual accumulations of non-aqueous phase liquids (NAPLs) and estimate changes in media porosity and permeability and relative aqueous permeability associated with heterogeneous chemical reactions are described. The addition of the radial grid geometries to the MIN3PD formulation, which facilitated efficient investigation of the permanganate remediation, is documented.

Chapter 4 provides the results of the benchmarking exercises performed to verify the MIN3PD code. Four general problem classes are utilized for code benchmarking. The first set of verification problems investigates the movement of fluids in variably saturated media. Fluid flow and solute transport problems are used to benchmark the implementation of the radial coordinate system. Variable density flow and solute transport problems are used to benchmark the MIN3PD formulation in simulating coupled flow and transport processes. The final two problems investigate reactive chemical transport.

Chapter 5 characterizes the general characteristics of permanganate-based remediation under free convection conditions. A sensitivity analysis identifies the system attributes which most significantly affect the distribution of aqueous species, and the utilization of the oxidant for contaminant treatment. The investigation demonstrates the role of density-driven fluid movement on

the distribution of permanganate and the reaction products. The strength of the coupling between fluid flow, chemical transport, and chemical reactions is characterized. The investigation of the remediation technology for a simplified hypothetical system provides a reference case applicable to the further utilization of the model to investigate site-specific cases.

Chapter 6 describes the development and calibration of the MIN3PD model of the North Haven remediation trial. The spatial and temporal evolution of the geochemical processes that occur in response to the permanganate injections are simulated and compared to the measured data. The detailed data set compiled at this facility provides the opportunity to employ the calibrated model to provide a system mass balance with a focus on a quantitative assessment of oxidant utilization for contaminant treatment. In addition, the data support an evaluation of the ability of a process-based numerical model to adequately simulate the evolution of permanganate-based groundwater remediation.

Chapter 7 documents the application of automated inverse modeling to investigate model parameterization for density-driven permanganate remediation. The iterative method employed to estimate optimal model parameters is documented. The reduction in the magnitude of model errors is characterized, and the improvement in the simulation of aqueous geochemistry is presented.

The final chapter of this study summarizes and further evaluates the findings of the previous chapters. In addition, the strengths and limitations of the current approach are described and recommendations for future work are given.

Chapter 2 Conceptual Model of Permanganate-Based Aquifer Remediation

The conceptual model of permanganate-based remediation of aquifers contaminated by chlorinated solvents involves the movement of fluids, solute transport, contaminant destruction, secondary geochemical reactions, and changes in porous media properties affecting fluid flow. This chapter introduces the problem posed by the remediation of TCE and PCE-contaminated aquifers, and summarizes key features of the remediation technology based on information from the literature and observations from a chemical oxidation field trial modeled later in this thesis. The chapter concludes with a discussion on the numerical implementation of the conceptual model.

2.1 Overview of Contaminants and Remediation Technology

The occurrence of the chlorinated solvents TCE and PCE in groundwater reflects the widespread use of these chemicals and their persistence in natural systems. Initially produced in North America in the 1920s, they were the most commonly used chemical solvents in the United States during the 1960s [Pankow and Cherry, 1996]. When present as a free phase product, TCE and PCE have densities greater than water, and are identified as dense non-aqueous phase liquids (DNAPLs). DNAPL dissolution in aquifers generates groundwater plumes with the contaminant present as dissolved aqueous species. Remediation of DNAPL-contaminated aquifers to comply with drinking water standards is complicated by the heterogeneous distribution and inaccessibility of the DNAPLs in the subsurface [Pankow and Cherry, 1996]. The difficulty posed by removing contaminant mass from heterogeneous DNAPL source areas has motivated research and development of in-situ destruction technologies, including chemical oxidation using the permanganate ion, hydrogen peroxide, Fenton's reagent, ozone, and the persulfate ion [Gonullu and Farquhar, 1989; USEPA, 1998; Siegrist et al., 2001; ITRC, 2005; Huling and Pivetz, 2006].

The permanganate ion has been used in the treatment of drinking water and wastewater to oxidize organic contaminants [Stewart, 1965; Siegrist et al., 2001]. The ion reacts with unsaturated carbon-carbon bonds, making the alkenes TCE and PCE susceptible to chemical oxidation [Yan and Schwartz, 2000; Huang et al., 2001]. The effectiveness and limitations in using permanganate for TCE and PCE remediation have been investigated in a variety of experimental settings, including column studies [Schnarr et al., 1998; Schroth et al., 2001; Al et al., 2006], two and three-dimensional

tank experiments [Reitsma and Marshall, 2000; Conrad et al., 2002; MacKinnon and Thomson, 2002; Lee et al., 2003], and at field remediation sites [West et al., 1997; Schnarr et al., 1998; Nelson et al., 2001; Stewart, 2002; Gavaska and Yoon, 2002]. While rapid oxidation of aqueous TCE and PCE by permanganate has been demonstrated in laboratory batch reactors [Yan and Schwartz, 1999; Huang et al., 1999; Hood et al., 2000; Huang et al., 2002; Dai and Reitsma, 2004], several factors have been identified which may limit the effectiveness of permanganate for in-situ treatment of contaminated aquifers. These factors include the reduction of porous media permeability due to the generation of gas bubbles and the precipitation of mineral phases [Schroth et al., 2001; MacKinnon and Thomson, 2002] and the reduction of pH and mobilization of trace metals in poorly buffered systems [Al et al., 2006].

Permanganate-based groundwater remediation is a technology that can be designed to take advantage of the density contrast between the oxidant solution and groundwater to drive the movement of the oxidant [Nelson et al., 2001]. Field investigations of permanganate-based remediation indicate that the oxidant generally sinks in an aquifer, and spreads along the upper surface of low permeability units [Nelson et al., 2001; Stewart, 2002]. A density-driven permanganate application may be implemented to promote oxidant spreading along the sedimentary interfaces where the DNAPLs are present, and promote oxidant diffusion into low permeability zones that have been contaminated by dissolved contaminants.

A field trial of density-driven permanganate remediation was performed in December 2000 at an industrial property in North Haven, USA, where TCE DNAPLs were present at the base of a sandy aquifer [Stewart, 2002]. The experiment was conducted within a driven sheet pile cell, which isolated the test area from the natural hydraulic gradient and the groundwater flow regime. A $KMnO_4$ solution (~44 g L^{-1}) approaching aqueous solubility was introduced into the aquifer using driven temporary injection points, and was not recovered following the injections, or affected by pumping or extraction wells. This experiment highlighted two elements that have provided specific motivation for the design of the current investigation. The absence of natural or imposed hydraulic gradients during the period following the oxidant injection emphasized the importance of gradients in fluid density in driving the movement of fluids and the transport of aqueous species. Field observations clearly demonstrated the sinking, spreading, and depletion of the oxidant. Secondly, geochemical data including major cations and anions, pH, and alkalinity measured near the center and edge of the oxidant plume indicate that chemical reactions extend beyond the area of contaminant treatment and significantly affect groundwater geochemistry. Including these additional geochemical parameters in

a performance assessment of the remediation technology provides additional constraints by incorporating multiple lines of evidence and facilitates the investigation of processes associated with competition for the oxidant and the feedback of geochemical system evolution on fluid flow.

In summary, the combination of chemical reactions with density-driven movement of fluids results in distributions of chemical reactants and reaction products which are difficult to interpret quantitatively in the absence of a coupled process simulator. Previous modeling investigations of permanganate oxidation of TCE/PCE have assumed the existence of constant density fluids [Hood, 2000; Hood and Thomson, 2000; Zhang and Schwartz, 2000; West et al., 2007; Mundle et al., 2007] or have significantly simplified the geochemical reaction network [Ibaraki and Schwartz, 2001]. The current investigation extends the scope of the modeling to consider coupling between fluid flow and reactive chemical transport including complex reaction networks, and investigates geochemical evolution in response to a permanganate application.

2.2 Movement of Variable Density Fluids

The density of a saturated solution of potassium permanganate is approximately 2.5 percent greater than pure water [CRC, 2001]. Results from laboratory experiments suggest that density variations of this magnitude can promote complex flow and mixing patterns [Schincariol and Schwartz, 1990; Oostrom et al., 1992; Swartz and Schwartz, 1998]. Monitoring data collected during permanganate remediation field trials depict the sinking of the oxidant and reaction products [Nelson et al., 2001; Stewart, 2002]. Therefore, an appropriate mathematical representation of the dynamics of movement of variable density fluids was a fundamental requirement for this investigation.

Density-dependent flow occurs when gradients in fluid density affect the movement of fluids [Zheng and Bennett, 2002], driven by gradients in fluid density primarily related to differences in temperature or solution composition [Voss, 1984]. The term density-driven flow is used throughout this thesis to describe the situation in which free (density-driven) convection is predominant over forced (hydraulically driven) convection in controlling the movement of fluids and solutes [Schincariol and Schwartz, 1990; Simmons et al., 2001]. The permanganate oxidation technology modeled in the current investigation includes an initial period of forced convection during the oxidant injection, followed by an extended period of free convection.

The primary variables affecting fluid density include pressure, temperature, and the concentration of dissolved solutes [Voss, 1984; Kipp, 1986]:

$$\rho = f(P,T,C) \tag{2-1}$$

where ρ is the fluid density [ML^{-3}] and P, T, and C represent applied pressure, fluid temperature, and the concentration of dissolved solutes. Variable density flow problems may be generalized to consider the movement and interaction of multiple fluid phases [White and Oostrom, 2000; Xu et al., 2004]. The current research focuses on the case in which water comprises the only mobile fluid present.

The minimal compressibility of water is reflected in the weak dependence of water density on applied pressure. An increase in fluid pressure of 10^6 Pascals (equivalent to approximately 100 m of hydraulic head) increases the density of water by approximately 0.04 percent [Kipp, 1986]. In contrast, an increase in fluid temperature from 10 to 20 degrees Celsius results in a decrease in water density of approximately 0.15 percent [CRC, 2001]. The movement of groundwater driven by gradients in fluid temperature has been investigated in hydrothermal settings [Steefel and Lasaga, 1994; Alt-Epping, 2000] and in the context of radioactive waste disposal [Kipp, 1986; Herbert et al., 1988; Oldenberg and Pruess, 1995; Konikow et al., 1997; Kolditz et al., 1998]. Research performed on permanganate has not identified significant changes in system temperatures resulting from permanganate oxidation of TCE/PCE or reduced phases present in aquifer sediments [Yan and Schwartz, 1999; Siegrist et al., 2001]. The density of a 44 g L^{-1} solution of potassium permanganate is approximately 2.5 percent greater than pure water [CRC, 2001]. Accordingly, gradients in dissolved solute concentrations are the principal component of fluid density gradients in the current investigation.

The average density of seawater is approximately 1.025 Kg L^{-1} [CRC, 2001], similar to the injected permanganate solutions modeled in the current investigation. Saltwater intrusion into freshwater aquifers has been a primary focus in modeling the movement of variable density fluids and the transport of dissolved chemicals [Henry, 1964; Pinder and Cooper, 1970; Segol et al., 1975; Segol and Pinder, 1976; Frind, 1982; Huyakorn et al., 1987; Voss and Souza, 1987; Sanford and Konikow, 1989; Voss and Souza, 1998; Shoemaker, 2004; Sanz and Voss, 2006]. Results of these investigations have indicated that density contrasts between freshwater and saltwater were significant in affecting patterns of fluid flow and mass transport. Investigations of the behavior of variable

density fluids in heterogeneous media revealed a propensity for dense fluids to sink and spread along the top of low permeability sediments [Schincariol and Schwartz, 1990], consistent with behavior reported from field experiments performed with permanganate solutions [Nelson et al., 2001; Stewart, 2002]. Two-dimensional laboratory experiments [Schincariol and Schwartz, 1990] indicated that spatial variation in hydraulic conductivity plays a major role in controlling solute transport in a variable density system. Reductions in hydraulic conductivity on the order of ½-order of magnitude influenced the movement of dense plumes. Mounding of dense fluids along the top of low permeability units resulted in the movement of dense plumes upstream against the hydraulic gradient [Schincariol and Schwartz, 1990].

Variable density flow and chemical transport exhibits fully coupled behavior due to the interdependence of the movement of fluids and the movement and accumulation of dissolved solutes [Holzbecher, 1998; Diersch and Kolditz, 2002]. When dilute concentrations of dissolved aqueous species are present, fluid movement affects the distribution of chemicals, but the distribution of dissolved chemicals does not significantly affect fluid flow patterns. However, elevated solute concentrations affect fluid flow patterns, and bi-directional coupling occurs. Maximum coupling and resulting non-linearity in behavior occur in the presence of high density contrasts, sharp gradients in fluid density, and in the absence of imposed hydraulic gradients driving fluid flow patterns [Oldenberg and Pruess, 1995; Simpson and Clement, 2003; Simpson and Clement, 2004]. Convective instabilities may develop when a higher density fluid overlies a lower density fluid [Schincariol and Schwartz, 1990; Swartz and Schwartz, 1998; Ibaraki et al., 2000; Diersch and Kolditz, 2002]. The occurrence of fluid convection cells results in the development of lobe-shaped protuberances that form along the bottom edge of the dense plume, which act to enhance the vertical spreading of solutes [Simmons et al., 2002]. Figure 2-1 illustrates the development of convective instabilities documented by Schincariol and Schwartz [1990]. The authors reported that the locations of convection cells were not reproduced in consecutive experiments, a condition interpreted to indicate chaotic behavior. In natural porous media, heterogeneities at multiple scales may generate instabilities [Schincariol et al., 1994; Schincariol et al., 1997]. The sensitivity of the movement of variable density fluids to pore-scale properties of porous media provides a challenging problem for mathematical modeling; this issue is explored at the conclusion of this chapter.

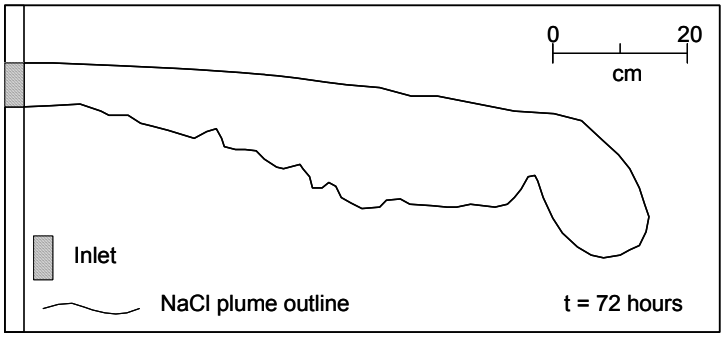

Figure 2-1. Instability development in a salt plume in homogeneous porous media. Direction of flow is from left to right, and the salt source is 2,000 mg L^{-1} NaCl. A vertical cross-section view is depicted [Schincariol and Schwartz, 1990].

A fundamental difference between the current research and most previous investigations of variable density flow and transport processes arises from the reactivity of the oxidant solution. A dense plume is established by the injection of an oxidant solution [Nelson et al., 2001]. The chemical composition of the plume evolves as the oxidant reacts with reduced phases present in the porous media, generating reaction byproducts [MacKinnon and Thomson, 2002; Lee et al., 2003]. The reaction byproducts differ in their solubility, reactivity, and mobility in porous media [Al et al., 2006]. The chemical reactions may affect the density and strength of the oxidant plume, and affect the permeability of the porous media [Schroth et al., 2001; Conrad et al., 2002; MacKinnon and Thomson, 2002; Lee et al., 2003]. Accordingly, the progress of chemical reactions represents additional variables affecting the distribution of the oxidant.

2.3 Reaction Network

The reaction network associated with permanganate-based remediation of aquifers contaminated with TCE and PCE DNAPLs includes multiple chemical reactions, which are categorized in the following discussion as primary and secondary reactions. Primary reactions are defined as those which directly involve the oxidant, including the oxidation of targeted contaminants [Yan and Schwartz, 1999; Huang et al., 1999; Hood et al., 2000; Yan and Schwartz, 2000; Huang et al., 2002], non-targeted oxidation of aquifer solids [Mumford et al., 2005; Honning et al., 2007], and decomposition of the oxidant by autocatalysis [Rees, 1987; Siegrist et al., 2001]. Secondary reactions, which do not directly involve the oxidant, reflect system response to the primary reactions. DNAPL dissolution is

an example of a secondary reaction which may be significant in determining the progress of primary reactions [Urynowicz, 2000; Urynowicz and Siegrist, 2005; Kim and Gurol, 2005]. The following discussion describes the reaction network and the stoichiometries of the individual reactions. Reaction kinetics are discussed in Section 2.4.

2.3.1 Primary Oxidation Reactions

The fundamental chemical reaction associated with the oxidation of chlorinated solvents by permanganate is the transfer of electrons from the aqueous chlorinated solvent species to the permanganate [Siegrist et al., 2001; ITRC, 2005]. The theoretical reaction stoichiometry for the mineralization of TCE and PCE using permanganate is given by Siegrist et al. [2001]:

$$C_2HCl_{3(aq)} + 2MnO_4^- \rightarrow 2CO_2 + 3Cl^- + 2MnO_{2(s)} + H^+ \quad (2\text{-}2)$$

$$C_2Cl_{4(aq)} + \tfrac{4}{3}MnO_4^- + \tfrac{4}{3}H_2O \rightarrow 2CO_2 + 4Cl^- + \tfrac{4}{3}MnO_{2(s)} + \tfrac{8}{3}H^+ \quad (2\text{-}3)$$

Detailed investigation of the mechanisms for TCE and PCE oxidation indicate that mineralization proceeds as a series of sequential reactions. The permanganate reacts with aqueous TCE/PCE to form an intermediate cyclic compound, which rapidly decomposes to generate carboxylic acids including formic, oxalic, and glyoxylic acids [Yan and Schwartz, 1999; Yan and Schwartz, 2000; Huang et al., 2002]. These reactions are illustrated for the oxidation of TCE:

$$C_2HCl_{3(aq)} + MnO_4^- \rightarrow I_c \rightarrow \gamma CA + 3Cl^- + MnO_{2(s)} \quad (2\text{-}4)$$

where I_c represents the intermediate cyclic ester, and CA and γ represent the carboxylic acids and corresponding stoichiometric coefficients. In the final reaction step, the carboxylic acids react with permanganate, generating carbon dioxide:

$$\gamma CA + MnO_4^- \rightarrow \beta CO_2 + MnO_{2(s)} \quad (2\text{-}5)$$

where β is the stoichiometric coefficient for carbon dioxide. Laboratory investigations have indicated nearly complete dechlorination of TCE and PCE [Yan and Schwartz, 1999; Yan and Schwartz, 2000; Huang et al., 2002; Kim and Gurol, 2005]. However, incomplete conversion of carboxylic acids to carbon dioxide has been identified by several investigators [Yan and Schwartz 2000; Huang et al.,

2002; Kim and Gurol, 2005], resulting in the consumption of less permanganate than predicted using Equations (2-2) and (2-3).

The manganese oxides generated by the reduction of permanganate by target and non-targeted reactions (see below) affect many aspects of permanganate-based remediation, including reaction rates and the permeability of the porous media [Schroth et al., 2001; MacKinnon and Thomson, 2002; Urynowicz, 2000; Urynowicz and Siegrist, 2005]. The manganese oxides have been interpreted to consist of colloidal manganese (IV) dioxides [Yan and Schwartz, 1999], while Al et al. [2006] determined that the Mn valence in the particles ranged between Mn(II) and Mn(IV). In acidic solutions (pH < 3.5), manganese dioxides may continue to oxidize aqueous TCE and PCE, generating Mn^{2+} ions [Hood et al., 2000; MacKinnon and Thomson, 2002; Kim and Gurol, 2005]:

$$C_2HCl_{3(aq)} + 3MnO_{2(s)} + 3H^+ \rightarrow 2CO_2 + 3Mn^{2+} + 3Cl^- + 2H_2O \quad (2\text{-}6)$$

$$C_2Cl_{4(aq)} + 2MnO_{2(s)} \rightarrow 2CO_2 + 2Mn^{2+} + 4Cl^- \quad (2\text{-}7)$$

Permanganate injected into an aquifer is affected by non-targeted reactions, due to the indiscriminant behavior of the oxidant [ITRC, 2005; Crimi and Siegrist, 2005; Mumford et al., 2005; Honning et al., 2007; Urynowicz et al., 2008]. The total consumption of permanganate resulting from reactions with the porous medium defines the natural oxidant demand (NOD). Soil organic matter (SOM) is expected to be the main contributor to the NOD in aerobic sandy aquifers, while reduced iron, manganese, and sulfides may be significant contributors to the NOD in reducing environments [Barcelona and Holm, 1991; Mumford et al., 2005; Honning et al., 2007].

SOM in aquifer sediments is a complex mixture derived from the weathering of parent organic materials [Schwarzenbach et al., 1993; Hartog et al., 2004]. The chemical composition of SOM may be modeled as a simple carbohydrate (CH_2O with C in oxidation state 0) [Stumm and Morgan, 1996; Mumford et al., 2005]. Alternatively, Honning et al. [2007] modeled organic carbon as $C_7H_8O_4$ (C in oxidation state 0). Using these representations, the reaction stoichiometries for oxidation of SOM take the following forms:

$$3CH_2O_{(s)} + 4MnO_4^- + 4H^+ \rightarrow 3CO_2 + 4MnO_{2(s)} + 5H_2O \quad (2\text{-}8)$$

$$3C_7H_8O_{4(s)} + 28MnO_4^- + 28H^+ \rightarrow 21CO_2 + 28MnO_{2(s)} + 26H_2O \quad (2\text{-}9)$$

Although different reaction stoichiometries are indicated in Equations (2-8) and (2-9), the ratio between the mass of permanganate and the mass of organic carbon is equivalent [Honning et al., 2007]. However, the presence of more oxidized or reduced forms of SOM will affect the mass ratio in the reaction between permanganate and organic matter [Mumford et al., 2005].

If present in the aquifer sediments, reduced mineral phases are also prone to oxidation by permanganate. For example, oxidation of pyrite in aquifer sediments may be indicated by increases in aqueous sulfate concentrations [Nelson et al., 2001]:

$$FeS_2 + 5MnO_4^- + 4H^+ \rightarrow Fe^{3+} + 2SO_4^{2-} + 5MnO_{2(s)} + 2H_2O \quad (2\text{-}10)$$

Manganese oxide particles may catalyze the decomposition of permanganate [Rees, 1987; Siegrist et al., 2001; Honning et al., 2007], providing the third primary reaction pathway for oxidant consumption:

$$4MnO_4^- + 2H_2O \rightarrow 3O_2 + 4OH^- + 4MnO_{2(s)} \quad (2\text{-}11)$$

Although studies have indicated that minimal decomposition occurred in a pure permanganate solution over a period of several years [Rees, 1987], the extent of autocatalyzed permanganate decomposition in porous media represents a potential loss mechanism for an injected oxidant solution [Siegrist et al., 2001; Honning et al., 2007]. Reaction stoichiometry for permanganate oxidation of water indicates that the generation of hydroxyl ions may result in increased pH.

2.3.2 Secondary Chemical Reactions

Chemical reactions consuming the oxidant affect solution chemistry, which in turn motivates a set of secondary chemical reactions which do not directly involve the oxidant [Stewart, 2002]. The consideration of secondary chemical reactions is necessary to interpret many of the geochemical response patterns observed during a permanganate injection [Nelson et al., 2001; Stewart, 2002]. These reactions, in particular the mass transfer reactions described below, may be significant in affecting the availability of aqueous species which react with the oxidant [Kim and Gurol, 2005].

At many contaminated sites, including the field site modeled in the current investigation, TCE is present in three phases, consisting of free phase DNAPLs, dissolved species, and contaminants adsorbed onto aquifer solids [Stewart, 2002]. DNAPL dissolution is illustrated for the case of TCE:

$$C_2HCl_{3(DNAPL)} \rightarrow C_2HCl_{3(aq)} \tag{2-12}$$

In the context of permanganate-based remediation of DNAPLs, the progress of Equation (2-12) is central to the effectiveness of the remediation method [Urynowicz and Siegrist, 2005; Kim and Gurol, 2005]. Sorption and desorption reactions represent a second mass transfer mechanism affecting dissolved TCE and PCE concentrations [Chiou et al., 1983]. The partitioning of organic contaminants into SOM has been identified as the principal sorption mechanism, evidenced by linear sorption isotherms over a range of dissolved concentrations, and the absence of competitive effects in the sorption of binary solutes [Chiou et al., 1983; Chiou et al., 1990; Schwarzenbach et al., 1993]. Linear chemical partitioning results in a fixed ratio between the concentrations of the dissolved and sorbed species:

$$C_2HCl_{3(aq)} = \frac{C_2HCl_{3(s)}}{K_d} \tag{2-13}$$

with K_d [L^3M^{-1}] representing the chemical-specific partitioning coefficient between the SOM and water.

Major cation (K^+, Na^+, Ca^{2+}, and Mg^{2+}) concentrations in groundwater evolve in response to a potassium permanganate injection due to the loading of potassium [Nelson et al., 2001; Stewart, 2002]. Aqueous cation concentrations are interrelated due to cation exchange reactions with clay minerals, SOM, and iron and manganese oxyhydroxides [Langmuir, 1997]. Potassium loading is expected to result in the desorption of Na^+, Ca^{2+}, and Mg^{2+} cations, increasing the dissolved concentrations of these cations:

$$K^+ + Na - X \leftrightarrow K - X + Na^+ \tag{2-14}$$

$$K^+ + 0.5Ca - X_2 \leftrightarrow K - X + 0.5Ca^{2+} \tag{2-15}$$

$$K^+ + 0.5Mg - X_2 \leftrightarrow K - X + 0.5Mg^{2+} \tag{2-16}$$

Although these reactions do not directly affect remediation efficiency, consideration of the cation exchange reactions allows these components to be included in the evaluation of measured system response behavior [Nelson et al., 2001] and provides an additional constraint for model predictions.

The oxidation of TCE and PCE by permanganate generates hydrogen ions, potentially resulting in a reduction of groundwater pH [Siegrist et al., 2001]. In contrast, the non-targeted oxidation of aquifer SOM and permanganate decomposition reactions consume hydrogen ions. Changes in aquifer pH reflect the cumulative result of these reactions, and the pH buffering characteristics of the aquifer. Aquifer pH buffering is provided primarily by calcite, dolomite, and clay minerals [Al et al., 2006]. A simple representation of aquifer pH buffering uses calcite dissolution and carbonate complexation reactions to approximate the aquifer buffering capability:

$$CaCO_{3(s)} + H^+ \leftrightarrow Ca^{2+} + HCO_3^- \quad (2\text{-}17)$$

$$HCO_3^- + H^+ \leftrightarrow H_2CO_3 \quad (2\text{-}18)$$

$$CO_3^{2-} + H^+ \leftrightarrow HCO_3^- \quad (2\text{-}19)$$

$$H_2CO_3 \leftrightarrow H_2O + CO_{2(aq)} \quad (2\text{-}20)$$

Previous investigations have indicated that the rate of TCE and PCE oxidation by permanganate is not sensitive to pH [Yan and Schwartz, 1999; Yan and Schwartz, 2000; Huang et al., 2002]. However, the speciation of manganese, the oxidation of carboxylic acids by permanganate, and behavior of trace metals are affected by pH [Yan and Schwartz, 2000; Siegrist et al., 2001; Huang et al., 2002; Kim and Gurol, 2005]. Trace metals, including arsenic, cadmium, cobalt, copper, chromium, lead, nickel, and zinc, may be present in the permanganate solution, or may be released through the oxidative dissolution of minerals [Siegrist et al., 2001; Crimi and Siegrist, 2003; Crimi and Siegrist 2004a; Al et al., 2006]. The latter condition is illustrated using the case of permanganate-mediated oxidative dissolution of chlorite, generating dissolved metal species:

$$Mg_4Fe_{0.94}Cr_{0.02}Mn_{0.03}Al_2Si_3O_{10}(OH)_8 + 0.35KMnO_4 + 17.13H^+ \rightarrow 4Mg^{2+} + 0.94Fe^{3+} + 0.02CrO_4^{2-} + 2Al^{3+} + 0.35K^+ + 0.38MnO_{2(s)} + 3H_4SiO_4 + 6.57H_20 \quad (2\text{-}21)$$

In addition to pH, the presence of manganese oxides generated by the reduction of permanganate represents a controlling factor on the mobility of trace metals [Siegrist et al., 2001; Crimi and Siegrist, 2004a]. Aqueous trace metal concentrations may be decreased through sorption onto manganese oxides and by co-precipitation of trace elements with the manganese oxides [Al et al., 2006].

2.4 Reaction Kinetics

Given the co-occurrence of multiple reactions which consume permanganate and the variable rates of fluid movement driven by gradients in fluid density, modeling chemical reaction rates is central to the current investigation. The following discussion summarizes the existing data regarding reaction rates, focusing on the three principal oxidant consumption pathways described previously.

2.4.1 Oxidation of Chlorinated Solvents

The rate of aqueous PCE/TCE oxidation by permanganate in laboratory batch reactors is proportional to the product of the permanganate and chlorinated solvent concentrations [Yan and Schwartz, 1999; Huang et al., 1999; Hood et al., 2000; Yan and Schwartz, 2000]:

$$R_{tce}^{ox} = -k_{tce}^{ox}[C_2HCl_{3(aq)}][MnO_4^-] \quad (2\text{-}22)$$

$$R_{pce}^{ox} = -k_{pce}^{ox}[C_2Cl_{4(aq)}][MnO_4^-] \quad (2\text{-}23)$$

where R_{tce}^{ox} is the reaction rate per unit volume [$ML^{-3}\ T^{-1}$] and k_{tce}^{ox} represents the second order rate constant [$mol^{-1}\ L^2\ H_2O\ L^{-1}$ bulk s^{-1}]. The time frame for the depletion of aqueous chlorinated solvents in the presence of excess permanganate is indicated by half lives of approximately 18 and 257 minutes for TCE and PCE in the presence of 1 x 10^{-3} mol L^{-1} permanganate [Yan and Schwartz, 1999]. DNAPL dissolution rates may govern the extent of TCE and PCE oxidation by permanganate [Urynowicz and Siegrist, 2005; Kim and Gurol, 2005]. NAPL dissolution behavior in

advecting water has been investigated in column experiments [Miller et al., 1990; Imhoff et al., 1994; Mayer and Miller, 1996; Nambi and Powers, 2003]. Although the mass transfer reaction depends on unknown pore-scale properties including the NAPL-water interfacial area, NAPL dissolution rates have been modeled as a function of the aqueous species concentration [Miller et al., 1990; Nambi and Powers; 2003]:

$$R_C^{diss} = -k_{diss}(C_s - C) \tag{2-24}$$

where R_C^{diss} is the dissolution rate per unit volume [$ML^{-3}\,T^{-1}$], k_{diss} is the mass transfer coefficient that incorporates effects of the chemical-specific mass transfer characteristics and the DNAPL-water interfacial area [T^{-1}], C_s is the solubility of the NAPL [ML^{-3}], and C is the aqueous species concentration [ML^{-3}]. Equation (2-24) may be generalized to consider DNAPL dissolution in the presence of permanganate and the effect of progressing NAPL dissolution:

$$R_C^{diss} = -\left(k_{diss} + k_{diss,ox}[MnO_4^-]\right)(C_s - C)\left(\frac{\varphi}{\varphi_0}\right)^{\alpha_{DNAPL}} \tag{2-25}$$

where $k_{diss,ox}$ relates the dissolution rate to the permanganate concentration [$M^{-1}L^3T^{-1}$], φ and φ_0 represent the current and initial volume fractions of DNAPL, and α_{DNAPL} is a fitting coefficient used to model reduction in DNAPL accessibility associated with DNAPL depletion. The inclusion of a second reaction rate coefficient ($k_{diss,ox}$) provides a mechanism to account for reaction-enhanced NAPL dissolution [Cussler, 1997; Urynowicz and Siegrist, 2005]. Reaction enhancement is conceptualized as the result of permanganate diffusion into stagnant groundwater separating the NAPL phase from the mixed or flowing aqueous phase. The depletion of aqueous TCE or PCE in the immediate vicinity of NAPL-water interfaces increases mass transfer to the aqueous phase [Cussler, 1997].

Using Equation (2-25) to model DNAPL dissolution in the presence of permanganate requires fitting three unknown parameters ($k_{diss,}$ $k_{diss,ox}$, α_{DNAPL}). The relationship between the lumped rate constant k_{diss} to groundwater flow and porous media characteristics can be estimated using the following relationship:

$$k_{diss} = \frac{ShD_m}{(d_{50})^2} \tag{2-26}$$

where d_{50} is the mean grain size diameter [L] and D_m is the free-phase diffusion coefficient of the dissolved species [L^2T^{-1}]. The correlations developed by Miller et al. [1990] and Nambi and Powers [2003] compute the Sherwood number (Sh) using the following expressions:

$$Sh = 12\,Re^{0.75}\,\varphi_{NW}^{0.6}\,Sc^{0.5} \tag{2-27}$$

$$Sh = 37.15\,Re^{0.61}\,S_{NW}^{1.24} \tag{2-28}$$

where Re is the Reynolds number, φ_{NW} is the volume fraction of the non-wetting phase, S_{NW} is the saturation of the non-wetting phase, and Sc is the Schmidt number. The Reynolds and Schmidt numbers are given by:

$$Re = \frac{d_{50}\rho\nu}{\mu} \tag{2-29}$$

$$Sc = \frac{\mu}{\rho D_m} \tag{2-30}$$

where ρ is the fluid density [ML^{-3}], ν is fluid seepage velocity [LT^{-1}], and μ is the dynamic viscosity [$ML^{-1}T^{-1}$]. Estimates of k_{diss} as a function of fluid velocity for a medium-grained sand using the Miller et al. [1990] and Nambi and Powers [2003] correlations are illustrated in Figure 2-2.

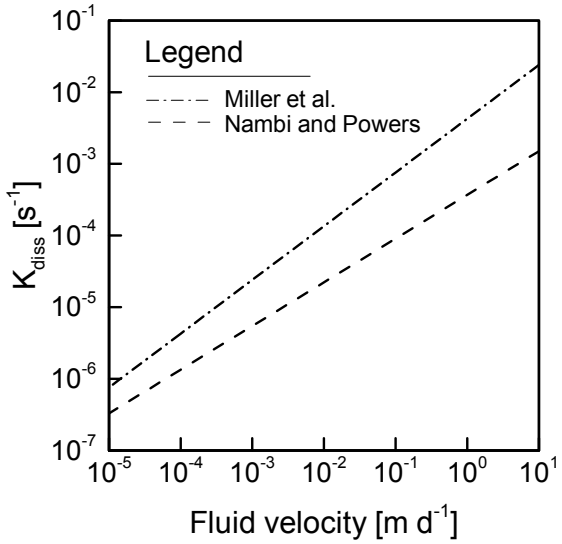

Figure 2-2. Relationship between fluid seepage velocity and DNAPL dissolution rate constant in a medium-grained sand.

As indicated in Figure 2-2, the dissolution coefficient increases with fluid velocity, reflecting the importance of fluid advection in removing chemical mass from water-DNAPL interfaces for non-reactive systems.

2.4.2 Organic Carbon Oxidation

Reaction kinetics between permanganate and aquifer SOM have been investigated in Borden aquifer sands [Schnarr et al., 1998; Mumford et al., 2005] and in sediments collected from various investigation sites [Honning et al., 2007; Urynowicz et al., 2008]. These results indicate that SOM is comprised of fractions with varying degrees of reactivity with permanganate. Honning et al. [2007] modeled the initial 8 - 12 hours of the reaction between permanganate and reactive SOM using first order reaction kinetics:

$$R^{ox}_{CH_2O} = -k^{ox}_{CH_2O}[MnO_4^-] \tag{2-31}$$

where $R^{ox}_{CH_2O}$ is the oxidation rate per unit volume and $k^{ox}_{CH_2O}$ is a rate constant.

The presence of recalcitrant SOM was indicated by continued permanganate consumption over a period of approximately one week [Honning et al., 2007], and 21 weeks [Mumford et al., 2005]. The investigations of permanganate oxidation of SOM indicate that the reactivity of reactive and recalcitrant fractions differ by several orders of magnitude [Mumford et al., 2005; Honning et al., 2007].

A general expression for permanganate consumption of SOM includes decreases in reactivity which occur with progressing depletion of SOM:

$$R^{ox}_{CH_2O} = -k^{ox}_{CH_2O}\left[MnO_4^-\right]\left(\frac{\varphi_{CH_2O}}{\varphi_{CH_2O,0}}\right)^{\alpha_{CH_2O}} \tag{2-32}$$

where φ and φ_0 represent the current and initial volume fractions of SOM, and α_{CH_2O} is a fitting coefficient.

2.4.3 Autocatalytic Decomposition of Permanganate

Laboratory investigation of permanganate oxidation of water indicates that the reaction rate is negligible in an aqueous system [Rees, 1987]. However, permanganate may decompose more rapidly in the presence of manganese oxides [Rees, 1987; Siegrist et al., 2001], though the extent of the catalysis is not known [Honning et al., 2007]. Traces of MnO_2 initially present in the permanganate or formed by the reaction of permanganate with reducing agents, such as organic matter or $C_2HCl_{3(aq)}$, may lead to catalyzed decomposition of permanganate [Honning et al., 2007]. A literature search did not identify data to constrain the rate of manganese-oxide catalyzed permanganate oxidation of water. For simplicity, an empirical description of the decomposition kinetics assumes first-order dependence of the decomposition reaction on the permanganate concentration:

$$R^{ox}_{H_2O} = -k^{ox}_{H_2O}[MnO_4^-] \tag{2-33}$$

2.5 Evolution of Media Permeability

The effective permeability for the movement of water in an aquifer is a function of the intrinsic permeability of the porous medium, and the relative permeability with respect to the aqueous phase [Scheidegger, 1974; Mualem, 1976; Zheng and Bennett, 2002]. Chemical reactions which occur during permanganate-based aquifer remediation affect both the intrinsic permeability of the porous medium and the relative permeability of the aqueous phase [Schroth et al., 2001; MacKinnon and Thomson, 2002]. The intrinsic permeability of the porous medium is determined by the morphology and geometry of the network of connected pore spaces [Scheidegger, 1974]. In a reactive system, the precipitation and dissolution of minerals affect the intrinsic permeability [Sanford and Konikow, 1989; Bryant et al., 1993; Reis and Acock, 1994]. In the current investigation, changes in intrinsic permeability of the porous medium are expected to be dominated by the precipitation of manganese oxides [Siegrist et al., 2001].

The accumulation of manganese oxides has been interpreted to limit the extent of DNAPL remediation in laboratory experiments [MacKinnon and Thomson, 2002; Conrad et al., 2002; Li and Schwartz, 2004b]. Laboratory and field investigations have documented a general correspondence between the location of DNAPLs with the accumulation of manganese oxides [Nelson et al., 2001; MacKinnon and Thomson, 2002; Conrad et al., 2002; Lee et al., 2003]. Calculations of bulk porosity losses derived from accumulations of manganese oxides indicate porosity reductions in the range of 1 to 3 percent [MacKinnon and Thomson, 2002; Stewart, 2002]. These calculations indicate that pore spaces do not appear to be filled with manganese oxides. However, the reduction of the permeability of individual pore throats, and the modification of a pore network due to pore throat clogging represent potential mechanisms for bulk permeability losses [Wise, 1992; Reis and Acock, 1994; MacKinnon and Thomson, 2002]. The behavior of manganese oxide particles is affected by several factors, including DNAPL saturations, aqueous geochemistry, hydrodynamic conditions, and the electrostatic properties of the particles [Siegrist et al., 2001; Crimi and Siegrist, 2004b; Al et al., 2006]. This complicates the development of a functional relationship between the generation of manganese oxides and reductions in intrinsic permeability of the porous medium.

The concept of relative permeability is applied in modeling the movement of a fluid in the presence of multiple fluid phases [Mualem, 1976; Van Genuchten, 1980; Lenhard and Parker, 1987; Parker et al., 1987]. In addition to water and DNAPLs, gases generated by the chemical oxidation reactions may accumulate in the porous medium, resulting in the presence of three fluid phases

[Schroth et al., 2001; Li and Schwartz, 2004b]. The presence of gases and DNAPLs reduces the water-filled porosity of the medium and the corresponding relative permeability for the movement of water [Lenhard et al., 2004]. The presence of trapped gas bubbles may result in significant reductions in the relative aqueous permeability [Schroth et al., 2001; Amos and Mayer, 2006]. The mineralization of TCE and PCE generates carbon dioxide [Siegrist et al., 2001; MacKinnon and Thomson, 2002]. Aqueous carbon dioxide is subject to the pH-dependent speciation reactions described previously in Equations (2-17) through (2-20). Schroth et al. [2001] noted a reduction in bubble formation associated with TCE DNAPL oxidation in the presence of a pH buffering agent. These results were indicative of the predominance of more soluble HCO_3^- species at neutral pH. These results confirmed the importance of chemical reactions including buffering reactions in the accumulation of gas bubbles.

While several laboratory experiments have documented permeability reductions associated with permanganate-based aquifer remediation, the extrapolation of these results to a density-driven permanganate application at a field site is uncertain. Fluid flow dynamics in a density-driven permanganate application differ from forced flow regimes characteristic of the laboratory experiments, and DNAPL distributions are expected to exhibit a higher degree of heterogeneity than present in laboratory analogues [Huling and Pivetz, 2006].

2.6 Implications for Model Development

The conceptual model of permanganate-based aquifer remediation describes the reactive system, and the coupling between fluid movement, solute transport, and chemical reactions. It is based on laboratory investigations of density-dependent flow [Elder, 1967; Schincariol and Schwartz, 1990; Oostrom et al., 1992; Schincariol and Schwartz, 1994], intra-aqueous oxidation of chlorinated solvents by MnO_4^- [Yan and Schwartz, 1999; Hood et al., 2000; Huang et al., 2001], and inter-phase mass transfer resulting from DNAPL dissolution [Nambi and Powers, 2003; Kim and Gurol, 2005; Urynowicz and Siegrist, 2005]. The current conceptual model incorporates the results from field investigations of the inject-and-leave permanganate remediation technology [Nelson et al., 2001; Stewart, 2002]. Results from these field trials indicate that gradients in fluid density are significant regarding the movement of the oxidant, and documented temporal changes in aqueous geochemistry resulting from the oxidant injections.

A significant step in numerical model development is identifying the processes to be represented in the model, and the processes which will not be explicitly represented. This evaluation considers the objectives of the modeling, the data available to constrain the modeling, and the computational burden associated with model execution. The following discussion summarizes the decisions made in guiding the development of numerical model capabilities.

2.6.1 Density-dependent Flow

The results of previous field experiments [Nelson et al., 2001; Stewart, 2002] indicate that density effects are significant to the delivery of the oxidant, evidenced by the sinking and spreading of the oxidant solution. The movement of the treatment solution affects the contact and reaction of the oxidant with the DNAPLs, a primary element controlling the efficiency of the technology. Process-based models of this technology require a formulation relating solute concentrations, fluid density, and the movement of fluids. In comparison with constant density fluids, modeling variable density flow and chemical transport requires the use of different sets of conservation and constitutive equations, which are developed in Chapter 3.

2.6.2 Reactive Transport

The formulation of MIN3P [Mayer et al., 2002] addresses the reaction and transport aspects of permanganate remediation, and provides the basis for the development of the computer code used in the current investigation. MIN3P employs the representative elementary volume (REV) approach in representing physiochemical attributes. Several elements of the current investigation, including the movement of variable density fluids, the existence of DNAPLs, and the movement of colloidal manganese oxide particles are governed by conditions present at the pore scale [Schincariol and Schwartz, 1990; Miller et al., 1990; Mayer and Miller, 1992; Siegrist et al., 2001; Nambi and Powers, 2003; Thomson, 2004]. Nevertheless, the scale of interest inherent to permanganate-based aquifer remediation dictates a REV-based approach, and the use of model parameters to represent upscaled or effective properties of the system investigated.

2.6.3 Changes in Media Permeability

The MIN3P program includes an empirical relationship between media porosity and permeability [Carman, 1937], allowing changes in media permeability to be related to mineral dissolution and precipitation. A limitation of this approach is that the actual pore-scale processes are not represented.

However, minimal data is available to quantify permeability changes at the scale of the field site. As a result, the development of alternate porosity-permeability models was not justified.

The issue of gas bubble formation during chemical oxidation with permanganate has not been investigated quantitatively. No data are available to evaluate the occurrence or distribution of gas bubbles at field sites. The generation of gas bubbles, and the associated reduction in media permeability are not represented in the numerical model formulation. Pore-scale processes affecting media permeability and relative aqueous permeability are represented by REV-scale relationships predicting media permeability [Carman, 1937; Parker et al., 1987]. This approach was determined suitable to represent processes that are poorly constrained by the available data.

2.6.4 Computational Constraints

Modeling fate and transport of multiple reactive components in three dimensions presents a computationally intensive problem. The development and investigation of a simplified analogue is advantageous to various stages of model development and evaluation. Many aspects of the current problem are consistent with two-dimensional radial symmetry about the oxidant injection point. The modular programming structure of MIN3P facilitates the development of radial grids, which are addressed in the model formulation.

Chapter 3 Theoretical Development

Coupled process models have been developed previously to investigate variable density flow systems [Voss, 1984; Kipp, 1986; Frolkovic, 1999; Diersch, 2002; Langevin and Guo, 2006], but were mostly associated with the movement of non-reactive solutes [Ackerer et al., 1999; Oltean and Buès, 2001; Frolkovic and De Schepper, 2001; Johannsen et al., 2002]. Numerical studies included assessments of the saline water intrusion into coastal aquifers [Huyakorn et al., 1987; Sanz and Voss, 2006], fluid flow in the vicinity of salt deposits [Konikow et al., 1997] and simulations of the influence of tides on contaminant migration [Brovelli et al., 2007].

Investigations of reactive variable density problems include calcite dissolution and precipitation in saltwater-freshwater mixing zones [Sanford and Konikow, 1989; Rezaei et al., 2005], geochemical reactions within hydrothermal systems [Steefel and Lasaga, 1994; Alt-Epping, 2000], transport of reactive solutes in aquifers [Zhang and Schwartz, 1995; Zhang et al., 1998], reaction front instabilities in carbonate media [Freedman and Ibaraki, 2002], coupled thermohaline flow in fractured media [Graf and Therrien, 2007], the effect of chemical reactions on salt plume development [Post and Prommer, 2007], and the study of interactions between evapo-concentration and geochemical reactions on the evolution of flow patterns [Bauer-Gottwein et al., 2007]. However, a model for the simulation of MnO_4-based groundwater remediation that includes the movement of variable density fluids, the relevant geochemical reactions, and changes in media porosity and permeability has not been developed to date.

This chapter describes the mathematical basis and the formulation of the computer program developed to model permanganate-based aquifer remediation under free convection conditions, incorporating the elements of the conceptual model described in Chapter 2. A new modeling program, MIN3PD, was developed from the existing MIN3P reactive transport code [Mayer et al., 2002]. The MIN3P formulation included the capabilities for simulating the chemical reaction network described in the previous chapter, but did not include capabilities for density-dependent flow and transport, or the coupling between solution density and reaction progress. MIN3PD represents a generalization of MIN3P which simulates fully coupled fluid flow and reactive transport problems. The program simulates the movement of variable density fluids in variably saturated media under isothermal conditions and reactive chemical transport. Physical properties of the fluids, including density and viscosity, are computed as a function of dissolved solute concentrations. Additional

program modifications were implemented to address specific aspects of permanganate-based remediation. The net result of these changes was the development of a computer code with the capabilities necessary to simulate the processes incorporated in the conceptual model describing permanganate-based remediation aquifers contaminated with DNAPLs.

The following sections describe the governing and constitutive equations which provide the basis of the modeling. Subsequently, the numerical methods employed to approximate and solve the governing equations are described. The benchmarking of MIN3PD program is summarized in Chapter 4.

3.1 Governing Equations

The movement and reaction of a dense permanganate solution is described by governing equations for variable density groundwater flow and multicomponent reactive transport. The dependence of fluid density on aqueous chemical concentrations results in coupling between the movement of fluids and the movement and accumulation of dissolved chemical species [Voss and Souza, 1987; Oldenburg and Pruess, 1995; Diersch and Kolditz, 2002]. The reactive transport model MIN3P [Mayer et al., 2002] was reformulated to simulate the movement of variable density fluids, compute fluid density and viscosity based on aqueous component concentrations, and solve the coupled sets of equations describing fluid flow, chemical transport, and chemical reactions.

3.1.1 Variable Density Fluid Flow

The continuum modeling approach replaces the discontinuous physical media comprised of sediments and pore spaces with an equivalent continuous media, parameterized to represent system properties [Zheng and Bennett, 2002]. The movement of constant density water in fully saturated media is provided as a point of reference in the development of the generalized fluid flow equation:

$$S_s \frac{\partial h}{\partial t} = \nabla \cdot (K \nabla h) + Q_a \tag{3-1}$$

where S_s is the specific storage coefficient [L^{-1}], K is the hydraulic conductivity [LT^{-1}], Q_a represents fluid sources/sinks [T^{-1}], and h is the hydraulic head [L], representing the sum of fluid potentials associated with pressure and position [Zheng and Bennett, 2002]:

$$h = \frac{P_a}{\rho g} + z \tag{3-2}$$

where ρ is the density of the fluid [ML^{-3}], g is the magnitude of gravitational acceleration [LT^{-2}], and z is the height above datum [L]. In cases where fluid density is constant, hydraulic heads provide a measure of the total mechanical fluid potential, and Equation (3-1), formulated on the principle of conservation of fluid volume, conserves fluid mass. The generalization to variable density systems requires a change in variables used to quantify fluid potential, and the specification of constitutive relations necessary to compute fluid density. The conservation of fluid mass in variably saturated porous media with internal sources/sinks in a continuum takes the following form [Bear, 1979; Ackerer et al., 1999]:

$$\frac{\partial}{\partial t}(S_a \phi \rho) + \nabla \cdot (\rho \mathbf{q}_a) = \rho Q_a \tag{3-3}$$

where S_a is the aqueous phase saturation [-], ϕ is the porosity [L^3 void L^{-3} porous medium], and $\mathbf{q_a}$ is the specific discharge vector [LT^{-1}]. The specific discharge is formulated as a function of fluid pressures [Voss, 1984]:

$$\mathbf{q}_a = \frac{-k_r \mathbf{k}}{\mu}(\nabla P_a + \rho g \nabla z) \tag{3-4}$$

where $\mathbf{k}$ is the permeability tensor [L^2], μ is the dynamic viscosity [$ML^{-1}T^{-1}$], and P_a is the fluid pressure [$ML^{-1}T^{-2}$]. As described in subsequent sections, fluid density and viscosity are affected by the presence of dissolved solutes.

Computer programs simulating the movement of variable density fluids have been formulated using either freshwater heads or using fluid pressures. The freshwater head represents a theoretical quantity, computed using a reference freshwater density ρ_0 [Frind, 1982; Holzbecher, 1998; Langevin and Guo, 2006]:

$$h_f = \frac{P_a}{\rho_0 g} + z \tag{3-5}$$

A review of the variable density literature did not reveal a computational advantage in the use of either quantity in formulating the governing equations for fluid flow [Frind, 1982; Voss 1984; Holzbecher, 1998; Guo and Langevin, 2002]. Zheng and Bennett [2002] indicate that a fluid pressure-based formulation is generally preferable in modeling variable density problems. Fluid pressures are physical quantities which may be directly measured at field sites, and were selected for use in the current formulation.

The fluid mass accumulation term in Equation (3-3) includes temporal changes in fluid pressure, saturation, and the total solute concentration:

$$\frac{\partial}{\partial t}\left(S_a \phi \rho\right) = S_a \rho S_p \frac{\partial P_a}{\partial t} + \rho\phi \frac{\partial S_a}{\partial P}\frac{\partial P_a}{\partial t} + S_a \phi \frac{\partial \rho}{\partial c_t}\frac{\partial c_t}{\partial t} \tag{3-6}$$

where S_p is the specific storage coefficient [$M^{-1}LT^2$] defined with respect to changes in fluid pressure, and c_t is the total dissolved solute concentration [ML^{-3}]:

$$c_t = \sum_{i=1}^{i=nc} mw_i * T_i^a \tag{3-7}$$

where mw_i is the molecular weight of each component [g mol^{-1}], and T_i^a is the total aqueous component concentration for component A_i^c [mol L^{-1} H_2O]. The S_p coefficient is related to the specific storage coefficient S_s in Equation (3-1) by the following relationship:

$$S_p = \frac{S_s}{\rho_f g} \tag{3-8}$$

The elasticity of fluid is incorporated in the specific storage coefficient [Zheng and Bennett, 2002]. It is assumed that the elasticity of the fluid and porous media are independent of the dissolved solute concentration [Frind, 1982; Voss, 1984; Guo and Langevin, 2002].

The statement of fluid mass conservation for variable density fluids in variably saturated media is obtained by substituting Equation (3-4) into Equation (3-3):

$$\frac{\partial}{\partial t}(S_a \phi \rho) - \nabla \cdot (\rho \frac{k_r \mathbf{k}}{\mu}(\nabla P_a + \rho g \nabla z)) = \rho Q_a \tag{3-9}$$

The Oberbeck-Boussinesq (OB) approximation may be employed to simplify Equation (3-9) by conserving fluid volume instead of fluid mass [Holzbecher, 1998; Kolditz et al., 1998; Langevin and Guo, 2006]. In the expression of fluid volume conservation, spatial gradients in fluid density are considered only in the computation of specific discharge [Senger and Fogg, 1990; Holzbecher 1998]. The resulting equation, employing the OB approximation for variably saturated media is:

$$\frac{\partial}{\partial t}(S_a \phi) + \nabla \cdot (\frac{-k_r \mathbf{k}}{\mu}(\nabla P_a + \rho g \nabla z)) = Q_a \tag{3-10}$$

The errors associated with using the OB approximation increase with the magnitude of density variations present in the system investigated [Kolditz et al., 1998]. No advantage in employing the OB approximation was identified in the current investigation, and the mass-conservative fluid flow Equation (3-9) provided the basis for the development of the MIN3PD program.

3.1.2 Reactive Chemical Transport

Modeling the movement of variable density fluids requires concurrent modeling of the spatial distribution of parameters which affect fluid density. In the current study, fluid density is computed as a function of solute concentrations. MIN3PD solves a mass conservation equation for each aqueous component, which is given by:

$$\begin{aligned} &\frac{\partial}{\partial t}\left[S_a \phi T_j^a\right] + \frac{\partial}{\partial t}\left[S_g \phi T_j^g\right] + \nabla \cdot \left[\mathbf{q_a} T_j^a\right] - \nabla \cdot \left[S_a \phi \mathbf{D_a} \nabla T_j^a\right] \\ &- \nabla \cdot \left[S_g \phi \mathbf{D_g} \nabla T_j^g\right] - Q_j^{a,a} - Q_j^{a,s} - Q_j^{a,ext} - Q_j^{g,ext} = 0 \end{aligned} \tag{3-11}$$

where T_j^a is the total aqueous component concentration for component A_j^c [mol L^{-1} H_2O], S_g is the saturation of the gaseous phase [m^3 gas m^{-3} void], T_j^g [mol L^{-1} gas] is the total gaseous concentration for component A_j^c, $\mathbf{q_a}$ is the Darcy flux vector, $\mathbf{D_a}$ is the dispersion tensor for the aqueous phase, and $\mathbf{D_g}$ is the diffusion tensor for the gaseous phase. $Q_j^{a,a}$ [mol dm^{-3} porous medium] and $Q_j^{a,s}$ [mol dm^{-3}

porous medium] are internal source and sink terms from intra-aqueous kinetic reactions and kinetically controlled dissolution-precipitation reactions, and $Q_j^{a,ext}$ [mol dm^{-3} porous medium] and $Q_j^{g,ext}$ [mol dm^{-3} porous medium] are external source and sink terms for the aqueous and gaseous phase, respectively [Mayer et al., 2002].

Hydrodynamic dispersion in Equation (3-11) is modeled as a Fickian process, resulting in dispersive chemical fluxes proportional to the gradient in solute concentrations [Cussler, 1997]. However, when large contrasts in fluid density are present, dispersive fluxes may be affected by small-scale convective flow patterns. Research into the transport of brines [Hassanizadeh, 1986; Hassanizadeh and Leijnse, 1995; Schotting et al., 1999] indicates that Fickian models over-predicted chemical dispersion in the presence of sharp concentration gradients and low flow velocities. These results were interpreted to indicate the presence of small-scale vortices in fluid motion, reducing the longitudinal dispersion in the main flow direction [Schotting et al., 1999].

MIN3PD employs the Fickian dispersion model in simulating variable density flow and transport. This approach is consistent with recent model formulations [Frolkovic, 1999; Guo and Langevin, 2002; Langevin and Guo, 2006]. This approach was deemed appropriate for the focus of the current investigation.

3.2 Constitutive Relationships

Modeling permanganate-based remediation of aquifers contaminated with DNAPLs requires constitutive relationships between dissolved aqueous species concentrations and fluid density and dynamic viscosity. A second set of constitutive relationships is necessary to relate the medium permeability to the progress of chemical reactions. These relationships quantify the relative permeability of the medium for water in the presence of DNAPLs and air, and relate the intrinsic permeability of the medium to the dissolution and precipitation of mineral phases [Carman, 1937; Mualem, 1976].

3.2.1 Fluid Density and Viscosity

The relationship between fluid density and solute concentrations has been measured on mixtures of brines, seawater, and freshwater [Millero et al., 1982], and modeled using empirical relationships

[Frind, 1982; Voss, 1984; Kharaka et al., 1988; Guo and Langevin, 2002; Oldenburg and Pruess, 1995; Frolkovic and De Schepper, 2001] and Pitzer's ion interaction approach [Monnin, 1989; Monnin, 1994; Freedman and Ibaraki, 2002; Post and Prommer, 2007]. A commonly employed approach treats fluid density as a linear function of solute concentrations [Frind, 1982; Voss, 1984; Kharaka et al., 1988; Guo and Langevin, 2002]:

$$\rho = \rho_0 + \frac{\partial \rho}{\partial c_t} c_t \tag{3-12}$$

where ρ_0 is the freshwater density and $\frac{\partial \rho}{\partial c_t}$ is assumed to be constant. Reported values for the constant $\frac{\partial \rho}{\partial c_t}$ were 0.688 and 0.714 for geochemical modeling applications and seawater intrusion modeling, respectively [Kharaka et al., 1988; Guo and Langevin, 2002].

The linearity of the relationship between dissolved solute concentrations and fluid density was evaluated at the onset of the current investigation using the ion interaction modeling approach in the Volumetric Properties (VOPO) computer program [Monnin, 1994] obtained from the author. VOPO computes solution volume and density based on the concentrations of Na^+, K^+, Ca^{2+}, Mg^{2+}, Cl^-, SO_4^{2-}, HCO_3^-, and CO_3^{2-}, the ionic strength of the solution, and coefficients quantifying ion interactions [Monnin, 1994]. The modeling was performed using a series of dilutions and concentrations of seawater chemistry reported by Clegg and Whitfield [1991]. Modeling results indicated a linear relationship is present between the total dissolved solute concentration and fluid density between 1.0 and 100 g L^{-1} total dissolved solids (TDS), illustrated in Figure 3-1.

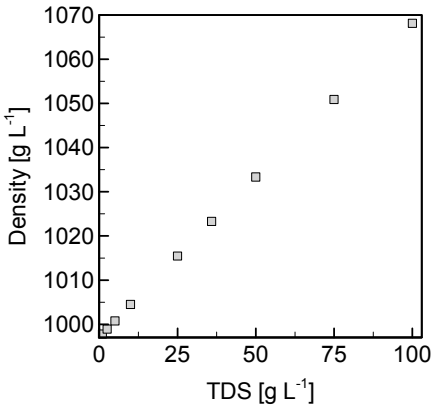

Figure 3-1. Relationship between total dissolved solids and fluid density for dilutions and concentrations of seawater between 1 and 100 g L^{-1}.

These results indicated that a linear relationship is appropriate for the range of solute concentrations present in the current investigation. A linear relationship of the form of Equation (3-12) was programmed in MIN3PD to relate fluid density to the TDS concentration. A more sophisticated approach based on the Pitzer ion interaction model [Monnin, 1989; Monnin, 1994] was not implemented in the current investigation due to the lack of ion interaction parameters for permanganate. Fluid density is not related to fluid temperature, limiting MIN3PD applicability to cases in which isothermal conditions prevail.

Fluid viscosity affects the specific discharge computed in Equation (3-9). The relationship between fluid dynamic viscosity and solute concentration was modeled using a polynomial of the form:

$$\mu = \mu_0 \left(1. + k_1 c_m + k_2 c_m^2 + k_3 c_m^3\right) \tag{3-13}$$

where μ_0 is the freshwater dynamic viscosity and c_m is the solute mass fraction [MM^{-1}]. The values of 0.4819, -0.2774, and 0.7814 for the three coefficients in Equation (3-13) were taken from Herbert et al. [1988].

3.2.2 Relative Media Permeability

The computation of relative permeability is required to simulate the movement of water in the presence of non-wetting fluids, including NAPLs and air. In the current investigation, the focus is on

remediation of unconfined aquifers. Under these conditions, sediments overlying the water table contain air and water. Water table mounding occurs in response to the injection of the oxidant solution. NAPLs are simulated in MIN3PD as immobile phases, but are distinguished from mineral phases in order to represent the effect of NAPL saturation on the movement of water.

In the current investigation, unsaturated conditions are present in the upper portion of the aquifer, and DNAPL is present at the base of the aquifer, which allows simplification of the relative permeability relationships to 2-phase conditions anywhere in the domain. In the current formulation, the total NAPL saturation S_n [-] is computed as a function of NAPL volume fractions and the media porosity:

$$S_n = \sum_{i=1}^{i=nnpl} \frac{\varphi_i}{\phi} \tag{3-14}$$

where S_n [-] is the NAPL saturation, and φ_i represents the volume fraction of each NAPL component within the NAPL phase. The parameter nnpl represents the number of chemicals making up the NAPL phase. In this thesis, the NAPL phase is restricted to a single component (e.g. TCE). However, MIN3PD allows for NAPL dissolution from multicomponent mixtures. Transient NAPL saturations are a function of the initial NAPL condition assigned, and chemical reactions depleting the NAPLs.

The aqueous phase saturation S_a is calculated using the following relations:

$$S_a = S_{ra} + \frac{1 - S_{ra}}{(1 + |\alpha P_a|^n)^m} \qquad P_a < P_{entry}\text{, gas phase present, NAPL absent} \tag{3-15}$$

$$S_a = 1 - S_n \qquad P_a \geq P_{entry}\text{, NAPL potentially present, gas phase absent} \tag{3-16}$$

where S_{ra} [-] defines the residual saturation of the aqueous phase, α [$M^{-1}LT^2$], n, [-] and m [-] are soil hydraulic function parameters, and P_{entry} is the air entry pressure [$ML^{-1}T^{-2}$]. The relative permeability k_{ra} is calculated as a function of the effective aqueous saturation using the relationships given by Parker et al. [1987]:

$$k_{ra} = S_{ea}^{l}\left[1 - \left(1 - S_{ea}^{1/m}\right)^m\right]^2 \tag{3-17}$$

$$S_{ea} = \frac{S_a^{agn} - S_{ra}}{1 - S_{ra}} \tag{3-18}$$

where S_{ea} [-] is the effective saturation of the aqueous phase and l is a dimensionless soil hydraulic parameters.

3.2.3 Intrinsic Media Permeability

MIN3PD estimates reductions in aquifer permeability due to the precipitation of minerals using the Carman-Kozeny relationship [Carman, 1937]. This relationship represents the permeability of porous media using an analogous straight-walled capillary tube. The relationship estimates permeability as a function of porosity and three fitting factors [Reis and Acock, 1994]:

$$k = \frac{\phi^3}{S_f \left(\frac{L_e}{L} \right)^2 (1-\phi)^2 S_g^2} \tag{3-19}$$

where S_f is the shape factor, $(L_e/L)^2$ is the tortuosity factor, and S_g is the specific surface area per grain volume. The shape factor approximates flow channels which do not have a circular cross-section, and the tortuosity factor accounts for flow channels which are not aligned with the overall flow direction. The specific surface area is a measure of the average pore size in the medium [Reis and Acock, 1994].

Application of Equation (3-19) to quantify permeability reductions requires an assessment of changes in the three fitting factors resulting from mineral precipitation. If the precipitate uniformly coats the pore walls, the tortuosity and shape factors are not expected to change significantly, while the specific surface area may change significantly [Reis and Acock, 1994]. Data generated by the current investigation does not support the development of a functional relationship between mineral precipitation and the morphology of connected pore spaces, represented by the fitting factors. Therefore, the present formulation incorporates the simplifying assumption that none of these factors change during mineral dissolution/precipitation reactions, and the relationship takes the following form:

$$k^t = \left[\frac{\phi^3}{(1-\phi)^2}\right]^t \left[\frac{(1-\phi)^2}{\phi^3}\right]^{initial} k^{initial} \quad (3\text{-}20)$$

where k^t and $k^{initial}$ represent the current and initial medium permeabilities.

3.3 Numerical Methods and Solution Methodology

Obtaining solutions to the governing equations describing the movement of variable density fluids in variably saturated media and reactive chemical transport developed in the previous sections requires the use of numerical methods. Primary issues in code development include the formulation of the discrete algebraic equations used to approximate the governing equations, and the mechanism employed to solve the interdependent fluid flow and chemical transport equations. These issues are described in the following sections.

3.3.1 Spatial Discretization

The finite volume method, which enforces fluid and chemical mass conservation in each model control volume, is used to discretize the spatial domain in MIN3PD. The grid geometry is equivalent to a block-centered finite difference grid, supporting simulations in one, two, and three spatial dimensions [Mayer et al., 2002]. This scheme was augmented by the development of the radial grid geometry, which may be employed in one and two spatial dimensions. The simulation of variable density flow and transport requires the specification of the orientation of the principle axes. The current MIN3PD formulation assumes that the x and y-directions in the model grid correspond to horizontal directions in space, and the z-axis is aligned with the direction of gravity.

3.3.2 Solution Methods

Following the MIN3P conventions, the set of fluid flow conservation equations and the set of reactive chemical transport equations are solved using Newton's method [Mayer et al., 2002]. The coupling between fluid density and solute concentrations is resolved using the Picard iterative approach [Putti and Paniconi, 1995]. This method linearizes the combined set of flow and reactive transport equations by computing fluid density and solving the fluid conservation equations using chemical concentrations computed during the previous Picard iteration [Voss, 1984]. The Picard

approach is conceptually straightforward, and is commonly used in computer programs simulating variable density flow and transport problems [Voss, 1984; Kipp, 1986; Ackerer et al., 1999; Frolkovic, 1999; Guo and Langevin, 2002; Diersch, 2002; Langevin and Guo, 2006]. The Picard approach has previously been used to combine individual computer programs to simulate reactive transport problems under variable density conditions [Mao et al., 2006].

The primary alternative to the use of the operator splitting approach underlying the Picard method is to employ Newton's method in solving the flow and reactive transport equations simultaneously [Putti and Paniconi, 1995; Ibaraki, 1998]. Investigators have noted that a Newton scheme may facilitate the use of longer time steps, and exhibit superior convergence properties relative to the Picard approach in solving coupled non-linear problems [Putti and Paniconi, 1995; Mayer et al., 2002]. The primary disadvantage associated with the use of the Newton approach in the current investigation was the significantly greater scope of program modification required relative to implementing the Picard method. As described in subsequent chapters of this thesis, the Picard method led to accurate results during computer code verification and provided a suitable alternative for simulation of field investigation.

3.3.3 Discrete Equations

The MIN3PD fluid mass conservation equations were formulated using an implicit time weighting scheme [Mayer et al., 2002]. Using the Picard iterative approach, time step and Picard iteration indices must be specified for all dynamic variables. Using the superscripts N+1 and N to indicate current and previous time steps, and superscripts i+1 and i to indicate current and previous Picard iterations, the following fluid mass conservation equation was implemented:

$$V_{ivol}\left[S_p S_a^{N+1,i+1}\rho^{N+1,i}\frac{P^{N+1,i+1}-P^N}{\Delta t}+\theta^N\rho^{N+1,i}\frac{S_a^{N+1,i+1}-S_a^N}{\Delta t}+S_a^{N+1,i+1}\theta^N\frac{\partial\rho}{\partial c}\frac{c_t^{N+1,i}-c_t^N}{\Delta t}\right]$$
$$-\sum_{jvol=1}^{ncon}k_r^{N+1,i+1}k^N\frac{\rho_{ups}^{N+1,i}}{\mu_{ups}^{N+1,i}}\frac{A}{\Delta l}\left[P_{jvol}^{N+1,i+1}-P_{ivol}^{N+1,i+1}+\rho_{av}^{N+1,i}g\left(z_{jvol}-z_{ivol}\right)\right]=\rho_s Q_a \qquad (3\text{-}21)$$

where V is the cell volume [L^3], Δt is the time step length [T], Δl is distance between connected control volume nodes [L], A is the cross-sectional area between connected volumes [L^2], and ρ_s [ML^{-3}] is the fluid density of external sources/sinks. The subscript *ivol* identifies the subject control volume, connected control volumes are identified by the subscript *jvol*, and *ncon* is the total number

of connected control volumes. The first term of Equation (3-21) refers to control volume *ivol*, with the subscripts omitted for clarity. The subscript *ups* indicates upstream-weighting was employed for a property for a connected pair of control volumes, and the subscript *av* denotes the arithmetic average.

Implementation of Equation (3-21) requires the representation of effective parameters for each set of connected control volumes. The permeability values assigned to connected cells is computed using the cell thickness-weighted harmonic mean. Centered or upstream weighting options are provided to represent the relative permeability term. These options were provided in MIN3P [Mayer et al., 2002] and retained in the MIN3PD program.

Upstream weighting of fluid density and viscosity is employed in the computation of fluid fluxes to promote a numerically stable solution [Forsyth et al., 1995]. Fluid densities in the final bracketed term in Equation (3-21) are used in computing differences in fluid potential related to position of connected control volumes. In this case, there is no reason to preferentially weight the density of either control volume, and the arithmetic average is used. This approach in calculating both upstream and average fluid densities at boundaries between model cells is similar to the approach used by Guo and Langevin [2002].

In the Cartesian coordinate system, interfacial areas between connected cells, and the cell volumes are computed based on the user-specified computational grid. The interfacial areas and cell volumes for the radial grid are computed using the following formulas [Lapalla et al., 1987]:

$$A_{i-1/2,j} = 2\pi\Delta z_j\left(r_i - \Delta r_i / 2\right) \tag{3-22}$$

$$A_{i+1/2,j} = 2\pi\Delta z_j\left(r_i + \Delta r_i / 2\right) \tag{3-23}$$

$$A_{i,j-1/2} = A_{i,j+1/2} = 2\pi r_i \Delta r_i \tag{3-24}$$

$$V_{ij} = 2\pi r_i \Delta r_i \Delta Z_j \tag{3-25}$$

3.3.4 Solution Strategy

Updates in fluid density provide the criterion to evaluate the convergence of the Picard iterations. Picard iterations continue until the maximum update in fluid density is reduced to a user-specified

tolerance [Guo and Langevin, 2002]. A non-iterative solution approach may be employed by setting the convergence criterion to an arbitrarily high value. In this case, fluid densities are computed using solute concentrations computed from the previous time step.

A convergent model time step requires maximum updates for fluid pressures and solute concentrations to fall below user-specified Newton convergence criteria, and fluid densities to fall below Picard convergence criteria. Following Picard convergence, mineral volume fractions, and the porosity and permeability values are updated and the code proceeds to the next time step. These updates are lagged under the assumption that the changes in these properties in one time step are small enough not to significantly affect the accuracy of the simulation. The MIN3PD solution sequence is summarized in Figure 3-2.

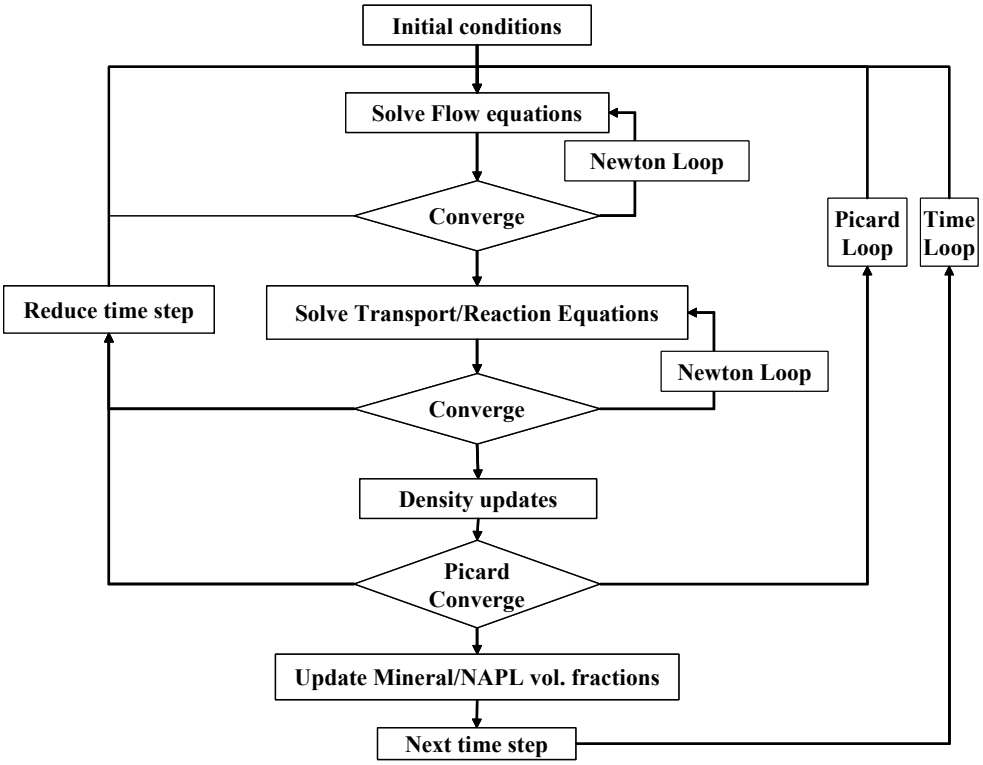

Figure 3-2. Summary of MIN3PD program execution structure. Time step reductions occur when the maximum number of Newton or Picard iterations has occurred and convergence criteria have not been achieved.

MIN3PD does not provide the option of simulating a steady-state condition for variable density fluid flow and chemical transport; variable density flow and transport simulations in MIN3PD require that a transient simulation is performed.

3.3.5 Adaptive Time Stepping Scheme

The MIN3P program computes time step lengths based on changes in the concentrations of aqueous components and the target number of Newton iterations [Mayer et al., 2002]. In addition to these parameters, MIN3PD incorporates a Courant number target and the target number of Picard iterations to compute time step lengths. A Courant number criterion was added in response to the use of the operator splitting approach for coupling the flow equation with the reactive transport equations. The Picard iteration criterion was programmed to enhance the efficiency of the MIN3PD program.

3.3.6 Initial and Boundary Conditions

Initial hydrologic conditions and boundary conditions may be assigned in units of fluid pressure, pressure heads, hydraulic heads, or freshwater heads. Initial fluid pressures are assigned to the model grid using the following relationships:

$$P_{ivol} = \psi_{ivol} * |g| * \rho_{ivol} \tag{3-26}$$

$$P_{ivol} = (h_f - z_{ivol}) * |g| * \rho_f \tag{3-27}$$

$$P_{ivol} = (h_{ivol} - z_{ivol}) * |g| * \rho_{ivol} \tag{3-28}$$

where ψ is the pressure head [L], $|g|$ is the magnitude of gravitational acceleration [L T^{-2}], h_f and h represent freshwater and hydraulic heads [L], ρ_f is the freshwater density [M L^{-3}], and the density ρ is calculated using Equation (3-12). Initial and boundary conditions specified for geochemical system are read and assigned to the model grid before initial and boundary conditions are assigned to the flow system. This order of execution allows the density of fluids at assigned model boundaries to be computed, and facilitates the calculation of initial fluid pressures when pressure or hydraulic heads are used to assign initial conditions. A hydrostatic fluid pressure profile may be assigned to a vertical interval in the model domain containing a uniform solute concentration using the following relationship:

$$P_{ivol} = P_0 + |g| * \rho_{ivol} [z_0 - z_{ivol}] \tag{3-29}$$

where P_0 and z_0 represent the fluid pressure and elevation of the top of the interval. This calculation provides an efficient mechanism to assign initial fluid pressures when dense fluids are present as an

initial condition in a simulation, and ensures that the initial distribution of fluid pressures is consistent with solute concentrations and fluid densities [Voss, 1984].

Specified fluid head, pressure or Darcy flux boundary conditions may be assigned to the exterior boundaries of the model domain. The seepage boundary algorithm developed in MIN3P [Mayer et al., 2002] was modified for variable density fluids to maintain the generality of the MIN3PD program. Boundary conditions for the solutes include specified concentration, specified mass flux, and a free exit boundary condition.

Injection of potassium permanganate into an interior node of the model domain was simulated using as a point source boundary condition. The fluid boundary condition requires that a volumetric injection or extraction rate is specified. When fluids are added to a model cell, a Cauchy (specified mass flux) boundary condition is used to assign solute concentrations to the injected fluids. When fluids are removed from the model cell, a free exit boundary condition is applied to simulate an extraction well. Boundary conditions, including fluid injection/extraction rates and locations, may be modified throughout a simulation. The explicit representation of well dynamics, such as well behavior screened across multiple lithologic units, was beyond the scope of the current investigation.

Chapter 4 Computer Code Benchmarking

Major elements in the development of the MIN3PD program included the implementation of the fluid mass conservation equations and the iterative solution scheme for solving coupled fluid flow and reactive transport problems. A preferred method for numerical model verification utilizes exact analytical solutions of initial or boundary value problems to evaluate the accuracy of numerical model predictions [Zheng and Bennett, 2002]. However, non-linear and coupled processes which occur in variable density flow and transport limit the availability of analytical solutions to simplified problems [Diersch and Kolditz, 2002]. The MIN3PD formulation was tested using a diverse set of problems comprised of physical and theoretical benchmarking problems. Physical benchmarking problems provide response data for relevant laboratory experiments [Wooding et al., 1997; Schincariol and Schwartz, 1990; Simmons et al., 1999; Simmons et al., 2002; Oswald and Kinzelbach, 2004]. Theoretical benchmarking problems range from simple tests to identify numerical errors [Voss and Souza, 1987; Diersch and Kolditz, 2002] to highly coupled flow and transport problems which require a comparison of model results to numerical solutions of accepted quality [Elder, 1967; Konikow et al., 1997; Diersch and Kolditz, 2002].

While the emphasis of the MIN3PD code development and testing was placed on variable density flow and transport problems, three additional categories of benchmarking problems were utilized to evaluate the performance of the program. MIN3PD was benchmarked using a series of laboratory experiments performed in variably saturated porous media. These test problems investigate the movement of fluids in the absence of solute concentration gradients. This benchmarking was performed to verify the correct formulation of the fluid flow conservation equations, and the formulation of the constitutive relationships between aqueous saturation, relative permeability, and fluid pressures. A second set of test problems, simulating fluid flow and conservative solute transport, were used to verify the implementation of the radial coordinate system. The third set of test problems investigated reactive chemical transport. The suite of test problems and benchmarking results are described in the following sections.

4.1 Variably Saturated Fluid Flow

The MIN3PD formulation was benchmarked using six test problems depicting water infiltration [Abeele, 1984; Haverkamp et al., 1977], water drainage [Abeele, 1984], water table mounding

[Vauclin et al., 1979], and the development of a seepage face [Davis and Neuman, 1983] in variably saturated media. These problems were utilized for benchmarking the MIN3P program [Mayer et al., 2002] which provided reference results for the current investigation. For brevity, the focus of the following discussion is on benchmarking results, and the individual test problems are not described in detail.

MIN3PD fluid pressures were converted to hydraulic heads using Equation (3-2) and compared with MIN3P results. Model predictions of computed heads, aqueous saturations, and fluid Darcy velocities were compared at multiple simulation times for each problem. The maximum absolute difference in these three output variables was recorded for the six test problems. Maximum relative percent differences (RPD_i^{max}) for each variable were computed to scale the maximum recorded differences between the two programs to the corresponding MIN3P prediction:

$$RPD_i^{\max} = \frac{\max\left[VAR_{ij}(MIN3PD) - VAR_{ij}(MIN3P)\right]_{j=1}^{NN}}{VAR_{ij}(MIN3P)} * 100 \qquad (4\text{-}1)$$

where the subscript i refers to the output variables (hydraulic heads, saturations, and velocities).

Predicted hydraulic heads, water saturations, and Darcy velocities indicated excellent agreement between MIN3PD and MIN3P simulation results for all six test problems. Table 4-1 summarizes the results. The differences between the two programs generally fell in the range of the output precision, and in all cases the magnitude of the RPD_i^{max} was less than 0.01 percent.

	Hydraulic Head		Water Saturation		Darcy Velocity	
Problem	[m]	[RPD]	[-]	[RPD]	[m/d]	[RPD]
Haverkamp 1-D	0.0	0.0	0.0	0.0	0.0	0.0
Abeele 1-D (infiltration)	$8.3\text{x}10^{-5}$	$-3.3\text{x}10^{-3}$	$3.8\text{x}10^{-6}$	$7.9\text{x}10^{-4}$	$-5.3\text{x}10^{-7}$	$8.1\text{x}10^{-4}$
Abeele 1-D (drainage)	0.0	0.0	0.0	0.0	0.0	0.0
Vauclin 2-D	$-1.0\text{x}10^{-6}$	$-9.9\text{x}10^{-5}$	$-9.0\text{x}10^{-7}$	$-1.4\text{x}10^{-4}$	$-2.3\text{x}10^{-6}$	$-3.1\text{x}10^{-4}$
Davis & Neuman 2-D	$-3.0\text{x}10^{-6}$	$-4.7\text{x}10^{-4}$	$-9.0\text{x}10^{-6}$	$-1.2\text{x}10^{-3}$	$-1.2\text{x}10^{-5}$	$4.2\text{x}10^{-4}$
Vauclin 3-D	$1.0\text{x}10^{-6}$	$9.7\text{x}10^{-5}$	$1.8\text{x}10^{-6}$	$2.6\text{x}10^{-4}$	$-6.0\text{x}10^{-6}$	$5.3\text{x}10^{-4}$

Table 4-1. Maximum differences and RPD_i^{max} values for hydraulic heads, water saturations, and Darcy velocities between MIN3PD and MIN3P formulations.

4.2 Radial Coordinate Simulations

The testing of the radial coordinate system in MIN3PD was performed using three problems used in the verification of the U.S. Geological Survey SUTRA and VS2DT programs [Voss, 1984; Lapalla et al., 1987]. These problems simulated transient reductions in fluid potentials, and the transport of non-reactive solutes. Problem descriptions, model setup, and benchmarking results are described in the following sections.

4.2.1 Time-Drawdown Problem

The time-drawdown problem investigates transient response in fluid potentials resulting from the constant extraction of fluid from a confined aquifer of infinite lateral extent [Theis, 1935]. The problem was simulated in a one-dimensional radial grid extending 1000 meters in the horizontal direction. The model domain was divided into 65 control volumes, ranging from 1.3 to 25 meters in length, with successive model cells increasing in length by a factor of 1.06 until the length of 25 m was achieved. Model boundary conditions included an extraction rate of 0.05 L s^{-1} assigned to the left model boundary, and a constant head assigned to the right boundary. The initial condition across the domain was 1.0 m hydraulic head, and the total simulated time was 48 hours. Model parameters are summarized in Table 4-2.

Hydrologic Parameters	Symbol	Value	Units
Transmissivity	T	1.00×10^{-4}	$m^2\ s^{-1}$
Specific storage	S_s	5.00×10^{-5}	m^{-1}
Pumping rate	Q_{out}	-5.00×10^{-5}	$m^3 s^{-1}$

Table 4-2. Model parameters for the Theis time-drawdown problem.

Three observation points were specified at distances 11.3, 103.0, and 306.7 m from the pumping boundary. MIN3PD model results were compared to the Theis analytical solution for the reduction in hydraulic head:

$$s = \frac{Q}{4\pi T} W(u) \tag{4-2}$$

$$u = \frac{r^2 S}{4Tt} \tag{4-3}$$

where s is the drawdown [m], Q is the pumping rate [m^3 s^{-1}], T [m^2 s^{-1}] is the media transmissivity, W(u) is the well function, r [m] is the radial distance between pumping and observation wells, S [m^3 m^{-3}] is the storage coefficient, and t is the elapsed time since pumping began. Figure 4-1 compares MIN3PD head reductions at these points to those predicted using the Theis analytical solution. As the Figure indicates, model predictions reproduce the Theis analytical solution at all three locations throughout the duration of the simulation.

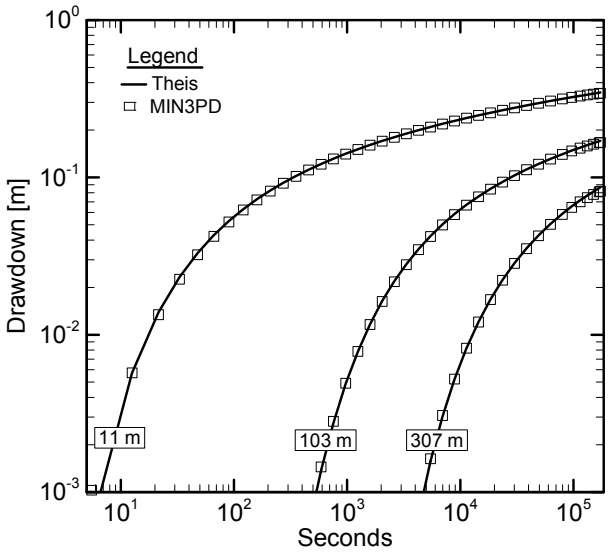

Figure 4-1. Comparison of simulated drawdowns with the Theis analytical solution. Observation points are 11.3, 103.0, and 306.7 m from the pumping well.

4.2.2 Cylindrical Solute Transport

The cylindrical solute transport problem investigates the radial spreading of a non-reactive solute in a confined infinite aquifer resulting from the constant injection of fluid containing a fixed solute concentration [Voss, 1984; Lapalla et al., 1987]. The model domain and grid were identical to the time-drawdown problem described previously. MIN3PD boundary conditions included a water injection rate of 6.25 L s^{-1} assigned to the left boundary of the model domain, and a constant head of 1.0 m assigned to the right boundary. The initial condition across the domain was 1.0 m hydraulic head, and the total simulated time was 83.8 days. The solute was initially absent from the model domain. Model parameters are summarized in Table 4-3.

Hydrologic Parameters	Symbol	Value	Units
Transmissivity	T	1.00×10^{-4}	$m^2 s^{-1}$
Porosity	ϕ	0.2	-
Specific storage	S_s	1.00×10^{-10}	m^{-1}
Longitudinal dispersivity	α_L	10.0	m
Molecular diffusion coefficient	D_m	1.00×10^{-10}	$m^2 s^{-1}$
Pumping rate	Q_{in}	6.25×10^{-3}	$m^3 s^{-1}$

Table 4-3. Model parameters for the cylindrical solute transport verification problem.

MIN3PD model results were compared to the approximate analytical solution developed by Gelhar and Collins [1971] for cylindrical solute transport [Voss, 1984]:

$$\frac{C}{C_{inj}} = \frac{1}{2}\operatorname{erfc}\left[\frac{r^2 - \hat{r}^2}{2\left[\frac{4}{3}\alpha_L \hat{r}^3 + \frac{D_m}{A}\hat{r}^4\right]^{\frac{1}{2}}}\right] \tag{4-4}$$

$$\hat{r} = \left[2At\right]^{\frac{1}{2}} \tag{4-5}$$

$$A = \left(\frac{Q_{tot}}{2\pi\phi b\rho}\right) \tag{4-6}$$

where C is the solute concentration [g m^{-3}], C_{inj} is the injected solute concentration [g m^{-3}], r is the distance [m] from the injection point, α_L is the longitudinal dispersivity [m], D_m is molecular diffusion coefficient [$m^2 s^{-1}$], and erfc is the complementary error function. As the Figure indicates, model predictions are in good agreement with the Gelhar and Collins solution (Figure 4-2). Voss [1984] presented results similar to those depicted in Figure 4-2. The Gelhar and Collins solution is approximate, and exhibits errors at early times in the vicinity of the injection well [Voss, 1984].

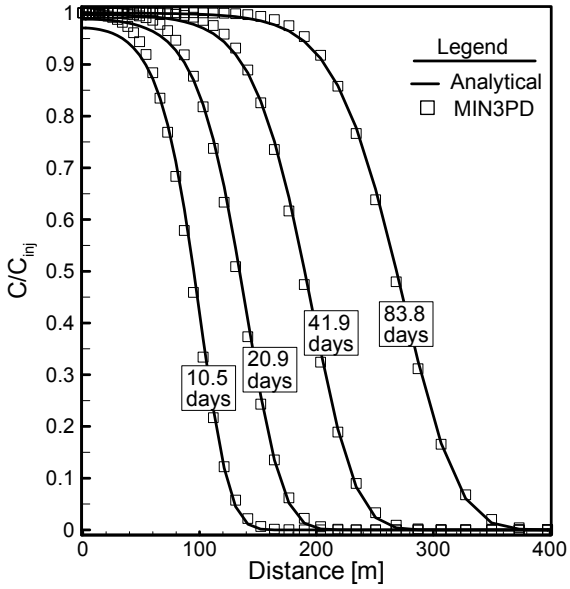

Figure 4-2. Comparison of MIN3PD solute distribution with the Gelhar and Collins analytical model.

4.2.3 Solute Transport in a Vertical Column

The Ogata-Banks [Ogata and Banks, 1961] analytical solution for one-dimensional solute transport was employed to test solute transport within a vertical column simulated using a two-dimensional radial grid. The test was set up to complement the cylindrical solute transport problem, which tested horizontal flow in a radial coordinate system. In simulating a vertical flow problem, each column of cells differs from neighboring columns of cells in the area through which fluid advection and chemical transport occurs. This benchmarking problem compared chemical transport through each column of cells with the Ogata-Banks analytical solution.

The model domain was 160 m tall with a radius of 5 m, and was subdivided using a uniform grid comprised of 1601 rows and 6 columns. A steady-flow field was simulated with a downward fluid seepage velocity of 2.74×10^{-4} m s^{-1} by assigning constant head values to the top and bottom of the column. A fixed concentration of 1.0 g L^{-1} was assigned to the top of the column throughout the simulation. The column was initially free of solute, and the total simulated period was 7,200 seconds. Model parameters are summarized in Table 4-4.

Hydrologic Parameters	Symbol	Value	Units
Hydraulic conductivity	K	9.80×10^{-4}	$m\ s^{-1}$
Hydraulic gradient	I	0.14	$m\ m^{-1}$
Porosity	ϕ	0.5	-
Specific storage	S_s	1.00×10^{-10}	m^{-1}
Longitudinal dispersivity	α_L	10	m
Transverse dispersivity	α_T	10	m
Molecular diffusion coefficient	D_m	1.00×10^{-10}	$m^2\ s^{-1}$

Table 4-4. Model parameters for the Ogata-Banks verification problem.

The vertical distribution of the solute at the conclusion of the simulation was compared to the Ogata-Banks analytical solution for one-dimensional transport of a non-reactive solute:

$$\frac{C}{C_0} = \frac{1}{2}\left[\operatorname{erfc}\left(\frac{x - vt}{\sqrt{4Dt}} \right) + \exp\left(\frac{xv}{D} \right) \operatorname{erfc}\left(\frac{x + vt}{\sqrt{4Dt}} \right) \right] \tag{4-7}$$

MIN3PD and Ogata-Banks predicted solute distributions at 7,200 seconds are compared in Figure 4-3. An excellent match was obtained between the MIN3PD results and the analytical solution. Inspection of MIN3PD results indicated that the vertical migration of solute was uniform for all six columns of model cells.

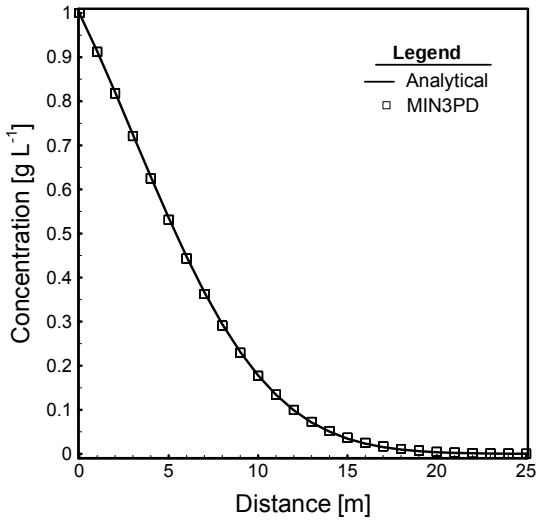

Figure 4-3. Comparison of MIN3PD solute distribution with Ogata-Banks analytical solution at 7,200 seconds.

4.3 Variable Density Flow and Chemical Transport

The development and evaluation of variable density flow and transport benchmarking problems are active areas of research [Konikow et al., 1997; Frolkovic and De Schepper, 2001; Simpson and Clement, 2003; Weatherill et al., 2004; Oswald and Kinzelbach, 2004; Simpson and Clement, 2004; Ataie-Ashtiani and Aghayi, 2006]. Five benchmarking problems [Voss and Souza, 1987; Diersch and Kolditz, 2002; Simpson and Clement, 2004; Weatherill et al., 2004; Oswald and Kinzelbach, 2004] are presented to document the accuracy of MIN3PD in solving coupled variable density flow and transport problems. The emphasis was placed on benchmarking problems with solutions constrained by established mathematical or laboratory results.

Theoretical box problems were simulated to evaluate error-driven spreading of solutes in static and advecting fluids [Voss and Souza, 1987; Diersch and Kolditz, 2002]. The Elder fluid convection benchmarking problem, for which an exact solution does not exist [Diersch and Kolditz, 2002], was included in the current evaluation due to its extensive use in model benchmarking [Oldenburg and Pruess, 1995; Ackerer et al. 1999; Oltean and Buès, 2001; Frolkovic and De Schepper, 2001; Diersch and Kolditz, 2002; Simpson and Clement, 2003]. The modified Henry seawater intrusion problem [Henry, 1964; Simpson and Clement, 2004] and the modified Horton-Rogers-Lapwood problem [Weatherill et al., 2004] were benchmarked against established mathematical solutions. The final benchmarking problem simulated three-dimensional laboratory experiments of saltwater upconing and mixing with freshwater documented by Oswald and Kinzelbach [2004]. The following sections describe these benchmarking problems and the MIN3PD modeling results.

4.3.1 Box Problems

The spreading or smearing of freshwater-saltwater interfaces resulting from numerical errors has been identified as a useful test scenario for benchmarking variable density computer programs [Voss and Souza, 1987; Diersch and Kolditz, 2002]. Two box problems were benchmarked, investigating stable density stratifications under hydrostatic conditions and in advecting fluids. A stable density stratification when the density of the fluid increases with depth [Diersch and Kolditz, 2002]. In these benchmarking problems, model errors result in spurious fluid movement and enhanced solute flux from the saltwater into the freshwater, widening the transition zone [Voss and Souza, 1987; Diersch and Kolditz, 2002].

The hydrostatic box test [Diersch and Kolditz, 2002] compares chemical diffusion in variable density fluids with chemical diffusion in freshwater. The representation of hydrodynamic dispersion in MIN3PD results in solute diffusion from saltwater into freshwater independent of the density contrast between the two fluids. This condition provides the basis for the benchmarking test.

The hydrostatic box test was simulated in a 20 m horizontal by 40 m vertical profile, with a saltwater layer located below a freshwater layer, separated by a sharp horizontal interface in the middle of the domain [Diersch and Kolditz, 2002]. The domain was surrounded by no flow boundaries for water and solutes. The decoupled (reference) case was simulated by setting the coefficient of density variation $\partial\rho/\partial c$ to zero, resulting in the freshwater density assigned to all fluids in the model domain. The coupled variable density scenario was simulated by setting the coefficient of density variation to 0.7, resulting in a three percent density contrast between the saltwater and freshwater layers. The model was discretized using a 40,200-node grid with $\Delta x = 1.0$ m and $\Delta z = 0.2$ m. The simulations were executed for a period of 1000 days. Model parameters are summarized in Table 4-5.

Hydrologic Parameters	Symbol	Value	Units
Hydraulic conductivity	K	1.0×10^{-4}	$m\ s^{-1}$
Porosity	ϕ	0.4	-
Specific storage	S_s	0.0	m^{-1}
Longitudinal dispersivity	α_L	5.0	m
Transverse dispersivity	α_T	0.5	m
Molecular diffusion coefficient	D_m	1.0×10^{-8}	$m^2\ s^{-1}$
Saltwater density	ρ_s	1030	$Kg\ m^{-3}$
Freshwater density	ρ_0	1000	$Kg\ m^{-3}$
Maximum density ratio	ρ_{max}	1.03	-
Coefficient of density variation	$\partial\rho/\partial c$	0.0 / 0.7	-
Saltwater concentration	C_s	43	$g\ L^{-1}$

Table 4-5. Model parameters used for the simulation of the hydrostatic box problem.

Figure 4-4 compares the diffusive chemical profiles for constant density and variable density fluids at 1000 days. As the Figure indicates, an excellent level of agreement was obtained for the two cases, indicating an absence of spurious fluid movement for the coupled case.

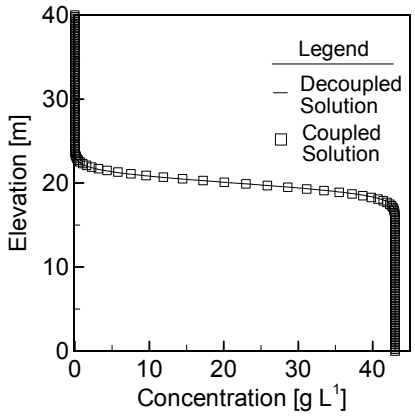

Figure 4-4. Vertical chemical profiles at 1000 days for decoupled (solid line) and coupled (square symbols) cases.

The second box problem was simulated to identify the smearing of sharp concentration gradients in the direction normal to the direction of fluid movement [Voss and Souza, 1987]. Similar to the hydrostatic problem, a layer of freshwater overlying a layer of dense water was investigated. A constant groundwater seepage velocity of 5 m d^{-1} in the positive x-direction was simulated by assigning different hydrostatic pressure profiles to the left and right sides of the model domain. Fixed solute concentrations were assigned to the influent (left) boundary of the model, and were set equal to the initial concentrations assigned to the model domain. A free exit chemical boundary condition was assigned to the right side of the model domain. Model dimensions were 2000 m in height and length, and the domain was discretized using 21 control volumes in the x and z directions. The coefficients of molecular diffusion and transverse chemical dispersion were set to zero (Table 4-6). Given this condition, no mechanism was present to cause the vertical spreading of solutes except for model errors. The simulation was run for a total of 4000 days.

Hydrologic Parameters	Symbol	Value	Units
Hydraulic conductivity	K	1.16×10^{-3}	$m\ s^{-1}$
Porosity	ϕ	0.01	-
Specific storage	S_s	0.0	m^{-1}
Longitudinal dispersivity	α_L	100.0	m
Transverse dispersivity	α_T	0.0	m
Molecular diffusion coefficient	D_m	0.0	$m^2\ s^{-1}$
Saltwater density	ρ_s	1025	$Kg\ m^{-3}$
Freshwater density	ρ_0	1000	$Kg\ m^{-3}$
Maximum density ratio	ρ_{max}	1.025	-
Coefficient of density variation	$\partial\rho/\partial c$	0.71	-
Saltwater concentration	C_s	35	$g\ L^{-1}$

Table 4-6. Model parameters used for the simulation of the chemical advection box problem.

Simulation results indicate negligible spreading of solutes in the vertical direction. As Figure 4-5 indicates, the solute iso-concentration lines at the conclusion of the simulation are identical to those depicting the initial solute distribution. The simulations did not provide any evidence of error-driven solute spreading, or smearing of the solute concentration gradient.

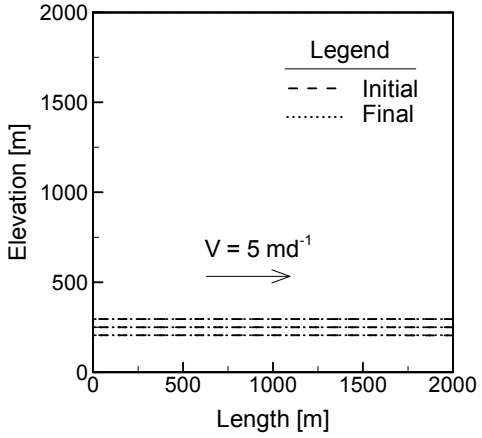

Figure 4-5. Box problem solute distributions at 0 and 4000 days. Concentration contours from top to bottom represent 5, 50, and 95 percent of the maximum salt concentration (35 g L^{-1}).

4.3.2 Elder Problem

Voss and Souza [1987] utilized laboratory investigations of fluid convection driven by a thermal gradient [Elder, 1967] to develop a benchmarking problem investigating fluid convection patterns driven by gradients in dissolved solute concentrations. The Elder problem domain consists of a two-

dimensional vertical cross-section depicting a zone of freshwater underlying a source of brines. The source of dense fluids is present along a portion of the top of the model domain, which initially contains freshwater. Convective fluid flow patterns evolve during the problem, which resolve into stationary zones of fluid upwelling and downwelling [Frolkovic and De Schepper, 2001; Diersch and Kolditz, 2002]. The problem depicts the interactions of fluids differing in density by a factor of 20 percent, consistent with the contrast between brines and freshwater [Millero et al., 1982]. The non-linearity and sensitivity of this problem provide a rigorous test of numerical simulators [Simpson and Clement, 2003]. However, numerical simulation results are sensitive to the level of grid refinement [Oldenberg and Pruess, 1995; Kolditz et al., 1998; Oltean and Buès, 2001; Diersch and Kolditz, 2002] and the numerical parameters including the convergence criteria applied to the solution of the model equations [Ackerer et al., 1999]. Accordingly, the Elder benchmarking problem relies on comparisons to accepted numerical modeling results [Diersch and Kolditz, 2002].

Initial investigations of the Elder problem simulated the entire domain [Voss and Souza, 1987], while recent investigations have simulated the left half of the symmetrical problem domain to facilitate grid refinement investigations [Oltean and Buès, 2001; Frolkovic and De Schepper, 2001; Diersch and Kolditz, 2002]. MIN3PD benchmarking is illustrated using the left half of the domain with dimensions 300 meters horizontal by 150 meters vertical, and discretized using a 8192-node mesh with $\Delta x = \Delta z = 2.4$ m. A constant concentration of 0 g L^{-1} was assigned to the entire bottom boundary segment, and no flow boundaries were assigned to all four sides of the domain. A constant fluid pressure of 0 Pa was assigned to the upper left corner of the domain [Voss and Souza, 1987]. The model domain and boundary conditions for the Elder problem are illustrated in Figure 4-6.

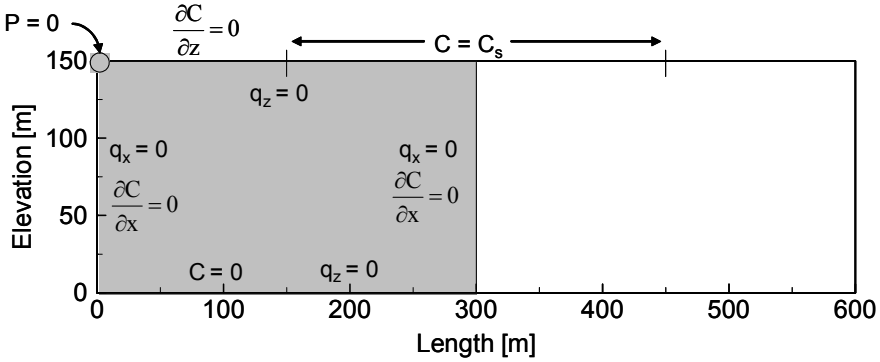

Figure 4-6. Domain and boundary conditions applied for solving the Elder problem. The left half of the Elder problem domain was simulated, corresponding to the grey region of the Figure.

The Elder problem was simulated for a period of 20 years using the parameter values tabulated by Voss and Souza [1987]. The Van Leer flux limiting scheme [Van Leer, 1974] was used to minimize numerical dispersion. Model parameters are summarized in Table 4-7.

Hydrologic Parameters	Symbol	Value	Units
Hydraulic conductivity	K	4.75×10^{-6}	$m\ s^{-1}$
Porosity	ϕ	0.1	-
Specific storage	S_s	0.0	m^{-1}
Longitudinal dispersivity	α_L	0.0	m
Transverse dispersivity	α_T	0.0	m
Molecular diffusion coefficient	D_m	3.57×10^{-6}	$m^2\ s^{-1}$
Brine density	ρ_s	1200	$Kg\ m^{-3}$
Freshwater density	ρ_0	1000	$Kg\ m^{-3}$
Maximum density ratio	ρ_{max}	1.2	-
Coefficient of density variation	$\partial\rho/\partial c$	0.7	-
Brine concentration	C_s	285.7	$g\ L^{-1}$

Table 4-7. Model parameters used for the simulation of the Elder convection problem.

Figure 4-7 compares MIN3PD simulation results with published results generated using the d^3f simulator for the same level of grid discretization [Frolkovic and De Schepper, 2001]. Model output times of 4, 7, and 20 years depict the density-driven solute movement facilitated by the development and downward movement of dense brine fingers. The stationary solute distributions at 20 years depicted in Figure 4-7 are consistent with published simulation results for a comparable level of grid discretization for several investigations [Oldenburg and Pruess, 1995; Kolditz et al.,1998; Ackerer et al. 1999; Oltean and Buès, 2001].

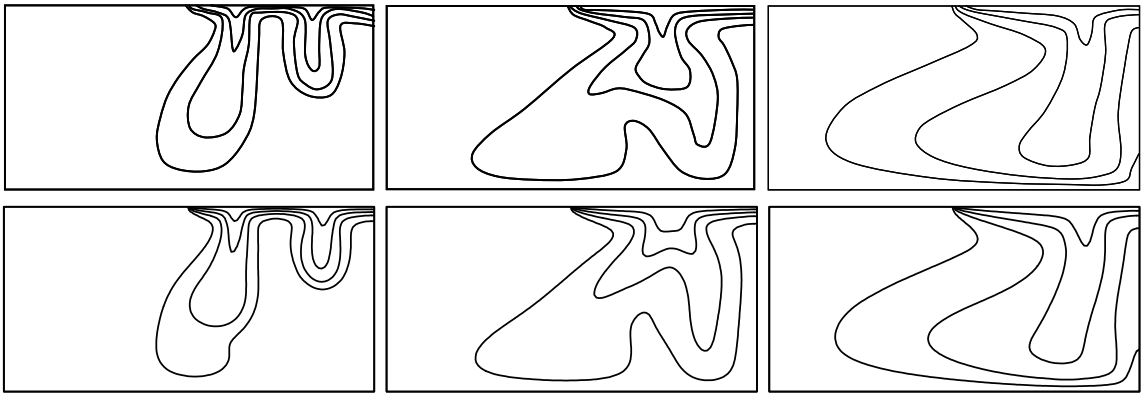

Figure 4-7. Comparison of d^3f (top) and MIN3PD (bottom) model predictions for the Elder problem at 4 (left), 7 (center), and 20 (right) years. Normalized concentration contours from top to bottom are 0.8, 0.6, 0.4, and 0.2. Model domain is 300 meters horizontal by 150 meters vertical. The d^3f results taken from Frolkovic and De Schepper [2001].

A comparison of the MIN3PD and d^3f model predictions indicates a good level of agreement for all three output times. Three successive grid refinements were performed reducing the horizontal and vertical dimensions of each model cell by a factor of 0.5, culminating in a 524,288-node grid. Model predictions for the refined grids were nearly identical to solutions presented in Figure 4-7. Grid refinement investigations performed by Diersch and Kolditz [2002] and Frolkovic and De Schepper [2001] indicated that a different solution to the Elder problem was obtained at higher levels of grid refinement, a condition not indicated in the MIN3PD simulations. The cause for this discrepancy was not determined, but is expected to be attributable to differences in numerical solution methods.

4.3.3 Modified Henry Problem

The Henry problem [Henry, 1964] depicts saltwater intrusion into a homogeneous confined aquifer and the development of a mixing zone between freshwater and saltwater. The Henry problem has been widely used as a test case of density-dependent groundwater flow models [Pinder and Cooper, 1970; Frind, 1982; Kipp, 1986; Voss and Souza, 1987; Ackerer at al., 1999; Guo and Langevin, 2002]. However, the merits of this problem for code benchmarking have been scrutinized due to the weak coupling between flow and transport processes [Simpson and Clement, 2003]. Simpson and Clement [2004] proposed a modification to the Henry problem, reducing the freshwater flux by 50 percent to increase the coupling between fluid flow and chemical transport and the rigorousness of the test problem. This modified problem definition was used to benchmark MIN3PD.

The Henry problem domain consists of a two-dimensional vertical cross-section. A constant freshwater flux is applied to the left boundary, representing aquifer flow. The right model boundary represents a hydrostatic column of seawater, with a fixed concentration. The model domain was 2 m horizontal by 1 m vertical, and discretized using a uniform grid with 861 control volumes with $\Delta x = \Delta z = 0.05$ m. Figure 4-8 illustrates model domain and boundary conditions of the modified Henry problem.

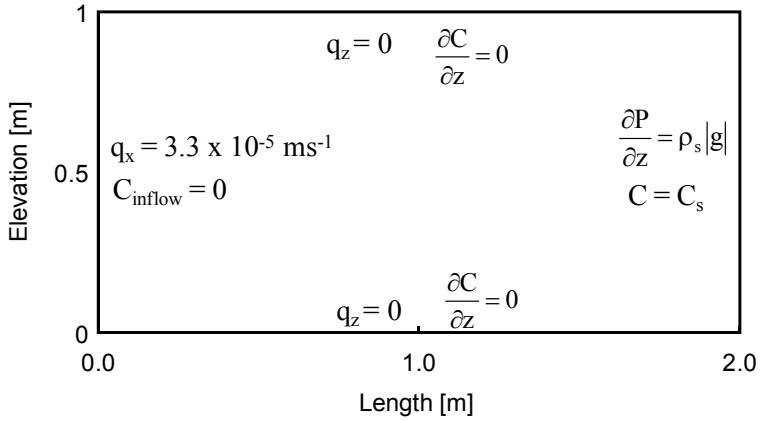

Figure 4-8. Domain and boundary conditions applied for solving the modified Henry problem.

MIN3PD simulations of the modified Henry problem were performed using the parameter values provided by Simpson and Clement [2004] and compared to the semi-analytical results of the same authors. The Henry problem was simulated for a period of 0.833 days, representing the point at which a stationary chemical distribution was achieved. Model parameters are summarized in Table 4-8.

Hydrologic Parameters	Symbol	Value	Units
Hydraulic conductivity	K	1.0×10^{-2}	$m\ s^{-1}$
Porosity	ϕ	0.35	-
Specific storage	S_s	0.0	m^{-1}
Longitudinal dispersivity	α_L	0.0	m
Transverse dispersivity	α_T	0.0	m
Molecular diffusion coefficient	D_m	1.886×10^{-5}	$m^2\ s^{-1}$
Recharge per unit width	Q	3.3×10^{-5}	$m^2\ s^{-1}$
Saltwater density	ρ_S	1025	$Kg\ m^{-3}$
Freshwater density	ρ_0	1000	$Kg\ m^{-3}$
Maximum density ratio	ρ_{max}	1.025	-
Coefficient of density variation	$\partial\rho/\partial c$	0.7125	-
Seawater concentration	C_s	35.0	$g\ L^{-1}$

Table 4-8. Model parameters used for the simulation of the modified Henry problem.

Figure 4-9 compares the MIN3PD simulation results with results from the semi-analytical solution computed by Simpson and Clement [2004]. The results indicate that a wedge of saltwater encroaches into the freshwater aquifer, in the opposite direction of groundwater flow. As the Figure indicates, MIN3PD simulation results are in excellent agreement with the semi-analytical solution computed by Simpson and Clement [2004].

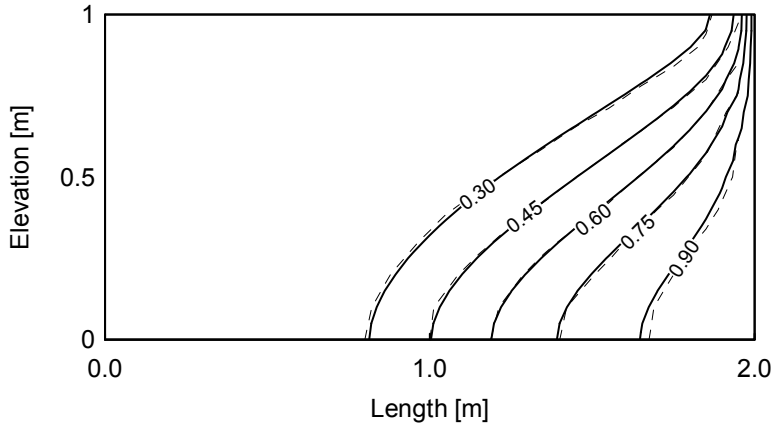

Figure 4-9. Modified Henry problem verification results. Isocontour lines depict normalized salinity concentrations. MIN3PD simulation results are represented by solid lines; the semi-analytical solution [Simpson and Clement, 2004] is represented by dashed contour lines.

4.3.4 Horton-Rogers-Lapwood Problem

The modified Horton-Rogers-Lapwood (HRL) test problem compares the onset of fluid convection in a numerical model to analytical stability criteria [Rayleigh, 1916; Horton and Rogers, 1945; Lapwood, 1948; Weatherill et al., 2004]. Given an unstable horizontal stratification of variable density fluids, the Rayleigh number of $4\pi^2$ (≈ 39.5) identifies the point at which convective movement of fluid is predicted. The Rayleigh number incorporates system properties including the medium permeability, the vertical thickness of the domain, and the vertical gradient in the solute concentration:

$$R_a = \frac{kgH\partial\rho / \partial c(\Delta C)}{\phi\mu D_m} \tag{4-8}$$

where k is the media permeability [L^2], g is the magnitude of gravitational acceleration [LT^{-2}], H [m] is the layer thickness, ΔC [g L^{-3}] is the difference between the maximum and minimum solute concentrations, and D_m [m^2 s^{-1}] is the molecular diffusion coefficient of the solute in water. The onset and degree of convective fluid movement is quantified using the increase in the solute flux across the domain above background diffusive flux, and by the development of sinusoidal solute concentration distributions [Weatherill et al., 2004]. Investigations performed by Ataie-Ashtiani and Aghayi [2006] determined that the threshold of instability formation was appropriate for code benchmarking purposes.

The HRL problem domain consists of a two-dimensional vertical cross-section, bounded on all four sides by no flow boundary conditions. A constant fluid pressure of 0 Pa was assigned to the upper left and right corners of the domain. Fixed solute concentrations were assigned to the top and bottom of the model domain, resulting in fluid densities of 1,200 and 1,000 g L^{-1}, respectively.

The model domain had dimensions 200 meters horizontal by 10 meters vertical, and was discretized using a 2211-node grid with $\Delta x = \Delta z = 1.0$ m. A linear equilibrium solute concentration profile, reflecting diffusive chemical transport between the assigned boundary conditions, comprised the initial solute distribution. The concentration assigned to the node in the center of the domain was increased by 10 percent, serving as a potential trigger for the onset of unstable convective fluid movement [Weatherill et al., 2004]. Figure 4-10 illustrates the model domain and boundary conditions used to simulate the HRL problem.

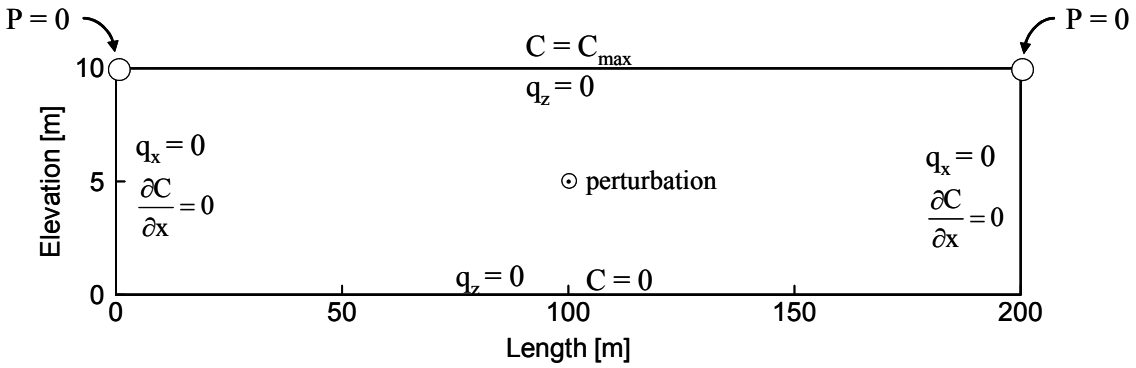

Figure 4-10. Boundary and initial conditions applied for solving the HRL problem.

The dependence of system stability on the permeability of the porous media was investigated by modifying the permeability to generate system Rayleigh numbers ranging from 20 to 80. The remaining model parameters were not varied in the simulations. All simulations were executed for a period of 20 years. Table 4-9 summarizes model parameters for the HRL problem.

Hydrologic Parameters	Symbol	Value	Units
Hydraulic conductivity	K	3.20×10^{-6}	$m\ s^{-1}$
Porosity	ϕ	0.1	-
Specific storage	S_s	0.0	m^{-1}
Longitudinal dispersivity	α_L	0.0	M
Transverse dispersivity	α_T	0.0	M
Molecular diffusion coefficient	D_m	3.57×10^{-6}	$m^2\ s^{-1}$
Brine density	ρ_s	1200	$Kg\ m^{-3}$
Freshwater density	ρ_0	1000	$Kg\ m^{-3}$
Maximum density ratio	ρ_{max}	1.2	-
Coefficient of density variation	$\partial\rho/\partial c$	0.7	-
Brine concentration	C_s	285.7	$g\ L^{-1}$

Table 4-9. Base case model parameters used for the HRL problem (Ra = 20).

Figure 4-11 depicts solute concentration contours at 20 years for three permeability cases reflecting system Rayleigh numbers of 30, 50, and 70. At Rayleigh number 30, the system remains horizontally stratified, but sinusoidal solute concentration distributions develop at Rayleigh numbers 50 and 70. The development of sinusoidal solute concentrations is caused by density-driven fluid convection, resulting in zones of fluid upwelling and downwelling. As expected, the intensity of fluid convection increases with the Rayleigh number.

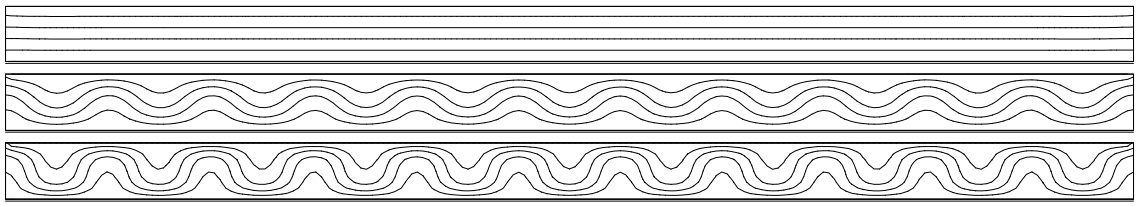

Figure 4-11. HRL problem normalized solute concentrations at 20 years for system Rayleigh numbers 30 (top), 50 (center), and 70 (bottom). Model domain is 200 meters horizontal by 10 meters vertical. Concentration contours from top to bottom are 0.8, 0.6, 0.4, and 0.2.

HRL modeling results were quantified using the increase in chemical flux across the domain resulting from the convective movement of fluids, and the spatial distribution of solutes [Weatherill et al., 2004]. Figure 4-12 illustrates the increase in solute flux across the domain and the corresponding decrease in the minimum elevation of the normalized 0.5- concentration contour plotted against the system Rayleigh number. Both criteria indicate that fluid convection does not occur below the critical Rayleigh number, but above the critical Rayleigh number, fluid convection does occur. These criteria measuring the onset of convection are in agreement with the system Rayleigh number.

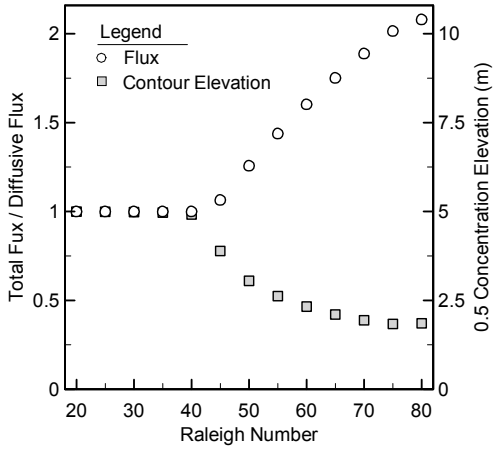

Figure 4-12. HRL problem results, depicting fluid flux (circles) and the minimum elevation of the normalized 0.5 concentration contour (squares) vs. the system Rayleigh number. Above the critical Rayleigh number of 39.5, fluid convection-driven chemical flux increases, and the minimum elevation of the 0.5 concentration contour decreases.

4.3.5 Saltpool Problem

Laboratory experiments investigating salt water upconing within a box filled with spherical glass beads were designed to provide three-dimensional data sets for benchmarking variable density computer programs [Oswald and Kinzelbach, 2004]. In these experiments, a 6 cm saltwater layer was present below a freshwater layer 14 cm in thickness, and a constant recharge and discharge of water occurred through two openings at the top of the box. The transient upwelling behavior of saltwater containing one percent (saltpool_1 experiment) and ten percent (saltpool_10 experiment) salt mass fractions was recorded using nuclear magnetic resonance imaging (NMRI). In addition, salt concentrations at the outlet were measured throughout each experiment [Johannsen et al., 2002; Oswald and Kinzelbach, 2004]. Figure 4-13 depicts the set-up of the saltpool experiments.

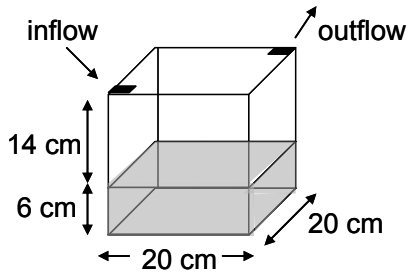

Figure 4-13. Schematic of the saltpool experimental set-up. Saltwater was initially present in the bottom 6 cm of the experimental apparatus.

Fluid and medium parameter values were assigned based on experimental data or were estimated [Oswald and Kinzelbach, 2004]. Johannsen et al. [2002] improved the model fit to the measured data by adjusting the hydraulic conductivity, porosity, and transverse dispersivity values. MIN3PD simulations of the saltpool problem were performed using centered spatial weighting for solute transport, which required the use of a fine grid discretization to meet Peclet criteria:

$$\mathrm{Pe} = \frac{\nu \Delta x}{D} < 2 \qquad (4\text{-}9)$$

where ν is the advective velocity [LT^{-1}], Δx is the distance between the center of the two adjacent control volumes [L], and D is the hydrodynamic dispersion coefficient [L^2T^{-1}]. Model control volumes ranged from 1.1 x 10^{-3} to 1.7 x 10^{-3} m in the horizontal x- and y- directions, and were 8.8 x 10^{-4} m in the vertical direction, resulting in a 3041056-node grid. Model input parameters were taken

from Johannsen et al. [2002]. The parameter values used in the saltpool_1 and saltpool_10 cases are summarized in Table 4-10. The total simulation times were 140.2 and 159.9 minutes, respectively.

Hydrologic Parameters	Symbol	Value	Units
Hydraulic conductivity	K	1.17×10^{-2}	$m\ s^{-1}$
Porosity	ϕ	0.358	-
Specific storage	S_s	0.0	m^{-1}
Longitudinal dispersivity	α_L	1.2×10^{-3}	m
Transverse dispersivity	α_T	4.32×10^{-5}	m
Molecular diffusion coefficient	D_m	1.0×10^{-9}	$m^2\ s^{-1}$
Saltwater density	ρ_s	1005.8 / 1070.6	$Kg\ m^{-3}$
Freshwater density	ρ_0	998.4	$Kg\ m^{-3}$
Maximum density ratio	ρ_{max}	1.0074 / 1.074	-
Coefficient of density variation	$\partial\rho/\partial c$	0.754 / 0.685	-
Saltwater concentration	C_s	10.058 / 107.16	$g\ L^{-1}$

Table 4-10. Model parameters used for the simulation of the one and ten percent saltpool experiments.

Figure 4-14 illustrates the geometry of the interface between freshwater and saltwater at the conclusion of the two experiments. The Figures depict a vertical cross-section extending between the fluid inlet and outlet points of the experiment. The width and position of the mixing zone is reproduced well by the MIN3PD model for both cases.

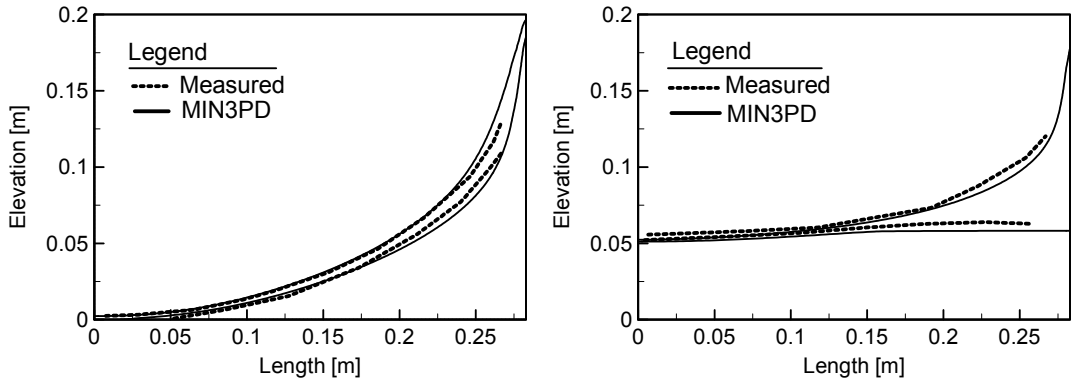

Figure 4-14. NMRI measurements and MIN3PD results for the saltpool_1 (left) and saltpool_10 (right) experiments. Concentration isolines are 10% (upper) and 50% (lower) of the initial solute concentration at 140.2 (left) and 159.9 (right) minutes.

A comparison of measured and modeled effluent concentrations for the two experiments is presented in Figure 4-15. A good match between the modeled and measured effluent concentrations was obtained for the saltpool_1 experiment. However, the model over-predicted the saltpool_10 effluent concentrations. Johannsen et al. [2002] concluded that a very high spatial grid resolution,

using up to 16 million grid points was necessary to simulate the saltpool_10 experiment, due to the importance of transverse chemical dispersion in mixing freshwater and saltwater. It is expected that model predictions using a finer grid and a lower value for transverse dispersivity may improve MIN3PD predictions of the measured effluent concentrations. However, the matches between measured and modeled results were deemed to be satisfactory.

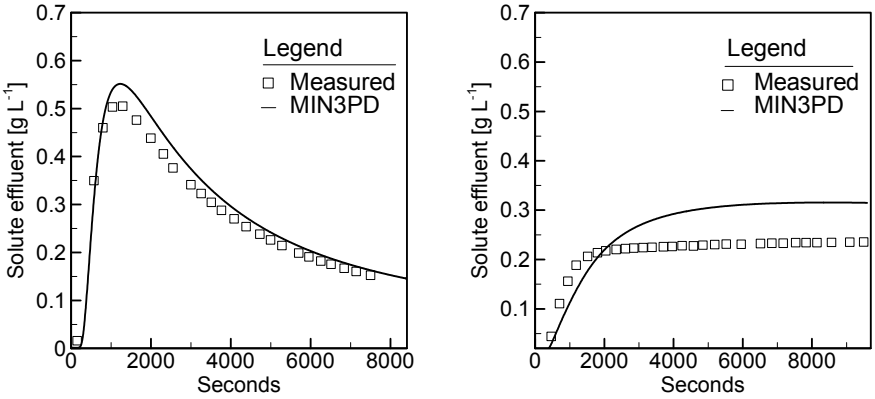

Figure 4-15. Comparison of measured and simulated breakthrough curves for the saltpool_1 and saltpool_10 experiments.

4.4 Reactive Transport Simulations

The development of the MIN3PD program required minor alterations to the routines used to simulate reactive chemical transport. Two reactive transport problems were utilized to test the MIN3PD code. The first problem investigates the oxidation of PCE DNAPL in a column experiment [Schnarr et al., 1998]. The second problem investigates the generation of acid mine drainage from pyrite oxidation in variably saturated soils. In both cases, MIN3P simulation results were used to benchmark the MIN3PD code. MIN3P has been verified for all reaction classes [Calderhead and Mayer, 2004]. Problem descriptions, model setup, and benchmarking results are provided below.

4.4.1 PCE Oxidation Column Experiment

Column experiments conducted by Schnarr et al. [1998] investigated MnO_4^- oxidation of PCE DNAPL under an imposed hydraulic gradient. Each column was filled with Borden aquifer sands, and included a 10-cm interval containing PCE DNAPL. The experiment utilizing a 10 g L^{-1} $KMnO_4$

solution and a Darcy flow velocity of 63 cm d^{-1} [Schnarr et al., 1998] was simulated. A MIN3P model was developed and calibrated using MnO_4^-, Cl^-, and $C_2Cl_{4\,(aq)}$ concentrations measured in the column effluent. The calibrated MIN3P model was subsequently used as a benchmark for the verification of MIN3PD. Table 4-11 summarizes model parameters used to represent sediment properties and experimental conditions.

Parameter	Symbol	Value	Units
Hydraulic conductivity	K	1.0×10^{-5}	$m\ s^{-1}$
Porosity	ϕ	0.41	-
Hydraulic gradient	i	0.73	$m\ m^{-1}$
Darcy velocity	q	7.3×10^{-6}	$m\ s^{-1}$
Longitudinal dispersivity	α_L	0.0	m
DNAPL source saturation	S_{DNAPL}	0.012	$m^3\ m^{-3}$
Reactive SOM fraction	$\varphi_{CH2O,r}$	5.0×10^{-4}	$m^3\ m^{-3}$
Stable SOM fraction	$\varphi_{CH2O,s}$	5.0×10^{-4}	$m^3\ m^{-3}$
Calcite fraction	$\varphi_{calcite}$	0.1	$m^3\ m^{-3}$
Aqueous diffusion coefficient	D_a	2.0×10^{-9}	$m^2\ s^{-1}$

Table 4-11. Model parameters used for the PCE oxidation column experiment.

The reaction network used to simulate the column experiment consisted of 10 aqueous components ($C_2Cl_{4(aq)}$, H_2O, K^+, Na^+, H^+, Ca^{2+}, Mg^{2+}, MnO_4^-, Cl^-, and CO_3^{2-}), two mineral phases (calcite and manganese oxide), organic matter (CH_2O), and the PCE DNAPL. The organic matter present in the Borden aquifer was simulated using two individual fractions, representing reactive ($CH_2O_{(r)}$) and stable ($CH_2O_{(s)}$) SOM. The reaction network is summarized in Table 4-12.

Reaction	Rate Expression
(1) $C_2Cl_{4(DNAPL)} \rightarrow C_2Cl_{4(aq)}$	$R_{pce}^{ox} = -\left[k_{pce,1}^{diss} + k_{pce,2}^{diss}[MnO_4^-]\right]\left([C_2Cl_{4(aq)}]_{sat} - [C_2Cl_{4(aq)}]\right)\left(\frac{\varphi_{C_2Cl_4}}{\varphi_{C_2Cl_4,0}}\right)$
(2) $C_2Cl_{4(aq)} + \frac{4}{3}MnO_4^- + \frac{4}{3}H_2O \rightarrow 2CO_2 + 4Cl^- + \frac{4}{3}MnO_{2(s)} + \frac{8}{3}H^+$	$R_{pce}^{ox} = -k_{pce}^{ox}[C_2Cl_{4(aq)}][MnO_4^-]\left[\frac{[C_2Cl_{4(aq)}]}{K_{pce}^{ox} + [C_2Cl_{4(aq)}]}\right]$
(3) $3CH_2O_{(r)} + 4MnO_4^- \rightarrow 4MnO_{2(am)} + 3CO_3^{2-} + 2H^+ + 2H_2O$	$R_{CH_2O,r}^{ox} = -k_{CH_2O,r}^{ox}[MnO_4^-]\left(\frac{\varphi_{CH_2O,r}}{\varphi_{CH_2O,0}}\right)^{\frac{2}{3}}$
(4) $3CH_2O_{(s)} + 4MnO_4^- \rightarrow 4MnO_{2(am)} + 3CO_3^{2-} + 2H^+ + 2H_2O$	$R_{CH_2O,s}^{ox} = -k_{CH_2O,s}^{ox}[MnO_4^-]\left(\frac{\varphi_{CH_2O,s}}{\varphi_{CH_2O,0}}\right)^{\frac{2}{3}}$
(5) $CaCO_3 \leftrightarrow Ca^{2+} + CO_3^{2-}$	$R_{CaCO_3} = -k_{CaCO_3}\left[1 - \frac{IAP_{CaCO_3}}{K_{CaCO_3}}\right]$

Notes:

(1) $k_{pce,1}^{diss}$ = 2.0 x 10^{-4} s^{-1} , $k_{pce,2}^{diss}$ = 1.9 x 10^{-2} $Lmol^{-1}s^{-1}$ from model calibration

(2) k_{pce}^{ox} = 8.0 x 10^{-2} $mol^{-1}\cdot L^2$ H_2O L^{-1} bulk s^{-1} from model calibration

(3) $k_{CH_2O,r}^{ox}$ = 4.0 x 10^{-4} L H_2O L^{-1} bulk s^{-1} from model calibration

(4) $k_{CH_2O,s}^{ox}$ = 1.0 x 10^{-5} L H_2O L^{-1} bulk s^{-1} from model calibration

(5) k_{CaCO_3} = 1.0 x 10^{-5} $mol\cdot L^{-1}$ bulk s^{-1} to simulate quasi-equilibrium reaction kinetics

Table 4-12. Geochemical reaction network used for the PCE oxidation column experiment.

The one-dimensional model domain was 30 cm in length, and discretized using 81 control volumes with half-cells on the boundary, resulting in a spatial discretization interval of 0.375 cm for interior control volumes and 0.1875 cm for boundary control volumes. Constant head boundaries were assigned to each end of the model domain to simulate a Darcy flux of 63 cm d^{-1}. The simulation was conducted for a period of 700 hours. Application of the oxidant solution to the column influent was simulated for a period of 214 hours, followed by 486 hours of flushing with deionized water. Column influent concentrations are summarized in Table 4-13.

Component	Solution 1	Solution 2	Units
K^+	0.063	1.0×10^{-10}	mol L^{-1}
MnO_4^-	0.063	1.0×10^{-10}	mol L^{-1}
$C_2Cl_{4(aq)}$	1.0×10^{-8}	1.0×10^{-8}	mol L^{-1}
Cl^-	1.0×10^{-6}	1.0×10^{-6}	mol L^{-1}
CO_3^{2-}	1.0×10^{-6}	1.0×10^{-6}	mol L^{-1}
Ca^{2+}	1.0×10^{-6}	1.0×10^{-6}	mol L^{-1}
Na^+	1.0×10^{-6}	1.0×10^{-6}	mol L^{-1}
Mg^{2+}	1.0×10^{-6}	1.0×10^{-6}	mol L^{-1}
pH	7.0	7.0	standard units

Table 4-13. Simulated chemical concentrations in the column influent. Solution 1 represents the 10 g L^{-1} $KMnO_4$ solution applied for 214 hours, and solution 2 is the deionized water applied for the subsequent 486 hours.

Aqueous MnO_4^-, Cl^-, and C_2Cl_4 concentrations were measured in the column effluent [Schnarr et al., 1998]. The MIN3P model was calibrated to reproduce the measured data through trial and error adjustment of model parameters controlling reaction rates (see Table 4-12). As indicated in Figures 4-16 and 4-17, the calibrated model reproduced transient concentrations of all three aqueous components.

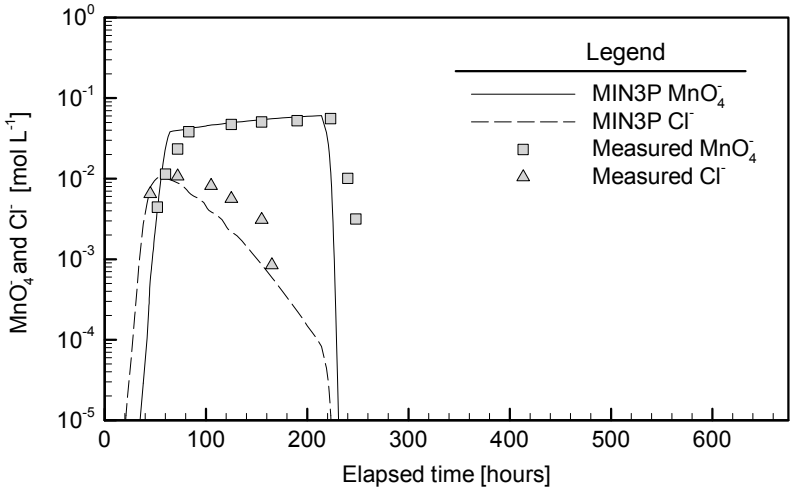

Figure 4-16. Comparison of measured and MIN3P-simulated MnO_4^- and Cl^- concentrations in the effluent from the PCE oxidation column experiment.

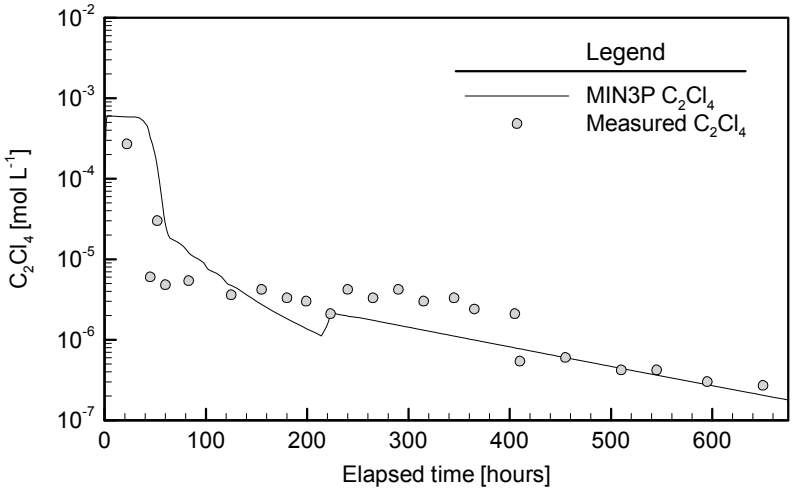

Figure 4-17. Comparison of measured and MIN3P-simulated C_2Cl_4 concentrations in the effluent from the PCE oxidation column experiment.

The MIN3P simulation results depicted in Figures 4-16 and 4-17 were used to benchmark the MIN3PD code. The MIN3PD simulation was performed using identical model input parameters incorporated in the calibrated MIN3P model. The coefficient of density variation ($\partial\rho/\partial c$) in MIN3PD was assigned a value of 0.0 to simulate uniform fluid density. A comparison of simulation results indicates that MIN3PD effluent concentrations were nearly identical to the MIN3P results (Figure 4-18).

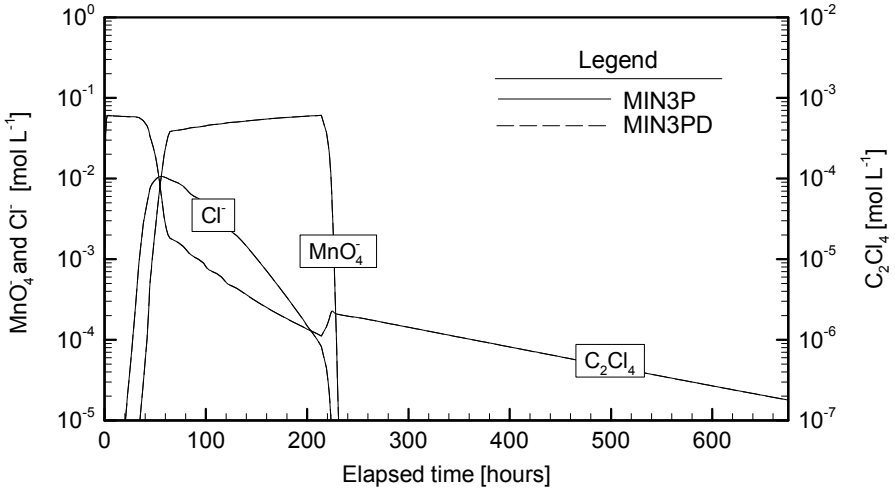

Figure 4-18. Comparison of MIN3P and MIN3PD-simulated MnO_4^-, Cl^-, and C_2Cl_4 breakthrough curves for the PCE oxidation column experiment.

4.4.2 Acid Mine Drainage Problem

The acid mine drainage problem [Lichtner, 1997] investigates the oxidation of pyrite in variably saturated media. The problem simulates the generation of acidity, iron, and sulfate resulting from the oxidation of pyrite. In addition, the dissolution of primary minerals and the formation of secondary mineral phases are investigated [Lichtner, 1997; Mayer, 1999]. This problem was utilized in the verification of the MIN3P code [Mayer, 1999]. These results are employed in the current investigation to benchmark MIN3PD. An overview of the reactive system is provided to describe the benchmarking problem. A complete description of the problem is provided by Mayer [1999].

Acid mine drainage is generated by the diffusion of gaseous oxygen into the subsurface, which partitions into the aqueous phase and reacts with pyrite and ferrous iron:

$$FeS_{2(s)} + \frac{7}{2}O_{2(aq)} + H_2O \rightarrow Fe^{2+} + 2SO_4^{2-} + 2H^+ \tag{4-10}$$

$$Fe^{2+} + \frac{1}{4}O_{2(aq)} + H^+ \rightarrow Fe^{3+} + \frac{1}{2}H_2O \tag{4-11}$$

The problem domain consists of a 20 m vertical soil column. The movement of water through the column is assumed to be at steady-state. A constant water recharge rate of 0.1 m y^{-1} was applied to the top model boundary which corresponds to the ground surface, and a constant head boundary condition was assigned to the bottom of the model domain. The boundary conditions result in a water table 10 m below the ground surface [Mayer, 1999]. Pyrite, K-feldspar, kaolinite, and quartz comprise the soil material. The soil mineralogy is assumed to be uniform, with the exception of pyrite. Pyrite is absent from ground surface to 1 m depth, but present in the bottom 19 m of the model domain [Lichtner, 1997; Mayer, 1999]. Model input characterizing the porous media and chemical transport parameters are summarized in Table 4-14.

Parameter	Symbol	Value	Units
Hydraulic conductivity	K	1.09×10^{-7}	$m\ s^{-1}$
Residual water saturation	S_{res}	0.05	-
Bubbling pressure	α	0.195	m^{-1}
Pore size distribution	n	6.67	-
Quartz fraction	φ_{quartz}	0.4	$m^3\ m^{-3}$
K-feldspar fraction	$\varphi_{feldspar}$	0.2	$m^3\ m^{-3}$
Kaolinite fraction	$\varphi_{kaolinite}$	0.2	$m^3\ m^{-3}$
Pyrite fraction (0-1 m depth)	$\varphi_{pyrite,0\text{-}1m}$	0.0	$m^3\ m^{-3}$
Porosity (0-1 m depth)	$\phi_{0\text{-}1m}$	0.20	-
Pyrite fraction (1-20 m depth)	$\varphi_{pyrite,1\text{-}20m}$	0.04	$m^3\ m^{-3}$
Porosity (1-20 m depth)	$\phi_{1\text{-}20m}$	0.16	-
Longitudinal dispersivity	α_L	0.0	m
Gas diffusion coefficient	D_g	2.13×10^{-5}	$m_2\ s^{-1}$
Aqueous diffusion coefficient	D_a	1.0×10^{-9}	$m^2\ s^{-1}$

Table 4-14. Model parameters used for the simulation of the acid mine drainage problem after Lichtner [1997] and Mayer [1999].

The reactive system was modeled using 11 primary aqueous components ($H_4SiO_{4(aq)}$, $O_{2(aq)}$, H_2O, H^+, K^+, Fe^{2+}, Fe^{3+}, Al^{3+}, HS^-, CO_3^{2-}, and SO_4^{2-}), four primary mineral phases (pyrite, K-feldspar, kaolinite, and quartz), and four secondary mineral phases (ferrihydrite, alunite, jarosite, and jurbanite). The water initially present in the porous medium is in equilibrium with the primary mineral phases quartz, kaolinite, K-feldspar, pyrite and additionally muscovite with a neutral pH [Mayer, 1999]. The infiltrating water is assumed to be saturated with oxygen under atmospheric conditions (pO_2 = 0.2 atm), is slightly acidic (pH = 5) and is in equilibrium with quartz and ferrihydrite (Table 4-15). Chemical dissolution and precipitation reactions involving primary and secondary mineral phases are summarized in Table 4-16.

Component	Initial Pore Water	Infiltrating Water	Units
K^+	6.34×10^{-3}	1.00×10^{-4}	$mol\ L^{-1}$
Al^{3+}	1.73×10^{-9}	1.00×10^{-8}	$mol\ L^{-1}$
$H_4SiO_{4(aq)}$	1.00×10^{-4}	1.00×10^{-4}	$mol\ L^{-1}$
CO_3^{2-}	1.88×10^{-4}	3.55×10^{-4}	$mol\ L^{-1}$
$O_{2(aq)}$	1.74×10^{-69}	2.53×10^{-4}	$mol\ L^{-1}$
Fe^{2+}	1.00×10^{-4}	2.04×10^{-13}	$mol\ L^{-1}$
Fe^{3+}	1.65×10^{-11}	1.81×10^{-6}	$mol\ L^{-1}$
SO_4^{2-}	3.19×10^{-3}	4.82×10^{-5}	$mol\ L^{-1}$
HS^-	8.91×10^{-11}	3.57×10^{-139}	$mol\ L^{-1}$
pH	7.0	5.0	standard units

Table 4-15. Composition of initial and infiltrating water for the acid mine drainage problem.

Mineral	Reaction
(1) Pyrite	$FeS_{2(s)} + 3.5O_{2(aq)} + H_2O \leftrightarrow Fe^{2+} + 2SO_4^{2-} + 2H^+$
(2) K-feldspar	$KAlSi_3O_8 + 4H^+ + 4H_2O \leftrightarrow K^+ + Al^{3+} + 3H_4SiO_4$
(3) Kaolinite	$Al_2Si_2O_5(OH)_4 + 6H^+ \leftrightarrow 2Al^{3+} + 2H_4SiO_4 + H_2O$
(4) Quartz	$SiO_2 + 2H_2O \leftrightarrow H_4SiO_4$
(5) Ferrihydrite	$Fe(OH)_3 + 3H^+ \leftrightarrow Fe^{3+} + 3H_2O$
(6) Alunite	$KAl_3(SO_4)_2(OH)_6 + 6H^+ \leftrightarrow K^+ + 3Al^{3+} + 2SO_4^{2-} + 6H_2O$
(7) Jarosite	$KFe_3(SO_4)_2(OH)_6 + 6H^+ \leftrightarrow K^+ + 3Fe^{3+} + 2SO_4^{2-} + 6H_2O$
(8) Jurbanite	$Al(OH)SO_4 + 5H_2O + H^+ \leftrightarrow Al^{3+} + SO_4^{2-} + 6H_2O$

Table 4-16. Mineral dissolution-precipitation reactions for the acid mine drainage problem after Lichtner [1997] and Mayer [1999].

MIN3PD model input parameters were taken directly from Mayer [1999]. Variations in fluid density were neglected in the evaluation ($\partial\rho/\partial c = 0.0$). Following Mayer [1999], the MIN3PD solution domain was discretized using 201 control volumes with half cells on the boundary, resulting in a spatial discretization interval of 10 cm for interior control volumes and 5 cm for boundary control volumes. The simulation was conducted for a 50 year period. Benchmarking was performed using the transient evolution of pore water pH (Figure 4-19), and the volume fractions of primary and secondary mineral phases at elapsed times of 25 and 50 years (Figure 4-20). MIN3PD simulation results were compared directly to the results presented in Mayer [1999]. The comparison indicates that MIN3PD simulation results are nearly identical to the MIN3P results.

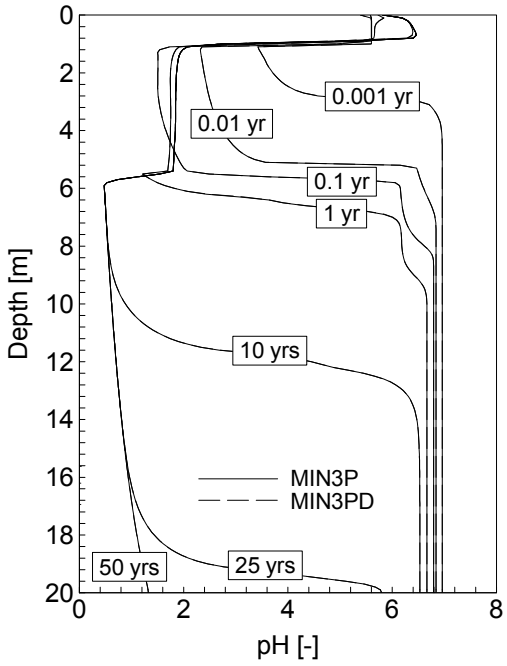

Figure 4-19. Comparison of MIN3P and MIN3PD-simulated pH profiles for the acid mine drainage problem.

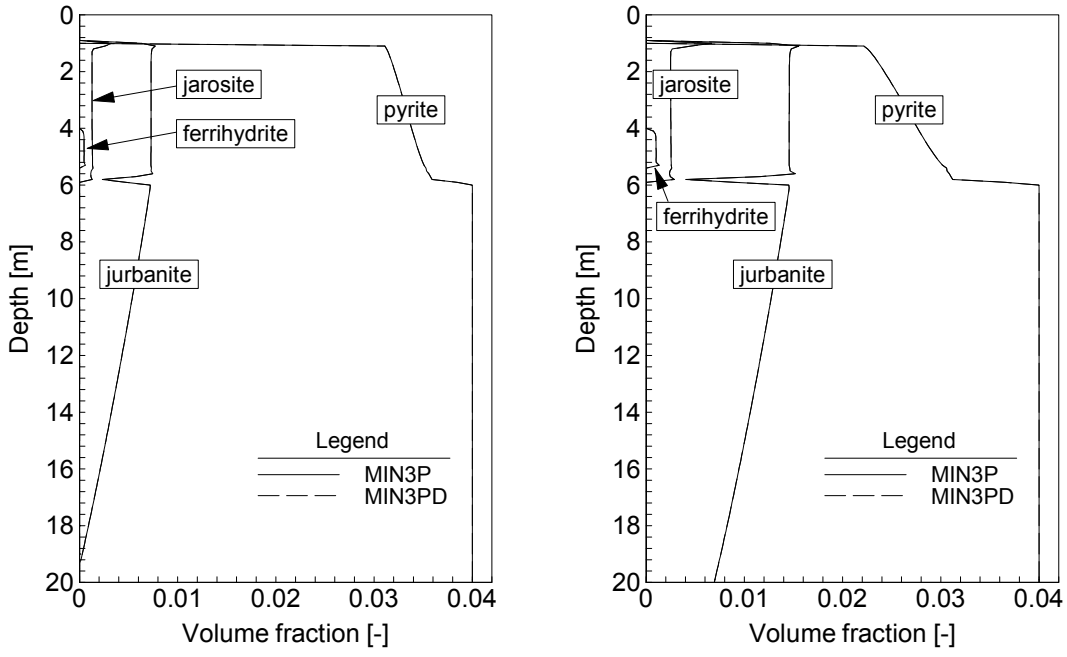

Figure 4-20. Comparison of MIN3P and MIN3PD-simulated mineral volume fractions at 25 years (left) and 50 years (right) for the acid mine drainage problem.

Chapter 5 Analysis of Coupled System Behavior

Groundwater monitoring data collected during a field trial of permanganate-based remediation of chlorinated solvents detail the accumulation and depletion of aqueous components, and indicate the evolution of plume geometries over the course of the experiment [Nelson et al., 2001; Stewart, 2002]. However, incomplete knowledge of heterogeneous system properties, the complexity of the reaction network, and the coupling between fluid flow, chemical transport, and chemical reactions complicate the interpretation of the data [Stewart, 2002].

Work presented in this chapter provides the foundation for the assessment of coupled behavior of density-driven permanganate remediation. Simplified mathematical models are employed to characterize the result of coupling between processes in the absence of heterogeneity, and evaluate the relative importance of individual coupling mechanisms. Insights into principal cause-and-effect relationships are gained through a sensitivity analysis performed to identify system parameters which exert the largest influence on the distribution of dissolved species and the efficiency of the technology. Cause-and-effect relationships between system parameters and plume geometries are illustrated, and related to the fate of the injected oxidant. The investigation is intended to set the stage for the subsequent development of a three-dimensional model of the field trial investigated in this thesis.

5.1 Problem Definition

Coupled system behavior is investigated using a zero-dimensional batch reactor and a two-dimensional representation of a field-scale permanganate remediation trial. The batch reactor simulations are used to investigate the relationship between chemical reactions and fluid density in the absence of fluid mixing and chemical transport. Interactions between the movement of fluids and reactive transport in a two-dimensional system are investigated in a hypothetical problem incorporating general features present at the North Haven field trial [Stewart, 2002]. The problem domain consists of two homogeneous sediment layers, representing an aquifer overlying an aquitard. The injection site is surrounded by a sheet pile enclosure, which isolates the aquifer from the natural hydraulic gradient. The two sediment layers are separated by a sharp contact of uniform elevation. Reactive phases present in the sediments consist of TCE, SOM, and calcite. An interval of TCE

DNAPL is present at the base of the aquifer, and SOM and calcite are distributed uniformly throughout each sediment layer (Figure 5-1).

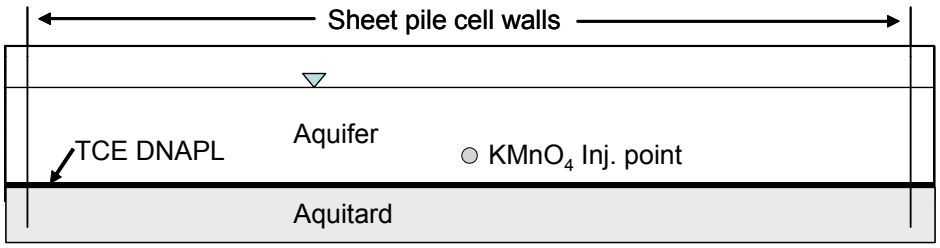

Figure 5-1. Cross-sectional view of the hypothetical $KMnO_4$ remediation problem.

A 40 g L^{-1} $KMnO_4$ solution is introduced 1 m above the aquitard at a rate of 5 L min^{-1} for a period of 0.5 day. Following the injection, no external hydrologic stresses are applied. System response is simulated for a 100-day period. The horizontal symmetry around the injection point allows the problem to be modeled using a two-dimensional radial grid. MIN3PD boundary conditions for this configuration are illustrated in Figure 5-2.

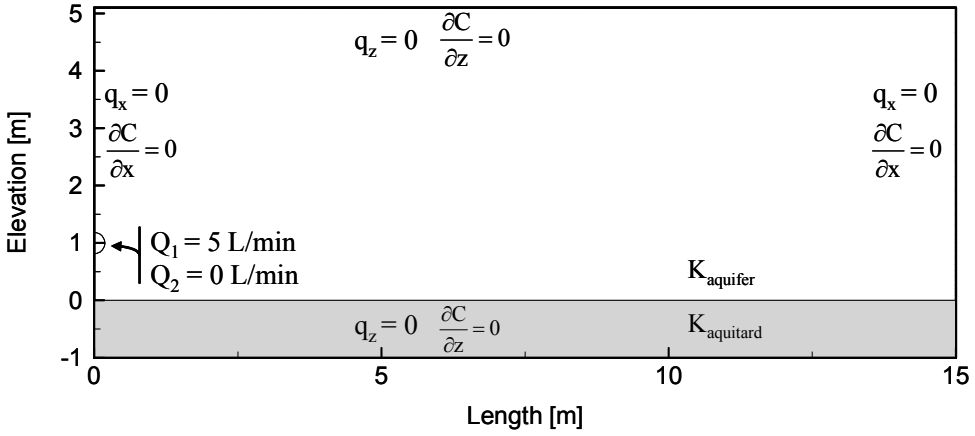

Figure 5-2. Model domain and boundary conditions for the hypothetical $KMnO_4$ remediation problem. The initial fluid injection rate (Q_1) is applied for 0.5 day, and the second rate (Q_2) is applied for the remaining 99.5 days.

5.2 MIN3PD Model Development

5.2.1 Hydrogeologic Model Parameters

MIN3PD input parameters quantifying the physical properties of the sediments and fluids are summarized in Table 5-1. The model incorporates generic properties for a medium-grained sand aquifer and a clay aquitard (e.g. hydraulic conductivity, porosity, pore-size distribution, residual moisture content, air entry pressure) tabulated by Carsel and Parrish [1988] and Domenico and Schwartz [1990]. The TCE DNAPL saturation at the base of the aquifer was set to 2 percent. This saturation is assigned to depict an average saturation integrated over the bottom 0.1 m of the aquifer. Detailed investigation of residual DNAPL source zones at field sites has indicated the presence of thin, vertically stratified layers of DNAPL separated by zones with no DNAPL [Parker et al., 2003]. Explicit representation of this complexity in DNAPL geometry would require a substantial refinement of the model grid, which was not considered necessary to meet the objectives of the current work. The 2 percent DNAPL saturation results in a reduction of the relative aqueous permeability of aquifer sediments by approximately 23 percent, using the constitutive relationship described in Chapter 3. The coefficient of density variation ($\partial\rho/\partial c_t$) was taken from Kharaka et al. [1988], resulting in a fluid density contrast of 2.8 % between the 40 g L^{-1} oxidant solution and the groundwater.

Hydrogeologic Parameters	Symbol	Value	Units
$KMnO_4$ injection rate	Q_{inj}	5.0	$L\ min^{-1}$
Injection duration	Inj	0.5	d
Oxidant solution density	ρ_{inj}	1.025	$g\ L^{-1}$
Groundwater density	ρ_f	0.998	$g\ L^{-1}$
Fluid density coefficient	$\partial\rho / \partial c$	0.688	-
Aquifer Properties			
Hydraulic conductivity	K_{aq}	2.0×10^{-4}	$m\ s^{-1}$
Porosity	ϕ_{aq}	0.43	-
Specific storage coefficient	S_p	1.0×10^{-4}	m^{-1}
Longitudinal dispersivity	α_L	0.10	m
Transverse dispersivity	α_T	0.010	m
DNAPL thickness	L_{DNAPL}	0.1	m
DNAPL saturation	S_{DNAPL}	0.02	$m^3\ m^{-3}$
Residual water saturation	S_{res}	0.045	-
Bubbling pressure	α	14.5	m^{-1}
Pore size distribution	n	2.68	-
Van Genuchten exponent	l	0.5	-
Aquitard Properties			
Hydraulic conductivity	K_{aqt}	5.6×10^{-8}	$m\ s^{-1}$
Porosity	ϕ_{aqt}	0.36	-
Specific storage coefficient	S_p	1.0×10^{-4}	m^{-1}
Longitudinal dispersivity	α_L	0.10	m
Transverse dispersivity	α_T	0.010	m
DNAL thickness	L_{DNAPL}	0.0	m
DNAPL saturation	S_{DNAPL}	0.0	$m^3\ m^{-3}$
Residual water saturation	S_{res}	0.07	-
Bubbling pressure	α	0.5	m^{-1}
Pore size distribution	n	1.09	-
Van Genuchten exponent	l	0.5	-

Table 5-1. MIN3PD hydrogeological parameters used for the hypothetical test problem of permanganate-based aquifer remediation.

5.2.2 Description of Reactive System

The reaction network utilized in the current investigation was designed based on the conceptual model introduced in Chapter 2 and consists of the primary chemical reactions resulting from the oxidant injection (Table 5-2):

Reaction	
(1)	Consumption of MnO_4^- due to reaction with SOM present in the porous media
(2)	Oxidation of $C_2HCl_{3(aq)}$ by MnO_4^-
(3)	DNAPL dissolution generating $C_2HCl_{3(aq)}$ within the aqueous phase
(4)	Reversible sorption of $C_2HCl_{3(aq)}$ to aquifer sediments
(5)	Cation exchange reactions involving K^+, Na^+, Ca^{2+}, Mg^{2+}
(6)	Buffering of groundwater pH provided by calcite dissolution/precipitation

Table 5-2. Conceptual model of reaction network.

Using the MIN3PD conventions described in Chapter 2, the reactive system is defined using a combination of primary aqueous components, secondary aqueous species, immobile phases (including minerals, SOM, and TCE DNAPL), and sorbed species. The reactive system is modeled using 11 primary aqueous components ($C_2HCl_{3(aq)}$, H_2O, MnO_4^-, Cl^-, Br^-, CO_3^{2-}, K^+, Na^+, H^+, Ca^{2+}, and Mg^{2+}), two mineral phases (calcite and manganese oxide), SOM, and the TCE DNAPL. The component Br^-, which does not participate in any chemical reactions, was included in the simulations as a conservative tracer to depict the movement of variable density fluids.

Table 5-3 summarizes the network of chemical reactions involving the primary aqueous components. Reactions (1) through (4) in the Table reflect the reactions driven by the introduction of MnO_4^-, and reactions (5) through (10) are cation exchange reactions driven primarily by the loading of K^+. Equation (11) describes reversible calcite dissolution which provides pH buffering.

	Reaction
(1)	$C_2HCl_{3(aq)} + 2MnO_4^- + 2H_2O \rightarrow 2MnO_{2(am)} + 3Cl^- + 2CO_3^- + 5H^+$
(2)	$3CH_2O + 4MnO_4^- \rightarrow 3CO_3^{2-} + 4MnO_{2(aq)} + 2H_2O + 2H^+$
(3)	$C_2HCl_{3(DNAPL)} \rightarrow C_2HCl_{3(aq)}$
(4)	$C_2HCl_{3(sorbed)} \leftrightarrow C_2HCl_{3(aq)}$
(5)	$K^+ + Na - X \leftrightarrow K - X + Na^+$
(6)	$K^+ + 0.5Ca - X_2 \leftrightarrow K - X + 0.5Ca^{2+}$
(7)	$K^+ + 0.5Mg - X_2 \leftrightarrow K - X + 0.5Mg^{2+}$
(8)	$Na^+ + 0.5Ca - X_2 \leftrightarrow Na - X + 0.5Ca^{2+}$
(9)	$Na^+ + 0.5Mg - X_2 \leftrightarrow Na - X + 0.5Mg^{2+}$
(10)	$Ca^+ + Mg - X_2 \leftrightarrow Ca - X_2 + Mg^{2+}$
(11)	$CaCO_3 \leftrightarrow Ca^{2+} + CO_3^{2-}$

Table 5-3. MIN3PD reaction network expressed using primary aqueous components.

The reaction network does not include trace metals (e.g., Cu, Pb, Zn, Mo, Ni, Cr) which may be mobilized due to the oxidative dissolution of reduced mineral phases, and may be introduced as impurities in the oxidant solution [Crimi and Siegrist, 2003]. Factors affecting metal mobility during a field application of permanganate, including co-precipitation and surface complexation reactions were investigated by Al et al. [2006]. The complexity in simulating these processes governing the mobility of trace metals was determined to be outside the scope of the current investigation.

A total of 11 secondary species were defined based on aqueous complexation reactions involving the primary aqueous components (Table 5-4). The majority of the secondary species are represented by aqueous complexation reactions involving the component CO_3^{2-}. The concentrations of individual carbonate species (e.g. H_2CO_3, HCO_3^-, CO_3^{2-}) are computed based on the reaction stoichiometries and equilibrium coefficients summarized in Table 5-4.

Reaction			log K_{eq}
OH^-	$\leftrightarrow$	$H_2O - H^+$	-13.998
HCO_3^-	$\leftrightarrow$	$H^+ + CO_3^{2-}$	10.330
H_2CO_3	$\leftrightarrow$	$2H^+ + CO_3^{2-}$	16.681
$MgOH^+$	$\leftrightarrow$	$Mg^+ + H_2O - H^+$	-11.440
$MgCO_3$	$\leftrightarrow$	$Mg^+ + CO_3^{2-}$	2.980
$MgHCO_3^+$	$\leftrightarrow$	$Mg^{2+} + CO_3^{2-} + H^+$	11.440
$CaOH^-$	$\leftrightarrow$	$Ca^{2+} + H_2O - H^+$	-12.780
$CaCO_{3(aq)}$	$\leftrightarrow$	$Ca^{2+} + CO_3^{2-}$	3.220
$CaHCO_3^+$	$\leftrightarrow$	$Ca^{2+} + CO_3^{2-} + H^+$	11.440
$NaCO_3^-$	$\leftrightarrow$	$Na^+ + CO_3^{2-}$	1.268
$NaHCO_3$	$\leftrightarrow$	$Na^+ + CO_3^{2-} + H^+$	10.080

Table 5-4. Aqueous complexation reactions. Equilibrium constants were taken from the WATEQ4F database [Ball and Nordstrom, 1991].

The sorption reactions (Table 5-3, reactions 4 through 10) and aqueous complexation reactions (Table 5-4) are assumed to be rapid, reversible reactions modeled using equilibrium-based expressions. The primary reactions affecting the fate of the MnO_4^- include the oxidation of $C_2HCl_{3(aq)}$ by MnO_4^-, the consumption of MnO_4^- by SOM, and the dissolution of TCE DNAPL [Schnarr et al., 1998; Stewart, 2002; MacKinnon and Thomson, 2002]. These reactions are simulated in the MIN3PD model as kinetic reactions using rate expressions developed in Chapter 2. The rate expressions are summarized in Table 5-5.

Name	Rate Expression
(1) C_2HCl_3 oxidation	$R_{tce}^{ox} = -k_{tce}^{ox}[C_2HCl_{3(aq)}][MnO_4^-]$
(2) SOM oxidation	$R_{CH_2O}^{ox} = -k_{CH_2O}^{ox}[MnO_4^-]\left(\frac{\varphi_{CH_2O}}{\varphi_{CH_2O,0}}\right)^{\alpha,CH_2O}$
(3) DNAPL dissolution	$R_{tce}^{diss} = -k_{tce}^{diss}\left([C_2HCl_{3(aq)}]_{sat} - [C_2HCl_{3(aq)}]\right)\left(\frac{\varphi_{C_2HCl_3}}{\varphi_{C_2HCl_3,0}}\right)^{\alpha,TCE}$
(4) Calcite dissolution/precipitation	$R_{CaCO_3} = -k_{CaCO_3}\left[1 - \frac{IAP_{CaCO_3}}{K_{CaCO_3}}\right]$

Table 5-5. Reaction rate expressions.

$C_2HCl_{3(aq)}$ sorption is modeled as a non-competitive partitioning reaction between water and SOM [Chiou et al., 1983]. Cation exchange reactions are modeled as competitive reactions using the Gaines-Thomas formulation [Langmuir, 1997]. Cation exchange selectivity coefficients are provided in Table 5-6.

Ion-exchanged species	log K_s
K^+-X	0.6990
$Mg^{2+}-X_2$	0.6021
$Ca^{2+}-X_2$	0.7959

Table 5-6. Selectivity coefficients for cation exchange reactions defined with respect to Na^+.

5.2.3 Reactive Transport Model Parameters

Reactive transport parameters in the MIN3PD model are summarized in Table 5-7. The rate constant for oxidation of $C_2HCl_{3(aq)}$ by MnO_4^- was taken from Yan and Schwartz [1999]. The TCE-DNAPL dissolution rate constant was estimated using the correlation developed by Nambi and Powers [2003] presented in Chapter 2, using the average fluid seepage velocity recorded at the base of the aquifer 1 m from the injection point. Reaction kinetics between SOM and permanganate were estimated in a series of preliminary simulations (data not shown) using the results for a set of column experiments measuring the consumption of permanganate by Borden aquifer sands [Mumford et al., 2005]. Identical values for SOM fraction, calcite content, and CEC were assigned to the aquifer and aquitard sediments. The partitioning of $C_2HCl_{3(aq)}$ between groundwater and aquifer SOM was computed using the following relationship:

$$K_d = (K_{oc})(SOM)\frac{\rho_b}{\phi} \tag{5-1}$$

where K_{oc} represents the organic carbon-water partitioning coefficient for $C_2HCl_{3(aq)}$ [Chiou et al., 1983; Pankow and Cherry, 1996].

Reactive Transport Parameters	Symbol	Value	Units
$C_2HCl_{3(aq)}$- MnO_4^- rate constant	k_{tce}^{ox}	0.65	$mol^{-1}\ L^2_{H2O}\ L^{-1}_{bulk}\ s^{-1}$
SOM-MnO_4 rate constant	$k_{CH_2O}^{ox}$	5.0×10^{-5}	$mol^{-1} L_{H2O}\ s^{-1}$
DNAPL dissolution rate constant	k_{tce}^{diss}	8.3×10^{-6}	s^{-1}
DNAPL reactivity exponent	α_{tce}	1.0	-
SOM reactivity exponent	α_{CH2O}	2.2	-
Chemical diffusion coefficient	D_m	1.0×10^{-9}	$m^2\ s^{-1}$
SOM-water partitioning coefficient	K_{oc}	126	LKg^{-1}
Soil-water partitioning coefficient	K_d	0.3	-
SOM fraction	φ_{CH2O}	5.0×10^{-4}	$m^3\ m^{-3}$
Calcite fraction	$\varphi_{calcite}$	1.0×10^{-3}	$m^3\ m^{-3}$
Bulk density	ρ_{aq}	1.5	$Kg\ L^{-1}$
Cation exchange capacity	CEC	5.0	$meq\ [100\ g]^{-1}$

Table 5-7. Reactive transport parameters. The K_{oc} and K_d partitioning coefficients apply to $C_2HCl_{3(aq)}$.

5.2.4 MIN3PD Model Setup

The problem was simulated using a two-dimensional radial model domain extending 15 meters in the horizontal direction and 6.1 meters in the vertical direction. The model was discretized using a 1476-node telescoping mesh, with model control volumes ranging from 0.05 to 1.5 m in length and from 0.05 to 0.48 m in thickness. The grid was refined in the vertical direction at the aquifer-aquitard contact, and near the top of the domain corresponding to the water table condition. The grid was refined in the horizontal direction at the origin, corresponding to the oxidant injection location. The aquitard was represented in the bottom meter of the model domain ($-1.0\text{m} \le z \le 0.0\text{m}$) while the aquifer was represented in the upper 5.1 m of the domain ($0.0\text{m} < z \le 5.1\text{m}$). Figure 5-3 illustrates the layout of the MIN3PD model grid.

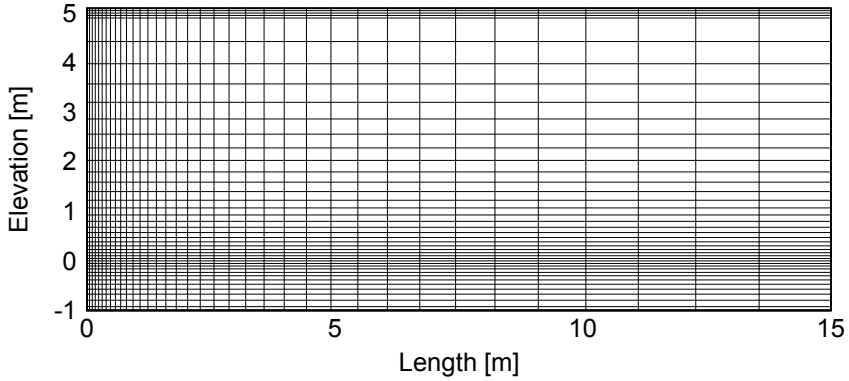

Figure 5-3. MIN3PD model grid for the hypothetical $KMnO_4$ remediation problem. Elevation of 0 m corresponds to the contact between the aquifer and aquitard in the model grid.

TCE in the model domain was present in dissolved form, adsorbed onto the solid phase, and as a DNAPL at the base of the aquifer. The pre-injection distribution of $C_2HCl_{3(aq)}$ (Figure 5-4) was computed using preliminary simulations modeling $C_2HCl_{3(aq)}$ diffusion and adsorption from the DNAPL zone at the base of the aquifer for a 10 year period. Table 5-8 summarizes the initial amounts of SOM and TCE (DNAPL, aqueous, and sorbed) in the model domain. As indicated in the Table, the DNAPL accounts for approximately 85 percent of the TCE initially present in the model.

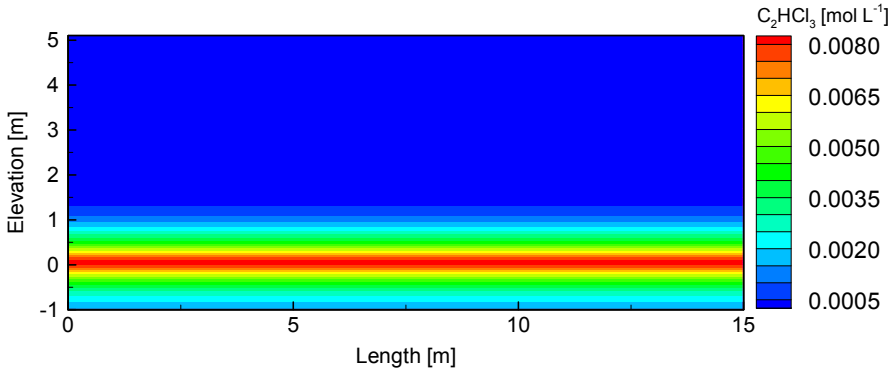

Figure 5-4. Pre-injection distribution of $C_2HCl_{3(aq)}$. Maximum $C_2HCl_{3(aq)}$ concentration (8.36×10^{-3} mol L^{-1}) corresponds to the solubility value of 1100 mg L^{-1}.

Phase	Moles
SOM	71814
TCE-DNAPL	7093
TCE-Aqueous	2514
TCE-Sorbed	553

Table 5-8. Cumulative amounts of SOM and TCE in the model domain.

The oxidant solution was applied to a single MIN3PD cell located at the origin of the horizontal axis with an elevation of 1.0 m. The oxidant solution was assumed to have a geochemical composition similar to the background geochemistry of the aquifer. The pH and concentrations of Na^+, Ca^{2+}, Mg^{2+}, Cl^-, and CO_3^{2-} of the oxidant solution were identical to the initial conditions present in the aquifer. The concentrations of K^+ and MnO_4^- in the oxidant solution were 0.25 mol L^{-1}, equivalent to a $KMnO_4$ concentration of approximately 40 g L^{-1}. Br^- was added to the oxidant solution to provide a chemical tracer using a dilute concentration (1.0×10^{-5} mol L^{-1}) which would not significantly affect fluid density. $C_2HCl_{3(aq)}$ was assumed to be absent in the oxidant solution. Table 5-9 summarizes the pre-injection geochemistry in the model and the oxidant solution composition.

Component	Pre-injection	Oxidant Solution	Units
K^+	1.0×10^{-4}	0.25	mol L^{-1}
MnO_4^-	1.0×10^{-15}	0.25	mol L^{-1}
$C_2HCl_{3(aq)}$	10 yr profile	1.0×10^{-15}	mol L^{-1}
Cl^-	5.0×10^{-3}	5.0×10^{-3}	mol L^{-1}
CO_3^{2-}	5.0×10^{-3}	5.0×10^{-3}	mol L^{-1}
Ca^{2+}	2.5×10^{-3}	2.5×10^{-3}	mol L^{-1}
Na^+	2.5×10^{-3}	2.5×10^{-3}	mol L^{-1}
Mg^{2+}	5.0×10^{-4}	5.0×10^{-4}	mol L^{-1}
pH	7.5	7.5	standard units
Br^-	1.0×10^{-15}	1.0×10^{-5}	mol L^{-1}

Table 5-9. Pre-injection groundwater and oxidant solution chemistry. Initial $C_2HCl_{3(aq)}$ concentrations were assigned to individual MIN3PD cells using the results computed from a preliminary simulation of $C_2HCl_{3(aq)}$ diffusion from the aquifer DNAPL zone.

5.3 Simulated System Response

5.3.1 Fluid Flow

Figure 5-5 illustrates fluid flow vectors and the spatial distribution of fluid densities at elapsed times of 1, 10, and 100 days. The orientation of the flow vectors coincide with the sinking of dense oxidant solution in the vicinity of the injection point, and its lateral movement along the base of the aquifer. The vector lengths in Figure 5-5 are scaled to the maximum seepage velocity magnitude recorded during each output time. The maximum fluid seepage velocity recorded at 1 day was 0.6 m d^{-1}, while the maximum fluid seepage velocity at 100 days was 0.02 m d^{-1} (data not shown). The presence of convective fluid flow patterns is consistent with the movement of variable density fluids [Rayleigh, 1916; Horton and Rogers, 1945; Lapwood, 1948; Elder, 1967]. The development of stationary fluid convection cells in the Elder and HRL problems reflect system response to boundary conditions which remain constant over time. The transient nature of the boundary conditions applied to the permanganate remediation problem results in the transient patterns of fluid movement over the course of the simulation.

The distribution of fluid densities indicates that groundwater affected by the oxidant solution has penetrated approximately 0.2 m into the aquitard at an elapsed time of 100 days. The permeability of the aquitard is 3.6 orders of magnitude less than the aquifer, limiting the bulk movement of fluids within the aquitard. As Figure 5-5 indicates, a sharp vertical gradient in fluid densities is present at the contact between the two units. The gradient of fluid density corresponds to a gradient in solute concentrations, which drives diffusive solute flux into the aquitard.

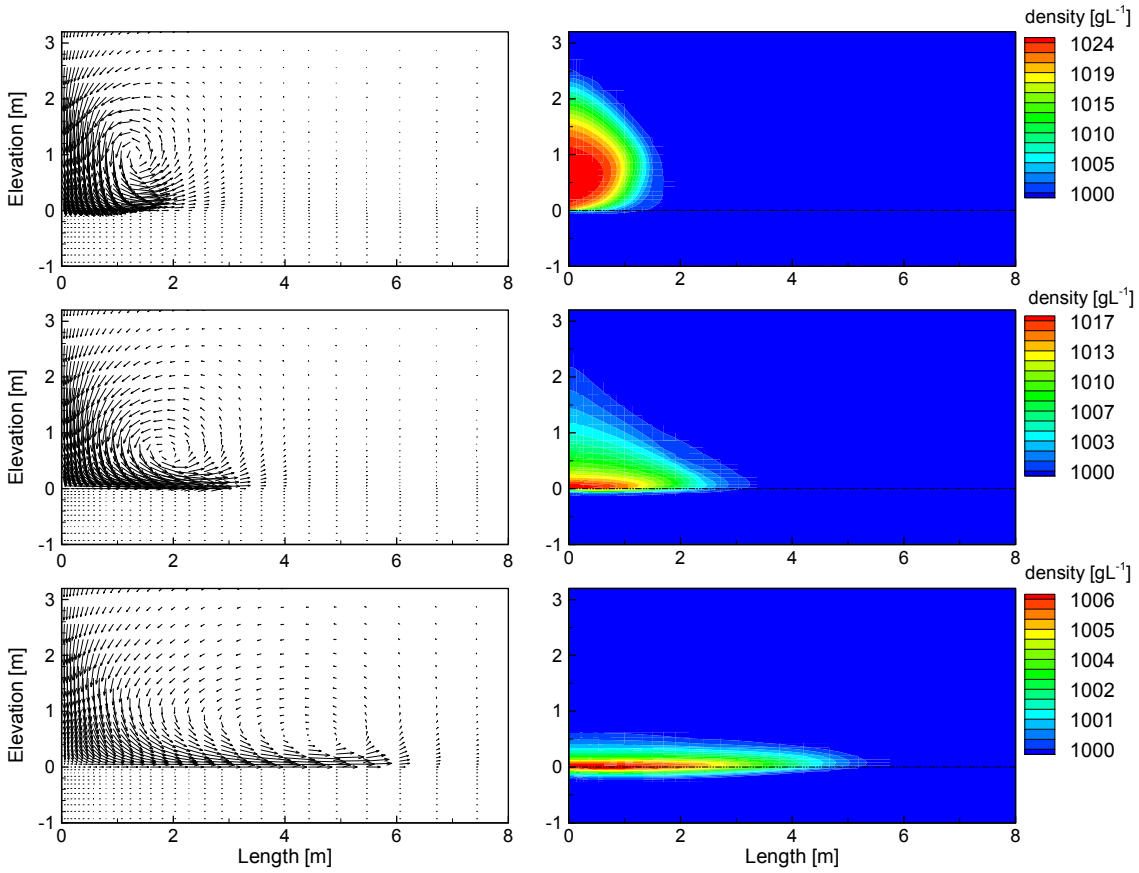

Figure 5-5. Scaled fluid velocity vector fields and fluid densities at 1 day (top), 10 days, and 100 days (bottom). Vector lengths are scaled to the maximum fluid velocities of 0.6, 0.1, and 0.02 m d^{-1} recorded during the 3 output times. The location of the aquifer-aquitard contact is depicted in the fluid density figures by a horizontal dashed line at an elevation of 0 m.

The fluid density contour plots (Figure 5-5) indicate a reduction in density within the groundwater plume affected by the oxidant solution with elapsed time. The initial density contrast was 2.8 percent between the oxidant solution and groundwater (fluid densities of 1.026 and 0.998 Kg L^{-1}, respectively); the density contrast decreased over the 100-day simulation to approximately 0.8 percent. Hydrodynamic dispersion, incorporating the result of solute diffusion and the mechanical mixing of fluids, is a process that reduces spatial gradients in fluid density and the density contrast [Voss and Souza, 1986]. In addition, contaminant treatment, consumption of permanganate, and other secondary geochemical reactions may also affect density. The relationship between chemical reactions and fluid density is analyzed in detail in Section 5.3.4.

5.3.2 Contaminant Treatment and Fate of Oxidant

The fate of the MnO_4^- is determined by the reactions with $C_2HCl_{3(aq)}$ and SOM, and the replenishment of $C_2HCl_{3(aq)}$ resulting from DNAPL dissolution. Cl^- is generated by the oxidation of $C_2HCl_{3(aq)}$, and provides a reaction tracer indicating the location and intensity of the reaction between MnO_4^- and $C_2HCl_{3(aq)}$ [Schnarr et al.,1998; Nelson et al., 2001]. Figure 5-6 illustrates the distribution of MnO_4^-, $C_2HCl_{3(aq)}$, and Cl^- at 1 and 100 days.

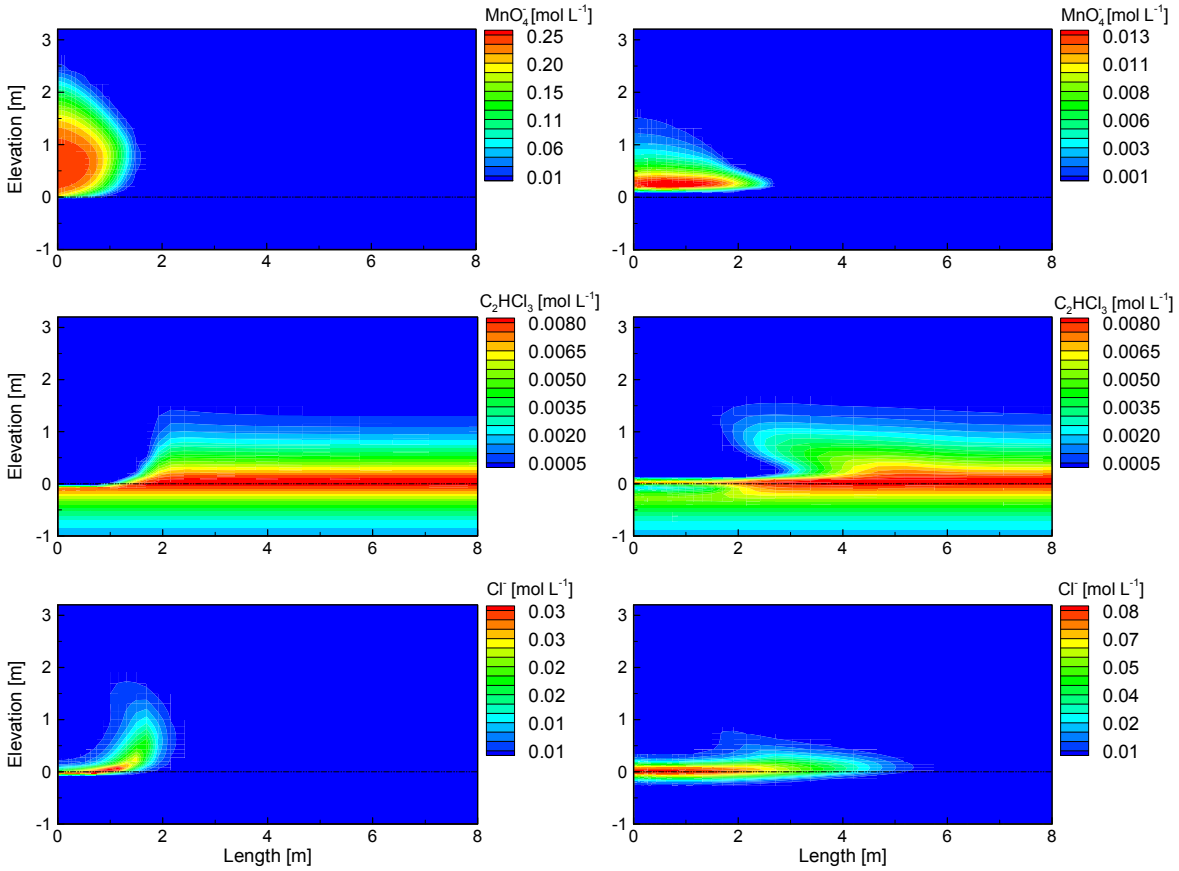

Figure 5-6. Aqueous MnO_4^- (top), $C_2HCl_{3(aq)}$, and Cl^- (bottom) distributions at 1 (left) and 100 days (right). The location of the aquifer-aquitard contact is depicted in the figures by a horizontal dashed line.

A comparison of the MnO_4^- and $C_2HCl_{3(aq)}$ plumes reveals minimal overlap in the distribution of the two components, indicative of rapid kinetics for the intra-aqueous reaction between MnO_4^- and $C_2HCl_{3(aq)}$ relative to the rate of fluid movement. At 100 days, the Cl^- plume has accumulated along the base of the aquifer, extending approximately twice as far (~7 m) from the injection point as the MnO_4^- plume (~3.5 m). Maximum Cl^- concentrations are present along the base of the aquifer, and Cl^- diffusion into the aquitard occurs. Lateral and upward displacement of $C_2HCl_{3(aq)}$ is indicated by its spatial distribution at 100 days, indicating limited mixing between the MnO_4^- and $C_2HCl_{3(aq)}$-contaminated groundwater.

5.3.3 Geochemical Response

Aqueous geochemistry evolves in response to the loading of K^+ and MnO_4^- provided by the oxidant injection and the density-driven movement of fluids. The injected K^+ participates in cation exchange reactions which affect aqueous and adsorbed concentrations of K^+, Na^+, Ca^{2+}, and Mg^{2+}. The sorption sites are initially occupied predominantly by Ca^{2+} (Figure 5-7). At the onset of the investigation, Ca^{2+} occupied approximately 86 percent of the cation exchange sites, and Mg^{2+}, Na^+, and K^+ occupied 11, 2, and 1 percent of the cation exchange sites, respectively. Following the injection, Ca^{2+}, Na^+, and Mg^{2+} are replaced by K^+ and accumulate along the edges of the K^+ plume. Figure 5-7 illustrates the cation exchange reactions recorded at the base of the aquifer, approximately 1.9 meters from the injection point in the horizontal direction. As the Figure indicates, increases in Ca^{2+}, Na^+, and Mg^{2+} occur prior to the arrival of K^+. This breakthrough pattern reflects the replacement of adsorbed Ca^{2+}, Na^+, and Mg^{2+} ions by K^+.

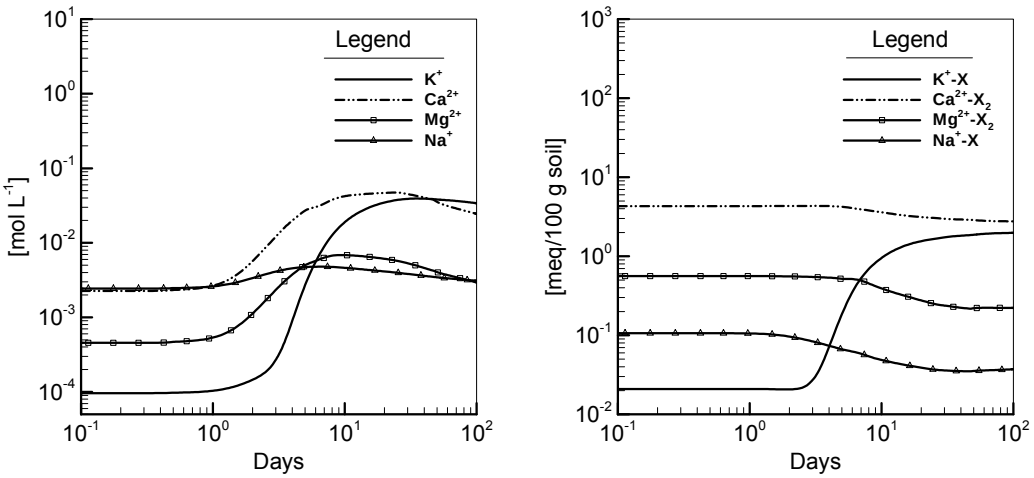

Figure 5-7. Aqueous (left) and adsorbed (right) K^+, Ca^{2+}, Mg^{2+}, and Na^+ concentrations recorded at the base of the aquifer approximately 1.9 m from the oxidant injection point.

Figure 5-8 illustrates the spatial distribution of K^+ and Na^+ recorded at 1, 10, and 100 days. At elapsed time of 1 day, direct correspondence between the geometry of the K^+ and Na^+ plumes is apparent, reflecting the replacement of adsorbed Na^+ by K^+. With increasing time, the correspondence between the plumes is complicated by the redistribution of aqueous components resulting from the variable density movement of fluids and continued sorption reactions. At 100 days, the decrease in aqueous Na^+ concentrations in the vicinity of the injection point corresponds to the partial replacement of sorbed K^+ by Na^+.

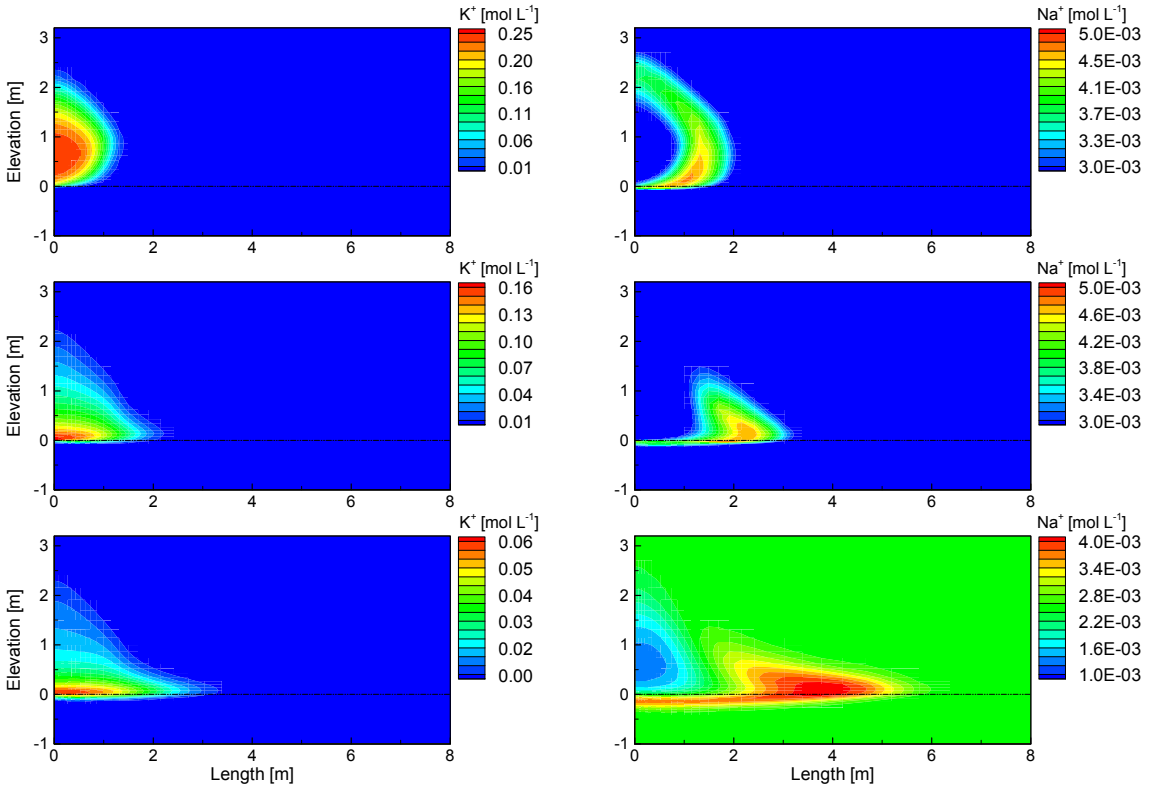

Figure 5-8. Aqueous K^+ (left) and Na^+ (right) distributions at 1 (top), 10, and 100 days (bottom). The location of the aquifer-aquitard contact is depicted in the figures by a horizontal dashed line at an elevation of 0 m.

A snapshot of the complete geochemical system 30 days following the oxidant injection is provided in Figure 5-9. The geometry of the Br^- plume indicates the spatial extent of the dense plume, with displacement of $C_2HCl_{3(aq)}$ indicated in a similar fashion to Figure 5-6. A reduction in pH to approximately 5.0 occurs at the base of the aquifer. In the current model, pH buffering is provided by calcite present in the aquifer and aquitard sediments. However, at 30 days, the calcite within the bottom 10 centimeters of the aquifer (corresponding to the thickness of the DNAPL interval) has been depleted near the injection point. A companion simulation performed with calcite absent from the sediments indicated pH reductions to 1.7 at the base of the aquifer (data not shown). Groundwater alkalinity is dominated by HCO_3^-, a complexed species of the primary component CO_3^{2-}. As indicated in Table 5-3, MnO_4^- oxidation of $C_2HCl_{3(aq)}$ and SOM generates CO_3^{2-} as a reaction product. In the buffered system studied, these reactions result in an increase in groundwater alkalinity (Figure 5-9).

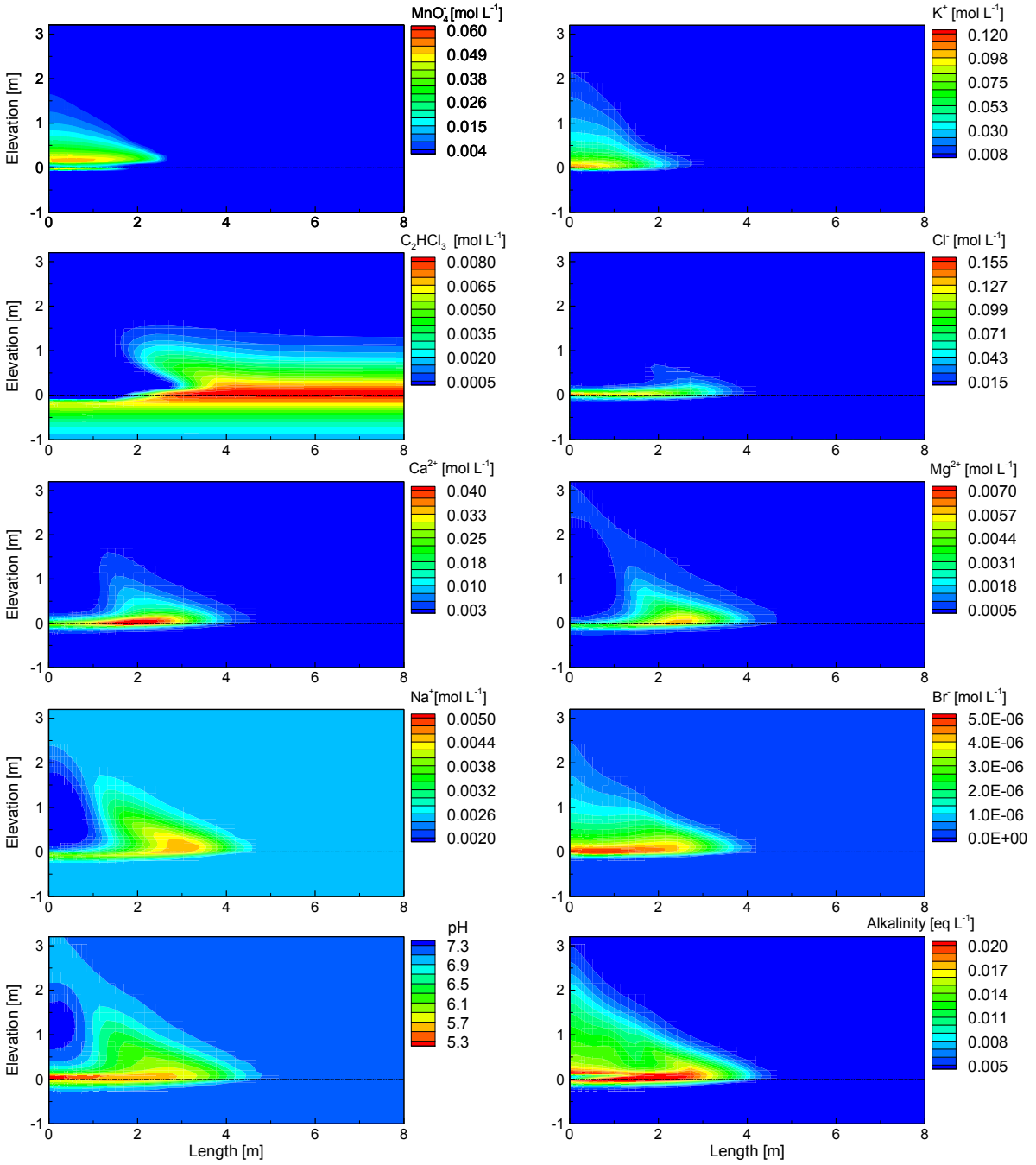

Figure 5-9. Distribution of aqueous components MnO_4^-, K^+, $C_2HCl_{3(aq)}$, Cl^-, Ca^{2+}, Mg^{2+}, Na^+, Br^-, groundwater pH, and alkalinity at 30 days.

The distribution of SOM, TCE DNAPL, manganese oxide, and calcite at the conclusion of the simulation is illustrated in Figure 5-10. The portion of the model invaded by MnO_4^- is indicated by the extent of the zone of SOM depletion. As the reduction of MnO_4^- by SOM generates insoluble manganese oxides, the geometry of the zone of SOM depletion corresponds to the zone of manganese

oxide accumulation. The highest simulated volume fractions of manganese oxide occur at the base of the aquifer, corresponding to the location of TCE DNAPL [Conrad et al., 2002; MacKinnon and Thomson, 2002; Stewart, 2002]. The pre-injection volume fraction of DNAPL exceeded the SOM volume fraction by over one order of magnitude (8.6 x 10^{-3} L_{DNAPL}/L_{bulk} vs. 5.0 x 10^{-4} L_{SOM}/L_{bulk}), focusing the consumption of MnO_4^- and generation of manganese oxide within the DNAPL interval. As indicated in Table 5-3, permanganate oxidation of $C_2HCl_{3(aq)}$ generates acidity, reflected in the depletion of calcite along the base of the aquifer corresponding to the area of DNAPL depletion [Nelson et al., 2001].

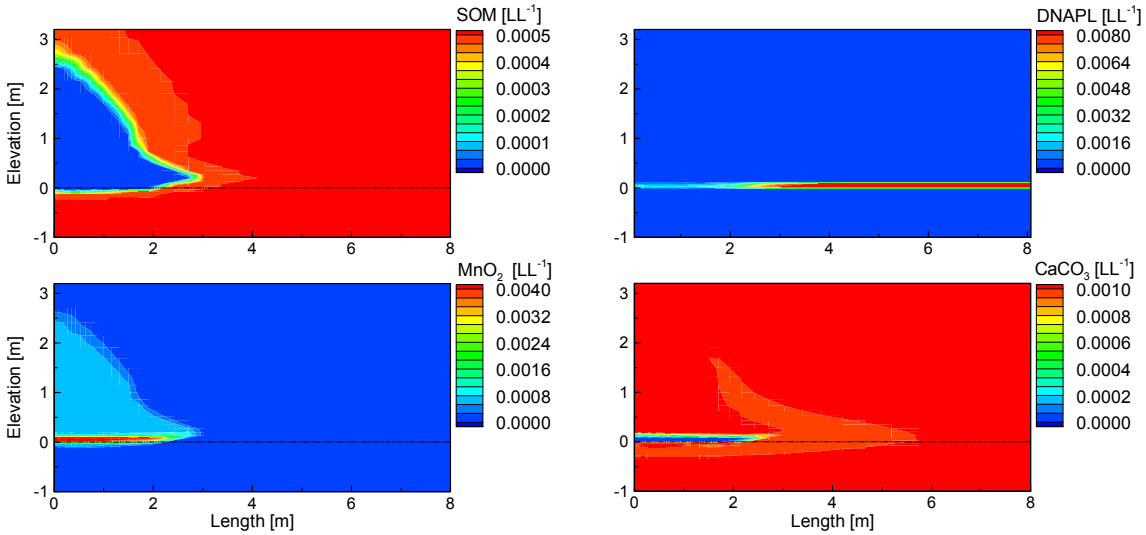

Figure 5-10. Volume factions of SOM, DNAPL, manganese oxide, and calcite present at 100 days.

The distribution of adsorbed K^+, Ca^{2+}, Na^+, and Mg^{2+} ions at the conclusion of the simulation is illustrated in Figure 5-11. The predominant cation exchange reaction is the replacement of Ca^{2+} by K^+. Adsorbed Na^+ and Mg^{2+} concentrations are generally reduced in the vicinity of the oxidant injection point, replaced by either Ca^{2+} or K^+.

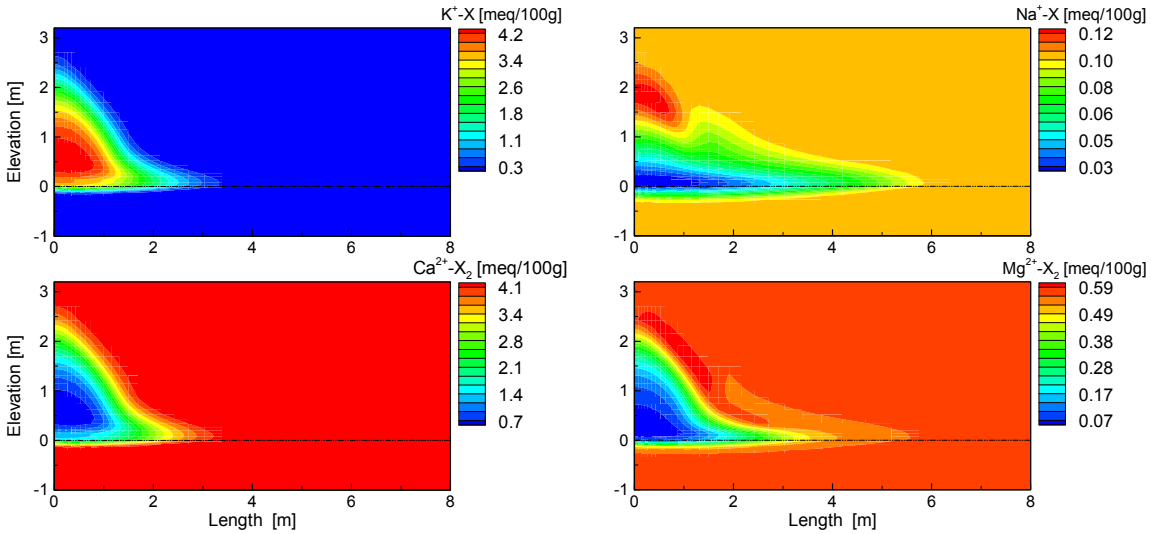

Figure 5-11. Adsorbed K^+, Ca^{2+}, Mg^{2+}, and Na^+ concentrations recorded at 100 days.

5.3.4 Coupling Mechanisms

A primary coupling mechanism in the conceptual model of permanganate-based aquifer remediation using the inject-and-leave method [Nelson et al., 2001] is the interdependence of dissolved aqueous species concentrations, fluid density, fluid movement, and the transport of aqueous species. The importance of the coupling between these processes is illustrated by comparing density-driven system response to an alternate case in which the gradients in fluid density are neglected. The alternate case was simulated by setting the coefficient of density variation (see Table 5-1) to 0.0, resulting in constant fluid density throughout the model domain over the course of the simulation. The non-reactive aqueous component Br^- is used to illustrate the movement of fluids for each case (Figure 5-12). Immediately following the oxidant injection (elapsed time of 1 day), the comparison indicates that gradients in fluid density enhance the downward movement of the Br^- plume relative to the constant density case. At 100 days, the Br^- distribution in the variable density case is markedly different from the Br^- distribution predicted in the absence of fluid density gradients. These results confirm the significance of density-driven flow in the movement of fluids, delivery of the oxidant solution, and transport of aqueous species for the defined problem. The spreading of the dense plume along the base of the aquifer enhances the delivery of MnO_4^- to the location of the TCE DNAPL, which represents the majority of the pre-injection TCE mass (see Table 5-8).

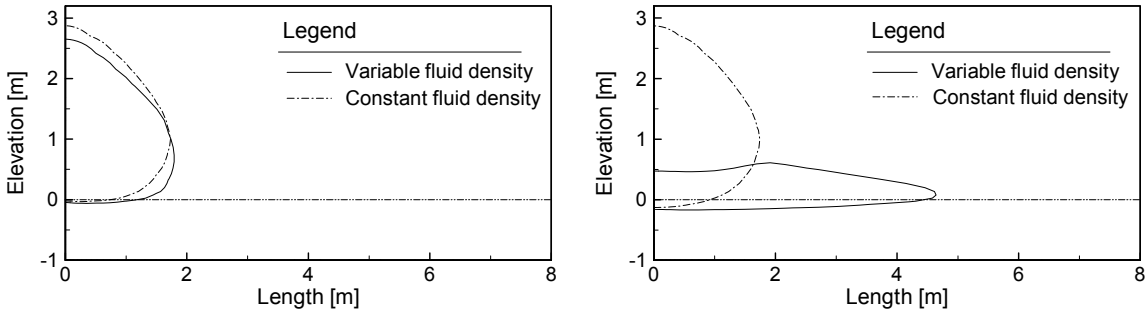

Figure 5-12. Aqueous Br^- distributions at 1 day (left) and 100 days (right) comparing the constant density distribution ($\partial\rho/\partial c = 0$) with the variable density distribution ($\partial\rho/\partial c = 0.688$). The Br^- concentration contour is 1.0×10^{-6} mol L^{-1}, which is 10 percent of the injected concentration.

Heterogeneous chemical reactions that involve mass transfer between the DNAPL, the solid phases, and the solution affect the density of the fluid. Permanganate may be consumed by reaction with the targeted organic compounds and by reaction with reduced phases in the aquifer matrix. In both cases, the reduction of permanganate generates insoluble manganese oxides. The reduction in fluid density associated with the consumption of permanganate is illustrated using the reaction between permanganate and SOM. If $KMnO_4$ is added to porous media containing excess SOM, the following reaction results:

$$3CH_2O + 4K^+ + 4MnO_4^- \rightarrow 3CO_3^{2-} + 4MnO_{2(s)} + 2H_2O + 4K^+ + 2H^+ \quad (5\text{-}2)$$

The TDS of the solution containing 0.25 mol L^{-1} $KMnO_4$ is 39.51 g L^{-1}. Assuming a freshwater density of 998.23 g L^{-1}, and a coefficient of density variation of 0.688, the density of the initial oxidant solution is 1025.4 g L^{-1}. The TDS of the final solution (MnO_4^- completely consumed) is 21.15 g L^{-1}, and the resulting density is 1012.8 g L^{-1}. The reduction of MnO_4^- by SOM generates insoluble MnO_2, reducing the solution TDS. A MIN3PD simulation illustrating the reduction in fluid density associated with the reaction of MnO_4^- and SOM is illustrated in Figure 5-13. This reaction was simulated in a single control volume using the reaction kinetics and rate expression provided in Table 5-5. These results indicate that the reaction of MnO_4^- with SOM affects patterns of fluid movement due to the reduction in the fluid density contrast which provides the primary mechanism driving the movement of fluids.

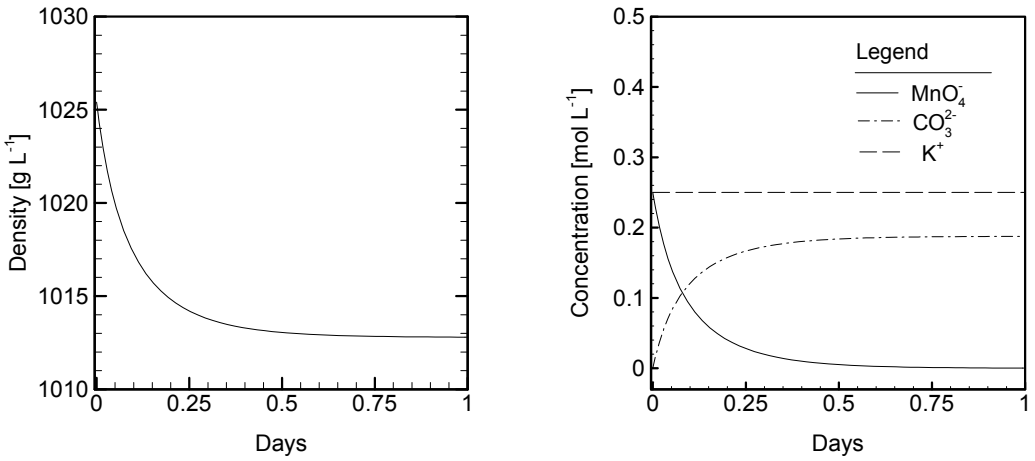

Figure 5-13. Reduction in fluid density (left) resulting from the reaction of $KMnO_4$ with excess SOM (right).

Similarly, changes in fluid density associated with MnO_4^- oxidation of $C_2HCl_{3(aq)}$ were investigated in a MIN3PD batch reactor in the presence of TCE DNAPL (Figure 5-14). The following reactions were simulated in a single control volume using the reaction kinetics and rate expression provided in Table 5-5:

$$C_2HCl_{3(aq)} + 2K^+ + 2MnO_4^- + 2H_2O \rightarrow 2MnO_{2(s)} + 3Cl^- + 2CO_3^- + 2K^+ + 5H^+ \quad (5\text{-}3)$$

$$C_2HCl_{3(DNAPL)} \rightarrow C_2HCl_{3(aq)} \quad (5\text{-}4)$$

A rapid reduction in fluid density occurs while the MnO_4^- reacts with $C_2HCl_{3(aq)}$, resulting in the precipitation of $MnO_{2(s)}$. Subsequently, a gradual decrease in fluid density reflects the limitation in the $C_2HCl_{3(aq)}$ available to react with the MnO_4^- imposed by the dissolution of the DNAPL. Subsequent to the complete consumption of MnO_4^-, DNAPL dissolution replenishes $C_2HCl_{3(aq)}$, and the fluid density increases to a level slightly less than the initial density at the conclusion of the simulation. A comparison of these results to Figure 5-13 indicates variations in fluid density of a smaller magnitude than predicted for the consumption of MnO_4^- by SOM.

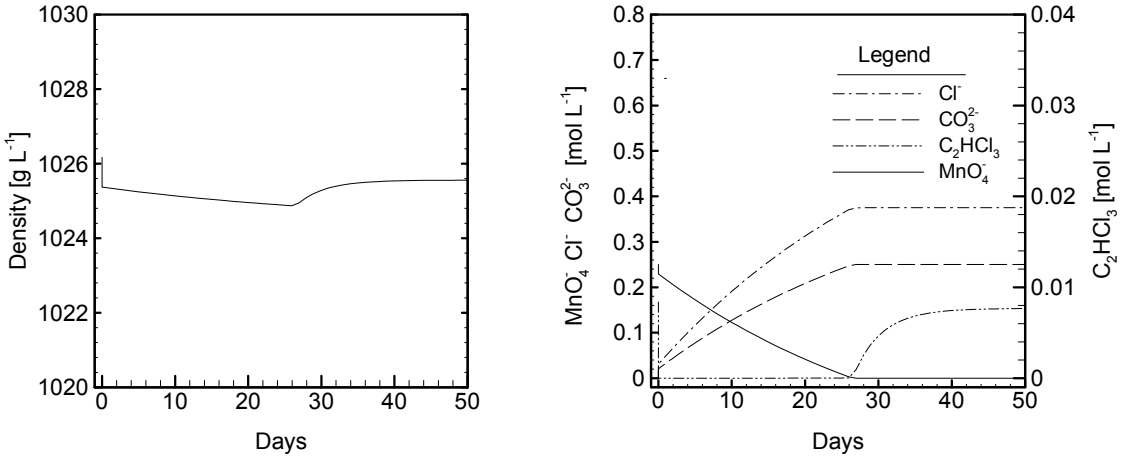

Figure 5-14. Reduction in fluid density (left) resulting from the reaction of $KMnO_4$ with $C_2HCl_{3(aq)}$ in the presence of DNAPL (right).

The cumulative effect of chemical reactions on the hypothetical permanganate remediation problem was evaluated by modeling an alternate case in which chemical reactions were not simulated. The alternate case was simulated by deactivating the reactions between MnO_4^- and $C_2HCl_{3(aq)}$ and SOM, and neglecting the cation exchange reactions. A comparison of Br^- plumes for the reactive and alternate cases (Figure 5-15) indicates that for the case considered here chemical reactions only slightly reduce the lateral spreading of the plume along the contact, indicative of a reduction in fluid density for the reactive case. However, it is expected that the coupling between heterogeneous reactions and fluid density will be enhanced in porous media containing a higher SOM content than simulated in this investigation (0.05% volume fraction).

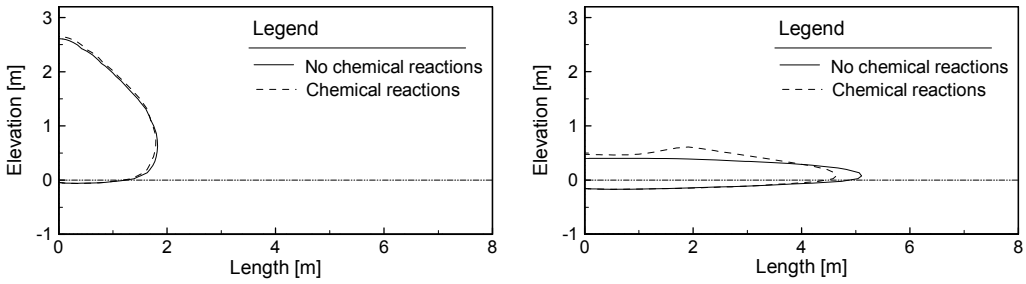

Figure 5-15. Aqueous Br^- distributions at 1 day (left) and 100 days (right) comparing the reactive and non-reactive simulations. The Br^- concentration contour is 1.0 x 10^{-6} mol L^{-1}, corresponding to 10 percent of the injected concentration.

5.4 Sensitivity Analysis

A sensitivity analysis was employed to provide insight into processes controlling remediation efficiency and the geochemical response to a $KMnO_4$ injection. The sensitivity to 24 model parameters representing physical and reactive characteristics were evaluated using methods developed by Poeter and Hill [1997] and Hill [1998]. This approach was employed to investigate a nonreactive variable density problem [Sanz and Voss, 2006], and is extended to investigate the behavior of a reactive variable density problem in the current work.

5.4.1 General Approach

MIN3PD model outputs quantify geochemistry at discrete locations and simulation times, and cumulative quantities which are integrated over the model domain, such as the mass balance for the injected MnO_4^-. The first type of MIN3PD output is referred to as model observations. A variety of model observations are generated for the permanganate remediation problem, which include aqueous component concentrations, DNAPL and SOM volume fractions, and sorbed species concentrations. The focus of the current investigation is placed on aqueous component concentrations, which comprise the bulk of the data typically collected at field sites, such as the field investigation site described in Chapter 6. Model observations incorporated in the sensitivity analysis consisted of fluid densities and the aqueous components $C_2HCl_{3(aq)}$, K^+, Na^+, H^+, Ca^{2+}, Mg^{2+}, MnO_4^-, Cl^-, and CO_3^{2-}. These observations were computed at simulation times of 1, 10, and 100 days to record transient distributions of these variables.

The second type of MIN3PD output employed in the sensitivity analysis consists of integrated quantities, which are identified in this analysis as model predictions. In the current analysis, the fate of the injected MnO_4^- is described by the following mass conservation statement:

$$M_{INJ} = M_{TCE} + M_{SOM} + M_{STOR} \tag{5-5}$$

where M_{INJ} represents the total amount of MnO_4^- injected [mol], M_{TCE} represents the total amount of MnO_4^- consumed by reaction with $C_2HCl_{3(aq)}$ [mol], M_{SOM} is the total amount of MnO_4^- consumed by reaction with SOM [mol], and M_{STOR} is the total amount of unreacted MnO_4^- in the model domain [mol]. The quantities M_{TCE}, M_{SOM}, and M_{STOR} were the model predictions included in the analysis to

facilitate an assessment of the influence of system attributes on the efficiency of the remediation effort.

5.4.2 Parameter Sensitivities

The sensitivity of model observation y_i and model prediction z_k to model parameter b_j is defined [Hill and Tiedeman, 2007]:

$$s_{ij} = \left(\frac{\partial y_i}{\partial b_j} \right) \Bigg|_{\mathbf{b}} \tag{5-6a}$$

$$s_{kj} = \left(\frac{\partial z_k}{\partial b_j} \right) \Bigg|_{\mathbf{b}} \tag{5-6b}$$

The vector **b** includes the subset of NP parameters for which model observation and prediction sensitivities are computed, and model parameters which remain at fixed values during the sensitivity analysis [Finsterle, 2004]. Model observations and predictions are non-linear functions of model parameters, and the sensitivities computed using Equation (5-6) are dependent on the model parameter values contained in **b** [Knopman and Voss, 1987; Hill and Tiedeman, 2007]. The sensitivities of model observations to model parameters define a Jacobian matrix **J** [Doherty, 2002]. This matrix provides a linear approximation to the MIN3PD model**:**

$$\mathbf{J} = \frac{\partial \mathbf{y}}{\partial \mathbf{b}} = \begin{bmatrix} \frac{\partial y_1}{\partial b_1} & \cdots & \frac{\partial y_1}{\partial b_n} \\ \vdots & & \vdots \\ \frac{\partial y_m}{\partial b_1} & \cdots & \frac{\partial y_m}{\partial b_n} \end{bmatrix} \tag{5-7}$$

Scaling the sensitivities to each parameter value b_j facilitates the comparison of model observation and prediction sensitivities to parameters differing in physical units and magnitude [Hill, 1998; Hill and Tiedeman, 2007]. Scaled sensitivities for model observations and model predictions are calculated:

$$ss_{ij} = \left(\frac{\partial y_i}{\partial b_j} \right) b_j \omega_{ii} \tag{5-8a}$$

$$ss_{kj} = \left(\frac{\partial z_k}{\partial b_j} \right) b_j \omega_{kk} \tag{5-8b}$$

where the ω terms are weighting factors, commonly assigned based on an estimate of measurement errors [Hill, 1998; Hill and Tiedeman, 2007]. The current analysis does not consider measurement uncertainty, and the weighting factors were assigned the value of unity [Essaid et al., 2003; Dai and Samper, 2004].

The composite scaled sensitivity provides a summary statistic which quantifies the sensitivity of individual model parameters [Hill, 1998]:

$$css_j = \sum_{i=1}^{NM} \left[(ss)_{ij}^2 \big|_{\mathbf{b}} / NM \right]^{1/2} \tag{5-9}$$

where css_j is the composite scaled sensitivity computed for the j^{th} model parameter.

5.4.3 Parameter Correlations

Parameter correlations affect the uncertainty in estimated model parameter values, and non-uniqueness in model predictions. Highly correlated model parameters are reflected by columns of **J** which are linearly dependent [Aster et al., 2005]. The parameter covariance matrix quantifies covariance between model parameters [Poeter and Hill, 1997; Doherty, 2002; Hill and Østerby, 2003]:

$$\text{cov}(\mathbf{b}) = (\mathbf{J}^T \mathbf{Q} \mathbf{J})^{-1} \tag{5-10}$$

where **Q** contains the weighting factors reflecting expected data measurement errors, represented in the current study using the identity matrix. Parameter correlation coefficients pcc_{ij} were computed from the covariance matrix using the following relationship:

$$pcc_{ij} = \frac{\sigma_{ij}}{\left[\sigma_{ii} \sigma_{jj} \right]^{1/2}} \tag{5-11}$$

where σ are the entries in the covariance matrix. Values of -1.0 and +1.0 indicate perfect correlation between model parameters [Hill, 1998].

5.4.4 Implementation

The MIN3PD model parameters considered in the sensitivity analysis include physical properties of the sediments, the volume fractions of reactive phases present in the sediments, and the reaction kinetics (Table 5-10). Parameter values were identical to those employed in the MIN3PD simulations described in the previous section. The set of model parameters evaluated in the sensitivity analysis was designed to provide a comprehensive assessment of model parameter sensitivity.

Parameters	Symbol	Value	Location	Units
Hydraulic conductivity	K_{aq}	2.0×10^{-4}	Aquifer	$m\ s^{-1}$
Porosity	ϕ_{aq}	0.43	Aquifer	-
Specific storage coefficient	S_p	1.0×10^{-4}	Aquifer	m^{-1}
Residual water saturation	S_{res}	0.045	Aquifer	-
Bubbling pressure	α	14.5	Aquifer	m^{-1}
Pore size distribution	n	2.68	Aquifer	-
Van Genuchten exponent	l	0.5	Aquifer	-
Longitudinal dispersivity	α_L	0.10	Aquifer	m
Transverse dispersivity	α_T	0.010	Aquifer	m
DNAPL saturation	S_{DNAPL}	0.02	Aquifer	$m^3\ m^{-3}$
SOM fraction	φ_{CH2O}	5.0×10^{-4}	Aquifer	$m^3\ m^{-3}$
Calcite fraction	$\varphi_{calcite}$	1.0×10^{-3}	Aquifer	$m^3\ m^{-3}$
Hydraulic conductivity	K_{aqt}	5.6×10^{-8}	Aquitard	$m\ s^{-1}$
Porosity	ϕ_{aqt}	0.36	Aquitard	-
SOM fraction	φ_{CH2O}	5.0×10^{-4}	Aquitard	$m^3\ m^{-3}$
$C_2HCl_{3(aq)}$- MnO_4^- rate constant	k_{TCE}^{ox}	0.65	Both units	$mol^{-1} L_{H2O}\ s^{-1}$
DNAPL dissolution rate constant	k_{TCE}^{diss}	8.3×10^{-6}	Both units	s^{-1}
SOM- MnO_4^- rate constant	$k_{CH_2O}^{ox}$	5.0×10^{-5}	Both units	$mol^{-1}\ L_{H_2O}^2\ L^{-1}{}_{bulk}\ s^{-1}$
DNAPL reactivity exponent	α_{TCE}	1.0	Both units	-
Fluid density coefficient	$\partial\rho / \partial c$	0.688	Both units	-
Chemical diffusion coefficient	D_m	1.0×10^{-9}	Both units	$m^2\ s^{-1}$
SOM reactivity exponent	α_{CH2O}	2.2	Both units	-
Cation exchange capacity	CEC	5.0	Both units	meq $[100\ g]^{-1}$
$C_2HCl_{3(aq)}$ partitioning coefficient	K_d	0.3	Both units	-

Table 5-10. MIN3PD model parameters evaluated in the sensitivity analysis.

Finite difference approximations to the derivatives $\partial y_i/\partial b_j$ and $\partial z_k/\partial b_j$ in Equations (5-6) through (5-8) were computed using forward finite differences using the Model-Independent Parameter Estimation Software [PEST; Doherty, 2002]:

$$\left(\frac{\partial x_i}{\partial b_j}\right) \approx \frac{x_i(\mathbf{b}+\mathbf{\Delta b}) - x_i(\mathbf{b})}{\Delta b_j} \qquad (5\text{-}12)$$

where x_i represents model observations and model predictions, and $\Delta\mathbf{b}$ is a vector of zeros with the exception of the j_{th} element, which is equal to Δb_j. The increment $\Delta\mathbf{b}$ was set as one percent of value of each model parameter [Barth and Hill, 2005; Sanz and Voss, 2006].

The sensitivities of model observations and model predictions to model parameters were computed separately. Model observations were recorded from the 1476 control volumes which comprised the MIN3PD model domain at simulation times of 1, 10, and 100 days. Composite scaled sensitivities were computed using model observations of Cl^- and $C_2HCl_{3(aq)}$. These two aqueous components were selected to focus the analysis on the oxidation of TCE, which is the objective of the remediation technology. A second analysis was performed incorporating nine aqueous component concentrations ($C_2HCl_{3(aq)}$, K^+, Na^+, H^+, Ca^{2+}, Mg^{2+}, MnO_4^-, Cl^-, and CO_3^{2-}) to provide a measure of total geochemical response to the permanganate injection.

5.4.5 Model Observation Sensitivity

Table 5-11 presents the composite scaled sensitivities calculated using Cl^- and $C_2HCl_{3(aq)}$ concentrations in each MIN3PD control volume at output times of 1, 10, and 100 days. Using this approach, the composite scaled sensitivity calculated for each of the 24 model parameters includes 8856 scaled sensitivities, defined by 1476 locations, three output times, and two aqueous components (see Equations (5-8a) and (5-9)). In addition to ranking parameter sensitivities, the range in which the composite scaled sensitivities vary is important [Hill and Tiedeman, 2007]. In the current problem, the range in sensitivity among the 12 most sensitive model parameters was less than one order of magnitude (Figure 5-16). This condition indicates the existence of multiple system characteristics which are significant in affecting the concentrations of Cl^- and $C_2HCl_{3(aq)}$.

Parameter	Location	CSS	Normalized CSS
Porosity	Aquifer	5.7×10^{-3}	1.00
Fluid density coefficient	Both units	3.0×10^{-3}	0.53
DNAPL dissolution rate constant	Aquifer	3.0×10^{-3}	0.52
Hydraulic conductivity	Aquifer	2.9×10^{-3}	0.51
SOM fraction	Aquifer	2.8×10^{-3}	0.49
Longitudinal dispersivity	Aquifer	2.0×10^{-3}	0.35
Porosity	Aquitard	1.9×10^{-3}	0.34
Chemical diffusion coefficient	Both units	1.8×10^{-3}	0.31
DNAPL saturation	Aquifer	1.4×10^{-3}	0.24
Pore size distribution	Aquifer	1.1×10^{-3}	0.19
Transverse dispersivity	Aquifer	9.2×10^{-4}	0.16
DNAPL reactivity exponent	Aquifer	6.2×10^{-4}	0.11
$C_2HCl_{3(aq)}$ partitioning coefficient	Both units	4.3×10^{-4}	0.08
Cation exchange capacity	Both units	3.8×10^{-4}	0.07
SOM fraction	Aquitard	3.1×10^{-4}	0.05
SOM reactivity exponent	Both units	$2.2\text{x } 10^{-4}$	0.04
Specific storage coefficient	Aquifer	2.1×10^{-4}	0.04
SOM- MnO_4^- rate constant	Both units	2.0×10^{-4}	0.03
Hydraulic conductivity	Aquitard	1.1×10^{-4}	0.02
$C_2HCl_{3(aq)}$- MnO_4^- rate constant	Both units	1.1×10^{-4}	0.02
Calcite fraction	Aquifer	4.3×10^{-5}	0.01
Van Genuchten exponent	Aquifer	2.4×10^{-5}	0.00
Residual water saturation	Aquifer	2.0×10^{-5}	0.00
Bubbling pressure	Aquifer	1.1×10^{-5}	0.00

Table 5-11. Composite scaled sensitivities (CSS) computed for model observations of aqueous component concentrations. The normalized values are scaled to the maximum composite scaled sensitivity, calculated for the aquifer porosity.

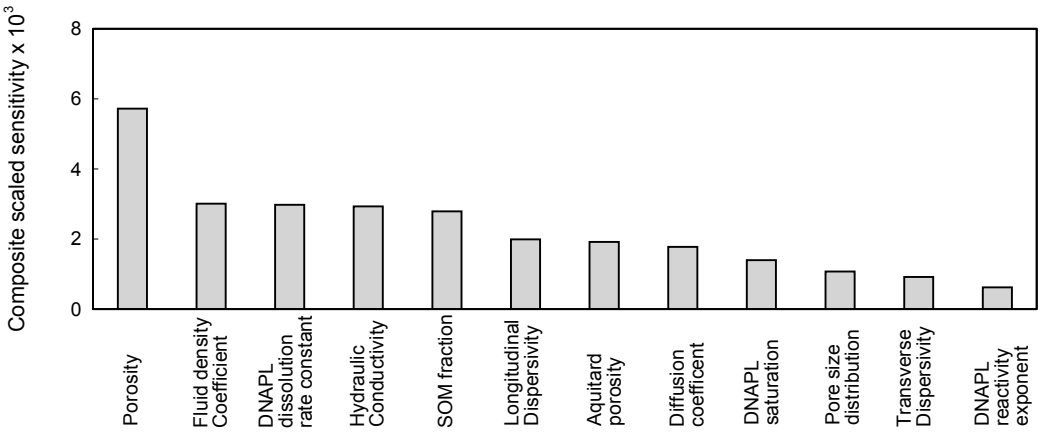

Figure 5-16. Composite scaled sensitivities for the 12 most sensitive model parameters.

The composite scaled sensitivities indicate that the aquifer porosity, the coefficient of density variation, the DNAPL dissolution rate constant, the aquifer hydraulic conductivity, and the SOM fraction in the aquifer sediments (ϕ_{aq}, $\partial\rho/\partial c$, k_{TCE}^{diss}, K_{aq}, and φ_{CH2O}) are the five most sensitive model parameters affecting the simulated Cl^- and $C_2HCl_{3(aq)}$ concentrations. In this coupled reactive system, the model parameters are inter-related. For example, the aquifer porosity determines the volume of aquifer invaded by the oxidant solution, which affects the amount of MnO_4^- consumed by reaction with SOM. As indicated in Figure 5-13, rapid reaction kinetics between MnO_4^- and SOM are indicated, with 90 percent of the oxidant consumed within 6 hours. Under the flow regime simulated, the amount of MnO_4^- consumed by SOM is primarily affected by the volume of aquifer invaded by the oxidant.

As described in greater detail below, the aquifer hydraulic conductivity and the coefficient of density variation exert a similar influence on component plume geometries. An increase in either model parameter enhances the sinking of the oxidant and the spreading of dense fluids at the base of the aquifer, enhancing the contact between the oxidant and the DNAPL. This flow behavior also reduces the volume of upper aquifer invaded by the oxidant, effectively reducing the consumption of the oxidant by SOM.

In the current analysis, DNAPL dissolution kinetics affect the Cl^- and $C_2HCl_{3(aq)}$ concentrations to a greater extent than the DNAPL saturation. This condition reflects the importance of the dissolution kinetics in generating $C_2HCl_{3(aq)}$ to react with MnO_4^- (see Figure 5-14). As indicated in Figure 5-10, the simulated DNAPL saturations were reduced but the DNAPL was generally not completely depleted within the zone invaded by MnO_4^-. Given this condition, dissolution kinetics provide the primary control on the oxidation of $C_2HCl_{3(aq)}$.

The importance of SOM in this system is consistent with previous investigation results [Barcelona and Holm, 1991; ITRC, 2005; Huling and Pivetz, 2006]. In addition to reducing the amount of MnO_4^- available to react with $C_2HCl_{3(aq)}$, SOM reduction of MnO_4^- results in a reduction of fluid density, reducing the delivery of the oxidant to the interval where the majority of the TCE mass is present.

The results indicate that predicted Cl^- and $C_2HCl_{3(aq)}$ concentrations are also sensitive to model parameters representing hydrodynamic dispersion (α_L, α_T, D_m). As indicated previously, hydrodynamic dispersion generally acts to reduce the spatial gradients in fluid density [Voss and Souza, 1986], which in this system drive the movement of fluids following the oxidant injection. The parameters used to define the functional relations between fluid pressure, saturation, and relative permeability (S_{res}, α, n, l) were generally insensitive, the exception of the pore size distribution parameter (n) which affects the relative permeability of the aqueous phase in the presence of non-wetting fluids. Model parameters defining reaction rate constants between MnO_4^-, $C_2HCl_{3(aq)}$ (k_{tce}^{ox} and $k_{CH_2O}^{ox}$), and SOM were not sensitive, and were interpreted to indicate rapid reaction kinetics relative to the rate of fluid movement.

Figure 5-17 illustrates composite scaled sensitivities calculated incorporating a larger geochemical system, consisting of $C_2HCl_{3(aq)}$, K^+, Na^+, H^+, Ca^{2+}, Mg^{2+}, MnO_4^-, Cl^-, and CO_3^{2-}. As the Figure illustrates, the consideration of this system increases the sensitivity of the cation exchange capacity (CEC). The results indicate that this parameter is important with regard to controlling overall geochemical system evolution. Although CEC is not a significant factor in controlling the oxidation of $C_2HCl_{3(aq)}$, an adequate description of the overall geochemical evolution may be of use when calibrating a model to a field data set.

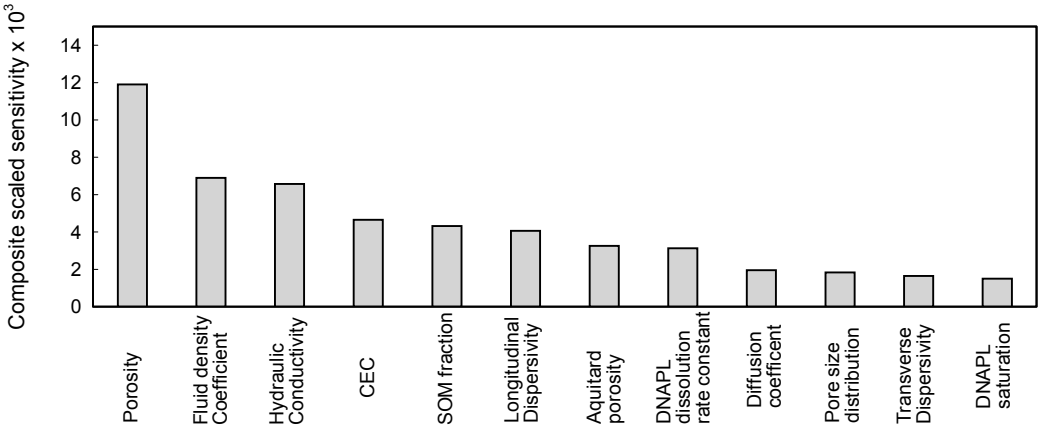

Figure 5-17. Composite scaled sensitivities computed using $C_2HCl_{3(aq)}$, K^+, Na^+, H^+, Ca^{2+}, Mg^{2+}, MnO_4^-, Cl^-, and CO_3^{2-} concentrations.

Scaled sensitivities computed using Equation (5-8a) were plotted to illustrate the relationships between the aquifer hydraulic conductivity and porosity and the distribution of MnO_4^-, Cl^-, and fluid density. These results identify spatial zones within the model domain which are sensitive to changes in model parameter values [Sanz and Voss, 2006]. Figure 5-18 illustrates the role of the hydraulic conductivity on system response. An increase in the hydraulic conductivity of the aquifer enhances the sinking of the MnO_4^- (indicated by the red region in the Figure) at 1.0 day elapsed time. An increase in the sinking and spreading of dense fluids enhances the delivery of MnO_4^- to the base of the aquifer, resulting in an increase in the amount of MnO_4^- which is consumed by reaction with $C_2HCl_{3(aq)}$. Increased consumption of MnO_4^- as a function of increased hydraulic conductivity is indicated by the predominance of negative scaled sensitivities for MnO_4^- at 100 days.

The spatial distribution of scaled sensitivities for the Cl^- plume depicts changes in the locations and intensity of the reactions between MnO_4^- and $C_2HCl_{3(aq)}$. At simulation times of 1 and 100 days, the displacement of the reaction zone away from the injection point is indicated. The changes in fluid density as a function of the hydraulic conductivity effectively combine the MnO_4^- and Cl^- results.

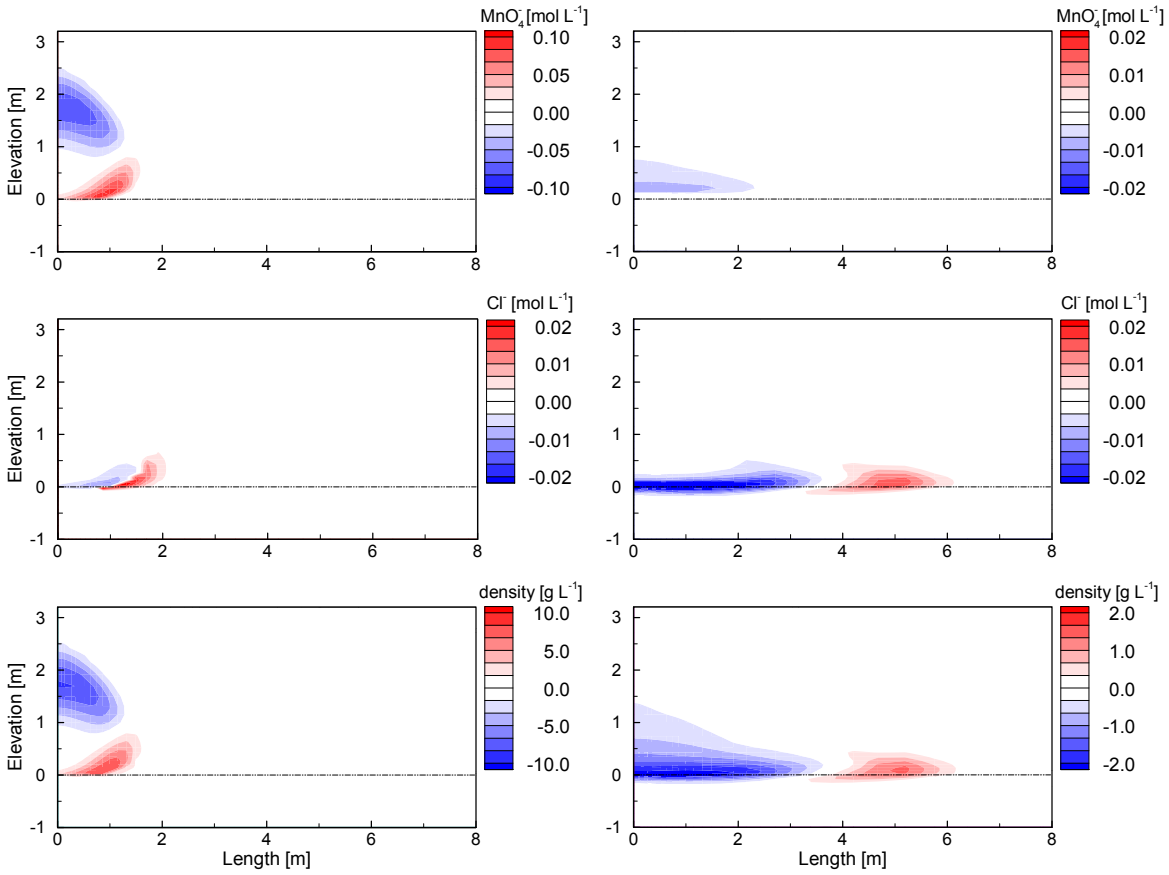

Figure 5-18. Parameter scaled sensitivities for MnO_4^- (top), Cl^- (middle), and fluid density (bottom) with respect to aquifer hydraulic conductivity at elapsed times of 1 (left) and 100 days (right). Zones where the model observations (MnO_4^- , Cl^-, density) are an increasing function of hydraulic conductivity are red, and areas where model observations are a decreasing function of hydraulic conductivity are blue.

Figure 5-19 illustrates the dependence of fluid density and MnO_4^- and Cl^- concentrations on aquifer porosity. At elapsed time of 1 day, a decrease in the spatial extent of the dense plume and the MnO_4^- plume is indicated. The distribution of scaled sensitivities at 100 days indicates that an increase in aquifer porosity results in reduced migration of the plume of dense groundwater and the plume of MnO_4^-, resulting in the generation of Cl^- closer to the injection point. A comparison of the distribution of scaled sensitivities in Figures 5-18 and 5-19 indicates that aquifer porosity and hydraulic conductivity exert opposing influences on the movement of dense fluids, and the distribution of MnO_4^- and Cl^-.

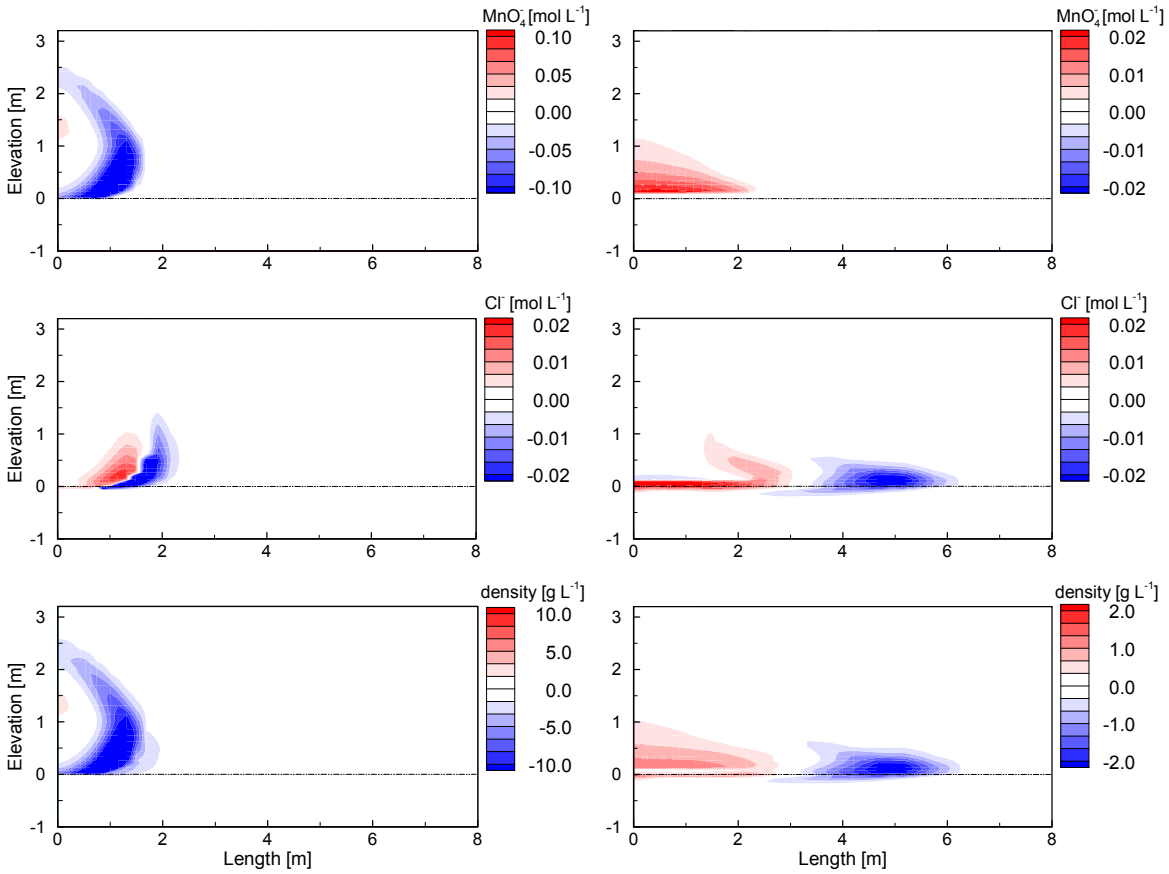

Figure 5-19. Parameter scaled sensitivities for MnO_4^- (top), Cl^- (middle), and fluid density (bottom) with respect to aquifer porosity at elapsed times of 1 (left) and 100 days (right). Zones where the model observations (MnO_4^-, Cl^-, density) are an increasing function of porosity are red, and areas where model observations are a decreasing function of porosity are blue.

5.4.6 Model Prediction Sensitivity

The analysis of model prediction sensitivity identifies the system attributes most important to the fate of the injected oxidant. Given that only three predictions (M_{TCE}, M_{SOM}, and M_{STOR}) are considered for each model parameter in this analysis, the scaled sensitivities values were calculated using Equation 5-8b and evaluated directly. While the primary model prediction of interest is the amount of MnO_4^- [mol] consumed by reaction with $C_2HCl_{3(aq)}$, consideration of the other two outcomes M_{SOM}, and M_{STOR} is beneficial in characterizing system behavior. These results are summarized in Table 5-12, and sorted by the magnitude of changes in the amount of MnO_4^- which reacts with $C_2HCl_{3(aq)}$. As the Table indicates, this prediction is most sensitive to the SOM content and porosity of the aquifer. The strong dependence of the remediation efficiency on the presence of SOM is expected and

consistent with the emphasis placed on the importance of NOD exerted by natural media [ITRC, 2005; Honning et al., 2007]. As the Table indicates, consumption of MnO_4^- by SOM reduces the amount of MnO_4^- that reacts with TCE, and reduces the amount of MnO_4^- present at the conclusion of the simulation.

Parameter	Location	∂M_{TCE} [mol]	∂M_{SOM} [mol]	∂M_{STOR} [mol]
SOM fraction	Aquifer	-196	230	-34
Porosity	Aquifer	156	-224	67
Longitudinal dispersivity	Aquifer	-39	18	22
DNAPL dissolution constant	Aquifer	32	-32	-0.66
Hydraulic conductivity	Aquifer	25	-5.6	-20
Transverse dispersivity	Aquifer	19	-33	14
Pore size distribution	Aquifer	16	-9.9	-5.6
Fluid density coefficient	Both Units	15	9.7	-25
DNAPL reactivity exponent	Aquifer	-12	7.9	3.7
DNAPL saturation	Aquifer	11	-7.7	-3.2
$C_2HCl_{3(aq)}$ partitioning coefficient	Both Units	10	-13	3.0
SOM fraction	Aquitard	-9.4	9.6	-0.22
Porosity	Aquitard	8.2	-7.4	-0.84
Specific storage coefficient	Aquifer	7.3	-5.5	-1.8
SOM reactivity exponent	Both Units	4.7	-5.5	0.78
$C_2HCl_{3(aq)}$-MnO_4 rate constant	Both Units	4.2	-3.4	-0.79
Chemical diffusion coefficient	Both Units	3.1	3.3	-6.4
Cation exchange capacity	Both Units	-2.6	-3.1	5.7
SOM- MnO_4 rate constant	Both Units	0.37	-0.49	0.13
Van Genuchten exponent	Aquifer	-0.36	0.22	0.14
Residual water saturation	Aquifer	-0.30	0.18	0.12
Calcite fraction	Aquifer	0.29	-0.23	-0.07
Hydraulic conductivity	Aquitard	0.04	0.68	-0.72
Bubbling pressure	Aquifer	-0.01	0.01	0.01

Table 5-12. Parameter-scaled derivatives for the MnO_4^- consumption pathways.

The aquifer porosity exerts an opposite influence to SOM. An increase in the aquifer porosity decreases the volume of aquifer material contacted by the injected MnO_4^- solution, decreasing the amount of MnO_4^- consumed by SOM. This results in an increase in the amount of oxidant reacting with TCE, and the amount present at the conclusion of the simulation. In general, an increase in remediation efficiency was promoted by increases in system parameters resulting in the sinking of the oxidant solution. This is illustrated by the positive sign of the change in ∂M_{TCE} as a function of increases in the aquifer hydraulic conductivity and the coefficient of fluid density coefficient. The remediation efficiency is a decreasing function of longitudinal dispersivity, which is expected to reduce the density contrast and the sinking of the treatment solution. In the current

investigation, hydrodynamic dispersion plays a primary role in the reduction of the gradients in fluid density, which drives the sinking of the oxidant. The importance of relative permeability is indicated by model sensitivity to the pore size distribution parameter, which affects the relative permeability of the zone containing DNAPLs. Consistent with the previous analysis, the rate constant for DNAPL dissolution is the primary reaction rate parameter of interest.

5.4.7 Parameter Correlation

Parameter correlations contribute to non-uniqueness in model predictions as different combinations of model parameters match observations equally well. If the absolute values of all parameter correlation coefficients are less than about 0.85, it is likely that all parameter values can be estimated uniquely [Hill and Tiedeman, 2007]. Correlations between 0.85 and 0.95 are moderate. Moderate correlations can contribute to large confidence intervals in some circumstances [Hill and Tiedeman, 2007].

Table 5-13 presents a subset of the overall parameter correlation matrix calculated using composite scaled sensitivities calculated using Equations (5-10) and (5-11) incorporating geochemical system consisting of $C_2HCl_{3(aq)}$, K^+, Na^+, H^+, Ca^{2+}, Mg^{2+}, MnO_4^-, Cl^-, and CO_3^{2-}. As the Figure indicates, the aquifer hydraulic conductivity and the coefficient of density variation exhibit nearly complete correlation.

	K_{aq}	k_{tce}^{diss}	φ_{DNAPL}	φ_{CH2O}	D_m	α_L	α_T	n	$\partial\rho/\partial c$	ϕ_{aqt}	ϕ_{aq}	CEC
K_{aq}	1.00	-0.14	0.07	0.50	0.37	0.00	-0.55	-0.02	-1.00	-0.71	-0.20	0.12
k_{tce}^{diss}		1.00	0.73	-0.09	0.15	-0.08	0.13	0.24	0.14	0.13	0.09	0.00
φ_{DNAPL}			1.00	0.04	0.14	0.03	-0.03	0.54	-0.06	-0.01	-0.04	0.02
φ_{CH2O}				1.00	0.09	-0.15	-0.22	-0.06	-0.51	-0.39	-0.17	0.13
D_m					1.00	0.12	-0.22	-0.06	-0.37	-0.50	-0.01	-0.04
α_L						1.00	-0.27	-0.09	-0.01	-0.33	-0.31	-0.19
α_T							1.00	0.06	0.55	0.22	-0.08	0.02
n								1.00	0.04	0.10	0.03	-0.03
$\partial\rho/\partial c$									1.00	0.70	0.25	-0.13
ϕ_{aqt}										1.00	0.20	0.01
ϕ_{aq}											1.00	-0.30
CEC												1.00

Table 5-13. MIN3PD model parameter correlation coefficients.

The negative value of the pcc indicates that an increase in one parameter could be compensated by a decrease in the other parameter. This condition is consistent with parameter grouping used to compute the Rayleigh number for the onset of fluid convection [Rayleigh, 1916; Horton and Rogers, 1945; Lapwood, 1948; Weatherill et al., 2004]. The media permeability and the coefficient of density contrast both occur in the numerator of the Rayleigh number expression:

$$R_a = \frac{kgH\,\partial\rho/\partial c\,(\Delta C)}{\phi\mu D} \tag{5-13}$$

With the exception of the correlation between aquifer hydraulic conductivity and the coefficient of fluid density, strong parameter correlations using the criteria proposed by Hill and Tiedeman [2007] were not recorded. In typical modeling applications, the coefficient of density variation represents a model parameter characterized by a significantly smaller estimation variance than the porous media hydraulic conductivity. Reported values for $\partial\rho/\partial c$ fall in the range of 0.68 – 0.72 [Kharaka et al., 1988; Guo and Langevin, 2002; Oswald and Kinzelbach, 2004], in contrast with reported hydraulic conductivity values which vary over several orders of magnitude for a sediment class. For this reason, this correlation may be addressed by setting the $\partial\rho/\partial c$ coefficient to a fixed value in model calibration exercises.

5.5 Discussion of Results

The analysis performed in this chapter was designed to characterize the geochemical response to the injection of $KMnO_4$ and system characteristics most important to the effectiveness of MnO_4^- in oxidizing $C_2HCl_{3(aq)}$. The analysis was directed to assess the strength of coupling between the movement of variable density fluids, transport of aqueous components, and heterogeneous chemical reactions. Investigation results confirmed the significance of density-driven flow in the movement of the oxidant. In the defined problem, sinking and density-driven spreading of MnO_4^- along the base of the aquifer is of primary importance in the oxidant delivery and the destruction of the targeted contaminant. Coupling between heterogeneous chemical reactions and fluid density occurs, but the primary coupling links solute concentrations, fluid density, and fluid fluxes.

The sensitivity analysis evaluated the importance of a diverse set of system attributes with regard to the distribution of aqueous components and the fate of the injected oxidant. The most important characteristics include the porosity, SOM content, hydraulic conductivity and non-uniformity (reflected in the dispersivity) of the aquifer sediments, and the kinetics of the DNAPL dissolution reaction. The results also indicate that the relationship between dissolved solute concentrations and fluid density is significant to this problem. The sensitivity analysis indicated that system attributes that control the delivery of the oxidant to the DNAPL interval are most important to the geochemical evolution and the remediation effectiveness. In contrast, reaction rates appeared to be generally insensitive with the exception of the DNAPL dissolution rate.

Several aspects of general behavior of the system simulated in this hypothetical problem are expected to be relevant to permanganate remediation conducted in heterogeneous systems. Limited mixing between the oxidant and contaminated groundwater is indicated, as well as physical displacement of contaminated groundwater by the oxidant. The spatial extent of geochemical effects of the remediation, specifically the development of a Cl^- plume, extends significantly beyond the oxidant plume. While Cl^- has been identified as a reaction tracer indicative of TCE/PCE oxidation [Schnarr et al., 1998, Nelson el al., 2001; MacKinnon and Thomson, 2002; Stewart, 2002], diffusion of this component into low permeability units as indicated in this investigations presents a complicating factor for the direct interpretation of field-measured data. The representation of DNAPL morphology and spatial distribution in the REV-based mathematical model provides a fundamental challenge to the current approach. Given the general lack of detailed measured data

characterizing DNAPL morphology, the physical scale of the field investigation site, and computational limitations associated with multicomponent reactive transport model, a simplified representation of DNAPL in the modeling of this technology appears to be required. This condition is expected to limit the ability of the mathematical model to precisely simulate heterogeneous field sites.

The existence of a large set of physical and chemical characteristics of comparable sensitivity (see Figures 5-16 and 5-17) complicates the process of model calibration to measured data, due to the existence of a large number of degrees of freedom [Zheng and Bennett, 2002] and non-linear relationships between model parameters and model output [Poeter and Hill, 1997]. However, with the exception of the correlation between the aquifer hydraulic conductivity and the coefficient of density variation, strong correlations between model parameters were not identified. This condition indicates that each of the attributes represented by a model parameter affects the overall geochemical response in a unique fashion.

Chapter 6 Numerical Model of North Haven Chemical Oxidation Trial

Field data collected during a 9-month permanganate field trial performed in North Haven, Connecticut [Stewart, 2002; Parker et al., 2003] were used to assess the conceptual model of permanganate-based aquifer restoration. This comprehensive data set provides an opportunity to employ the MIN3PD model for the quantitative numerical analysis of permanganate treatment of an aquifer contaminated with TCE DNAPL. The modeling investigation draws from the results obtained in the sensitivity analysis (Chapter 5) and provides a mechanism to interpret the spatial and temporal evolution of geochemical processes that occur in response to permanganate injections. The specific objectives of this chapter include (1) to evaluate the ability of the MIN3PD model to adequately simulate the evolution of permanganate-based groundwater remediation constrained by a detailed data set, (2) to assess the sensitivity of the model to parameters and processes that cannot be resolved on the grid scale for the field site under investigation, (3) to use the model to provide a system mass balance with a focus on a quantitative assessment of oxidant utilization for contaminant treatment, and (4) to further evaluate the role of density-driven fluid movement on remediation efficiency. This chapter is subdivided into a brief description of the North Haven field site, focusing on the aspects that are most relevant to the modeling analysis, followed by a description of the model implementation and the simulation results, and concluding with a discussion of the results that also addresses the benefits and limitations of the modeling approach.

6.1 Description of Field Experiment

A permanganate injection trial was performed at an industrial property in North Haven, Connecticut, USA with discontinuous accumulations of TCE DNAPL at the base of a sandy unconfined aquifer. TCE was used at the site from 1952 through 1972, and was stored in tanks at the east side of the facility. The tanks and underground pipelines were decommissioned in 1988. In 1994, the DNAPL source zone was isolated within a 900 m^2 steel sheet-pile cell, keyed into the underlying silty clay aquitard to isolate the TCE DNAPL zone from the moving groundwater (Figure 6-1) [Stewart, 2002; Parker et al., 2004].

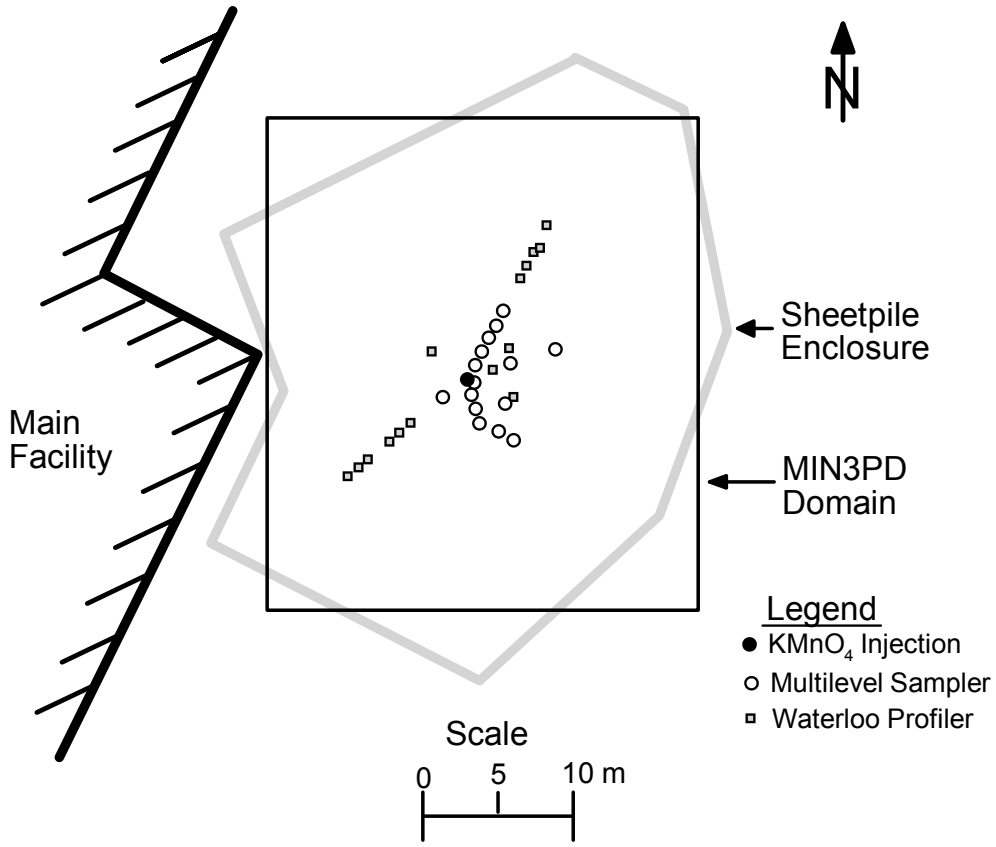

Figure 6-1. General site map of the North Haven field site illustrating geometry of the sheet pile enclosure, MIN3PD model domain, and locations multilevel samplers, Waterloo Profiler sampling locations, and the $KMnO_4$ injection point.

6.1.1 Site Characteristics

The contaminated aquifer is composed of fine- to coarse-grained sand with a saturated thickness of approximately 6 m and is underlain by a varved silt and clay aquitard [Parker et al., 2003; Parker et al., 2004]. The aquifer sediments were deposited in a glaciofluvial environment, and the aquitard is comprised of Pleistocene-age sediments deposited in a glacial lake [Stewart, 2002; Parker et al., 2004]. The bottom meter of the aquifer, where the DNAPL occurs, consists of medium and coarse-grained sand with exceptional uniformity [Parker et al., 2003; Parker et al., 2004]. Median hydraulic conductivity of the sandy aquifer is 1.9×10^{-4} m s^{-1} based on aquifer slug testing, and 3.2×10^{-4} m s^{-1} from falling head permeameter tests [Chapman and Parker, 2005; Chapman et al. 2007]. The aquitard is approximately 20 m thick, and overlies a lower confined sand aquifer [Stewart, 2002]. The potentiometric surface of the lower aquifer is lower than the water table elevation in the upper aquifer, indicating groundwater flow is downward through the aquitard [Parker et al., 2004].

The measured SOM in the aquifer sand ranges from 0.02 to 0.07 wt % [Stewart, 2002]. Analysis of the carbonate content ($CaCO_3$ equivalent) indicates a minor carbonate content in the range of 0.2 to 0.5 wt %. However, examination of petrographic thin-sections of the aquifer material suggests that carbonate minerals are not present [Stewart, 2002]. In addition, the average computed saturation index for calcite prior to the oxidant injection was -2.2, further suggesting that reactive calcite is not present in the aquifer. The CEC of the aquifer was determined at approximately 3 meq per 100 g of sediments. The aquifer pH prior to the injection was approximately 6.0, and groundwater alkalinity was approximately 30 mg L^{-1} as $CaCO_3$ [Stewart, 2002].

The underlying aquitard is a varved deposit, comprised of 1 cm thick silt and clayey-silt layers [Parker et al., 2004]. Although the aquifer-aquitard interface is abrupt, it is not planar, with the elevation of the interface varying by about 0.8 m within the area isolated by the sheet pile enclosure. The aquitard surface includes two large depressions in the eastern portion of the enclosure (Figure 6-2) [Stewart, 2002; Parker et al., 2004].

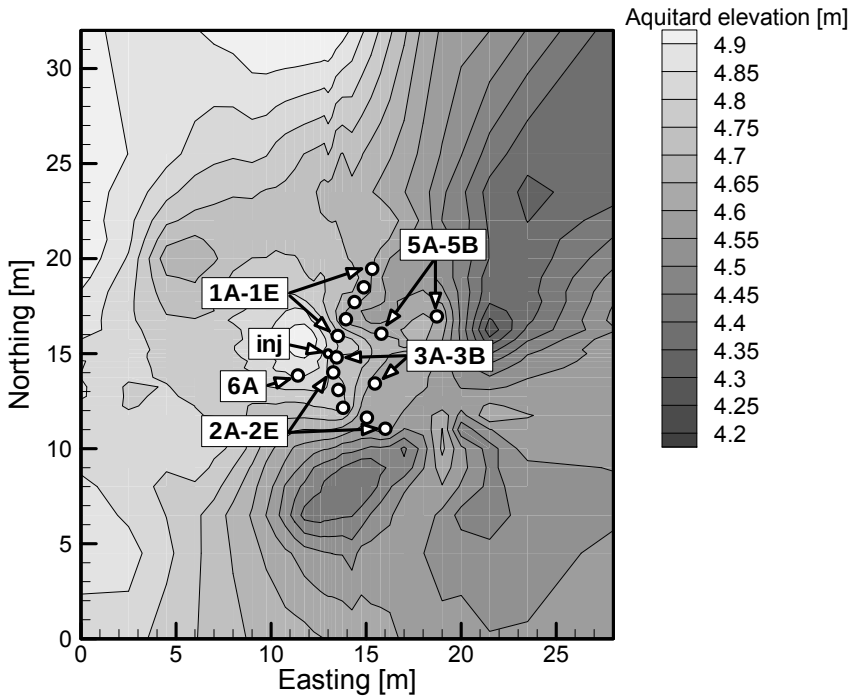

Figure 6-2. Plan view of the locations of the injection well and multilevel monitoring wells (15 total). The permanganate injection occurred at 13.0 m east, 15.0 m north.

Slug tests in piezometers completed within the aquitard indicated horizontal hydraulic conductivity values in the range of 10^{-8} to 10^{-9} m s^{-1}. The aquitard appears to have provided an effective barrier to the downward migration of DNAPL. The presence of DNAPL is mostly restricted to the lower regions of the aquifer near the aquifer-aquitard interface [Stewart, 2002]. However, $C_2HCl_{3(aq)}$ has diffused into the aquitard a maximum of 3 m below the aquifer-aquitard contact [Parker et al., 2004].

6.1.2 Permanganate Oxidation Trial

In December 2000, approximately 4,000 liters of 38 to 48 g L^{-1} potassium permanganate solution (estimated total of 175 Kg of $KMnO_4$) were injected near the center of the sheet pile containment cell, approximately 0.6 m above the bottom of the aquifer. The permanganate was injected in two 8-hour episodes separated by a period of four days. The experiment was designed to monitor the destruction of TCE, spreading of MnO_4^-, indicators for reaction progress, and geochemical changes in the aquifer.

The applied volume was adequate to treat a portion of the contamination within the cell; remediation of the entire cell was not pursued.

The spread of the permanganate solution and generation of aqueous reaction byproducts were monitored using 15 multilevel sampling devices, each containing 11 to 12 individual sampling points. The monitoring network consisted of 168 individual sampling points. Figures 6-2 and 6-3 depict the geometry of the monitoring network in plan and cross-sectional view. A total of six groundwater sampling events were performed over an eight month period, consisting of one pre-injection and five post-injection sampling events [Stewart, 2002; Parker et al., 2003]. Additional groundwater samples were collected using a Waterloo Profiler sampling device to characterize permanganate and chloride plume geometries [Stewart, 2002; Parker et al., 2003].

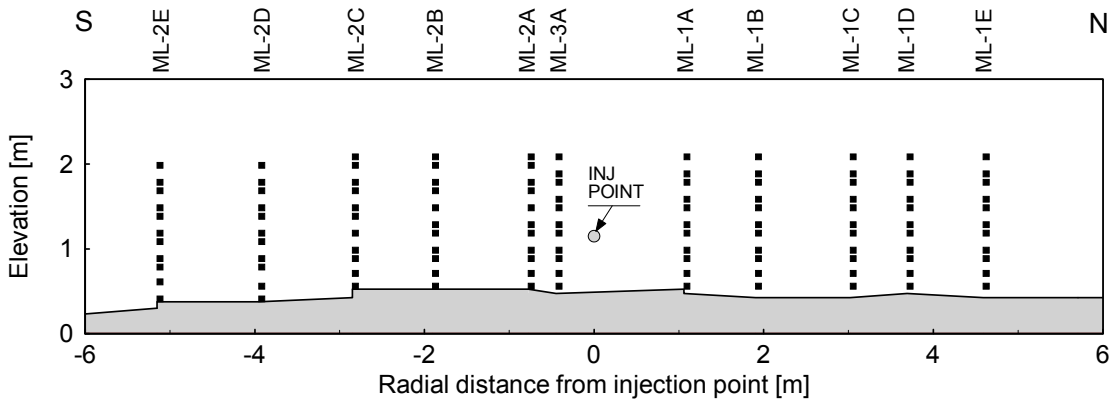

Figure 6-3. North-south cross section illustrating the interpolated aquitard surface, in the vicinity of the multilevel samplers (11 in this section). The elevation of 0 m in this figure corresponds to the minimum elevation of the aquitard in the 2-D section extracted from the 3-D model domain. The 3-D domain is 28 m east-west by 32 m north-south and 8.2 m vertical.

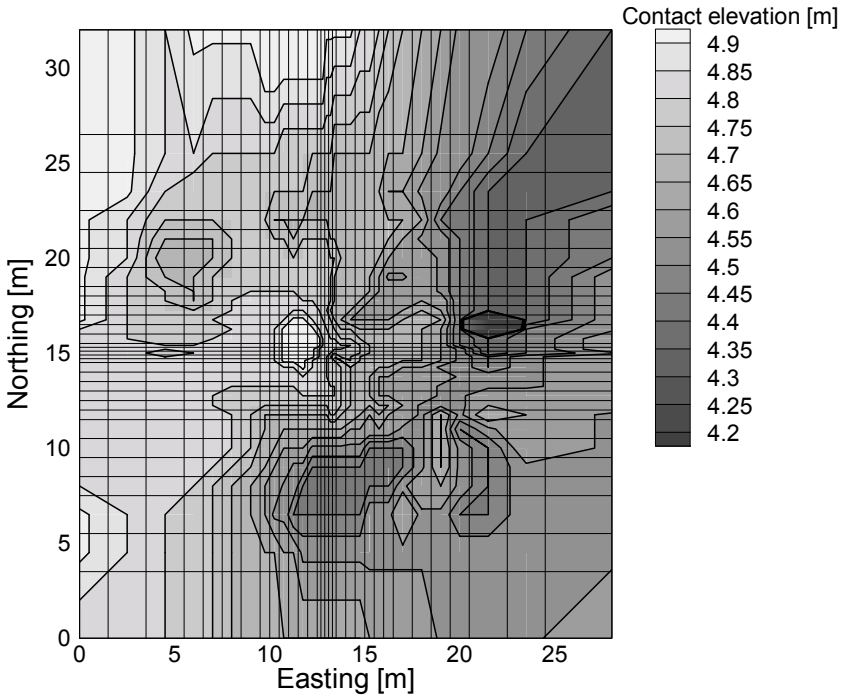

Figure 6-4. Plan view of telescoping model grid for the three-dimensional model. The rectangular elements represent the control volumes. The contoured surface depicts the elevation of aquifer-aquitard contact in the model.

The data set generated by the investigation includes MnO_4^-, $C_2HCl_{3(aq)}$, and Cl^- concentrations measured across the entire sampling network. These data document the sinking and spreading of the permanganate solution and the eventual depletion of the oxidant. Variable degrees of depletion and rebound in $C_2HCl_{3(aq)}$ concentrations and the accumulation and spreading of chloride are also captured. These attributes were measured across the entire monitoring network, producing a quasi three-dimensional data set. This data set is complemented by a subset of geochemical data that includes major cations, anions, trace metals, pH, Eh, and alkalinity measurements collected from two multilevel samplers located approximately 1 m south and 4 m northeast of the injection point [Stewart, 2002; Parker et al., 2003]. The locations characterize geochemical conditions near the center and the outer limit of the MnO_4^- plume. The data set generated during the experiment is summarized in Table 6-1.

Sampling event [days]	Cl^-	$KMnO_4$	C_2HCl_3	Major ions and Metals	pH	Alkalinity	Total Analyses
0	119	0	118	22	22	22	303
14	130	0	128	0	0	0	258
55	182	187	153	22	22	22	588
83	162	163	161	0	0	0	486
139	163	162	163	22	22	22	554
238	236	239	0	12	22	0	509

Table 6-1. Number of samples for key aqueous chemical parameters. The number of samples analyzed are provided in columns 2 through 7, and summed in the final column. A total of 303 analyses were performed prior to the permanganate injection, and 2395 analyses were performed following the injection. The post-injection analyses include 80 MnO_4^- and 98 Cl^- analyses of samples collected using the Waterloo Profiler.

6.2 Model Description

6.2.1 Reaction Network

A simplified representation of the true multiphase multicomponent reaction network, similar to the reaction network used in the sensitivity analysis (Chapter 5), was implemented into the MIN3PD model. The focus of the modeling was placed on the remediation of the TCE DNAPL, and on reactions involving the aqueous components monitored during the field trial. Similar to the Chapter 5 investigation, the DNAPL is assumed to be at or below residual saturation and immobile, and reactive organic carbon dominates the aquifer reductive capacity.

The primary difference in the current reaction network to the one employed in the Chapter 5 sensitivity analysis is the inclusion of manganese-oxide catalyzed permanganate oxidation of water. The reaction was included in the reaction network to account for permanganate consumption over the extended (~8 month) time frame of the field trial. A literature search did not identify any data to constrain the rate of this reaction in a field setting. The reaction was included in the reaction network in order to use the measured field data to evaluate the importance of this process at the site.

The reaction network is based on ten primary aqueous components (K^+, Na^+, H^+, Ca^{2+}, Mg^{2+}, MnO_4^-, Cl^-, CO_3^{2-}, $C_2HCl_{3(aq)}$, and $O_{2(aq)}$), eleven secondary aqueous species (OH^-, $MgOH^+$, $MgCO_3$, $MgHCO^{3+}$, $CaOH^+$, $CaHCO^{3+}$, $CaCO_{3(aq)}$, $NaCO^{3-}$, $NaHCO_3$, HCO_3, H_2CO_3), two mineral phases (calcite and manganese oxide), SOM, the TCE DNAPL, and the exchanged species K-X, Na-X, Ca-X_2, and Mg-X_2.

Homogeneous (intra-phase) reactions include the kinetically controlled oxidation of $C_2HCl_{3(aq)}$ and the auto-decomposition of MnO_4^- in water, as well as equilibrium aqueous complexation reactions involving the primary aqueous components. $C_2HCl_{3(aq)}$ oxidation is modeled as a second order kinetic reaction with an overall reaction rate proportional to MnO_4^- and $C_2HCl_{3(aq)}$ concentrations [Huang et al., 1999; Yan and Schwartz, 1999]. The auto-decomposition of MnO_4^- is simulated as a first order kinetic reaction, with a reaction rate proportional to the MnO_4^- concentration. Equilibrium controlled aqueous complexation is assumed with equilibrium constants from the WATEQ4F database [Ball and Nordstrom, 1991].

Reaction	Rate Expression	Rate Constant
(1) $C_2HCl_{3(DNAPL)} \rightarrow C_2HCl_{3(aq)}$	$R_{tce}^{diss} = -k_{tce}^{diss}\left([C_2HCl_{3(aq)}]_{sat} - [C_2HCl_{3(aq)}]\right)\left(\frac{\varphi_{C_2HCl_3}}{\varphi_{C_2HCl_3,0}}\right)$	3.4 x 10^{-6} [a]
(2) $C_2HCl_{3(aq)} + 2MnO_4^- + 2H_2O \rightarrow 2MnO_{2(am)} + 3Cl^- + 2CO_3^- + 5H^+$	$R_{tce}^{ox} = -k_{tce}^{ox}[C_2HCl_{3(aq)}][MnO_4^-]\left[\frac{[C_2HCl_{3(aq)}]}{K_{tce}^{ox} + [C_2HCl_{3(aq)}]}\right]$	0.65 [b]
(3) $3CH_2O + 4MnO_4^- \rightarrow 4MnO_{2(am)} + 3CO_3^{2-} + 2H^+ + 2H_2O$	$R_{CH_2O}^{ox} = -k_{CH_2O}^{ox}[MnO_4^-]\left(\frac{\varphi_{CH_2O}}{\varphi_{CH_2O,0}}\right)^{\frac{2}{3}}$	5.0 x 10^{-5} [c]
(4) $CaCO_3 \leftrightarrow Ca^{2+} + CO_3^{2-}$	$R_{CaCO_3} = -k_{CaCO_3}\left[1 - \frac{IAP_{CaCO_3}}{K_{CaCO_3}}\right]$	1.0 x 10^{-5} [d]
(5) $4MnO_4^- + 4H^+ \rightarrow 3O_2 + 2H_2O + 4MnO_2$	$R_{h_2o}^{ox} = -k_{h_2o}^{ox}[MnO_4^-]$	1.0 x 10^{-8} [e]

[a] model calibration parameter, mol L^{-1} bulk s^{-1}
[b] from Yan and Schwartz [1999], mol^{-1} L^2 H_2O L^{-1} bulk s^{-1}
[c] model calibration parameter, L H_2O L^{-1} bulk s^{-1}
[d] set to simulate quasi-equilibrium reaction kinetics, mol L^{-1} bulk s^{-1}
[e] model calibration parameter, L H_2O L^{-1} bulk s^{-1}

Table 6-2. Geochemical reaction network for TCE oxidation by MnO_4^- in aquifer sediments.

Heterogeneous (inter-phase) chemical reactions in the model consist of TCE DNAPL dissolution, permanganate oxidation of SOM, precipitation of MnO_2, dissolution-precipitation of calcite, and ion exchange reactions. The rate of DNAPL dissolution is proportional to the degree of undersaturation of $C_2HCl_{3(aq)}$, using a solubility value of 1,100 mg L^{-1} [Pankow and Cherry, 1996]. The rate of SOM oxidation by permanganate is proportional to the permanganate concentration. The reaction rate expressions for DNAPL dissolution and organic carbon oxidation include terms accounting for changes in phase volume fractions (see Table 6-2). This formulation provides a

mechanism to simulate a decrease in the DNAPL dissolution rate associated with a decrease in the DNAPL saturation [Miller et al., 1990; Nambi and Powers; 2003]. The decrease in the reactivity of soil organic carbon over time (observed by Mumford et al. [2005] and Honning et al. [2007]) can be accounted for in a similar fashion. $C_2HCl_{3(aq)}$ sorption is modeled using a linear partitioning coefficient (K_d = 0.062 ml g^{-1}), estimated as the product of the chemical-specific organic carbon-water partitioning coefficient (K_{oc}) and the aquifer SOM content. The cation exchange reactions are modeled using the Gaines-Thomas convention with selectivity coefficients also taken from the WATEQ4F database [Ball and Nordstrom, 1991].

Manganese oxide is assumed to be initially absent, but is allowed to precipitate instantaneously in response to $C_2HCl_{3(aq)}$ and SOM oxidation, and MnO_4^- auto-decomposition. The density of MnO_2 is approximated as birnessite (3.4 g cm^{-3}) and its precipitation represents the primary mechanism for porosity reduction. Calcite was not initially present in the aquifer, but was included as a possible secondary phase to assess the potential for calcite precipitation in regions dominated by acid-consuming organic carbon oxidation.

6.2.2 Model Parameterization and Discretization

The model consists of a two layer system representing the sandy aquifer and the upper portion of the silty clay aquitard with an abrupt and undulating contact. The permeability of each layer was assumed to be homogeneous and isotropic. The elevation of the irregular contact between the units was interpolated from the site assessment data, and used to assign nodal permeability values to the model grid. Initial conditions were set to reproduce the average pre-injection groundwater geochemistry for major ions, pH, and alkalinity (Table 6-3). The SOM was depicted as homogeneous throughout each sediment unit, and constrained by measured data [Stewart, 2002; Parker et al., 2004].

Component	Pre-injection	Oxidant Solution	Units
K^+	8.7×10^{-5}	2.7×10^{-1}	mol L^{-1}
MnO_4^-	1.0×10^{-15}	2.7×10^{-1}	mol L^{-1}
$C_2HCl_{3(aq)}$	10 yr profile	1.0×10^{-15}	mol L^{-1}
Cl^-	5.2×10^{-3}	7.3×10^{-4}	mol L^{-1}
CO_3^{2-}	2.4×10^{-3}	6.7×10^{-4}	mol L^{-1}
Ca^{2+}	1.3×10^{-3}	3.8×10^{-4}	mol L^{-1}
Na^+	2.5×10^{-3}	7.5×10^{-4}	mol L^{-1}
Mg^{2+}	5.4×10^{-4}	1.2×10^{-4}	mol L^{-1}
pH	6.0	6.9	standard units

Table 6-3. Pre-injection groundwater and oxidant solution chemistry. Initial $C_2HCl_{3(aq)}$ concentrations were assigned to individual MIN3PD cells using the results computed from a preliminary simulation of $C_2HCl_{3(aq)}$ diffusion from the aquifer DNAPL zone.

The pre-injection DNAPL distribution constitutes the main uncertainty of the modeling effort. Results from soil sampling of continuous, vertical cores taken over the bottom 1.5 m of the aquifer showed that the source zone was comprised of thin, vertically stratified layers of DNAPL separated by zones with no DNAPL [Parker et al., 2003], likely due to years of differential dissolution by groundwater flow through the source zone prior to sheet pile isolation. In addition, the distribution of $C_2HCl_{3(aq)}$ prior to the MnO_4^- injection was measured in the multilevel samplers. These data are consistent in constraining the vertical distribution of the DNAPL to the vicinity of the aquifer-aquitard interface [Parker et al., 2003]. Plotted in plan view (not shown), they indicate general areas where DNAPL was present or absent prior to the oxidant injection. Pre-injection DNAPL saturations were assigned to the model cells based on soil sampling results, and the interpolated DNAPL thickness across the model domain. Averaged saturations ranged from 0-8% and were interpolated along the bottom of the aquifer, yielding an initial TCE mass in the aquifer of 4470 Kg. The initial TCE DNAPL mass is similar to previous estimates that range from 4688-19924 Kg [Stewart, 2002].

Field observations also showed that $C_2HCl_{3(aq)}$ had diffused into the aquitard to a depth of up to 3 m below the aquifer-aquitard contact [Parker et al., 2004]. Preliminary simulations were performed to reproduce the measured $C_2HCl_{3(aq)}$ concentrations in the sheet pile cell prior to the permanganate injection. In these simulations, $C_2HCl_{3(aq)}$ diffused from the DNAPL source area for a period of 10 years, corresponding to the approximate length of time that the sheet pile cell was present prior to the permanganate injection. The resulting aqueous and sorbed TCE concentrations were used as initial conditions in the subsequent reactive transport simulations of the permanganate

oxidation trial. Approximately 4470 Kg of TCE were initially present in the model domain, with adsorbed TCE representing approximately 2 percent of the total, 5 percent present in dissolved form, and 93 percent present as DNAPL.

The three-dimensional model domain was 28 m east-west by 32 m north-south and 8.2 m vertical, and was set to generally reproduce the areal dimensions of the sheet pile cell (Figure 6-1), and the thickness of the sandy aquifer. No-flow boundary conditions were assigned to all six sides of the model domain. The upper portion of the domain was unsaturated, allowing the water table to rise in response to the injection of the treatment solution. A telescoping mesh was used, with cell dimensions ranging from 0.2 m to 5.5 m horizontally, and from 0.05 m to 3.25 m vertically, resulting in a total of 29,791 control volumes (Figure 6-4). Table 6-4 summarizes the model input parameters.

Parameter	Value	Units
Domain length, North-South	32	m
Domain length, East-West	28	m
Domain thickness	8.2	m
Aquifer hydraulic conductivity	5.0×10^{-4}	$m\ s^{-1}$
Aquifer porosity	0.35	$m^3\ m^{-3}$
Aquifer organic carbon fraction	1.5×10^{-4}	$m^3\ m^{-3}$
Aquifer cation exchange capacity	3	meq $[100\ g]^{-1}$
Aquifer bulk density	1.7	$g\ cm^{-3}$
Aquitard hydraulic conductivity	1.0×10^{-9}	$m\ s^{-1}$
Aquitard porosity	0.43	$m^3\ m^{-3}$
Aquitard organic carbon fraction	5.4×10^{-4}	$m^3\ m^{-3}$
Aquitard cation exchange capacity	3	meq $[100\ g]^{-1}$
$KMnO_4$ injection 1 - duration	6.5	hr
$KMnO_4$ injection 1 - rate	308	$L\ hr^{-1}$
$KMnO_4$ injection 2 - duration	9.5	hr
$KMnO_4$ injection 2 - rate	211	$L\ hr^{-1}$
$KMnO_4$ solution concentration	44	$g\ L^{-1}$
[a]Chemical diffusion coefficient	6.4×10^{-10}	$m^2\ s^{-1}$
[a]Longitudinal dispersivity	5.0×10^{-2}	m
[a]Transverse horizontal dispersivity	5.0×10^{-3}	m
[a]Transverse vertical dispersivity	5.0×10^{-3}	m
[b]Van Genuchten parameter α	14.5	m^{-1}
[b]Van Genuchten parameter n	2.68	-

[a] estimated value
[b] tabulated values from Carsel and Parrish [1988] for sandy soils

Table 6-4. Physical and chemical model parameters, based on field data [Stewart, 2002] unless otherwise noted.

6.2.3 Model Calibration Approach

The sensitivity analysis (Chapter 5) indicated that the aquifer porosity, hydraulic conductivity, organic carbon content, and the reaction rate constants applied to the dissolution of TCE DNAPLs are the primary parameters affecting the fate and transport of the injected oxidant and remediation efficiency. These model parameters were adjusted using a trial and error approach to reproduce the observed spatial and temporal distribution of MnO_4^-, Cl, and $C_2HCl_{3(aq)}$ throughout the monitoring network and the other geochemical parameters recorded at the center and edge of the oxidant plume.

6.3 Model Results

6.3.1 Groundwater Flow

The model simulations reveal two distinct flow regimes, consisting of the ~8 hour oxidant injection events, and the subsequent redistribution of groundwater and treatment solution following the injections. During the injections, model results show three-dimensional radial flow away from the injection point (results not shown), indicating that the imposed pressure gradient is initially the principal mechanism driving the movement of the fluids. The fluid flow patterns which develop after the injections indicate that gradients in fluid density provide the main driving mechanism for the movement of groundwater at later time. Figure 6-5 illustrates fluid seepage velocity vector fields in cross-sections extending north-south and east-west through the injection location. The vector fields depict the flow patterns 15 days following the initial injection episode. The results suggest that convective flow cells develop around the injection point, in response to the downward movement of the injected oxidant solution. The highest velocities occur at the base of the aquifer, in the east and south directions, corresponding to the downward slope in the aquifer-aquitard contact.

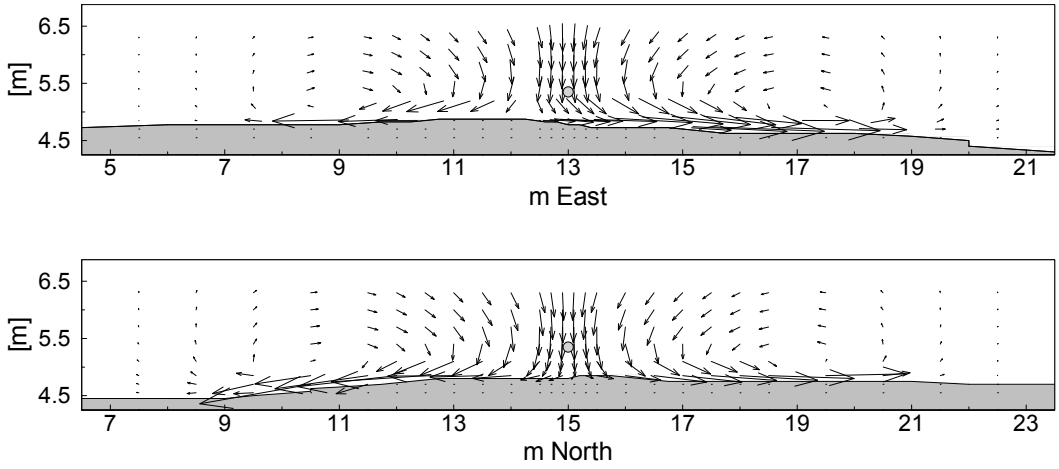

Figure 6-5. East-west (top) and north-south (bottom) cross-sections through the injection location (grey circle) depicting seepage velocity vector fields 15 days after the initial permanganate injection. Vector lengths are proportional to modeled velocities, with the maximum velocity approximately 0.14 m d^{-1}.

Figure 6-6 depicts the magnitude of fluid velocities computed over time at two points in the model domain, approximately 0.1 m above the aquifer-aquitard contact. These points correspond to locations where aqueous geochemistry was monitored, located 1 m south and 4 m northeast of the injection point. Model results indicate that maximum fluid seepage velocities on the order of 5 m d^{-1}

occurred during the oxidant injections. Modeled seepage velocities decreased rapidly following each oxidant injection. At the end of the experiment, fluid velocities at these points were approximately 4 x 10^{-3} m d^{-1}, respectively.

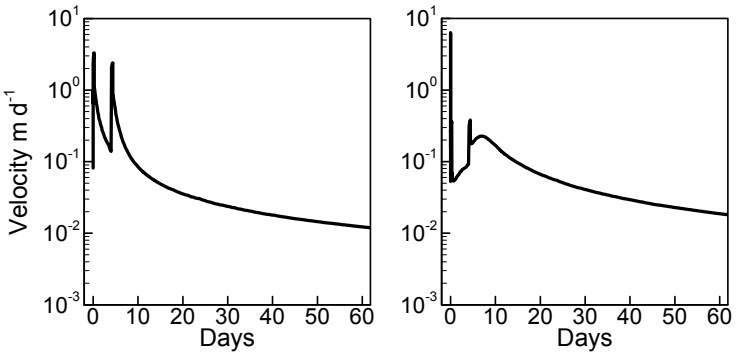

Figure 6-6. Fluid seepage velocity magnitude near the base of the aquifer 1 m (left) and 4 m (right) from the injection well corresponding to multilevel samplers 2A-11 and 1D-11. The two spikes in velocity reflect permanganate injections at 0.0 and 4.0 days.

6.3.2 Reactive Transport

The three-dimensional morphology of simulated permanganate, chloride, calcium, and pH distributions 55 days following the initial oxidant injection is depicted using isocontour plots (Figure 6-7). This time frame corresponds to the point at which the oxidant plume had achieved its approximate maximum dimensions [Stewart et al., 2002]. These results indicate that permanganate has spread along the base of the aquifer, with chloride and low-pH plumes developed at the base and margins of the permanganate plume. The accumulation of calcium is the product of cation exchange reactions driven by loading of potassium. The greater accumulation of calcium to the east and southeast of the injection point reflects the movement of potassium down the slope of the aquitard. The modeled groundwater pH distribution reflects both the slope of the contact, and the absence of DNAPLs to the west of the injection point.

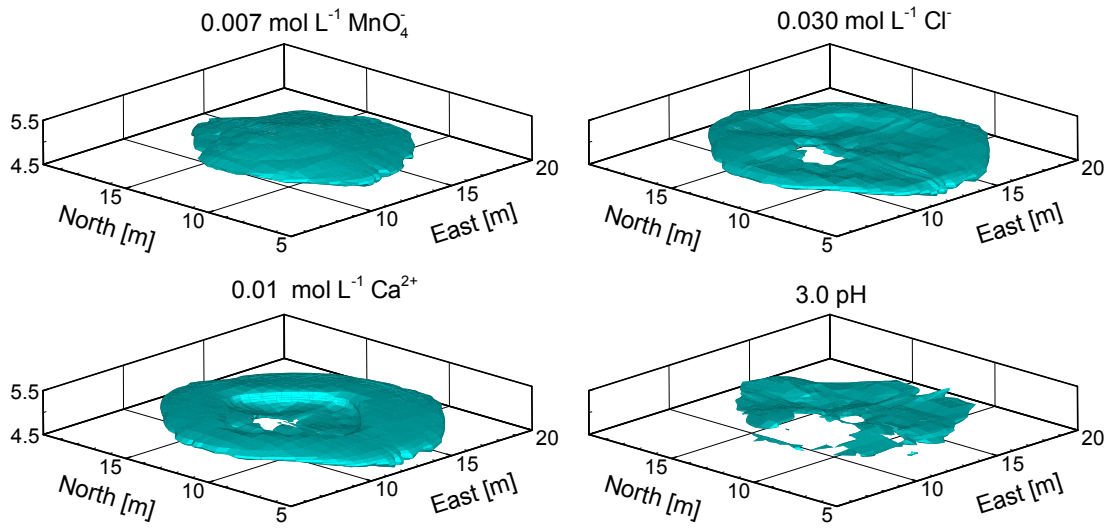

Figure 6-7. Isocontour plots of MnO_4^-, Cl^-, and Ca^{2+} concentrations and pH results 55 days following the initial potassium permanganate injection. Center portion of the model domain is illustrated, with 2x vertical exaggeration employed in all plots. Injection location in these plots is centered at 12.5 m east, 12.5 m north.

Two-dimensional cross-sections depicting observed and simulated MnO_4^-, $C_2HCl_{3(aq)}$, and Cl^- concentrations 55 days following the $KMnO_4$ injection are presented in Figures 6-8 and 6-9. These figures depict chemical concentrations measured across a segment of 11 multilevel samplers extending approximately 5 m southeast and 5 m northeast from the oxidant injection point (Figures 6-2 and 6-3). Concentration distributions are plotted on a rectangular grid representing the 121 sampling points (11 samplers with 11 points each). The spreading of the MnO_4^- and the generation of Cl^- at the bottom of the aquifer, and the corresponding depletion of $C_2HCl_{3(aq)}$ are adequately reproduced by the model.

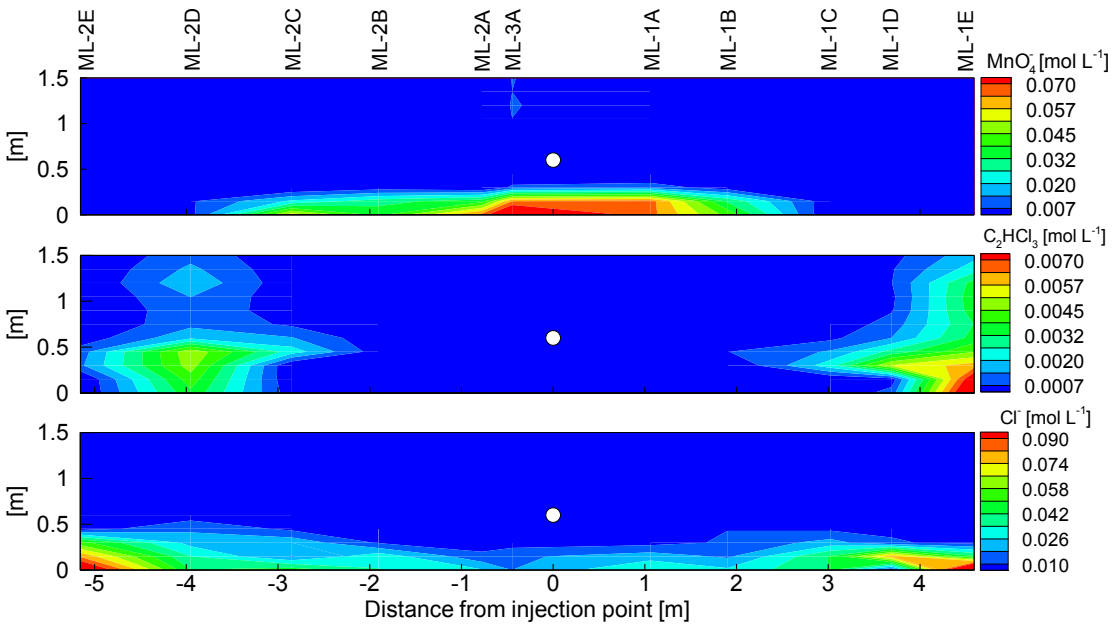

Figure 6-8. Measured MnO_4^-, $C_2HCl_{3(aq)}$, and Cl^- concentrations 55 days following the $KMnO_4$ injection. The bottom of each sampler is assigned an elevation of 0 m in the figure.

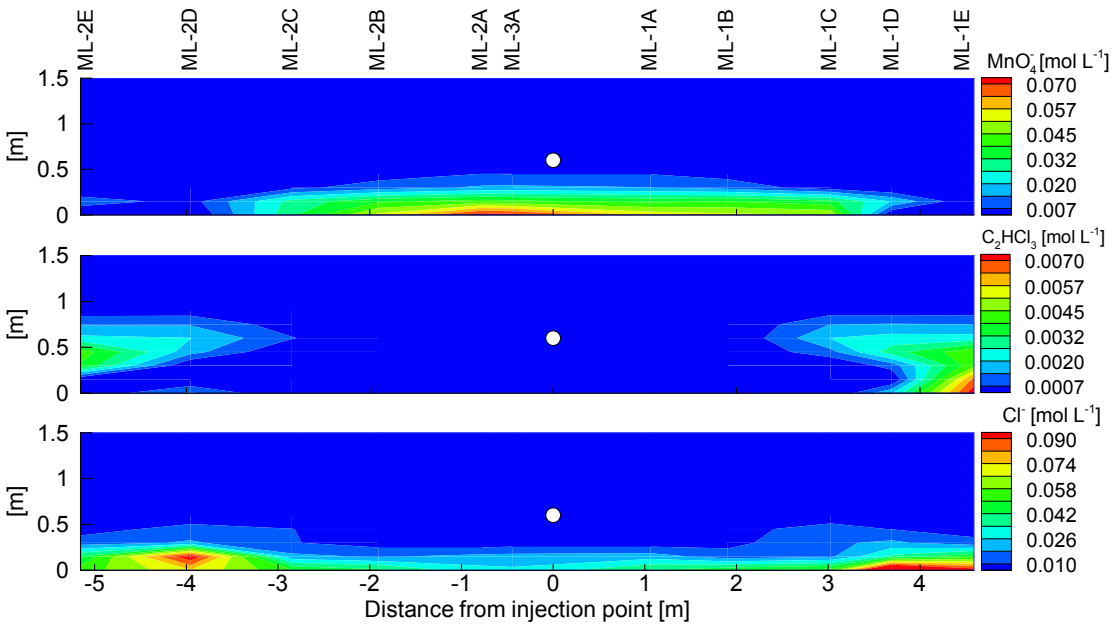

Figure 6-9. Modeled MnO_4^-, $C_2HCl_{3(aq)}$, and Cl^- concentrations 55 days following the $KMnO_4$ injection. The bottom of each multilevel sampler is assigned an elevation of 0 m in the figures.

The transient patterns in observed and simulated aqueous component concentrations are depicted in Figure 6-10 for two sampling points. The two points are located at the bottom of the two multilevel samplers which were monitored for geochemical parameters during the field trial. The two points illustrate system response at the base of the aquifer, approximately 1 m south (sampling point ML-2A-11) and 4 m northeast (ML-1D-11) of the injection point (Figures 6-2 and 6-3). Observed and simulated Cl^-, K^+, Ca^{2+}, and Mg^{2+} concentrations indicate an initial increase and subsequent decrease in concentration. The maximum breakthrough concentration of K^+ decreases with increasing distance from the injection point, while the opposite is observed for Ca^{2+}, Mg^{2+}, and Cl^-. This pattern is consistent with chemical oxidation and cation exchange reactions which occur at the margins of the plume as it sinks and spreads along the base of the aquifer. Cation exchange reactions (Ca increase) and oxidation of organic matter (alkalinity increase) also cause the precipitation of small amounts of calcite in regions where pH remains sufficiently high (not shown).

Observed and simulated $C_2HCl_{3(aq)}$ concentrations indicate its depletion within the region that remains in contact with the treatment solution, while $C_2HCl_{3(aq)}$ concentrations first decline at the outer edges of the oxidant plume, but then rebound (Figure 6-10). Values of pH near the center of the oxidant plume remain stable in the range of 6 to 6.5. Pre-injection sampling indicated the absence of DNAPLs in the immediate vicinity of the injection point, limiting the amount of TCE available to react with permanganate. The model was able to reproduce the pH decrease (as low as pH = 2.6) at the base of the aquifer near the edge of the plume, suggesting significant TCE oxidation in this region (Figure 6-10). Observed and simulated alkalinity exhibits an increase near the center of the oxidant plume attributed to SOM oxidation, and a decrease near the edge of the plume, consistent with decreases in groundwater pH due to $C_2HCl_{3(aq)}$ oxidation.

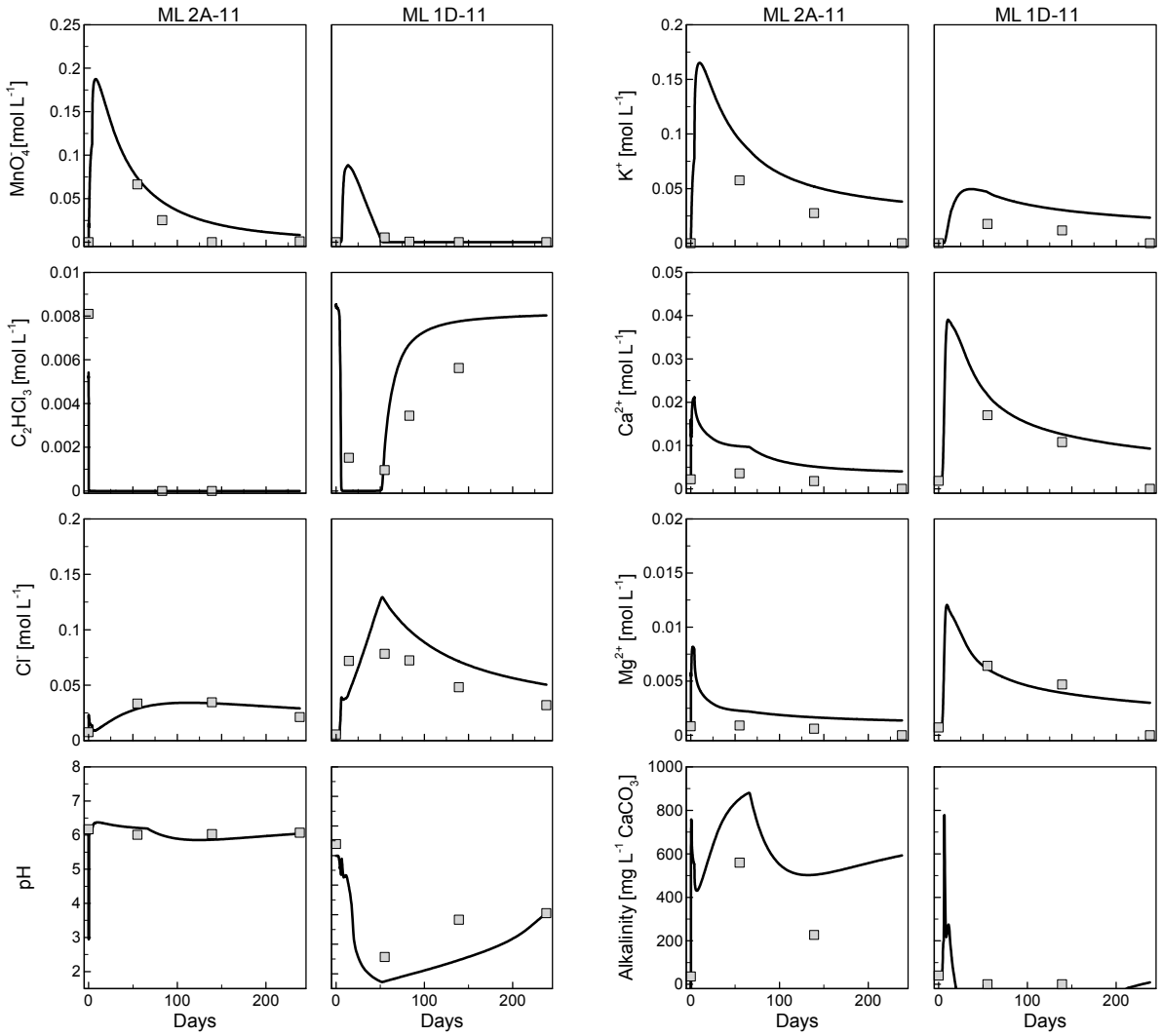

Figure 6-10. Observed (squares) and simulated (line) aqueous component concentrations at the bottom of the aquifer in multilevel sampling devices ML-2A-11 (left) and ML-1D-11 (right), located approximately 1 m south and 4 m northeast from the $KMnO_4$ injection point.

Vertical gradients in aqueous component concentrations are illustrated in Figure 6-11, using breakthrough data from the bottom four points of multilevel sampling device ML-1D (see Figures 6-2 and 6-3). Each of the four points illustrated is separated by approximately 15 cm vertically, extending from the aquifer-aquitard contact (ML-1D-11) to approximately 45 cm above the contact (ML-1D-08). Observed and simulated concentrations reveal the vertical dimensions of the permanganate and chloride plumes, and the depth-dependent and transient changes in TCE and pH response patterns above the aquitard surface.

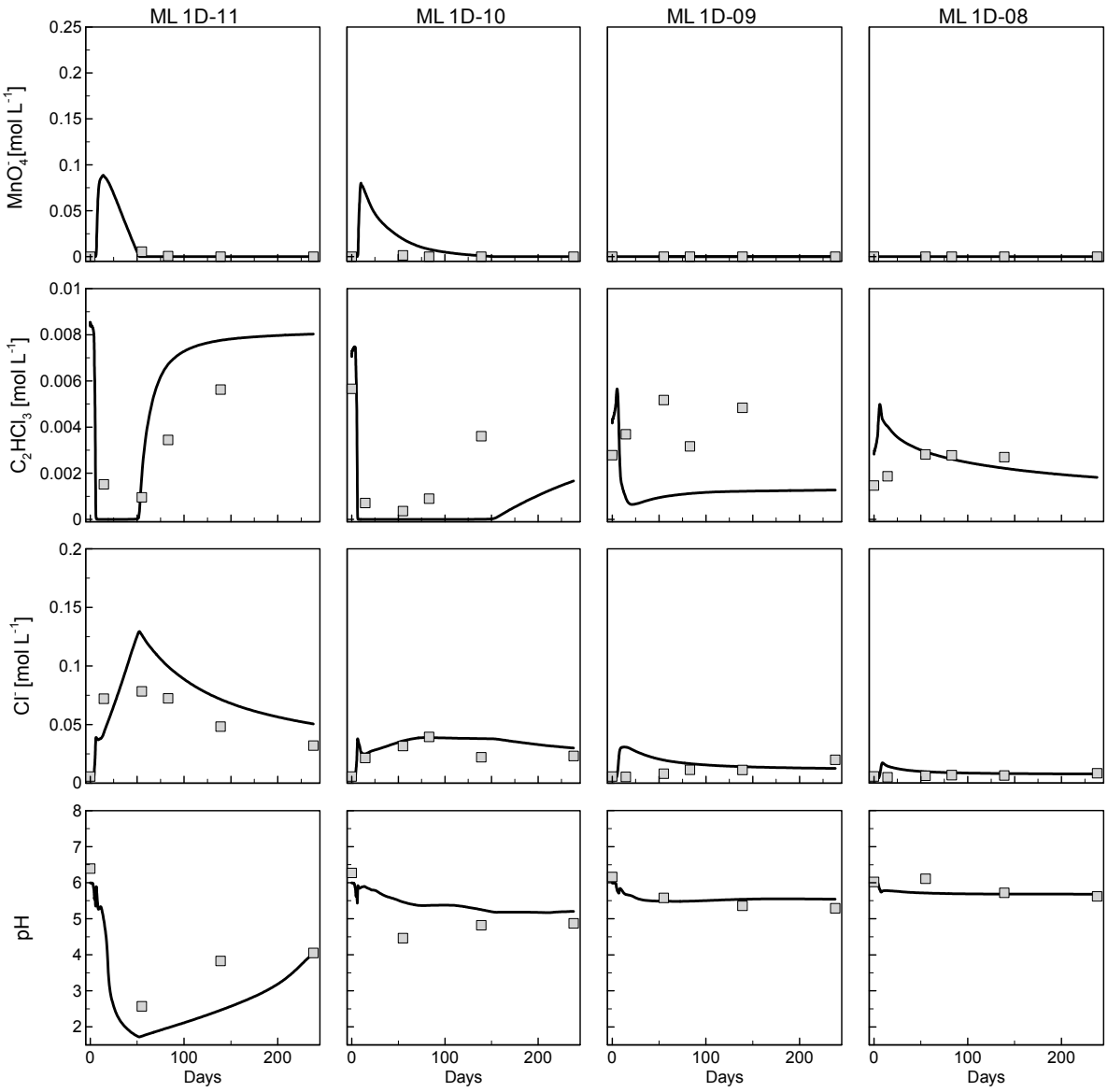

Figure 6-11. Aqueous component concentrations in four sampling points from multilevel sampling device ML-1D, located 4 m northeast from the $KMnO_4$ injection point. Vertical profiles are illustrated from left to right. The left-hand column of figures depicts measured (squares) and model (line) concentrations in sampling point ML-1D-11, located at the aquifer-aquitard contact. Sampling points ML-1D-10, ML-1D-09, and ML-1D-08, are located approximately 0.15 m, 0.30 m, and 0.45 m above the contact.

Figures 6-10 and 6-11 demonstrate that the model is successful in reproducing the concentration evolution for multiple chemical constituents monitored during the field trial in space and time. Precise reproduction of the measured data is not expected, given the complexity of the field system, which cannot be fully represented in a model.

6.3.3 Remediation Efficiency

A central component of this investigation is the utilization of the numerical model to evaluate remediation efficiency, defined as the fraction of the injected oxidant which reacts with $C_2HCl_{3(aq)}$. The other possible outcomes for the oxidant in the model include the reaction with SOM, autodecomposition, or persistence as unreacted oxidant.

Model results indicate that approximately 80 Kg of the 132 Kg of injected MnO_4^- oxidized TCE (60 %), 46 Kg oxidized organic carbon (35 %), 4 Kg were subject to autodecomposition (3 %), and 2 Kg (2 %) were present at the conclusion of the field experiment (238 days). Figure 6-12 illustrates the contribution of the different reaction pathways to the oxidant consumption over the course of the field trial.

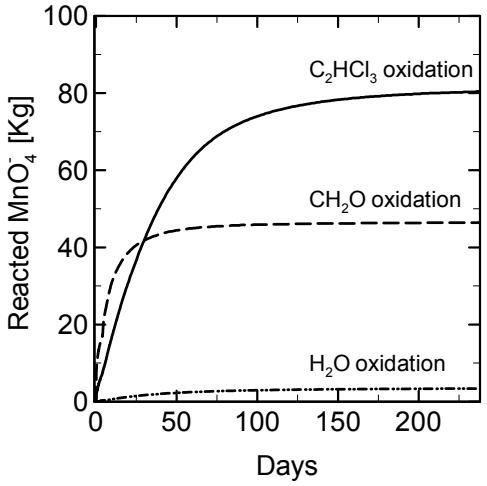

Figure 6-12. Cumulative mass of MnO_4^- consumed through intra-aqueous reaction with $C_2HCl_{3(aq)}$, oxidation of SOM, and oxidation of water. A total of 175 Kg of potassium permanganate were injected.

Observed changes in Cl^- concentrations offer an additional mechanism to estimate the amount of TCE oxidized by permanganate, and provide a means for comparison with model predictions. Dissolved Cl^- concentrations in the aquifer were measured at the conclusion of the field experiment along two sections extending radially from the injection point. The sections are indicated in Figure 6-1 by the linear segments of Waterloo Profiler points extending northeast and southwest of the injection point. Estimates of the total Cl^- mass were generated in the current investigation by interpolation of Cl^- concentrations in each of the two segments, and radial integration around the

injection point. These calculations resulted in estimates ranging from 17.5 to 40.5 Kg chloride present in the aquifer at the conclusion of the field trial. A comparison of initial and final chloride concentrations in the model indicates an increase of 24 Kg of chloride in the cells representing the aquifer, with an additional 13 Kg of chloride present in the aquitard. These results suggest a good level of agreement between the chloride mass increase estimated by interpolation of field data, and the chloride mass increase indicated by the MIN3PD model.

6.4 Discussion

The simulations clearly demonstrate the pronounced effects of the remediation on aquifer geochemistry reaching far beyond the treatment of the contaminant. The modeling also illustrates the beneficial effect of the high solution density, which leads to the sinking of the treatment solution and spreading along the aquifer-aquitard interface, focusing the delivery of the oxidant into regions where residual NAPL is present. Similar to the approach taken in the sensitivity analysis (Chapter 5), this hypothesis was tested for the field site under investigation by conducting a simulation that neglected the influence of solution composition on fluid flow. As expected, the simulations predict that the oxidant remains suspended in the vicinity of the injection well (results not shown). Mass balance results indicate that approximately 8 Kg of the 132 Kg of MnO_4^- oxidize TCE (6%), 19 Kg oxidize sediment organic matter (15%), and 105 Kg remain at the conclusion of the field experiment (238 days) or undergo auto-decomposition. These results point to a significant decrease of MnO_4^- utilization for both contaminant and organic matter oxidation (a 90 % and 50 % decrease, respectively). The fact that the predicted decrease for TCE oxidation is significantly higher relative to the oxidation of uniformly distributed SOM further highlights the ability of the dense treatment solution to follow the migration pathways of the DNAPL (mostly focused on the aquifer-aquitard interface). These results illustrate the important contribution of density-driven flow and transport towards remediation efficiency of the inject-and-leave method [Nelson et al., 2001; Parker et al., 2002].

As evaluated in Chapter 5, an additional aspect of interest is the effect of contaminant treatment and secondary reactions on fluid density, groundwater flow, and the delivery of the oxidant. Previous studies suggest that the effect of geochemical reactions on density-dependent flow and transport are relatively small for solution with high density contrast [Freedman and Ibaraki, 2002; Post and Prommer, 2007]. To assess this hypothesis for permanganate treatment, an additional simulation was conducted assuming conservative flow and transport following the injection of the dense treatment solution. For

the conditions at the North Haven site, the simulation results show a mild enhancement of the lateral spreading of the dense plume along the aquifer-aquitard interface for the conservative case (results not shown). The slower migration in the reactive case can be attributed to ion exchange reactions, and more importantly due to the immobilization of Mn as MnO_2 This effect is limited, because it is counteracted by oxidation of $C_2HCl_{3(aq)}$, causing enhanced dissolution of TCE DNAPL, resulting in the addition of Cl^- and CO_3^{2-} (in form of H_2CO_3 and HCO_3^-) to the solution. The delivery and distribution of MnO_4^- is therefore not significantly affected by changes in solution density due to treatment and other geochemical reactions. These results suggest that the only reactions that consume MnO_4^- have to be considered for the simulation of permanganate-based in-situ chemical oxidation, while other reactions such as ion exchange or calcite dissolution-precipitation may be neglected. However, the additional information contained in geochemical data including groundwater pH, alkalinity, and cation concentrations provides additional lines of evidence valuable in model calibration.

Suitable rate data for MnO_4^- auto-decomposition is not available in the literature; however, the model calibration constrained the maximum rate of this process. The stoichiometry of MnO_4^- auto-decomposition (Table 6-2) shows that this reaction is strongly acid-consuming and simulations with higher rates resulted in significant increases of pH, which is not consistent with field observations [Stewart, 2002]. As a result, the model calibration indicates minimal oxidant loss due to MnO_4^- auto-decomposition suggesting that this process can also be neglected. On the other hand, the mass balance results demonstrate that a significant fraction of the oxidant reacted with organic carbon despite the low organic carbon content at the site under investigation. This observation confirms that the permanganate treatment is most efficient at sites with low aquifer reduction capacity.

The current simulations predict only very moderate porosity and permeability reductions (max 0.5% and 5%, respectively) which seems to contradict results from previous investigations that attributed substantial permeability losses to Mn-oxide accumulation [Li and Schwartz, 2000; Schroth et al., 2001; MacKinnon and Thomson, 2002]. Similarly, employing a simplified mass transfer-based DNAPL dissolution model (Table 6-2) did not compromise the good agreement between the model results and observations, although inhibitory effects of Mn-oxide precipitation on DNAPL dissolution rates have been reported previously [Schroth et al., 2001; MacKinnon and Thomson, 2002; Lee et al., 2003; Urynowicz and Siegrist, 2005]. These results must be interpreted in a site-specific context and are likely due to the nature of the initial DNAPL distribution, which were constrained in a thin interval at the base of the aquifer and were accessible to the oxidant. The apparent absence of

DNAPL at high saturations within the treatment area, and the absence of a forced hydraulic gradient may explain the lack of model sensitivity towards MnO_2 accumulation. The current model formulation does not explicitly simulate pore-scale process [e.g., clogging of pore throats] which may contribute to more significant permeability reductions in porous media. Modeling DNAPL dissolution as a kinetic reaction proved critical in simulating the expansion and subsequent contraction of the oxidant plume, indicating that mass transfer limitations are important in controlling aquifer remediation using MnO_4^-.

The complexity of the problem requires a relatively coarse model discretization (minimum intervals in vertical and horizontal directions are 5 cm and 20 cm, respectively) to facilitate 3D-simulations within a reasonable time frame (on the order of 50 hours on a PC equipped with a 2.8 GHz processor and 2 GB of RAM). This grid resolution implies that initial NAPL saturations that showed variations on the mm to cm scale [Parker et al., 2003] had to be averaged for representation on the grid scale. Similarly, simulated maximum MnO_2 volume fractions were lower than observed in core samples due to a lack of resolution (0.5% vs. 3% [Stewart, 2002]). In addition, the limited model resolution does not allow for an adequate description of instability development due to strong density contrasts, considering that the dimensions of density fingers are likely on the order of centimeters. Despite these limitations, the simulation was able to reproduce the spatial distribution and transient evolution of the main components in an adequate fashion. This result suggests that lateral spreading of the dense plume along the aquifer-aquitard interface is of greater importance for oxidant delivery and distribution than instability development and fingering. In addition, limited NAPL accessibility and clogging by MnO_2 on the subgrid scale did not seem to significantly affect remediation reactions during the field trial.

The primary advantage of utilizing the multicomponent modeling approach to characterize the fate of the oxidant is the integration of multiple lines of evidence coupled by reaction stoichiometries, and the ability to estimate aqueous component concentrations beyond the limits of a field monitoring network. For the relatively simple stratigraphy and DNAPL distribution present at the simulated field trial, the model was able to successfully reproduce the observed evolution. The model was also able to demonstrate the important role of the density contrast between the treatment solution and groundwater in delivering the oxidant to the DNAPL that was concentrated at the aquifer-aquitard interface. As a result, the conceptual model as well as capabilities and resolution of the numerical model appear to provide a sound working basis for further investigations of this technology.

Chapter 7 Automated Inverse Modeling

The three-dimensional reactive transport modeling presented in Chapter 6 reproduced the fate and transport of the injected oxidant and the geochemical evolution monitored at the field trial. However, the trial and error method employed for model calibration did not support a thorough evaluation of model performance. Specifically, the investigation did not identify optimal parameter values or determine the quality of the calibration. Given the complexity of the model and the large number of parameter assignments required, the possibility that improvements in the model fit could be achieved using an alternate set of model parameters was investigated. Automated inverse modeling provides the framework for this investigation. The specific objectives of this chapter include (1) to systematically evaluate the quality of the calibration, (2) to identify optimal values for model parameters, (3) to analyze parameter sensitivity and uncertainty in model predictions, and (4) to evaluate the utility of automated inverse modeling in the investigation of reactive density-driven systems.

A fundamental benefit provided by automated inverse modeling is the ability to calculate parameter values that produce the best fit between measured data and corresponding model outputs [Yeh, 1986; Sun, 1994; Poeter and Hill, 1997]. In addition, the quality of the calibration, confidence limits on parameter estimates and predictions, and parameter sensitivity and correlation are quantified in the automated parameter estimation process. This approach has been employed to estimate optimal parameters in models simulating groundwater flow and non-reactive chemical fate and transport [Medina and Carrera, 1996; Iribar et al., 1997; Hill et al., 1998; Weiss and Smith, 1998a; D'Agnese et al., 1999; Liu and Ball, 1999; Barlebo et al., 2004]. Automated inverse modeling has recently been applied to multiphase flow simulations [Finsterle and Persoff, 1998; Finsterle, 2004], reactive chemical transport in constant density fluids [Essaid et al., 2003; Dai and Samper, 2004; Dai and Samper, 2006; Samper et al., 2008] and variable density flow and non-reactive transport problems [Sanz and Voss, 2006]. Based on the literature review, the current research represents the first study to apply automated inverse modeling to investigate a reactive density-driven system.

7.1 Approach

The potential utility of automated inverse modeling is suggested by the diversity of the measured field data and the existence of a large set of relevant model parameters. The existence of

multiple model parameters of comparable sensitivity also contributes to a difficult calibration problem, as the interaction between model parameters may not be apparent using a trial and error calibration approach. Automated inverse modeling was identified as a methodology to reduce subjectivity and enhance the efficiency of the parameter estimation process. The approach was also pursued to provide insight into characteristics of the modeled system and the information content of the data used to calibrate the model.

In the current work, the inverse problem is formulated as an optimization problem minimizing the misfit between model outputs and measured data, and solved using non-linear regression methods [Carrera and Neuman, 1986; Cooley and Naff, 1990; Doherty, 2002; Finsterle, 2004; Poeter et al., 2005]. The misfit between model outputs and measured data is quantified by an objective function; the parameter set which minimizes the objective function is interpreted as the most likely estimate of the optimal parameters for the specified model [Hill, 1998; Finsterle, 2004; Aster et al., 2005]. The computer program PEST [Doherty, 2002] includes inverse modeling algorithms developed to interface with independent simulation programs [Doherty, 2003; Tonkin and Doherty, 2005]. In the current investigation, inverse modeling is performed using a composite set of programs consisting of PEST, MIN3PD, and Fortran90 routines implemented to process MIN3PD output.

7.1.1 Weighted Objective Function

The residual vector **r** quantifies the difference between the measured data $\hat{\mathbf{y}}$ and the corresponding model outputs **y(b)**:

$$r_i = \hat{y}_i - y_i(\mathbf{b}) \qquad i = 1,...,m \tag{7-1}$$

where $\hat{y}_i$ and $y_i(\mathbf{b})$ represent the field measurement and the model outcome for the i^{th} observation, and a total of *m* residuals are calculated. The vector **b** contains the model parameters. Given that $\hat{\mathbf{y}}$ may include data that differ in physical units, magnitude, and accuracy, a weighting scheme is necessary to compute an aggregate measure of misfit [Hill, 1998; Finsterle, 2004; Hill and Tiedeman, 2007]. In the current investigation, field observations include K^+, Na^+, Ca^{2+}, Mg^{2+}, MnO_4^-, Cl^-, and $C_2HCl_{3(aq)}$ concentrations, and groundwater pH and alkalinity. The field data are characterized by a

wide range of concentrations, including MnO_4^- and $C_2HCl_{3(aq)}$ concentrations which varied over four and six orders of magnitude, respectively.

Errors in the measurement of aqueous chemical concentrations are expected to be proportional to the chemical concentrations [Wagner and Gorelick, 1986; Hill, 1998; Dai and Samper, 2004]. In the ideal case, the weight assigned to each observation is proportional or equal to the inverse of the variance of the measurement error [Cooley and Naff, 1990; Draper and Smith, 1998; Hill, 1998]:

$$\omega_i = \frac{1}{cv_i * \bar{y}_i} \tag{7-2}$$

where ω_i is the weighting factor for the i^{th} observation, cv_i is the coefficient of variation, and $\bar{y}_i$ is the unknown true concentration. In previous inverse modeling investigations, this concentration has been estimated using the measured or modeled concentration [Gorelick et al., 1983; Wagner and Gorelick, 1986]. Anderman and Hill [1999] investigated alternatives for estimating $\bar{y}_i$ using a synthetic test case employing inverse modeling and Monte Carlo analysis. Investigation results indicated that the use of simulated concentrations **y(b)** in weighting observations generating unbiased parameter estimates, while the use of measured concentrations $\hat{\mathbf{y}}$ resulted in biased parameter estimates.

An outcome of the application of Equation (7-2) is the assignment of large weights to small concentrations. Weighted residuals associated with small chemical concentrations along the edge of a plume may exert excessive influence on the objective function and the solution of the inverse problem [Barth and Hill, 2005; Hill and Tiedeman, 2007]. Individual weights in the current investigation were calculated using the following formula [Hill, 1998]:

$$\omega_i = \frac{1}{cv * y_i(\mathbf{b}) + \eta} \tag{7-3}$$

where η is a constant to prevent large relative differences at low concentrations from generating excessive weights [Keidser and Rosbjerg, 1991; Poeter and Hill, 1998]. Van Rooy et al. [1989] suggested setting this coefficient to 10 percent of the source strength.

The field data set incorporated in the inverse modeling includes aqueous component concentrations measured using portable field equipment (MnO_4^- , Cl^-, pH, and alkalinity) and aqueous component concentrations analyzed in an analytical laboratory (K^+, Na^+, Ca^{2+}, Mg^{2+}, Cl^-, and $C_2HCl_{3(aq)}$). Analysis of duplicate samples for inorganic constituents K^+, Na^+, Ca^{2+}, Mg^{2+}, and Cl^- at the analytical laboratory indicated that coefficients of variation ranging from 0 to 18 percent, with an average of 2.3 percent. Duplicate samples analyzed at the analytical laboratory for $C_2HCl_{3(aq)}$ generated coefficient of variations ranging from 0 to 125 percent, with an average of 13 percent. The coefficients of variation for field-measured Cl^- and MnO_4^- were approximately 3 and 13 percent, respectively. Table 7-1 summarizes the coefficient of variation and the weighting constant η assigned to each of the ten defined observation classes. As the table indicates, the pH measurements, which are subject to a logarithm transformation, were represented in the regression as untransformed hydrogen ion (H^+) concentrations. As described in subsequent sections, Na^+ and Mg^{2+} were incorporated in the evaluation of model performance, but were not incorporated into the inverse modeling regression.

Component	Analysis	cv_{ic}	c_{max}	η_{ic}
MnO_4^-	Field	0.15	6.62×10^{-2}	3.31×10^{-3}
$C_2HCl_{3(aq)}$	Laboratory	0.15	1.29×10^{-2}	6.45×10^{-4}
Cl^-	Field	0.05	1.34×10^{-1}	6.73×10^{-3}
Cl^-	Laboratory	0.05	7.84×10^{-2}	3.92×10^{-3}
K^+	Laboratory	0.05	1.76×10^{-2}	8.83×10^{-4}
Ca^{2+}	Laboratory	0.05	1.70×10^{-2}	8.51×10^{-4}
Na^+	Laboratory	0.05	9.26×10^{-3}	4.63×10^{-4}
Mg^{2+}	Laboratory	0.05	3.12×10^{-3}	1.56×10^{-4}
H^+	Field	0.20	2.69×10^{-3}	1.35×10^{-4}
Alkalinity	Field	0.20	$1.35 \times 10^{+2}$	6.76

Table 7-1. Summary of weighting factors employed in the investigation. The maximum detected concentration c_{max} and the constant η_{ic} are in mol L^{-1} units with the exception of alkalinity, which has units of mg L^{-1} as $CaCO_3$. The coefficient of variation cv_{ic} is unitless.

The constant $\eta_{(ic)}$ in Table 7-1 was calculated as 5 percent of the maximum detected concentration of each aqueous component:

$$\eta_{(ic)} = 0.05 * \hat{y}_{(ic,max)} \qquad ic = 1,10 \tag{7-4}$$

The measurement errors were assumed to be uncorrelated. The $m \times m$ weighting matrix employed in the inverse modeling contained the squared weights calculated using Equation (7-3) [Hill, 1998]:

$$\mathbf{Q} = \begin{bmatrix} \omega_{y_1}^2 & 0 & \cdots & 0 \\ 0 & \omega_{y_i}^2 & \cdots & 0 \\ \vdots & \vdots & \ddots & \vdots \\ 0 & 0 & 0 & \omega_{y_m}^2 \end{bmatrix} \tag{7-5}$$

The objective function minimized by the inverse modeling is the sum of squared weighted residuals, resulting in a weighted least-squares optimization problem [Hill, 1998]:

$$\Phi = \mathbf{r}^T \mathbf{Q} \mathbf{r} \tag{7-6}$$

7.1.2 Minimization Algorithm

For the current problem, direct mapping of the objective function Φ throughout the n-dimensional parameter space is computationally prohibitive, requiring an iterative approach to locate the minimum. The Levenberg-Marquardt minimization algorithm is a standard technique for automated parameter estimation in fluid flow and chemical transport problems [D'Agnese et al., 1999; Poeter and Hill, 1998; Hill et. al., 1998; Essaid et al., 2003; Dai and Samper, 2004; Barlebo et al., 2004; Sanz and Voss, 2006; Dai and Samper, 2006]. The objective function for the updated parameter vector $\mathbf{b_{k+1}}$ is approximated as quadratic function from a Taylor-series expansion [Finsterle, 2000]:

$$\Phi(\mathbf{b}_{k+1}) \approx \Phi(\mathbf{b}_k) + \mathbf{g}_k^T \Delta\mathbf{b} + \frac{1}{2} \Delta\mathbf{b}^T \mathbf{H}_k \Delta\mathbf{b} \tag{7-7}$$

where $\mathbf{g}$ is the gradient vector and $\mathbf{H}_k$ approximates the Hessian matrix, which contains second derivatives of the objective function.

Solving for the minimum of Equation (7-7) generates the linear system of equations to be solved for the parameter upgrade vector $\Delta\mathbf{b}$ [Weiss and Smith, 1998a; Finsterle, 2000]:

$$\mathbf{H}_k \Delta\mathbf{b} = -\mathbf{g}_k \tag{7-8}$$

where the approximate Hessian matrix and the gradient vector are given by:

$$\mathbf{H}_k = 2\mathbf{J}_k^T\mathbf{Q}\mathbf{J}_k \tag{7-9}$$

$$\mathbf{g}_k = -2\mathbf{J}_k^T\mathbf{Q}\mathbf{r}_k \tag{7-10}$$

The Hessian approximates the curvature of the objective function in the vicinity of parameter vector **b**, and the gradient vector –**g** is the direction of steepest descent [Doherty, 2002]. The Jacobian matrix contains derivatives of model output to model parameters, approximated in the current investigation using first-order finite differences:

$$\mathbf{J} = \frac{\partial \mathbf{y}}{\partial \mathbf{b}} = \begin{bmatrix} \frac{\partial y_1}{\partial b_1} & \cdots & \frac{\partial y_1}{\partial b_n} \\ \vdots & & \vdots \\ \frac{\partial y_m}{\partial b_1} & \cdots & \frac{\partial y_m}{\partial b_n} \end{bmatrix} \tag{7-11}$$

$$\left(\frac{\partial y_i}{\partial b_j}\right) \approx \frac{y_i(\mathbf{b}+\Delta\mathbf{b}) - y_i(\mathbf{b})}{\Delta b_j} \tag{7-12}$$

The solution of Equation (7-8) using the definitions in Equations (7-9) and (7-10) results in the Gauss-Newton iterative method [Weiss and Smith, 1998a; Finsterle, 2000]. The Levenberg-Marquardt algorithm modifies the Hessian, resulting in the following equation:

$$(\mathbf{H}_k + \alpha_k\mathbf{I})\Delta\mathbf{b} = -\mathbf{g}_k \tag{7-13}$$

where the scalar α_k is the Levenberg parameter [Levenberg, 1944], updated after each iteration following a scheme proposed by Marquardt [1963]. With increasing values of α, the update vector $\Delta\mathbf{b}$ approaches the steepest-descent direction **-g**, and the step length approaches zero [Finsterle, 2000]. This scheme enhances the ability of the method to accommodate poor initial estimates of model parameter values [Doherty, 2002]. In the current investigation, initial parameter values were estimated based on the Chapter 6 trial and error calibration. Testing of α values indicated that the value of 0.0 was generally optimal.

7.2 Implementation

7.2.1 MIN3PD Model

The inverse modeling required multiple MIN3PD model executions to iteratively update model parameters and search for the objective function minimum. The computational expense T_i associated with each inverse modeling simulation can be estimated based on the number of unknown parameters modeled (NP) and the time required for the execution of the forward model (T_f) [Hill, 1998]:

$$T_i = 2(NP) * T_f(1+NP) \quad (7\text{-}14)$$

where the term $T_f(1+NP)$ represents the computer time required to construct the Jacobian matrix using first-order finite differences (see Equation (7-12)), including one simulation performed at base parameter values and one forward simulation using an incremented value for each of the NP parameters. Hill and Tiedeman [2007] determined that the target execution times of the forward model was approximately 0.5 hour or less to facilitate the investigation of the model processes and data attributes in an inverse modeling investigation. The 50 hour simulation time required for the three-dimensional MIN3PD model of the North Haven field trial (based on a PC equipped with a 2.8 GHz processor and 2 GB of RAM) presents an excessive computational burden for an inverse modeling investigation. Approximately 23 days of processor time are required to construct the Jacobian for 10 unknown MIN3PD model parameters, and approximately 458 days of processor time may be required to complete an inverse modeling run using Equation (7-14).

Measures to reduce the computational burden of the MIN3PD model of the North Haven field trial include the reduction in the level of refinement of the model grid, reduction in the complexity of the reaction network, and reduction in the number of spatial dimensions simulated. Based on modeling objectives and the characteristics of the field data set, reduction of the spatial dimensions was implemented. The geometry of the monitoring network employed in the North Haven field investigation included radial segments of monitoring points extending from the oxidant injection point. Therefore, a two-dimensional radial model was able to incorporate much of the monitoring data collected during the investigation.

The most extensive radial segment of monitoring points included five multilevel sampling devices (ML-1A through ML-1E) and four Waterloo Profiler sampling locations in a segment

extending northeast of the injection point. The two-dimensional radial model extended from the injection point to the sheet pile cell along this line of monitoring locations, identified in the following discussions as the northeast section (Figure 7-1).

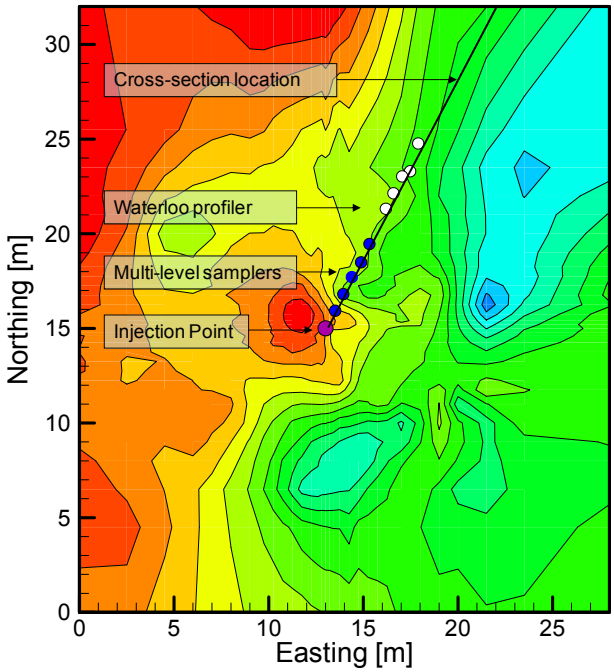

Figure 7-1. Location of the northeast section within the 3-D North Haven model, used to assign properties to the 2-D model.

The reaction network described in Chapter 6 was employed without modification. The spatial distribution of physiochemical properties, including sediment permeability and the pre-injection distribution of reactive phases and aqueous species was designed to approximate the northeast section of the three-dimensional model (Figure 7-1). The subset of MIN3PD control volumes comprising the northeast section was compiled, facilitating the assignment of properties to the two-dimensional model. Figure 7-2 illustrates the geometry of the contact between the aquifer and aquitard, and the initial TCE DNAPL distribution in the two-dimensional radial MIN3PD model.

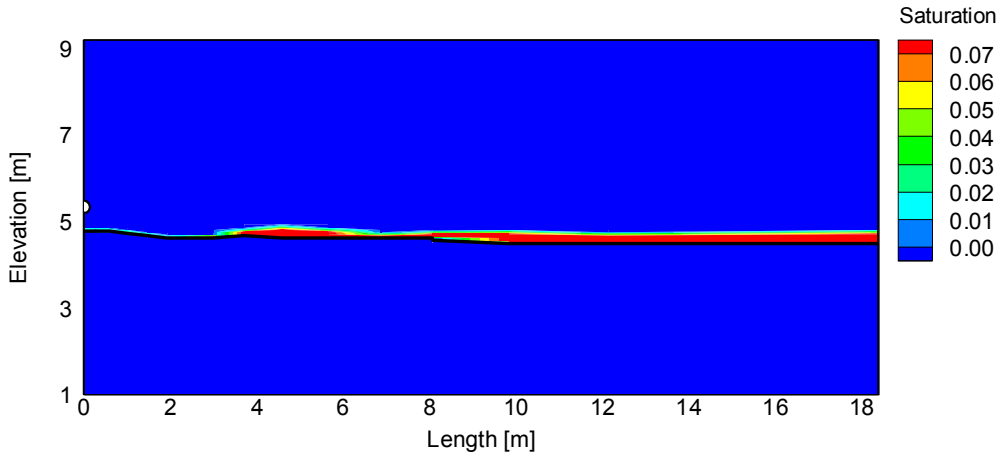

Figure 7-2. Initial distribution of TCE DNAPL. The contact between the aquifer and aquitard is depicted by the solid black line. The oxidant injection point is indicated by the white semi-circle.

The two-dimensional model domain extended 18.38 m in the horizontal direction and 8.2 m in the vertical direction. The model consisted of a total of 496 nodes. Grid spacing in the horizontal direction was defined by the radial distances between the model nodes and the injection point in the three-dimensional MIN3PD model. The vertical discretization was identical to the three-dimensional model (Figure 7-3).

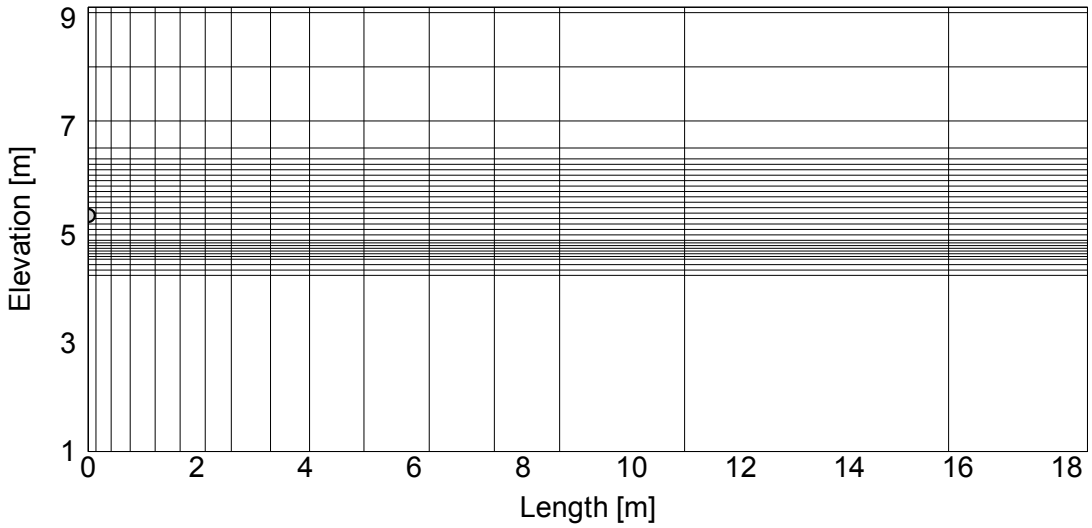

Figure 7-3. Two-dimensional radial MIN3PD model grid employed in the inverse modeling investigation. The oxidant injection point is represented by the grey semi-circle at x = 0 m. Vertical grid spacing is 0.1 m in the vicinity of the injection point. Minimum vertical grid spacing is 0.05 m, corresponding to the contact between the aquifer and aquitard.

A fundamental assumption incorporated by the two-dimensional MIN3PD model is that the physiochemical attributes of the modeled system exhibit radial symmetry. The monitoring data from

the North Haven field trial indicated that the MnO_4^- plume spread radially from the injection point and maintained approximate radial symmetry about the injection point during the field experiment. However, the pre-injection distribution of DNAPL and the elevation of the aquifer-aquitard contact were irregular across the field site [Stewart, 2002; Parker et al., 2003].

The errors attributable to the assumption of radial symmetry in modeling the field trial were investigated using the three-dimensional MIN3PD model as the benchmark. The comparison considered transient plume geometries, and mass balance results quantifying the fate of the injected MnO_4^-. Figures 7-4 and 7-5 depict the distribution of MnO_4^- and Cl^- predicted by the two- and three-dimensional models at 14.5, 83, and 238 days (the 1st, 3rd, and 5th sampling events) following the oxidant injection. In these figures, the distribution of the aqueous components in the two-dimensional model is compared with corresponding control volumes comprising the northeast section in the three-dimensional model.

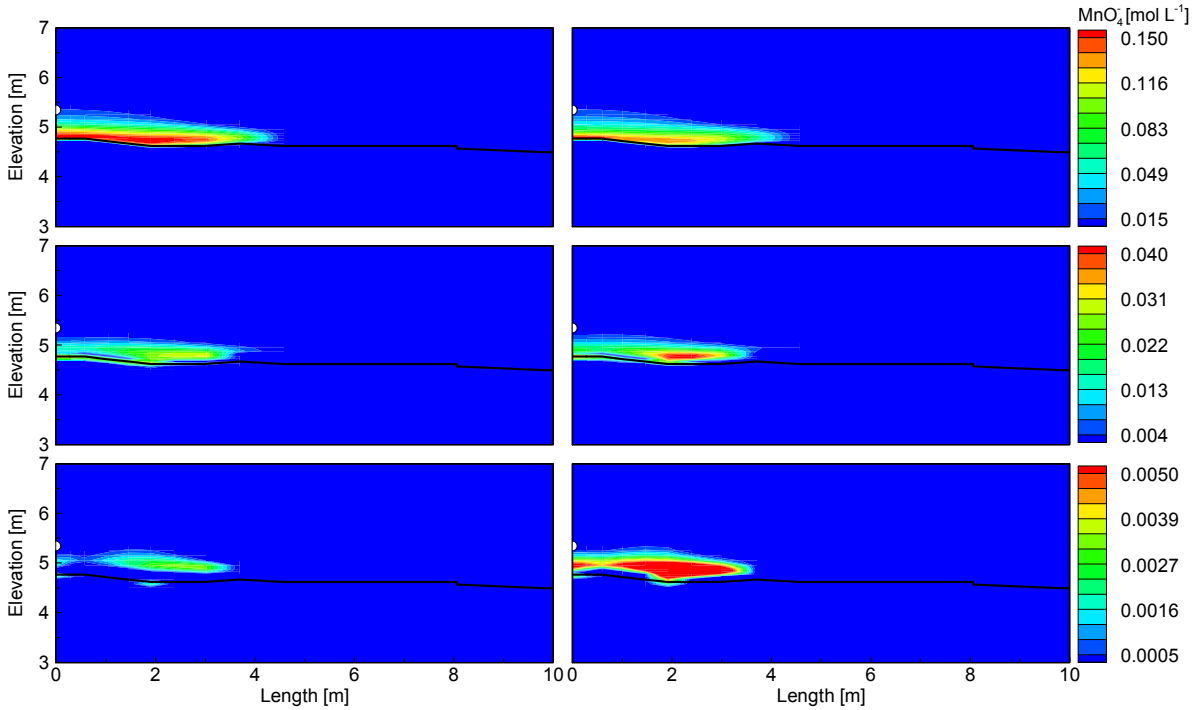

Figure 7-4. Comparison of predicted MnO_4^- concentrations using the three-dimensional model (left) and the two-dimensional radial model (right) of the North Haven field site at elapsed times of 14.5 (top), 83 (middle), and 238 days (bottom). The injection point is represented by the semi-circle at x = 0 m, and the aquifer-aquitard contact is represented by the solid black line.

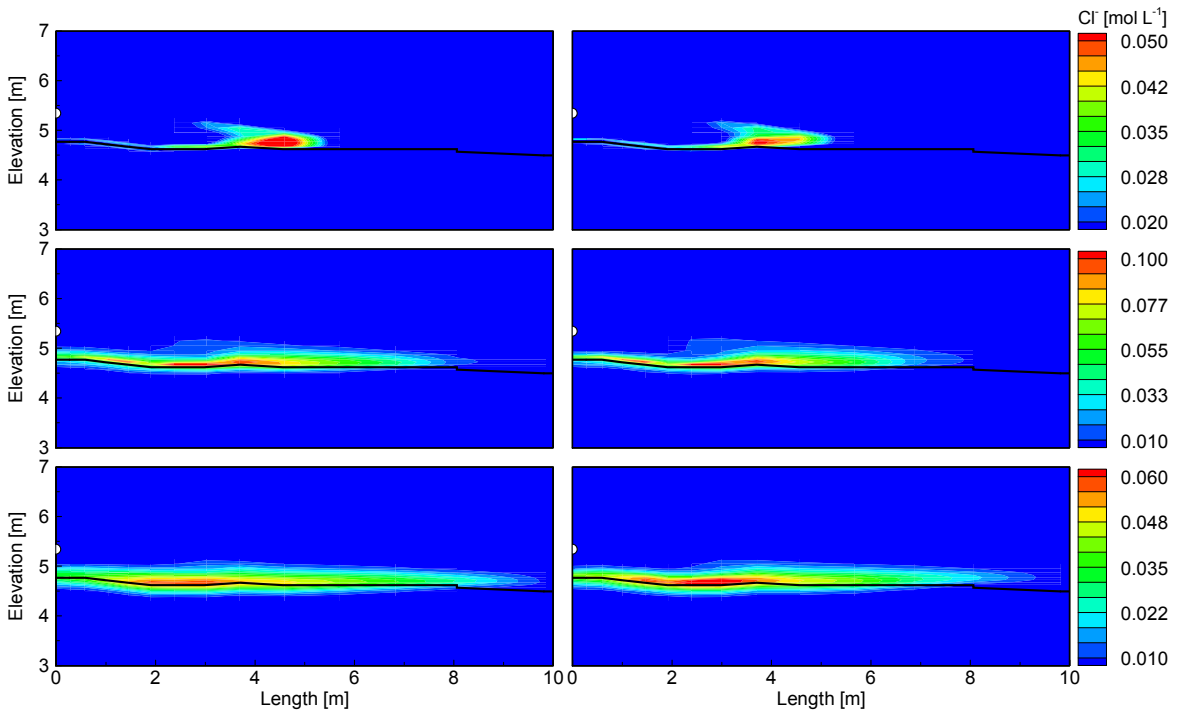

Figure 7-5. Comparison of predicted Cl^- concentrations using the three-dimensional model (left) and the two-dimensional radial model (right) of the North Haven field site at elapsed times of 14.5 (top), 83 (middle), and 238 days (bottom). The injection point is represented by the semi-circle at 0 m, and the aquifer-aquitard contact is represented by the solid black line.

While the transient geometry of the MnO_4^- plume is reproduced by the two-dimensional model, the MnO_4^- concentrations differ from the three-dimensional benchmark, notably at 238 days (end of simulation). However, at this time the absolute differences between the two models in MnO_4^- concentrations are small when scaled to the injected concentration. The comparison indicates excellent correspondence in Cl^- plumes between the two- and three-dimensional models for all three output times.

Table 7-2 summarizes the mass balance results quantifying the fate of the injected MnO_4^- in the two models. In the three-dimensional model, approximately 1.5 Kg of the 132 Kg of injected MnO_4^- was present at the conclusion of the experiment, compared to 3.4 Kg predicted by the two-dimensional model. The 2 Kg difference between the two models represents a small percentage of the total injected mass of MnO_4^-. The results summarized in the Table indicate that the two MIN3PD models are consistent with respect to the fate of the injected oxidant. Although the match between

the models is not exact, it was determined that the approximation was acceptable, and the two-dimensional model was employed in the inverse modeling investigation.

Quantity	3-D model	2-D model	Units
MnO_4^- injected	132(1.0)	132(1.0)	Kg (fraction of total)
MnO_4^- consumed by C_2HCl_3	80(0.60)	85(0.65)	Kg (fraction of total)
MnO_4^- consumed by SOM	46 (0.35)	40(0.29)	Kg (fraction of total)
MnO_4^- decomposition	3.4 (0.03)	3.6(0.03)	Kg (fraction of total)
MnO_4^- unreacted	1.5 (0.02)	3.4(0.03)	Kg (fraction of total)

Table 7-2. MIN3PD mass balance results comparing the fate of the injected MnO_4^- between the three- and two-dimensional models.

7.2.2 Inverse Modeling

The dimensions of the inverse problem are determined by the number of measured observations, the number of articles of prior information on system attributes, and the number of unknown model parameters. The data set collected along the northeast section of the field trial included 894 observations (Table 7-3). However, approximately 90 percent of the MnO_4^- data are censored by the lower limit of analytical detection. This condition reflects the reactivity of MnO_4^-, and density-driven flow patterns, which concentrated the MnO_4^- plume along the base of the aquifer following the injection (see Figure 7-4). Due to the existence of an extensive data set of uncensored observations, the censored data were not incorporated in the inverse modeling investigation. The MnO_4^-, $C_2HCl_{3(aq)}$, Cl^-, K^+, Ca^{2+}, pH, and alkalinity data were utilized in the regression, comprising a total of 625 observations. As described in subsequent sections, aqueous Na^+ and Mg^{2+} concentrations (43 observations total) were not included in the inverse modeling.

Component	Measurements	Detections	Median$_{(detections)}$	$\sigma_{(detections)}$	$\sigma_{(log\text{-}detections)}$
MnO_4^-	246	27	3.3×10^{-3}	1.9×10^{-2}	1.1
$C_2HCl_{3(aq)}$	211	204	4.3×10^{-4}	2.0×10^{-3}	1.2
Cl^- (field)	269	269	6.4×10^{-3}	1.4×10^{-2}	3.3×10^{-1}
Cl^- (lab)	28	28	5.8 x 10-3	1.7×10^{-2}	3.9×10^{-1}
K^+	22	22	1.0×10^{-4}	4.4×10^{-3}	7.7×10^{-1}
Ca^{2+}	22	22	1.7×10^{-3}	4.0×10^{-3}	3.5×10^{-1}
Na^+	22	22	3.0×10^{-3}	2.7×10^{-3}	3.7×10^{-1}
Mg^{2+}	21	21	6.3×10^{-4}	8.1×10^{-4}	5.7×10^{-1}
H^+	33	33	1.10×10^{-6}	4.7×10^{-4}	8.5×10^{-1}
Alkalinity	20	20	2.6×10^{1}	3.2×10^{1}	7.3×10^{-1}
Totals	894	668			

Table 7-3. Summary of field data. The median and standard deviation concentrations are in mol L^{-1} units except for the alkalinity data which are in units of mg L^{-1} as $CaCO_3$. The standard deviations are reported using untransformed detected concentrations $\sigma_{(detections)}$ and $\log_{10}$ transformed detected concentrations $\sigma_{(log\text{-}detections)}$.

The results of the parameter sensitivity analysis described in Chapter 5 were used to identify eleven MIN3PD model parameters which were estimated by inverse modeling. The most sensitive model parameters were selected based on the composite scaled sensitivity statistic [Hill, 1998]:

$$css_j = \left[(\mathbf{J}^T \mathbf{Q} \mathbf{J})_{jj} / m \right]^{\frac{1}{2}} \tag{7-15}$$

where css_j is the composite scaled sensitivity computed for the j^{th} model parameter. As reported in Chapter 5, the aquifer hydraulic conductivity and the coefficient of density variation exhibited nearly complete negative correlation. Reported values for $\partial\rho / \partial c$ fall in the range of 0.68 – 0.72 [Kharaka et al., 1988; Guo and Langevin, 2002; Oswald and Kinzelbach, 2004], in contrast with reported hydraulic conductivity values which vary over several orders of magnitude for a sediment class. In the current investigation, the coefficient of density variation was fixed at a value of 0.688 and the aquifer hydraulic conductivity was estimated by inverse modeling.

Table 7-4 summarizes the parameters estimated by inverse modeling. The initial parameter values were equal to the parameter assignments in the three-dimensional model of the North Haven field trial. The pre-injection DNAPL distribution was taken directly from the three-dimensional model, with a maximum DNAPL saturation of 8 percent (see Figure 7-2), corresponding to a volume fraction of 0.028 $L_{DNAPL} L_{bulk}^{-1}$. Volume fraction units are employed in this work to scale the DNAPL volume to the bulk volume of the porous media instead of the porosity.

Parameter	Symbol	Initial Value	CSS	Units
Aquifer porosity	ϕ_{aq}	0.35	1.00	-
DNAPL dissolution rate constant	k_{TCE}^{diss}	3.6×10^{-6}	0.52	s^{-1}
Aquifer hydraulic conductivity	K_{aq}	5.0×10^{-4}	0.51	$m\ s^{-1}$
Aquifer SOM fraction	φ_{CH2O}	1.5×10^{-4}	0.49	$m^3\ m^{-3}$
Longitudinal dispersivity	α_L	0.05	0.35	m
Aquitard porosity	ϕ_{aqt}	0.43	0.34	-
Chemical diffusion coefficient	D_m	6.4×10^{-10}	0.31	$m^2\ s^{-1}$
Maximum DNAPL fraction	φ_{DNAPL}	0.028	0.24	-
Aquifer pore size distribution	n	2.68	0.19	-
Transverse dispersivity	α_T	0.005	0.16	m
Cation exchange capacity	CEC	3.0	0.07	meq $[100\ g]^{-1}$

Table 7-4. MIN3PD model parameters estimated using inverse modeling. The composite scaled sensitivity values are the normalized values from the sensitivity analysis (Table 5-11).

As indicated previously, the spatial distribution of the DNAPL was imported from the three-dimensional MIN3PD model. The current effort did not attempt to estimate the DNAPL fractions in individual MIN3PD control volumes. Preliminary investigations indicated that the model output was insensitive to DNAPL volume fractions assigned to individual MIN3PD control volumes (results not shown). This result is consistent with the Chapter 5 sensitivity analysis, which indicated that DNAPL dissolution kinetics were more important than DNAPL volume fractions in the geochemical evolution and the permanganate utilization. Accordingly, DNAPL fractions throughout the model were adjusted by a uniform factor during each inverse modeling iteration.

The initial distribution of K^+, Na^+, Ca^{2+}, Mg^{2+}, pH, and alkalinity were taken from the three-dimensional model; these components were assigned uniform concentrations throughout the domain. In contrast to the geochemical data, pre-injection $C_2HCl_{3(aq)}$ and Cl^- concentrations were measured in all five multilevel sampling devices located in the northeast section (ML-1A through ML-1E; see Figure 7-1). The initial distributions of $C_2HCl_{3(aq)}$ and Cl^- were estimated by interpolating the pre-injection concentrations.

Field-measured data were collected characterizing several of the model parameters listed in Table 7-4, including the aquifer hydraulic conductivity, the porosity of the aquifer and aquitard, and the CEC and SOM fraction of the aquifer [Stewart, 2002]. The prior information was utilized as a reference for evaluating optimized MIN3PD model parameter values, instead of being directly incorporated in the inverse modeling regression. Prior information may incorporate measurement bias [Beckie, 1996; Weiss and Smith, 1998b; Barlebo et al., 2004], or mask the condition in which the

field observations do not contain enough information for accurate parameter estimation [Finsterle, 2000].

The inverse modeling program PEST version 9.0 was utilized to update model parameters and iteratively search for the objective function minimum. Parallel executions of MIN3PD were utilized to estimate the Jacobian matrix, reducing the overall simulation time. The Jacobian derivatives $\frac{\partial y_i}{\partial b_j}$ were estimated by incrementing the MIN3PD model parameters one percent of the parameter value [Zheng and Bennett, 2002]. A logarithm transformation was applied to the estimated parameters. In addition to preventing the parameters from becoming negative, this transformation has been reported to make the inverse problem more linear [Carrera and Neuman, 1986; Finsterle, 2000; Doherty, 2002]. Upper and lower limits on permissible parameter values were generally set so the bounds were not reached over the course of the regression. However, the bounds applied to the porosity of the aquifer and aquitard sediments were set to ± 25 percent of the field-measured values. This range was applied based on a review of literature resources [Carsel and Parrish, 1988] and the good level of agreement between measured porosity and bulk density in the aquifer and aquitard sediments.

Convergence was evaluated using updates in the objective function. A convergent iteration occurs when the relative improvement in the objective function is less than or equal to the user-specified tolerance [Doherty, 2002]:

$$\left(\Phi_{k+1} - \Phi_{min}\right) / \Phi_{k+1} \leq \text{PHIREDSTP} \tag{7-16}$$

where Φ_{k+1} and Φ_{min} represent the current and lowest achieved values of the objective function, and the variable PHIREDSTP is the user-supplied tolerance. The objective function is determined to have converged when Equation (7-16) has been satisfied for a target number of iterations, or a specified number of iterations has occurred since the minimum was achieved. Table 7-5 summarizes parameter assignments utilized in the inverse modeling.

Parameter	Value	Description
NOBS	625	Number of field observations incorporated in regression
NPRIOR	0	Number of articles of prior information incorporated in regression
NPAR	11	Number of adjustable MIN3PD parameters
DERINC	0.01	Finite difference parameter increment
RELPARMAX	2.0	Maximum factor change in parameter value
PHIREDSTP	0.005	Objective function convergence criteria
NPHISTP	3	Maximum number of iterations ≤ PHIREDSTP
NPHINORED	3	Maximum iterations past minimum objective function
RELPARSTP	0.005	Parameter convergence criteria
NRELPAR	3	Maximum number of convergent iterations
RLAMBDA1	0.0	Initial Marquardt parameter

Table 7-5. Summary of PEST model parameters.

7.3 Results

7.3.1 Non-optimized Model

Model results incorporating non-optimized model parameters are briefly summarized to assess the performance of the initial model, and provide a point of reference for evaluating the optimized MIN3PD model. Figures 7-6 through 7-8 compare measured and modeled MnO_4^-, $C_2HCl_{3(aq)}$, Cl^-, K^+, Ca^{2+}, Na^+, Mg^{2+}, pH, and alkalinity results from multilevel sampling device ML-1D. This location was selected due to the availability of geochemical data (K^+, Ca^{2+}, Na^+, Mg^{2+}, pH, and alkalinity), measured 55 and 139 days following the initial permanganate injection.

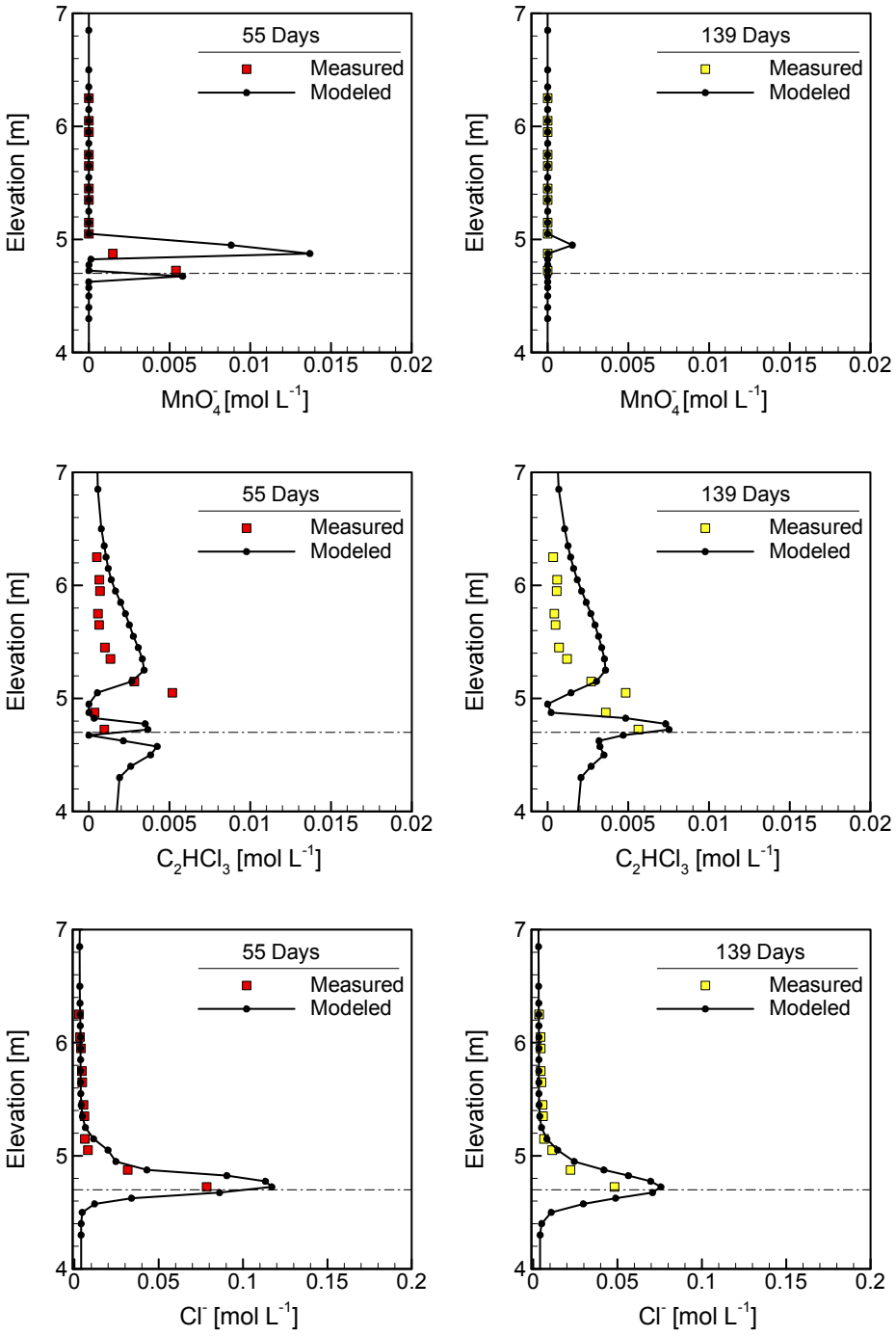

Figure 7-6. Comparison of measured and modeled MnO_4^-, $C_2HCl_{3(aq)}$, and Cl^- concentrations in multilevel sampling device ML-1D using the non-optimized model. Solid black circles indicate the center elevation of each MIN3PD control volume. The elevation of the aquifer-aquitard contact is indicated by the dashed horizontal line.

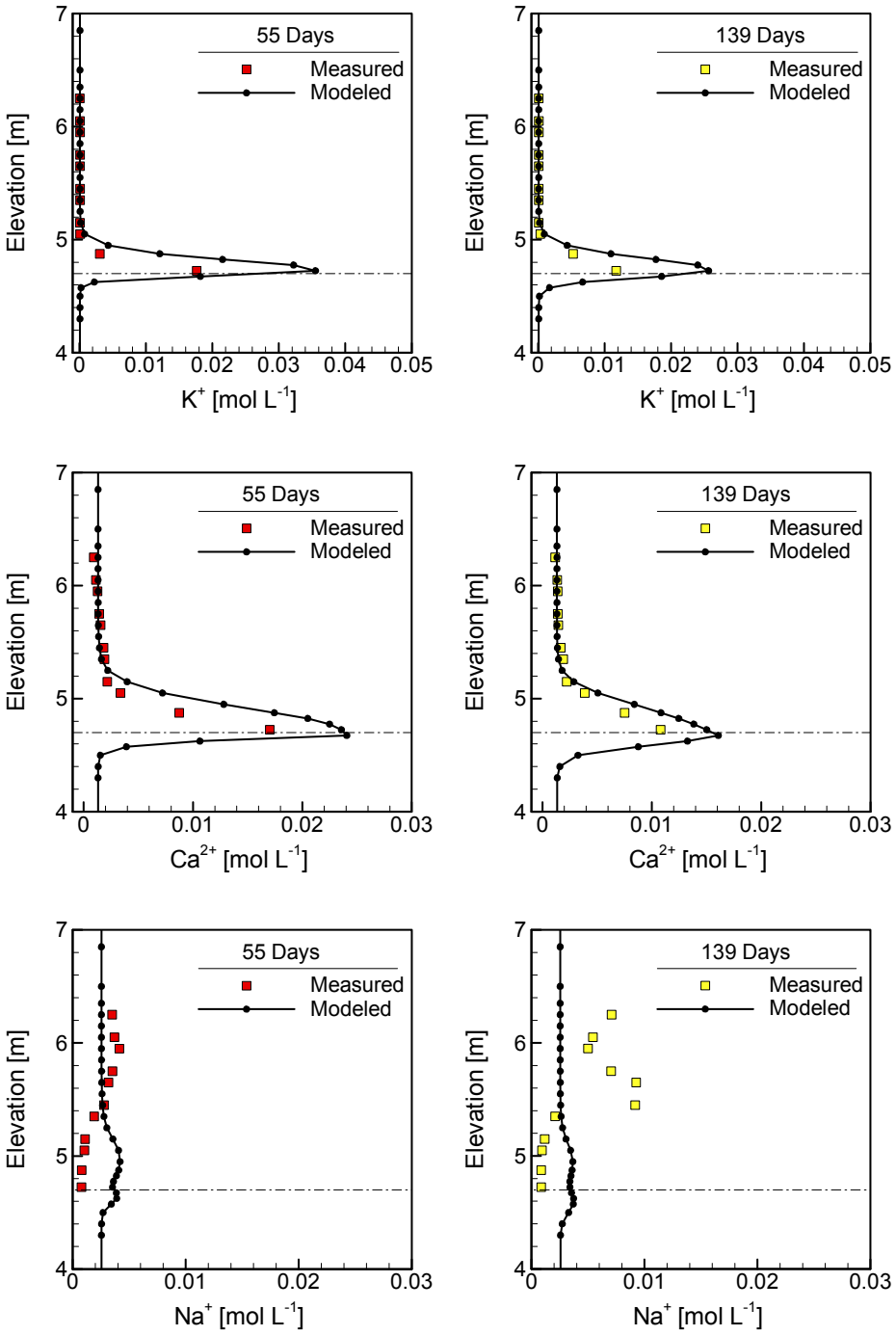

Figure 7-7. Comparison of measured and modeled K^+, Ca^{2+}, and Na^+ concentrations in multilevel sampling device ML-1D using the non-optimized model. Solid black circles indicate the center elevation of each MIN3PD control volume. The elevation of the aquifer-aquitard contact is indicated by the dashed horizontal line.

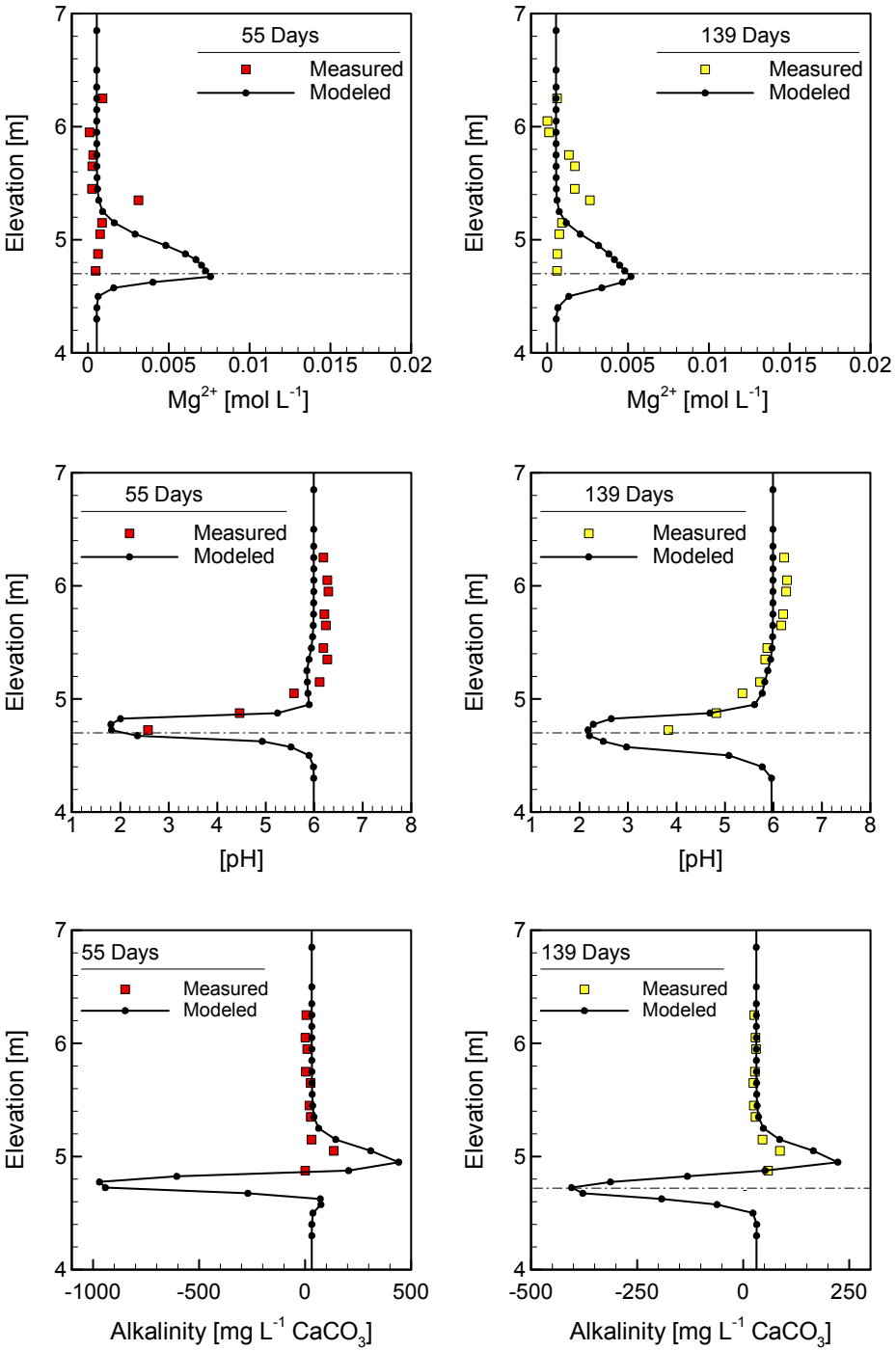

Figure 7-8. Comparison of measured and modeled Mg^{2+}, pH, and alkalinity in multilevel sampling device ML-1D using the non-optimized model. Solid black circles indicate the center elevation of each MIN3PD control volume. The elevation of the aquifer-aquitard contact is indicated by the dashed horizontal line.

The results illustrated in Figures 7-6 through 7-8 indicate that the non-optimized MIN3PD model reproduces the general plume geometries, defined by the accumulation of MnO_4^-, Cl^-, K^+, and Ca^{2+} in a narrow (~0.3 m) interval at the base of the aquifer. While the general geometry of these measured plumes is captured well, closer examination reveals that the model over-predicts the concentrations of all four components during both output times. In addition, the pH at the base of the aquifer is under-predicted, while the $C_2HCl_{3(aq)}$ concentrations measured in the top seven points of the sampling device (between 0.65 and 1.55 m above the aquitard) are over-predicted. These errors are consistent with the three-dimensional model (see Figures 6-10 and 6-11).

The measured Na^+ and Mg^{2+} data indicate that these components did not accumulate at the base of the aquifer. Increased Na^+ was measured in an interval extending from 0.75 to 1.55 m above the aquitard (see Figure 7-7), while minimal increases of Mg^{2+} above the background concentration were recorded (see Figure 7-8). However, the model predicts the accumulation of both components at the base of the aquifer, resulting from cation exchange reactions with the introduced K^+. In this case, the general response is not reproduced by the model. Preliminary inverse modeling simulations were unsuccessful in significantly improving the fit of either the Na^+ or Mg^{2+}. The match achieved for the remaining components (MnO_4^-, $C_2HCl_{3(aq)}$, Cl^-, K^+, Ca^{2+}, pH, and alkalinity) constrains the extent to which the current model may be adjusted to match the measured Na^+ or Mg^{2+} data. It was determined that these data reflect complexity in conditions at the field site which are not represented in the mathematical model. The Na^+ or Mg^{2+} data were excluded from the parameter estimation process, but were included in the evaluation of model errors.

Composite scaled sensitivities were calculated for the initial parameter set incorporating the set of 625 MIN3PD model observations (MnO_4^-, $C_2HCl_{3(aq)}$, Cl^-, K^+, Ca^{2+}, H^+, and alkalinity) corresponding to the field data set (Figure 7-9). The results indicate that the most sensitive parameter (aquifer porosity) is a factor of 6 more sensitive than the least sensitive parameter (aquifer pore size distribution coefficient). Although the relative order of parameter sensitivity slightly differs from the results presented in Chapter 5, both investigations indicate the existence of multiple MIN3PD model parameters of comparable sensitivity.

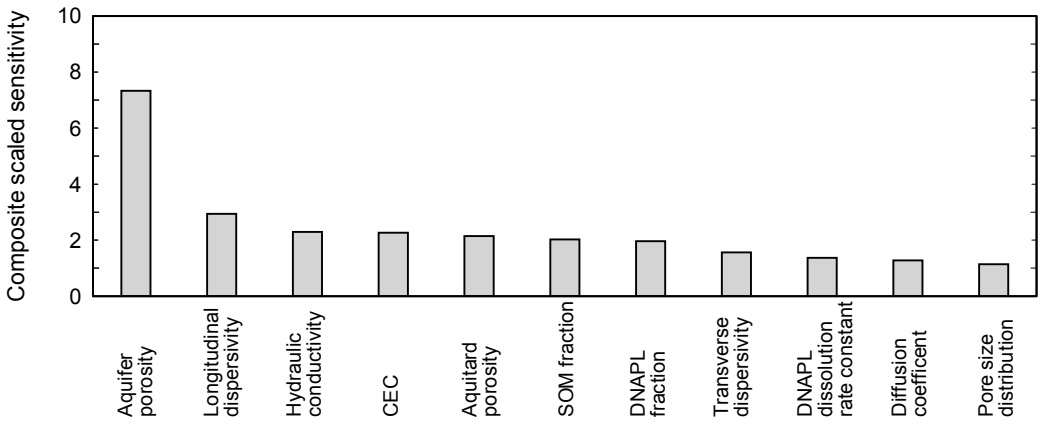

Figure 7-9. Composite scaled sensitivities calculated at initial MIN3PD parameter values.

7.3.2 Inverse Modeling Results

The Levenberg-Marquardt algorithm implemented in PEST calculates parameter updates to reduce the value of the weighted objective function Φ. The regression converged in a total of 8 parameter estimation iterations, resulting in an approximate two-fold reduction in Φ from an initial value of 1227 to a final value of 623. The mean value of the 625 weighted residuals for the optimized model was 6.9 x 10^{-3} (data not shown). The target mean value for the weighted residuals is 0 [Doherty, 2002].

The quality of the fit between the optimized MIN3PD model and the measured data was quantified by scaling the objective function Φ by the number of degrees of freedom [Hill, 1998]:

$$s^2 = \frac{\Phi}{m + npr - n} \tag{7-17}$$

where s^2 is the error variance of the regression, m is the number of observations included in the regression (625), npr is the number of articles of prior information (0), and n represents the number of adjustable model parameters in the regression (11). The error variance computed using Equation (7-17) is 1.0, equal to the expected value when the fit is consistent with the data accuracy reflected in the weighting [Hill, 1998]. Reduction of the error variance to 0 is possible only if the measured data and model do not contain error [Finsterle, 2000]. As indicated previously, the weighting scheme employed a factor to prevent small component concentrations from dominating the objective function

value (see Equation (7-3)). Accordingly, the calculated error variance of 1.0 is not interpreted to indicate absence of model error. The existence of model error is certain given the simplified model of the field investigation site. Although model error is unavoidable, the current approach is intended to reduce errors in model parameter values to facilitate an evaluation of conceptual errors incorporated in the MIN3PD model.

Figures 7-10 through 7-12 illustrate the discrepancies between measured and modeled concentrations for the optimized MIN3PD model. The Cl^- data are of primary interest as this component provides a reaction tracer associated with the oxidation of $C_2HCl_{3(aq)}$ by MnO_4^-, [Schnarr et al., 1998; Nelson et al., 2001] and was utilized in the assessment of the fate of the MnO_4^- injected at the North Haven field trial [Stewart, 2002]. As indicated in Figure 7-10, strong correlation between measured and modeled Cl^- concentrations is indicated. In addition, strong correlations between measured and modeled K^+, Ca^{2+}, and pH are indicated. Inspection of the weighted residuals for MnO_4^-, Cl^-, $C_2HCl_{3(aq)}$, K^+, Ca^{2+}, pH, and alkalinity do not reveal a pervasive positive or negative bias. As the objective function integrates weighted residuals from multiple components and sampling events, the regression does not prevent the occurrence of bias within subsets of the data.

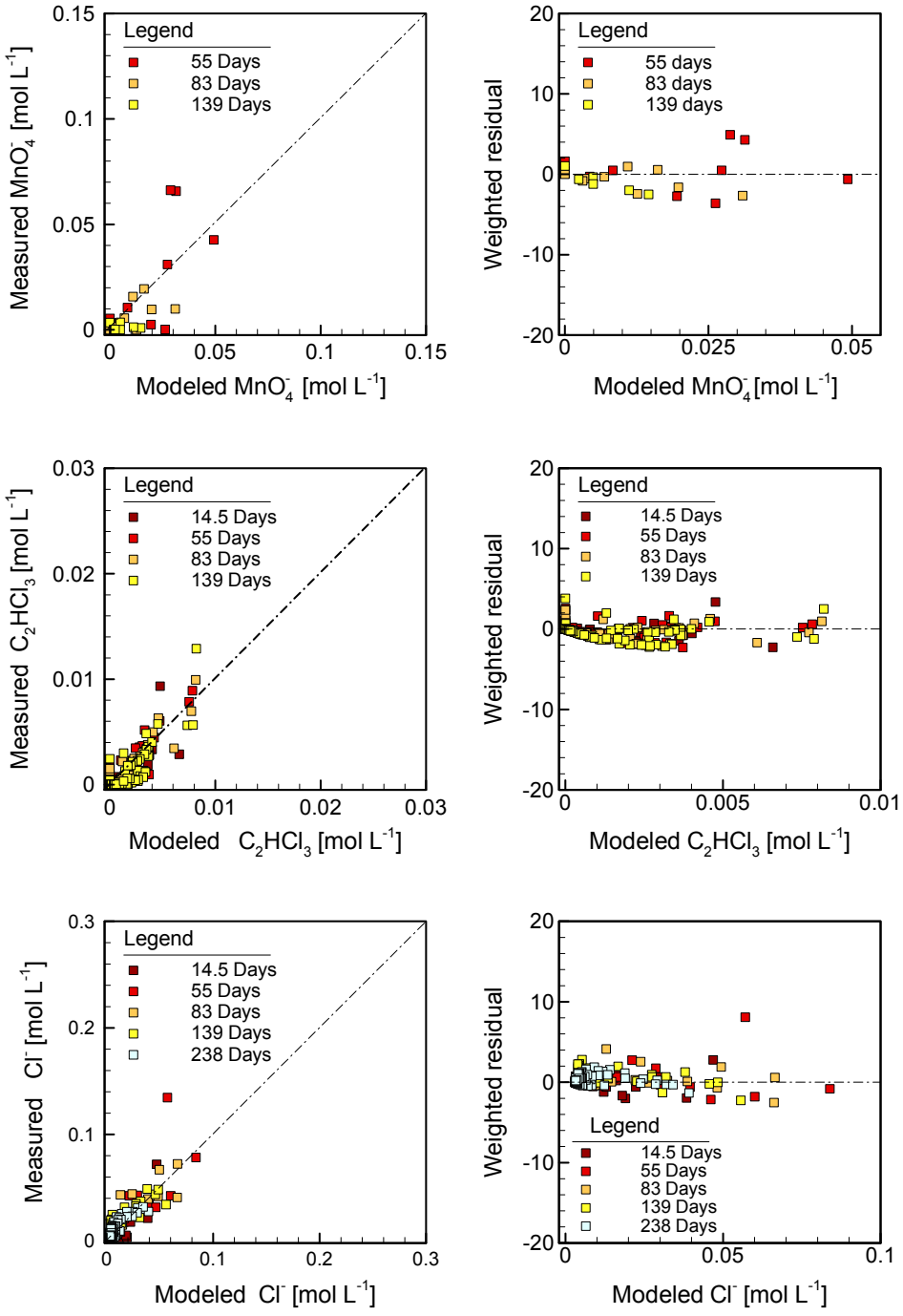

Figure 7-10. Comparison of measured and modeled MnO_4^-, $C_2HCl_{3(aq)}$, and Cl^- concentrations (left) and corresponding weighted residuals (right).

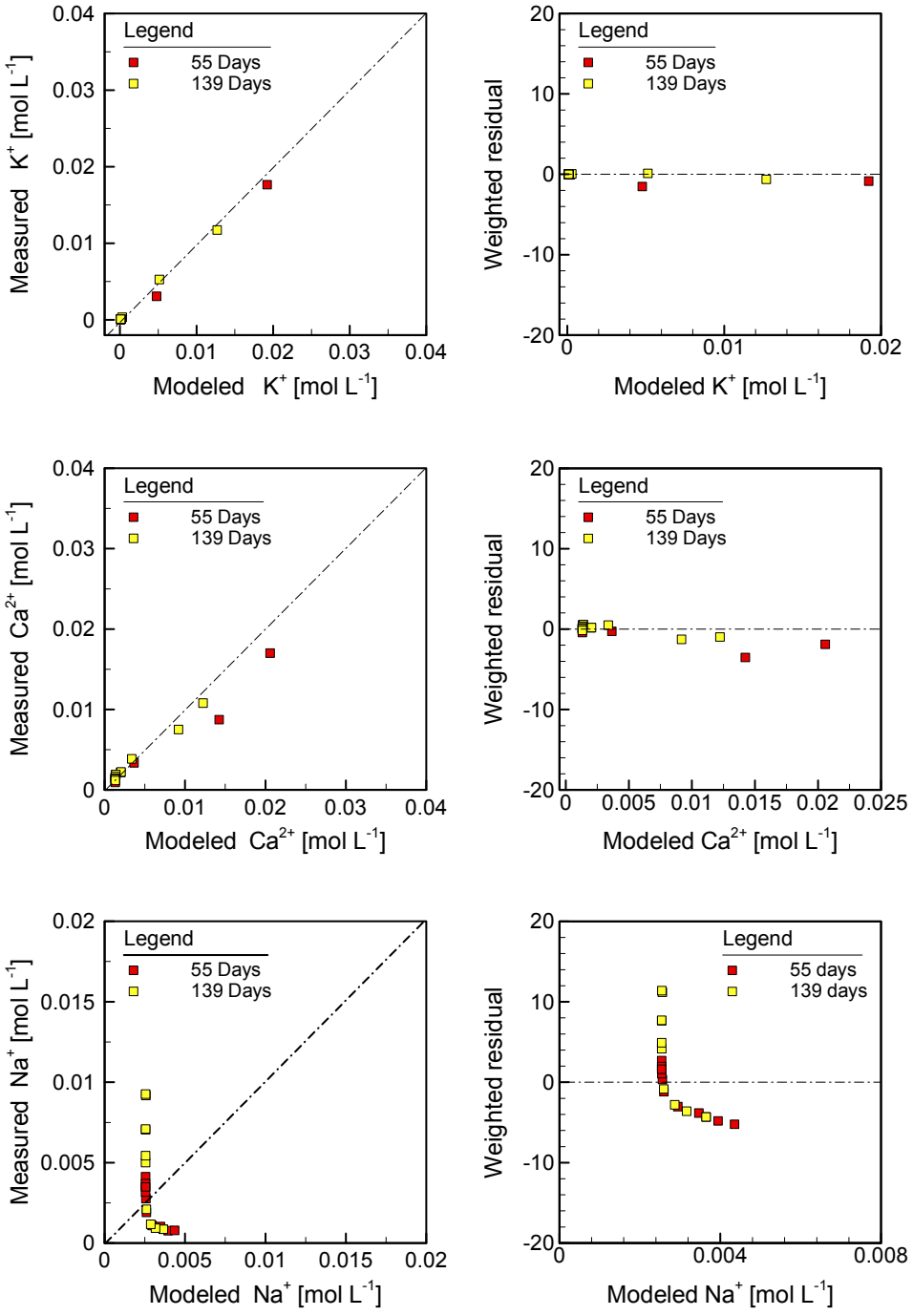

Figure 7-11. Comparison of measured and modeled K^+, Ca^{2+}, and Na^+ concentrations (left) and corresponding weighted residuals (right).

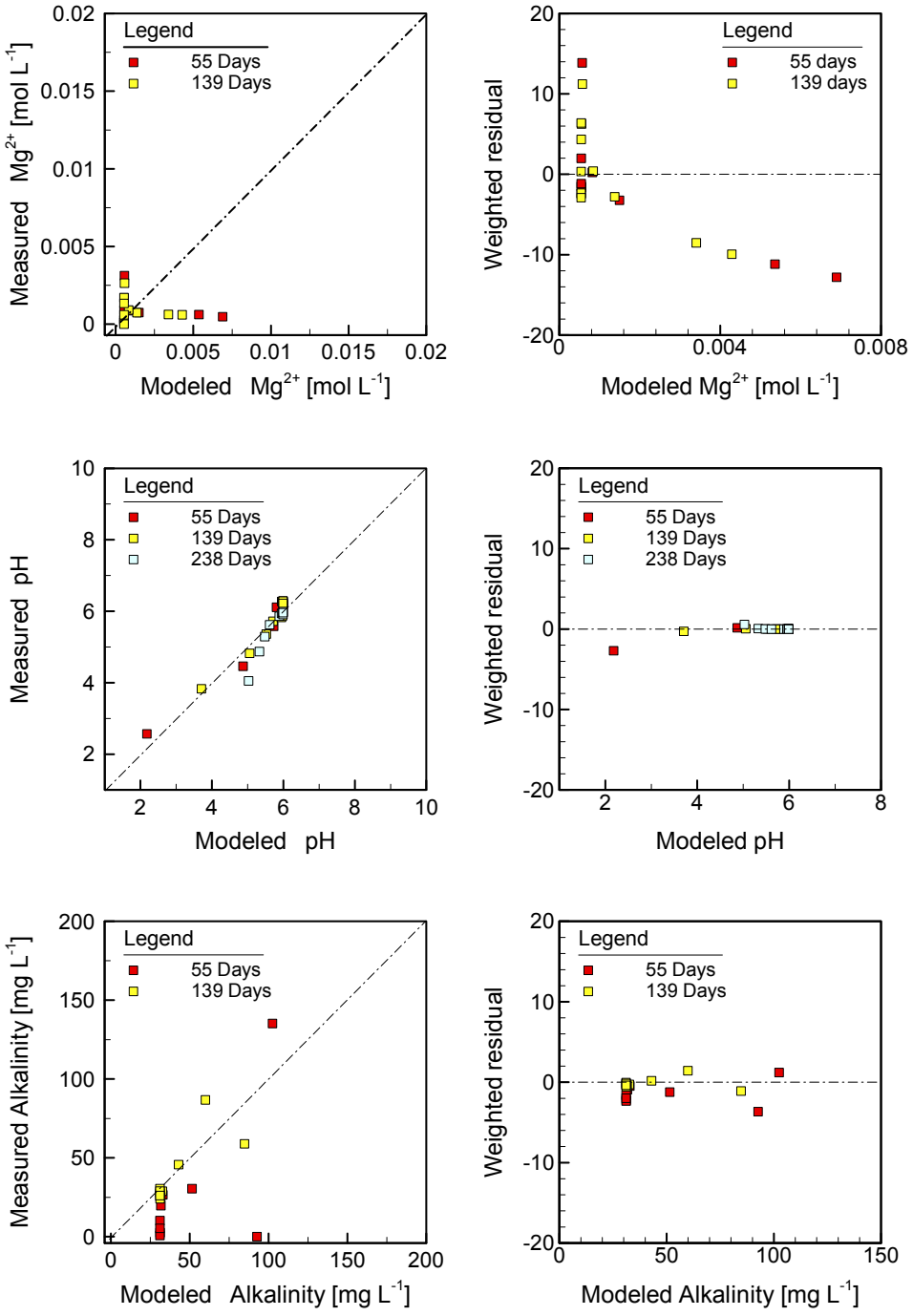

Figure 7-12. Comparison of measured and modeled Mg^{2+} concentrations, pH, alkalinity (left) and corresponding weighted residuals (right).

The lack of correlation between measured and modeled Na^+ and Mg^{2+} indicate that the factors determining the fate and transport of these components are not represented correctly by the model. Preliminary inverse modeling simulations incorporated these components, but did not significantly improve the fit. The focus of the investigation was the fate of the injected MnO_4^-, so the lack of fit exhibited by Na^+ and Mg^{2+} were not investigated further. The cation exchange reactions between K^+, Na^+, Ca^{2+}, and Mg^{2+} are modeled using equilibrium expressions based on the relative selectivity of the components for exchange sites. The modeling results indicate that factors at the field investigation site, including the presence of a concentrated chemical oxidant, organic liquids, and generated manganese oxide colloidal particles may result in complexity in cation adsorption reactions not simulated in the current model.

Additional evaluation of model errors was performed by utilizing the data collected at multilevel sampling device ML-1D to illustrate the vertical distribution of the measured and modeled plumes. Figures 7-13 through 7-15 compare the measured and modeled aqueous concentrations for the optimized model. As the Figures indicate, the model reproduction of the Cl^-, K^+, Ca^{2+}, pH, and alkalinity data is excellent at both sampling times, and the match is improved relative to the model simulation performed at initial parameter values (see Figures 7-6 through 7-8). The MnO_4^- concentrations, which were over-predicted at 55 days in the non-optimized model, are under-predicted in the optimized model. The optimization is directed to minimize a summed measure of the discrepancy between the model outputs and measured data; individual discrepancies may not be resolved during this process. The fit to the measured $C_2HCl_{3(aq)}$ data was minimally changed from the non-optimized model. The lack of model fit to the Na^+ and Mg^{2+} may reflect inaccurate representation of the selectivity of the cations in the true system. The field data indicate minimal desorption of Mg^{2+} occurred, indicating a higher selectivity of Mg^{2+} than represented in the model. It is probable that site-specific conditions, such as the presence of a saturated permanganate solution, DNAPLs, or the generation of manganese oxide solids complicated cation exchange reactions at the field site

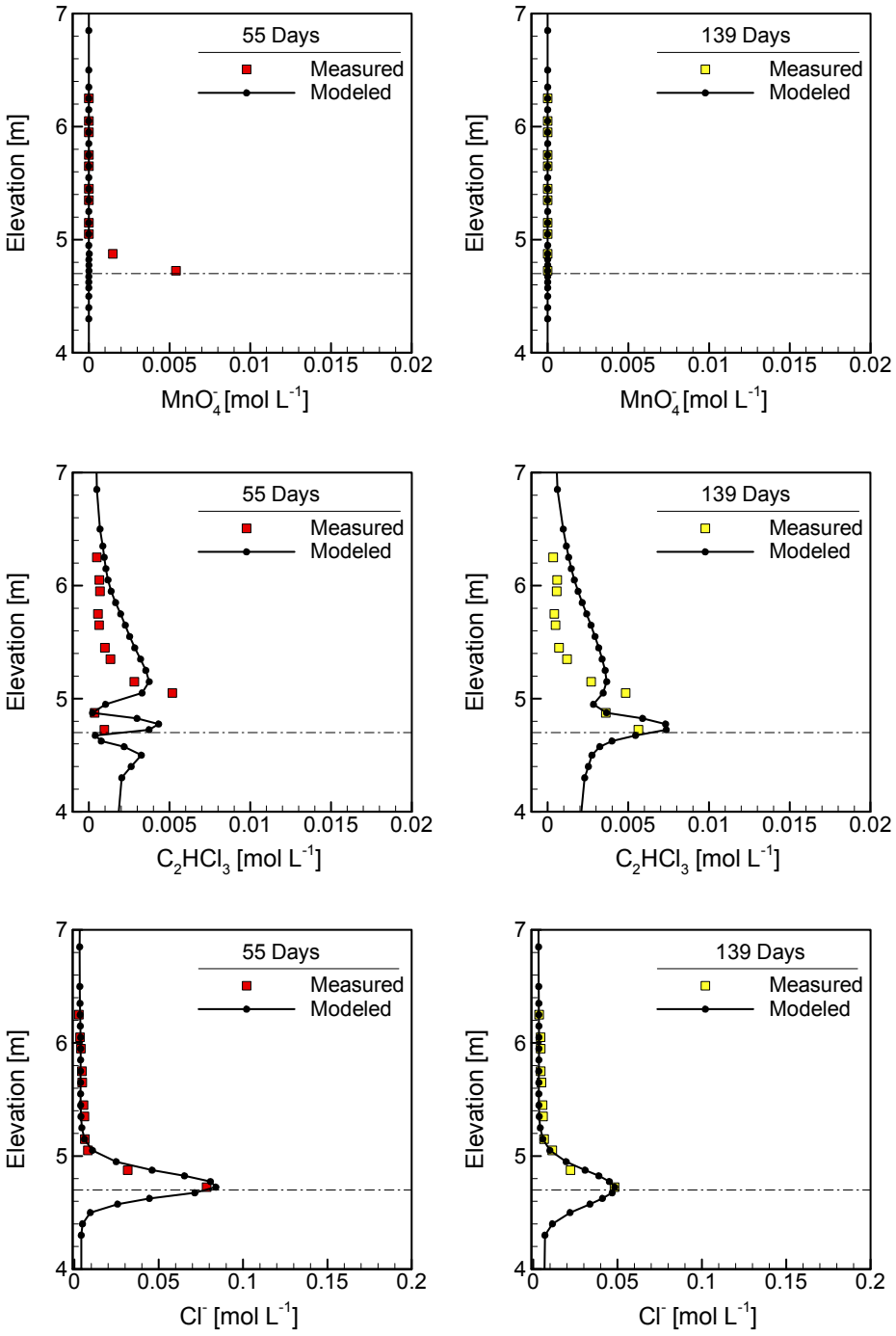

Figure 7-13. Comparison of measured and modeled MnO_4^-, $C_2HCl_{3(aq)}$, and Cl^- concentrations at multilevel sampling device ML-1D at 55 days (left) and 138 days (right) following the oxidant injection. Solid black circles indicate the center elevation of each MIN3PD control volume. The elevation of the aquifer-aquitard contact is indicated by the horizontal dashed line.

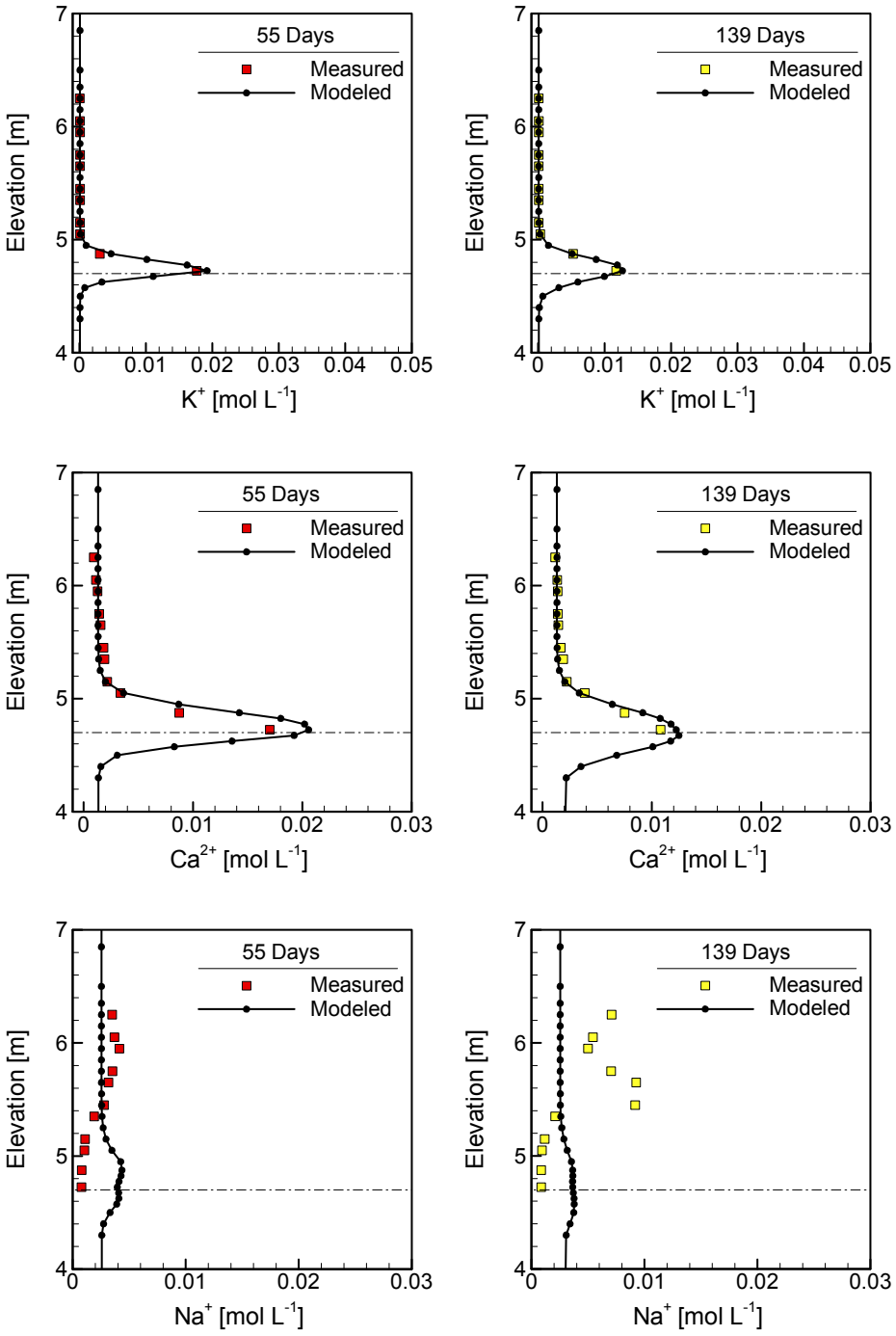

Figure 7-14. Comparison of measured and modeled K^+, Ca^{2+}, and Na^+ concentrations at multilevel sampling device ML-1D at 55 days (left) and 138 days (right) following the oxidant injection. Solid black circles indicate the center elevation of each MIN3PD control volume. The elevation of the aquifer-aquitard contact is indicated by the horizontal dashed line.

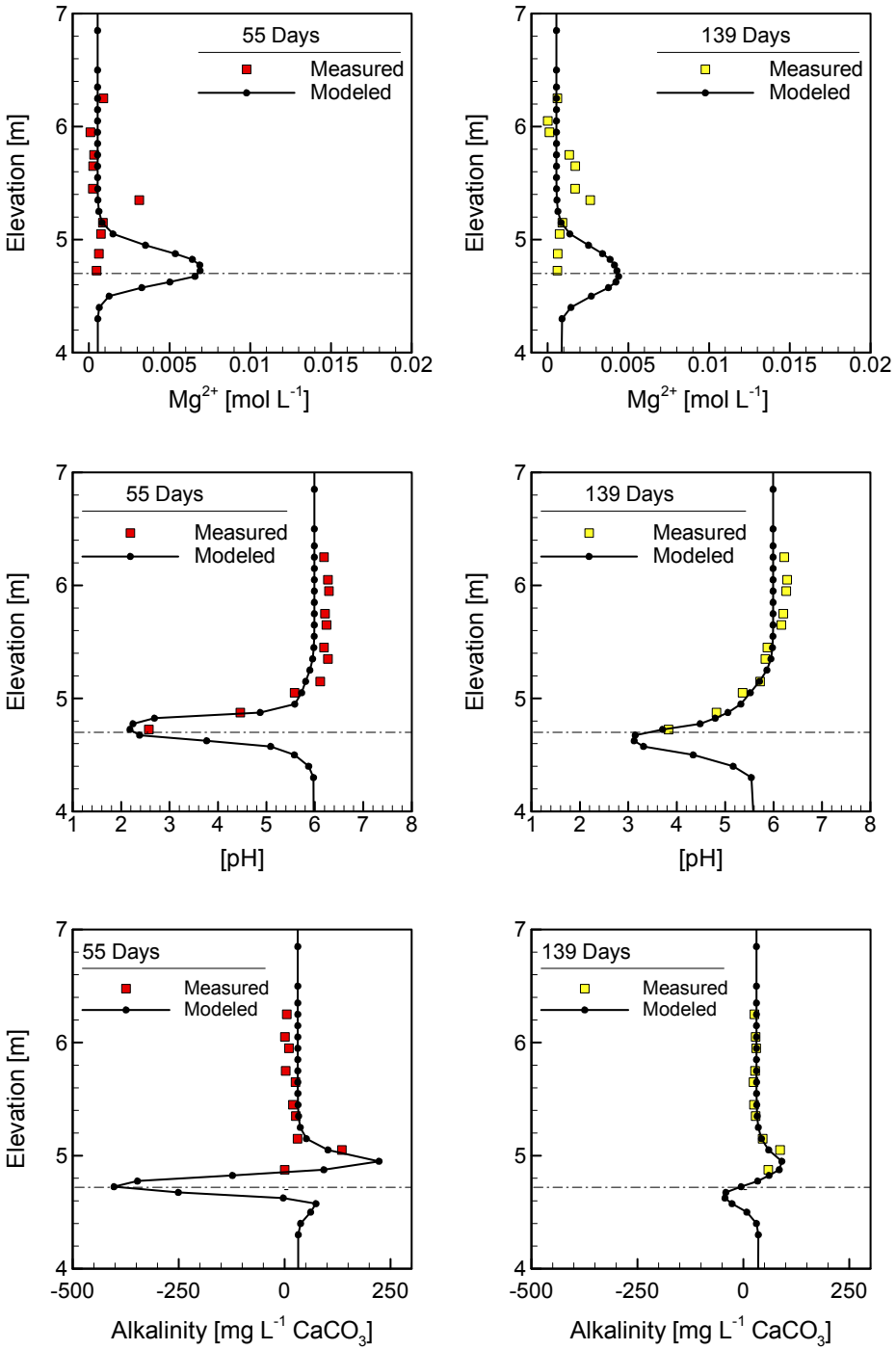

Figure 7-15. Comparison of measured and modeled Mg^{2+}, pH, and alkalinity at multilevel sampling device ML-1D at 55 days (left) and 138 days (right) following the oxidant injection. Solid black circles indicate the center elevation of each MIN3PD control volume. The elevation of the aquifer-aquitard contact is indicated by the dashed line.

The comparisons of measured and modeled component concentrations were presented to complement the residual analysis in characterizing the spatial distribution of the measured and simulated data. The bias present in the non-optimized model, manifested by the over prediction of MnO_4^-, Cl^-, K^+ and Ca^{2+} at the base of the aquifer, is significantly reduced in the optimized model.

7.3.3 Optimal Model Parameters

Table 7-6 compares estimated model parameters to available prior information, and the initial parameter values taken from the three-dimensional model. The prior information listed in the table is limited to measurements collected at the investigation site. The optimized hydraulic conductivity and porosity values are higher than indicated by the prior information. The hydraulic conductivity falls within the upper range of interpreted values from aquifer slug tests, but the aquifer and aquitard porosities are 25 percent greater than the field measured values. The estimated aquifer and aquitard porosities are equal to the upper bounds applied to these parameters during the automated inverse modeling.

Parameter	Prior Information	3-D model	2-D optimal	Units
Aquifer porosity	0.35	0.35	0.44	-
Aquifer hydraulic conductivity	3.8×10^{-4}	5.0×10^{-4}	7.3×10^{-4}	$m\ s^{-1}$
Cation exchange capacity	3.0	3.0	4.2	meq $[100\ g]^{-1}$
Aquifer SOM fraction	3.8×10^{-4}	1.5×10^{-4}	2.4×10^{-4}	$m^3\ m^{-3}$
Longitudinal dispersivity	None	5.0×10^{-2}	7.0×10^{-3}	m
Aquitard porosity	0.43	0.43	0.54	-
DNAPL dissolution rate constant	None	3.6×10^{-6}	3.9×10^{-6}	s^{-1}
Chemical diffusion coefficient	None	6.4×10^{-10}	1.7×10^{-9}	$m^2\ s^{-1}$
Aquifer pore size distribution	None	2.7	3.8	-
Transverse dispersivity	None	5.0×10^{-3}	5.2×10^{-3}	m
Maximum DNAPL fraction	0.028	0.028	0.024	$m^3\ m^{-3}$

Table 7-6. Comparison of optimized MIN3PD model parameters to initial model parameters and prior information.

7.3.4 Sensitivity and Covariance Analysis

Figure 7-16 compares the composite scaled sensitivities calculated at initial and final MIN3PD parameter values. Aquifer porosity is the most sensitive parameter for both models. However, the ratio between the largest and smallest composite scaled sensitivity values in the optimized model is approximately 3. This result indicates that trial and error model calibration by adjusting a relatively small subset of model parameters may not be effective in identifying optimal model parameters.

Changes in parameter sensitivities illustrate the non-linearity of the relationships between model parameters and model output [Knopman and Voss, 1987; Poeter and Hill, 1997; Sanz and Voss, 2006]. The sensitivity of the aquifer porosity and the longitudinal dispersivity in the optimized model were reduced in the final parameter values relative to the initial values. Testing confirmed that model parameters sensitivity is affected by its assigned value as well as the values assigned to remaining parameter values (data not shown).

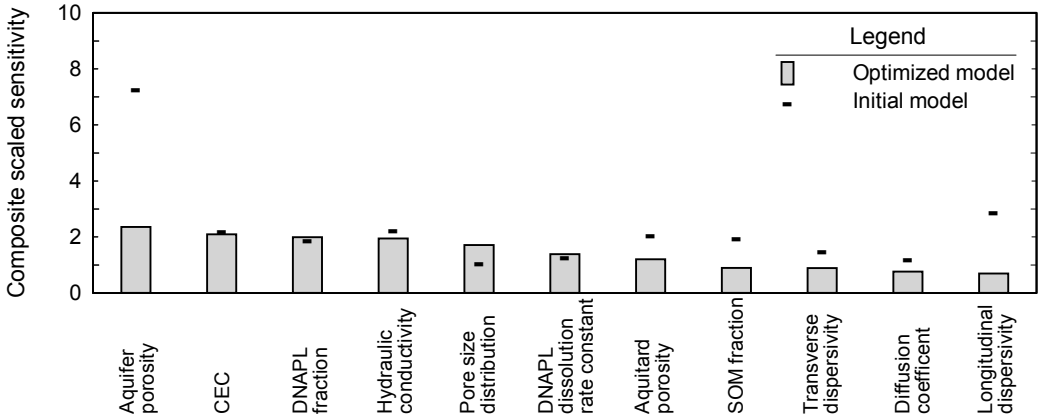

Figure 7-16. Composite scaled sensitivities for initial and optimized MIN3PD parameter values.

As described in Chapter 5, the parameter covariance matrix quantifies covariance between model parameters, which may contribute to model non-uniqueness [Doherty, 2002]:

$$\mathrm{cov}(\mathbf{b}) = s^2(\mathbf{J}^T\mathbf{Q}\mathbf{J})^{-1} \tag{7-18}$$

The diagonal elements of the covariance matrix represent the variances of the estimates of the base 10 logarithms of the adjustable parameters (Table 7-7). Standard deviations of the logarithms of the estimated model parameters, which are the square roots of diagonal elements of the covariance matrix, ranged from 0.01 (CEC) to 0.7 (transverse dispersivity).

	K_{aq}	k_{tce}^{diss}	φ_{DNAPL}	φ_{CH2O}	D_m	α_L	α_T	ϕ_{aqt}	ϕ_{aq}	n	CEC
K_{aq}	1.1	-0.29	0.35	0.059	-0.65	-0.13	0.97	-0.29	0.38	-1.2	-0.040
k_{tce}^{diss}		1.4	-0.70	-0.041	-0.27	-0.15	-0.77	-0.22	0.16	0.71	0.088
φ_{DNAPL}			1.2	0.00087	0.10	0.18	-0.16	0.047	0.18	-0.89	0.025
φ_{CH2O}				0.89	-0.29	-0.081	0.14	-0.017	0.055	0.30	0.18
D_m					1.5	0.085	-1.0	0.54	-0.37	0.39	-0.054
α_L						1.2	-0.21	0.47	-0.17	-0.18	-0.0075
α_T							4.3	-0.53	-0.080	-2.2	-0.20
ϕ_{aqt}								0.70	-0.23	0.17	0.079
ϕ_{aq}									0.46	-0.01	-0.0029
n										2.8	0.11
CEC											0.15

Note: All values x 10^{-3}

Table 7-7. Variance – covariance matrix for the optimized MIN3PD model. Results are reported for the base 10 logarithm of MIN3PD model parameters.

Parameter correlation coefficients pcc_{ij} are calculated directly from the covariance matrix using the following relationship:

$$pcc_{ij} = \frac{\sigma_{ij}}{\left[\sigma_{ii}\sigma_{jj}\right]^{1/2}} \tag{7-19}$$

where σ are the entries in the covariance matrix. Values of -1.0 and +1.0 indicate perfect correlation between model parameters [Hill, 1998; Hill and Østerby, 2003]. As indicated in Table 7-8, none of the model parameters in the current investigation exhibited high correlation. All parameter correlations fell between -0.7 and +0.7.

	K_{aq}	k_{tce}^{diss}	φ_{DNAPL}	φ_{CH2O}	D_m	α_L	α_T	ϕ_{aqt}	ϕ_{aq}	n	CEC
K_{aq}	1	-0.23	0.30	0.06	-0.50	-0.11	0.44	-0.33	0.54	-0.66	-0.10
k_{tce}^{diss}		1	-0.54	-0.04	-0.18	-0.12	-0.31	-0.22	0.20	0.35	0.19
φ_{DNAPL}			1	0.00	0.07	0.15	-0.07	0.05	0.24	-0.49	0.06
φ_{CH2O}				1	-0.24	-0.08	0.07	-0.02	0.09	0.19	0.49
D_m					1	0.06	-0.40	0.52	-0.43	0.19	-0.11
α_L						1	-0.09	0.52	-0.23	-0.10	-0.02
α_T							1	-0.31	-0.06	-0.62	-0.24
ϕ_{aqt}								1	-0.40	0.12	0.24
ϕ_{aq}									1	-0.01	-0.01
n										1	0.17
CEC											1

Table 7-8. Parameter correlation coefficients for optimized MIN3PD model.

7.3.5 Model Predictions

An objective of this investigation is the estimation of remediation efficiency using the combination of measured data and the calibrated MIN3PD model. The standard deviation associated with a given model prediction is computed as a function of the parameter covariance matrix: [Hill and Tiedeman, 2007]:

$$s_{z_\ell} = \left[s^2 \mathbf{x}_\ell \left(\mathbf{J}^T \mathbf{Q} \mathbf{J} \right)^{-1} \mathbf{x}_\ell^T \right]^{1/2} \tag{7-20}$$

where s_{z_ℓ} is the standard deviation of the ℓ^{th} model prediction, s^2 is the error variance calculated using Equation (7-17), and $\mathbf{x}_\ell$ is a row vector containing the derivatives of the ℓ^{th} model prediction to the model parameters. Model predictions quantified in the current investigation include the amount of MnO_4^- consumed through oxidation of $C_2HCl_{3(aq)}$ and oxidation of SOM, auto decomposition, and remaining as unreacted oxidant at the conclusion of the simulation. The derivatives $\frac{\partial z_\ell}{\partial b_j}$ are computed and stored in the Jacobian matrix.

Using Equation (7-20), the standard deviation in the prediction of the number of moles of MnO_4^- consumed by TCE was 14 moles, equal to approximately 1.6 Kg MnO_4^-. This calculation

incorporates the quality of the calibration represented by the error variance of the regression (s^2), the covariance matrix $(\mathbf{J}^T\mathbf{Q}\mathbf{J})^{-1}$, and the sensitivity of the remediation efficiency to model parameters. The low value of s_{z_ℓ} reflects the low value of the error variance of the regression (1.0), the absence of strong correlations between model parameters, and the sensitivity of the fate of the injected oxidant to the model parameters.

Optimized model results indicated that approximately 78 of the 132 kilograms of injected MnO_4^- oxidized $C_2HCl_{3(aq)}$, 50 Kg reacted with SOM, 3 Kg were consumed by auto decomposition, and 1 Kg remained unreacted at the conclusion of the simulation. These results are similar to the non-optimized two-dimensional model, and the three-dimensional model summarized in Chapter 6 (see Table 7-2). Therefore, the automated inverse modeling investigation did not significantly change the modeled assessment of the fate of the injected oxidant.

7.3.6 Discussion of Results

A primary benefit in applying the inverse modeling methodology is capacity to concurrently estimate a large set of unknown model parameters. Trial-and-error calibration applied to the three-dimensional model of the North Haven field trial was labor-intensive, and investigated a small subset of adjustable model parameters. Results from the sensitivity analyses performed using the hypothetical permanganate remediation problem and in the current problem determined that the geochemical evolution and MnO_4^- utilization are affected by a large set of model parameters with comparable sensitivity. The automated inverse modeling provided a mechanism to incorporate a larger set of MIN3PD model parameters in the calibration than was feasible using the non-automated approach. While manual parameter estimation incorporating 10 or more unknown model parameters does not appear to be effective or efficient for these conditions, automated inverse modeling provides an efficient mechanism to evaluate model sensitivity, parameter correlation, and optimal parameter values.

The inverse modeling succeeded in reducing the discrepancies between model output and measured data. Errors in the modeled distribution of Na^+ and Mg^{2+} are indicated, and are attributed to complexity at the field site which is not represented in the numerical model. Simplifications in the representation of cation exchange reactions in the model, as well as the unmodeled variability in aquifer permeability and fluid flow patterns are anticipated to account for these discrepancies. Given

the focus of the current investigation on aquifer remediation, and the good overall reproduction of the measured data the by the model, the errors exhibited by these two components were not investigated further.

The primary benefit achieved in the current work was the testing and evaluation of the North Haven field site model. Similar to the Chapter 5 sensitivity analysis results, the absence of strong correlations is indicated. Automated inverse modeling did not significantly revise the model estimates of the utilization of the injected oxidant. These results indicate that the trial and error calibration approach summarized in Chapter 6 was generally successful in selecting appropriate model parameters. The current discrepancies between the model output and the measured data are interpreted to indicate errors in model construction instead of the parameterization. Recent investigations utilizing automated inverse modeling methods have employed approaches to parameterize spatial heterogeneity [Doherty, 2003; Tonkin and Doherty, 2005]. This approach represents a possible area of expansion of the current work. However, the difficulty in representing pore-scale processes associated with NAPLs and the behavior of manganese oxide colloids is expected to limit the precision of the mathematical model of this technology regardless of the level of parameterization.

Chapter 8 Summary and Conclusions

The MIN3P reactive transport code [Mayer et al., 2002] has been enhanced to facilitate the investigation of permanganate-based remediation, and reactive transport problems characterized by gradients in groundwater density. The MIN3PD code implements a mass-conservative governing fluid flow equation incorporating fluid density into the calculation of fluid fluxes and storage. The coupling between fluid flow and reactive chemical transport is achieved using a Picard iterative solution scheme [Voss, 1984; Kipp; 1986; Ackerer et al., 1999; Frolkovic, 1999; Diersch, 2002]. The MIN3PD formulation was tested using a diverse set of benchmarking problems. Benchmarking results indicate that the program formulation correctly solves coupled fluid flow and chemical transport problems.

Fluid density in MIN3PD is estimated as a linear function of the total dissolved solids concentration. This approach follows previous model developments [Frind, 1982; Voss, 1984; Kharaka et al., 1988; Guo and Langevin, 2002]. Testing indicated that the assumption of linearity was justified for the range of fluid densities present in the current investigation. Although more sophisticated formulations based on the Pitzer ion interaction model are available [Monnin, 1994], this approach was not implemented in the current work due to the lack of ion interaction parameters for permanganate. The inclusion of such relationships represents a logical extension of the current model formulation. In addition, MIN3PD employs the simplifying assumption that gradients in fluid temperature are insignificant. Additional code development may be desired to further generalize the program for simulation of reactive transport processes under non-isothermal conditions.

A primary component of the current investigation was the evaluation of the importance of coupling between fluid flow, chemical transport, and chemical reactions. The significance of the coupling between solution composition and fluid flow was demonstrated using a hypothetical permanganate remediation problem, and confirmed using the site-specific model of the North Haven field trial. Investigation results confirmed that the representation of this coupling mechanism is critical to simulating the movement of the oxidant plume. Model simulations demonstrated the important role of the density contrast between the oxidant solution and groundwater in delivering the oxidant to DNAPL-contaminated intervals at the base of an aquifer. These results illustrate the important contribution of density-driven flow and transport towards the remediation efficiency of the inject-and-leave method [Nelson et al., 2001; Parker et al., 2002].

The importance of chemical reactions to density-driven flow and transport was investigated using the hypothetical permanganate remediation problem and the North Haven model. Previous studies suggest that the effect of geochemical reactions on density-dependent flow and transport are relatively small for solution with a high density contrast [Freedman and Ibaraki, 2002; Post and Prommer, 2007]. In both the hypothetical case and the North Haven site, the simulation results show a mild enhancement in the lateral spreading of the dense plume along the aquifer-aquitard interface when chemical reactions are neglected. The slight reduction in the migration of the reactive plume is attributed to the immobilization of Mn as MnO_2. This effect is counteracted by the oxidation of TCE, causing enhanced dissolution of DNAPL resulting in the addition of $C_2HCl_{3(aq)}$, Cl, and CO_3 (in the form of H_2CO_3 and HCO_3^-) to the solution. The delivery and distribution of MnO_4^- is therefore not significantly affected by changes in solution density due to chemical reactions. These results suggest that only the reactions that consume MnO_4^- must be considered for the simulation of permanganate-based in-situ chemical oxidation, while other reactions such as ion exchange or calcite dissolution-precipitation may be neglected. However, the additional information contained in geochemical data, including groundwater pH, alkalinity, and cation concentrations provides additional data valuable in model calibration.

A sensitivity analysis was employed to elucidate the characteristics of density-driven permanganate-based remediation focusing on remediation efficiency and the geochemical response to a permanganate injection. Results of this analysis indicate that remediation efficiency is generally controlled by system attributes which affect the delivery of the oxidant to the location where the DNAPL is present. The simulations confirm that the SOM content represents a primary limitation on efficiency, expected and consistent with the emphasis placed on the importance of natural oxidant demand (NOD) exerted by natural media [ITRC, 2005; Honning et al., 2007]. The sensitivity analysis demonstrated that the factors which enhance the sinking and spreading of the oxidant increase remediation efficiency. For example, a greater aquifer hydraulic conductivity results in enhanced sinking of the oxidant at early simulation times, and increased spreading of the dense plume along the base of the aquifer over the course of the simulation. In contrast, the remediation efficiency is a decreasing function of longitudinal dispersivity, which reduces the density contrast and the sinking of the treatment solution. An unanticipated result of the sensitivity analysis is the sensitivity of remediation efficiency to the aquifer porosity. This condition is related to the importance of SOM in consuming the injected oxidant. An increase in porosity effectively reduces the size of the oxidant plume, which minimizes the contact between the oxidant and the SOM. The most important kinetic

reaction parameter was the coefficient defining the rate of DNAPL dissolution, which controls the amount of $C_2HCl_{3(aq)}$ available to react with the oxidant.

A MIN3PD model was developed and calibrated to the North Haven field trial in order to characterize the behavior of the coupled reactive system, identify controlling processes, and utilize measured geochemical response to evaluate of the efficiency of the remediation. The modeling illustrates the beneficial effect of the high solution density, which leads to the sinking of the treatment solution and spreading along the aquifer-aquitard interface, focusing the delivery of the oxidant into regions where residual DNAPL is present. In addition, the pronounced effects of the remediation on aquifer geochemistry reaching far beyond the treatment of the contaminant were demonstrated. Modeling DNAPL dissolution as a kinetic reaction proved critical in simulating the expansion and subsequent contraction of the oxidant plume, indicating that mass transfer limitations are important in controlling aquifer remediation using MnO_4^-.

The modeling supported a quantitative evaluation of remediation efficiency, which is constrained by the model calibration using multiple aqueous components. The model calibration indicates minimal oxidant loss due to MnO_4^- auto-decomposition suggesting that this process can be neglected. On the other hand, the results demonstrate that a significant fraction of the oxidant reacted with organic carbon despite the low organic carbon content at the site. This observation confirms that the permanganate treatment is most efficient at sites with low aquifer reduction capacity. The model simulation predicts very moderate porosity and permeability reductions. The apparent absence of DNAPL at high saturations within the treatment area, and the absence of a forced hydraulic gradient may explain the lack of model sensitivity towards MnO_2 accumulation. The current model formulation does not explicitly simulate pore-scale process [e.g., clogging of pore throats] which may contribute to more significant permeability reductions in porous media.

An investigation employing automated inverse modeling was performed to evaluate the limitations of the trial-and-error calibrated MIN3PD model and to determine whether it is advantageous to use automatic calibration methods to improve simulation results. The investigation produced a twofold reduction in the sum of squares objective function. The bias present in the non-optimized model, manifested by the over prediction of MnO_4^-, Cl^-, K^+, and Ca^{2+} at the base of the aquifer, is significantly reduced in the optimized model. The optimized model indicated that permanganate utilization and remediation effectiveness were comparable to the North Haven model

calibrated using trial and error methods. A primary benefit of the effort was the generation of site-specific diagnostic information regarding the sensitivity and behavior of the system. Consistent with the results of the sensitivity analysis, multiple system attributes exhibited comparable sensitivity. A reduction in the complexity in model calibration may be realized when a small set of model parameters representing system attributes are dominant in controlling model predictions, effectively reducing the dimensionality of the parameter estimation problem. Sensitivity analysis results performed both on a hypothetical problem and a site-specific model indicate this condition is not applicable to density-driven permanganate remediation, which is affected by diverse attributes including DNAPL dissolution kinetics, the distribution and reactivity of SOM, and the permeability, porosity, and the dispersivity characteristic of the porous media. It is concluded that both trial and error calibration, which incorporate a degree subjectivity on the part of the modeler, and automated inverse modeling, which removes much of the subjectivity from the calibration process, provide advantages in modeling this system.

The MIN3PD program employs the representative elementary volume (REV) approach in representing physiochemical attributes. Several elements of the current investigation, including the movement of variable density fluids, the existence of DNAPLs, and the movement of colloidal manganese oxide particles are governed by conditions present at the pore scale [Schincariol and Schwartz, 1990; Miller et al.; 1990; Siegrist et al., 2001; Nambi and Powers, 2003]. Nevertheless, the scale of interest inherent to permanganate-based aquifer remediation dictates a REV-based approach, and the use of upscaled or effective model parameters to represent the properties of the system investigated. The good reproduction of the geochemical evolution at the North Haven field trial indicates that this approach can be applied successfully to model complex systems. However, it is not expected that these results would be obtained if more significant heterogeneity was present in the sediment properties or in the vertical distribution of DNAPLs.

In the current simulations, the movement of fluids and solutes was driven entirely by gradients in fluid density, with the exception of fluid pressure gradients imposed during the oxidant injection episodes. This focus was chosen to utilize the measured data for evaluating the capabilities of the numerical model and to quantitatively assess the conceptual model of permanganate treatment under free convection conditions. However, this hydrological regime, under which the remediation is isolated from the natural hydraulic gradient, represents a special case for an aquifer restoration effort. Additional work investigating the permanganate remediation incorporating both density contrasts and the existence of a natural hydraulic gradient presents a logical continuation of the current research.

The investigation achieved its objectives in characterizing the importance of coupling between processes, identifying the attributes most important to the efficiency of the technology, and relating the geochemical evolution to remediation efficiency in a quantitative fashion. The conceptual model as well as the capabilities of the numerical model appear to provide a sound working basis for further investigations of the permanganate-based remediation technology. In addition, it is worthwhile to note that MIN3PD is formulated in a general fashion, and the geochemical system can be defined through a database. The model is therefore not restricted to the simulation of aquifer restoration using permanganate. The flexibility of the formulation will allow using the MIN3PD code for a large variety of problems involving gradients in fluid density, fluid flow, solute transport, and geochemical reactions.

References

Abeele, W. V., 1984. Hydraulic testing of Bandelier Tuff, Los Alamos National Laboratory Report LA-10037.

Ackerer, P., Younes, A., Mose, R., 1999. Modeling variable density flow and solute transport in porous medium: 1. Numerical model and verification, *Transport in Porous Media* 35, 345–373.

Agency for Toxic Substances and Disease Registry, 1997. Toxicological profile for tetrachloroethylene, U.S. Department of Health and Human Services, Public Health Service.

Agency for Toxic Substances and Disease Registry, 1997. Toxilogical profile for trichloroethylene, U.S. Department of Health and Human Services, Public Health Service.

Al, T. A., Banks, V., Loomer, D., Parker, B. L., Mayer, K. U., 2006. Metal mobility during in situ chemical oxidation of TCE by $KMnO_4$, *Journal of Contaminant Hydrology* 88(1-2), 137-152.

Alt-Epping, P., 2000. Insights into the evolution of an oceanic hydrothermal system and a method for constraining estimates of the vigor of hydrothermal convection, Ph.D. Thesis, Department of Earth and Ocean Sciences, University of British Columbia.

Amos, R. T., Mayer, K. U., 2006. Investigating the role of gas bubble formation and entrapment in contaminated aquifers: reactive transport modeling, *Journal of Contaminant Hydrology* 87, 123-154.

Anderman, E. R., Hill, M. C., 1999. A new multistage groundwater transport inverse method: presentation, evaluation, and implications, *Water Resources Research* 35(4), 1053-1063.

Aster, R. C., Borchers, B., Thurber, C. H., 2005. Parameter Estimation and Inverse Problems, Elsevier Academic Press, 301 p.

Ataie-Ashtiani, B., Aghayi, M. M., 2006. A note on benchmarking of numerical models for density dependent flow in porous media, *Advances in Water Resources* 29 1918-1923.

Ball, J. W., Nordstrom, D. K., 1991. User's manual for WATEQ4F, with revised thermodynamic database and test cases for calculating speciation of major, trace and redox elements in natural waters. U.S. Geological Survey, Open-File Report 91-183, 189 pp.,

Barcelona, M. J., Holm, T. R., 1991. Oxidation-reduction capacities of aquifer solids, *Environmental Science & Technology* 25, 1565-1572.

Barlebo, H. C., Hill, M. C., Rosbjerg, D., 2004. Investigating the Macrodispersion Experiment (MADE) site in Columbus, Mississippi, using a three-dimensional inverse flow and transport model, *Water Resources Research* 40, W04211, doi:10.1029/2002WR001935.

Barth, G., Hill, M. C, 2005. Numerical methods for improving sensitivity analysis and parameter estimation of virus transport simulated using sorptive-reactive processes, *Journal of Contaminant Hydrology* 76, 251-277.

Bauer-Gottwein, P., Langer, T., Prommer, H., Wolski, P., Kinzelbach, W., 2007. Okavango Delta islands: interaction between density-driven flow and geochemical reactions under evapo-concentration, *Journal of Hydrology* 335, 389-405.

Bear, J., 1979. Hydraulics of Groundwater, Dover Publications, 592 p.

Beckie, R., 1996. Measurement scale, network sampling scale, and ground water model parameters, *Water Resources Research* 32(1), 65-76.

Brovelli, A., X. Mao, Barry, D.A., 2007. Numerical modeling of tidal influence on density-dependent contaminant transport, *Water Resources Research* 43, W10426, doi:10.1029/2006WR005173.

Bryant, S. L., Mellor, D. W., Cade, C. A., 1993. Physically representative network models of transport in porous media, *AIChE Journal* 39(3).

Calderhead, A., Mayer, K. U., 2004. Comparison of the suitability of the global implicit method and the sequential non-iterative approach for multicomponent reactive transport modelling, Proceedings of 5th Joint IAH-CNC/CGS Conference, Québec City, Québec, Canada, October 24-28, Session 6A:32-39.

Carman, P. C., 1937. Fluid flow through a granular bed, *Transactions of the Institute of Chemical Engineers of London*, 15, 150-156.

Carrera, J., Neuman, S. P., 1986. Estimation of aquifer parameters under transient and steady state conditions: 1. Maximum likelihood method incorporating prior information, *Water Resources Research* 22(2), 199–210.

Carsel, R. F., Parrish, R. S., 1988. Developing joint probability distributions of soil water retention characteristics, *Water Resources Research* 24(5) 755-769.

Chapman, S. W., Parker, B. L., 2005. Plume persistence due to aquitard back-diffusion following DNAPL source removal or isolation, *Water Resources Research* 41, W12411, doi: 10.1029/2005WR004224.

Chapman, S. W., Parker, B. L., Cherry, J. A., Aravena, R., Hunkeler, D., 2007. Groundwater-surface water interaction and its role on TCE groundwater plume attenuation, *Journal of Contaminant Hydrology* 91, 203-232.

Chiou, C. T., Porter, P. E., Schmedding, D. W., 1983. Partition equilibria of nonionic organic compounds between soil organic matter and water, *Environmental Science & Technology* 17(4), 227-231.

Chiou, C. T., Leet, J. F., Boyd, S. A., 1990. The surface area of soil organic matter, *Environmental Science & Technology* 24(8), 1164-1166.

Clegg, S., Whitfield, M., 1991. Activity coefficients in natural waters, in Pitzer, K., ed., Activity coefficients in electrolyte solutions: CRC Press, Chapter 6, 279-434.

Clement, T. P., Sun, Y., Hooker, B. S., Petersen, J. N., 1998. Modeling multispecies reactive transport in ground water, *Ground Water Monitoring & Remediation*, 18(2), 79-92.

Colombani, N., Mastrocicco, M., Gargini, A., Davis, G. B., Prommer, H., 2009. Modelling the fate of styrene in a mixed petroleum hydrocarbon plume, *Journal of Contaminant Hydrology* 105, 38-55.

Conrad, S., Glass, R., Peplinski, W., 2002. Bench-scale visualization of DNAPL remediation processes in analog heterogeneous aquifers: surfactant floods and in situ oxidation using permanganate, *Journal of Contaminant Hydrology* 58, 13-49.

Cooley, R. L., Naff, R. L., 1990. Regression modeling of groundwater flow, U.S. Geological Survey Techniques in Water Resources Investigations, Chapter B4, Book 3, 232 p.

Crimi, M. L., Siegrist, R. L., 2003. Geochemical effects on metals following permanganate oxidation of DNAPLs, *Ground Water* 41(4), 458-469.

Crimi, M. L., Siegrist, R. L., 2004. Association of cadmium with MnO_2 particles generated during permanganate oxidation, *Water Research* 38, 887-894.

Crimi, M. L., Siegrist, R. L., 2004. Impact of reaction conditions on MnO_2 Genesis during permanganate oxidation, *Journal of Environmental Engineering* 130(5), 562-572.

Crimi, M. L., Siegrist, R.L., 2005. Factors affecting effectiveness and efficiency of DNAPL destruction using potassium permanganate and catalyzed hydrogen peroxide, *Journal Of Environmental Engineering* 131(12), 1724-1732.

CRC, 2001. Handbook of Chemistry and Physics, 3rd electronic edition.

Cussler, E.L., 1997. Diffusion. Cambridge University Press, 2nd ed., 580 p.

D'Agnese, F. A., Faunt, C. C., Hill, M. C., Turner, A. K., 1999. Death Valley regional ground-water flow model calibration using optimal parameter estimation methods and geoscientific information systems, *Advances in Water Resources* 22(8), 777–790.

Dai, Q., Reitsma, S., 2004. Kinetic study of permanganate oxidation of tetrachloroethylene at a high pH under acidic conditions, *Remediation* doi: 10.1002/rem.20022.

Dai, Z., Samper, J., 2004. Inverse problem of multicomponent reactive chemical transport in porous media: formulation and applications, *Water Resources Research* 40, doi:10.1029/2004WR003248.

Dai, Z., Samper, J., 2006. Inverse modeling of water flow and multicomponent reactive transport in coastal aquifer systems, *Journal of Hydrology* 327, 447-461.

Davis, L., Neuman, S. P., 1983. Documentation and user's guide: UNSAT2 - Variably saturated flow model. U.S. Nuclear Regulatory Commission Report, NUREG/CR- 3390.

Diersch H. J. G., 2002. FEFLOW finite element subsurface flow and transport simulation system user's manual/reference manual/ white papers. Release 5.0. WASY Ltd.

Diersch, H. J. G., Kolditz, O., 2002. Variable density flow and transport in porous media: approaches and challenges, *Advances in Water Resources* 25, 899–944.

Doherty, J., 2002. PEST model-independent parameter estimation user's manual: 5th edition, Watermark Numerical Computing.

Doherty, J., 2003. Ground water model calibration using pilot points and regularization, *Ground Water* 41(2), 170-177.

Domenico, P. A., Schwartz, F. W., 1990. Physical and Chemical Hydrogeology, John Wiley and Sons, 824 p.

Draper, N. R., Smith, H., 1998. Applied Regression Analysis, 3rd ed., John Wiley and Sons, 706 p.

Elder J. W., 1967. Transient convection in a porous medium, *Journal of Fluid Mechanics* 27, 609-623.

Essaid, H. I., Cozzarelli, I. M., Eganhouse, R. P., Herkelrath, W. N., Bekins, B. A., Delin, G. N., 2003. Inverse modeling of BTEX dissolution and biodegradation at the Bemidji, MN crude-oil spill site, *Journal of Contaminant Hydrology* 67, 269 – 299.

Finsterle, S., Persoff, P., 1998. Determining permeability of tight rock samples using inverse modeling, *Water Resources Research* 33(8), 1803–1811.

Finsterle, S., 2000. iTOUGH2 user's guide, Report LBNL-40040 rev. 2, Lawrence Berkeley National Laboratory, Berkeley, California.

Finsterle, S., 2004. Multiphase inverse modeling: review and iTOUGH2 applications, *Vadose Zone Journal* 3, 747-762.

Forsyth, P. A., Wu, Y. S., Pruess, K., 1995. Robust numerical methods for saturated-unsaturated flow with dry initial conditions in heterogeneous media, *Advances in Water Resources* 18, 25-38.

Freedman, V., Ibaraki, M., 2002. Effects of chemical reactions on density-dependent fluid flow: on the numerical formulation and the development of instabilities, *Advances in Water Resources* 25, 439–453.

Frind, E. O., 1982. Seawater intrusion in continuous coastal aquifer-aquitard systems, *Advances in Water Resources* 5, 89-97.

Frolkovic P., 1999. Discretization. In: Fein E, editor. d3f - a simulator for density-driven flow, Gesellschaft fuer Anlagen-und Reaktorsicherheit, Braunschweig.

Frolkovic, P., De Schepper, H., 2001. Numerical modeling of convection dominated transport with density driven flow in porous media, *Advances in Water Resources* 24(1), 63–72.

Gandhi, R. K., Hopkins, G. D., Goltz, M. N., Gorelick, S. M., McCarty, P. L., 2002. Full-scale demonstration of in situ cometabolic biodegradation of trichloroethylene in groundwater 2. Comprehensive analysis of field data using reactive transport modeling, *Water Resources Research* 38(4), 11-1 – 11-18

Gavaska, A., Yoon, W. S., 2002. Demonstration of ISCO treatment of a DNAPL source zone at Launch Complex 34 in Cape Canaveral Air Station, final report prepared by Battelle Memorial Institute for the Interagency DNAPL Consortium, 295 p.

Gorelick, S. M., Evans, B., Remson, I., 1983. Identifying sources of groundwater pollution: an optimization approach, *Water Resources Research* 19 (3), 779-790.

Gelhar, L. W., Collins, M. A., 1971. General analysis of longitudinal dispersion in nonuniform flow, *Water Resources Research* 7(6), 1511-1521.

Gonullu, T., Farquhar, G., 1989. Oxidation to remove TCE from soil, Department of Civil Engineering, University of Waterloo, unpublished manuscript, available at http://www.civil.uwaterloo.ca/groundwater/oxlitrev.html.

Graf, T. Therrien, R., 2007. Coupled thermohaline groundwater flow and single-species reactive solute transport in fractured porous media, *Advances in Water Resources* 30, 742-771.

Guo, W., Langevin, C., 2002. User's Guide to SEAWAT: a computer program for simulation of three-dimensional variable density ground-water flow, U.S. Geological Survey Open File Report 01-434.

Hartog, N., Van Bergen, P. F., De Leeuw, J. E., Griffioen, J., 2004. Reactivity of organic matter in aquifer sediments: geological and geochemical controls, *Geochimica et Cosmochimica Acta*, 68(6), 1281-1292.

Hassanizadeh, S. M., 1986. Derivation of basic equations of mass transport in porous media Part 2. Generalized Darcy's and Fick's laws, *Advances in Water Resources* 9, 207-222.

Hassanizadeh, S. M., Leijnse, A., 1995. A non-linear theory of high-concentration- gradient dispersion in porous media, *Advances in Water Resources* 18(4), 203-15.

Haverkamp, R., Vauclin, M., Touma, J., Wierenga, P. J., Vachaud, G., 1977. A comparison of numerical simulation models for one-dimensional infiltration, *Soil Science Society of America Journal* 41, 285-294.

Henry, H. R., 1964. Effects of dispersion on salt encroachment in coastal aquifers, sea water in coastal aquifers, U.S. Geological Survey Water Supply Paper 1613-C, 70–84.

Herbert, A. W., Jackson, C. P., Lever, D. A., 1988. Coupled groundwater flow and solute transport with fluid density strongly dependent upon concentration, *Water Resources Research* 24(10), 1781-1795.

Hill, M. C., 1998. Methods and guidelines for effective model calibration, U.S. Geological Survey Water-Resources Investigations Report 98-4005.

Hill, M. C., Cooley, R. L., Pollock, D. W., 1998. A controlled experiment in ground water flow model calibration, *Ground Water* 36(3), 520-535.

Hill, M. C., Østerby, O., 2003. Determining extreme parameter correlation in ground-water models, *Ground Water*, 41(4), 420-430.

Hill, M. C., Tiedeman, C. R., 2007. Effective Groundwater Model Calibration: With Analysis of Data, Sensitivities, Predictions, and Uncertainty, Wiley-Interscience, 455p.

Holzbecher, E., 1998. Modeling Density-Driven Flow in Porous Media, Springer-Verlag, 286 p.

Honning, J., Broholm, M. M., Bjerg, P. L., 2007. Quantification of potassium permanganate consumption and PCE oxidation in subsurface materials, *Journal of Contaminant Hydrology* 90, 221-239.

Hood, E. D., 2000. Permanganate flushing of DNAPL source zones: experimental and numerical investigation, Ph.D. Thesis, Department of Civil Engineering, University of Waterloo.

Hood, E. D., Thomson, N. R., 2000. Numerical simulation of in situ chemical oxidation, In Chemical Oxidation and Reactive Barriers; Remediation of Chlorinated and Recalcitrant Compounds, International Conference on Remediation of Chlorinated and Recalcitrant Compounds, Columbus, Ohio: Battelle Press, 82–90.

Hood, E. D., Thomson, N. R., Grossi, D., Farquhar, G. J., 2000. Experimental determination of the kinetic rate law for the oxidation of perchloroethylene by potassium permanganate, *Chemosphere* 40, 1383-1388.

Horton, C. W., Rogers, F. T., 1945. Convection currents in a porous medium, *Journal of Applied Physics* 16, 367–70.

Huang, K-C., Hoag, G. E., Chheda, B. A., Dobbs, G. M., 1999. Kinetic study of the oxidation of trichloroethene by potassium permanganate, *Environmental Engineering Science* 16(5), 265-27.

Huang, K-C, Hoag, G. E., Chheda, P., Woody, B. A., Dobbs, G. M., 2001. Oxidation of chlorinated ethenes by potassium permanganate: a kinetics study, *Journal of Hazardous Materials* B87, 155-169.

Huang, K-C, Hoag, G. E., Chheda, P., Woody, B. A., Dobbs, G. M., 2002. Kinetics and mechanism of oxidation of tetrachloroethylene with permanganate, *Chemosphere* 46, 815-825.

Huling, S. G., Pivetz, B. E., 2006. Engineering Issue Paper: In Situ Chemical Oxidation, EPA 600-R-06-072.

Huyakorn, P. S., Anderson, P. F., Mercer, J. W., White, H. O., 1987. Saltwater intrusion in aquifers: development and testing of a three-dimensional finite element model, *Water Resources Research* 23(2), 293-312.

Ibaraki, M., 1998. A robust and efficient numerical model for analysis of density-dependent flow in porous media, *Journal of Contaminant Hydrology* 34, 235-246.

Ibaraki, M., Schwartz, F. W., Swartz, C. H., 2000. Modeling instability development in layered systems, *Journal of Contaminant Hydrology* 42, 337-352.

Ibaraki, M., Schwartz, F. W., 2001. Influence of natural heterogeneity on the efficiency of chemical floods in source zones, *Ground Water* 39(5), 660-666.

Imhoff, P. T., Jaffe, P. R., Pinder, G. F., 1993. An experimental study of complete dissolution of a nonaqueous phase liquid in saturated porous media, *Water Resources Research* 30(2), 307-320.

Interstate Technology & Regulatory Council, 2005. Technical and Regulatory Guidance for In Situ Chemical Oxidation of Contaminated Soil and Groundwater, 2nd edition.

Iribar V., Carrera J., Custodio E., Medina A., 1997. Inverse modeling of seawater intrusion in the Llobregat delta deep aquifer, *Journal of Hydrology* 198, 226-44.

Johannsen, K., Kinzelbach, W., Oswald, S., Wittum, G., 2002. The saltpool benchmark problem – numerical simulation of saltwater upcoming in a porous medium, *Advances in Water Resources* 25, 335-348.

Jurjovec, J., Blowes, D. W., Ptacek, C. J., Mayer K. U., 2004. Multicomponent reactive transport modelling of acid neutralization reactions in mill tailings, *Water Resources Research* 40, doi:10.1029/2003WR002233.

Keidser, A., Rosbjerg, D., 1991. A comparison of four inverse approaches to groundwater flow and transport parameter identification, *Water Resources Research* 27(9), 2219-2232.

Kharaka, Y., Gunter, W., Aggarwal, P., Perkins, E., Debraal, J., 1988. SOLMINEQ.88: a computer program for geochemical modeling of water-rock interactions, U.S. Geological Survey Report 88-4227.

Kim, K., Gurol, M. D., 2005. Reaction of nonaqueous phase TCE with permanganate, *Environmental Science & Technology* 39, 9303-9308.

Kipp, K. L., Jr., 1986. HST3D-A computer code for simulation of heat solute transport in three-dimensional ground-water flow systems: U.S. Geological Survey Water-Resources Investigations Report 86-4095.

Knopman, D. S., Voss, C. I., 1987. Behavior of sensitivities in the one-dimensional advection-dispersion equation: implications for parameter estimation and sampling design, *Water Resources Research* 23(2), 253-272.

Kolditz O., Ratke, R., Diersch, H. J. G., Zielke, W., 1998. Coupled groundwater flow and transport: 1. Verification of variable density flow and transport models, *Advances in Water Resources* 21, 27-46.

Konikow, L. F., Sanford, W. E., Campbell, P. J., 1997. Constant-concentration boundary condition: lessons from the HYDROCOIN variable density groundwater benchmark problem, *Water Resources Research* 33(10), 2253-2261.

Langevin, C. D., Guo, W., 2006. MODFLOW/MT3DMS-based simulation of variable-density ground water flow and transport, *Ground Water* 44(3), 339-351.

Langmuir, D., 1997. Aqueous Environmental Geochemistry, Prentice Hall, 600 p.

Lapalla, E. G., Healy, R. W., Weeks, E. P., 1987. Documentation of computer program VS2D to solve the equations of fluid flow in variably saturated porous media: U.S. Geological Survey Water-Resources Investigations Report 83-4099.

Lapwood, E. R., 1948. Convection of a fluid in a porous medium, *Proceedings of the Cambridge Philosophical Society*, 44, 508–521.

Lee, E. S., Seol, Y., Fang, Y. C., Schwartz, F. W., 2003. Destruction efficiencies and dynamics of reaction fronts associated with the permanganate oxidation of trichloroethylene, *Environmental Science & Technology* 37, 2540-2546.

Lenhard, R. J., Parker, J. C., 1987. A model for hysteretic constitutive relations governing multiphase flow: 2. Permeability - saturation relations, *Water Resources Research* 23, 2197-2206.

Lenhard, R. J., Oostrom, M., Dane, J. H., 2004. A constitutive model for air-NAPL-water flow in the vadose zone accounting for immobile, non-occluded (residual) NAPL in strongly water-wet porous media, *Journal of Contaminant Hydrology* 71, 261- 282.

Levenberg, K., 1944. A method for the solution of certain nonlinear problems in least squares, *Quarterly of Applied Mathematics* 2, 164-168.

Li, X. D., Schwartz, F. W., 2000. Efficiency problems related to permanganate oxidation schemes, In: Wickamanayake, G.B., Gavaskar, A.R., Chen, A.S.C. (Eds.), Chemical Oxidation and Reactive Barriers: Remediation of Chlorinated and Recalcitrant Compounds, Battelle Press, 41-48.

Li, X. D., Schwartz, F. W., 2004. DNAPL remediation with in situ chemical oxidation using potassium permanganate Part I. Mineralogy of Mn oxide and its dissolution in organic acids, *Journal of Contaminant Hydrology* 68, 39-53.

Li, X. D., Schwartz, F. W., 2004. DNAPL remediation with in situ chemical oxidation using potassium permanganate Part II. Increasing removal efficiency by dissolving Mn oxide precipitates, *Journal of Contaminant Hydrology* 68, 269-287.

Lichtner, P. C., 1997. Benchmark problem: acid mine drainage, Workshop on Subsurface Reactive Transport Modeling, Pacific Northwest National Laboratory, Richland, WA, Oct 29 - Nov 1.

Liu, C., Ball, W. P., 1999. Application of inverse methods to contaminant source identification from aquitard diffusion profiles at Dover AFB, Delaware, *Water Resources Research* 35(7), 1975-1985.

Lowe, K. S., Gardner, F. G., Siegrist, R. L., 2002. Field evaluation of in situ chemical oxidation through vertical well-to-well recirculation of NaMnO4, *Ground Water Monitoring & Remediation*, Winter, 106-115.

MacKinnon, L. K., Thomson, N. R., 2002. Laboratory-scale in situ chemical oxidation of a perchloroethylene pool using permanganate, *Journal of Contaminant Hydrology* 56, 49-74.

Mao, X., Prommer, H., Barry, D. A., Langevin, C. D., Panteleit, B., Li, L., 2006. Three-dimensional model for multi-component reactive transport with variable density groundwater flow, *Environmental Modelling Software* 21, 615-628.

Marquardt, D. W., 1963. An algorithm for least-squares estimation of nonlinear parameters, *Journal of the Society for Industrial and Applied Mathematics* 11(2), 431-441.

Mayer, A. S., Miller C. T., 1992. The influence of porous media characteristics and measurement scale on pore-scale distributions of residual nonaqueous-phase liquids, *Journal of Contaminant Hydrology* 11, 189-213.

Mayer, A. S., Miller C. T., 1996. The influence of mass transfer characteristics and porous media heterogeneity on nonaqueous phase dissolution, *Water Resources Research* 32(6), 1551-1567.

Mayer, K. U., 1999. A numerical model for multicomponent reactive transport in variably saturated porous media, Ph.D. Thesis, Department of Earth Sciences, University of Waterloo.

Mayer, K. U., Blowes, D. W., Frind, E. O., 2001. Reactive transport modelling of groundwater remediation by an in-situ reactive barrier for the treatment of hexavalent chromium and trichloroethylene, *Water Resources Research* 37, 3091-3103.

Mayer, K. U., Benner, S. G., Frind, E. O., Thornton, S. F., Lerner, D. L., 2001. Reactive transport modeling of processes controlling the distribution and natural attenuation of phenolic compounds in a deep sandstone aquifer, *Journal of Contaminant Hydrology* 53, 341-368.

Mayer, K. U., Frind, E. O., Blowes, D. W., 2002. Multicomponent reactive transport modeling in variably saturated porous media using a generalized formulation for kinetically controlled reactions, *Water Resources Research* 38, 13-1 – 13-21.

Medina, A., Carrera, J., 1996. Coupled estimation of flow and solute transport parameters, *Water Resources Research* 32(10), 3063-3076.

Miller, C., Poirier-McNeill, M., Mayer, A., 1990. Dissolution of trapped nonaqueous phase liquids: mass transfer characteristics, *Water Resources Research* 26(11), 2783-2796.

Millero, F. J., Mucci, A., Zullig, J., Chetirkin, P., 1982. The density of red sea brines, *Marine Chemistry* 11, 463-475.

Monnin, C., 1989. An ion interaction model for the volumetric properties of natural waters: density of the solution and partial molal volumes of electrolytes to high concentrations at 25° C, *Geochimica et Cosmochimica Acta* 53, 1177–88.

Monnin, C., 1994. Density calculations and concentration scale conversions for natural waters, *Computers & Geosciences* 20(10), 1435-1445.

Moran, M. J., Lapham, W. W., Rowe, B. L., Zogorski, J. S., 2002. Occurrence and status of volatile organic compounds in ground water from rural, untreated, self-supplied domestic wells in the United States, 1986-99, U.S. Geological Survey Water-Resources Investigations Report 02-4085.

Mualem, Y., 1976. A new model for predicting the hydraulic conductivity of unsaturated porous media, *Water Resources Research* 12, 513-522.

Mumford, K. G., Thomson, N. R., Allen-King, R. M., 2005. Bench-scale investigation of permanganate natural oxidant demand kinetics, *Environmental Science & Technology* 39(8), 2835-2840.

Mundle, K., Reynolds, D. A., West, M. R., Kueper, B. H., 2007. Concentration rebound following in situ chemical oxidation in fractured clay, *Ground Water* 45(6), 692-702.

Nambi, I. M., Powers, S. E., 2003. Mass transfer correlations for nonaqueous phase liquid dissolution from regions with high initial saturations, *Water Resources Research* 39(2), 4-1–4-11.

Nelson, M., Parker, B. L., Al, T. A., Cherry, J. A., Loomer, D., 2001. Geochemical reactions resulting from in situ oxidation of PCE-DNAPL by $KMnO_4$ in a sandy aquifer, *Environmental Science & Technology* 35(6), 1266-1275.

Ogata, A., Banks, R. B., 1961. A solution of the differential equation of longitudinal dispersion in porous media, U.S. Geological Survey Professional Paper 411-A.

Oldenburg, C., Pruess, K., 1995. Dispersive transport dynamics in a strongly coupled groundwater-brine flow system, *Water Resources Research* 31, 289-302.

Oostrom, M., Dane, J. H., Guven, O., Hayworth, J. S., 1992. Experimental investigation of dense solute plumes in an unconfined aquifer model, *Water Resources Research* 28, 2315–2326.

Oltean, C., Buès, A., 2001. Coupled groundwater flow and transport in porous media: a conservative or non-conservative form? *Transport in Porous Media* 44, 219–246.

Oswald, S. E., Kinzelbach, W., 2004. Three-dimensional physical benchmark experiments to test variable-density flow models, *Journal of Hydrology* 290, 22-42.

Pankow, J. F., Cherry, J. A., 1996. Dense Chlorinated Solvents and Other DNAPLs in Groundwater, Waterloo Press, 582 p.

Parker, J. C., Lenhard, R. J., Kuppusamy, T., 1987. A parametric model for constitutive properties governing multiphase flow in porous media, *Water Resources Research* 23(4), 618-624.

Parker, B. L., Cherry, J. A., Al, T. A., 2002. Passive permanganate remediation of a solvent DNAPL source zone. In: A.R. Gavaskar and A.S.C. Chen (eds.), Remediation of Chlorinated and Recalcitrant Compounds – 2002. Proceedings of the Third International Conference on Remediation of Chlorinated and Recalcitrant Compounds, May 20-23, Monterey, California, Paper 2C-05, 8 pp.

Parker, B. L., Cherry, J. A., Chapman, S. W. Guilbeault, M. A., 2003. Review and analysis of chlorinated solvent dense non-aqueous phase liquid distributions in five sandy aquifers, *Vadose Zone Journal* 2,116-137.

Parker, B. L., Cherry, J. A., Chapman, S.W., 2004. Field study of TCE diffusion profiles below DNAPL to assess aquitard integrity, *Journal of Contaminant Hydrology* 74, 197-230.

Pinder, G. F., Cooper, H. H., 1970. A numerical technique for calculating the transient position of the saltwater front, *Water Resources Research* 6(3), 875–82.

Poeter, E. P., Hill, M. C., 1997. Inverse models: a necessary step in ground-water modeling, *Ground Water* 35(2), 250-260.

Poeter, E. P., Hill, M. C., 1998. Documentation of UCODE, a computer code for universal inverse modeling, U.S. Geological Survey Water-Resources Investigations Report 98-4080.

Poeter, E. P., Hill, M. C., Banta, E. R., Mehl, S., Christensen, S., 2005. UCODE_2005 and six other computer codes for universal sensitivity analysis, calibration, and uncertainty evaluation: U.S. Geological Survey Techniques and Methods 6-A11, 283p.

Post, V. E. A., Prommer, H., 2007. Multicomponent reactive transport simulation of the Elder problem: effects of chemical reactions on salt plume development, *Water Resources Research* 43, doi:10.1029/2006WR005630.

Prommer H., Barry, D. A., Zheng, C., 2003. MODFLOW/MT3DMS based reactive multi-component transport modeling, *Ground Water* 41(2), 247-257.

Putti, M., Paniconi, C., 1995. Picard and Newton linearization for the coupled model of saltwater intrusion in aquifers, *Advances in Water Resources* 3, 159-170.

Rayleigh Lord (Strutt, J. W.), 1916. On convection currents in a horizontal layer of fluid when the higher temperature is on the underside, *Philosophical Magazine* 6(32), 529-46.

Rees, T., 1987. The stability of potassium permanganate solutions, *Journal of Chemical Education* 64, 1058.

Reis, J. C., Acock, A. M., 1994. Permeability reduction models for the precipitation of inorganic solids in Berea sandstone, *In Situ* 18(3), 347-368.

Reitsma, S., Marshall, M., 2000. Experimental study of oxidation of pooled NAPL. In: Wickamanayake, G.B., Gavaskar, A.R., Chen, A.S.C. (Eds.), Chemical Oxidation and Reactive Barriers: Remediation of Chlorinated and Recalcitrant Compounds, Battelle Press, 25-32.

Rezaei, M., Sanz, E., Raeisi, E., Ayora, C., Vásquez-Suné, E., Carrera, J., 2005. Reactive transport modeling of calcite dissolution in the fresh-salt water mixing zone, *Journal of Hydrology* 311, 282-298.

Samper, J., Zheng, L., Fernández, A. M., Montenegro, L., 2008. Inverse modeling of multicomponent reactive transport through single and dual porosity media, *Journal of Contaminant Hydrology* 98, 115-127.

Sanford, W. E., Konikow, L. F., 1989. Simulation of calcite dissolution and porosity changes in saltwater mixing zones in coastal aquifers, *Water Resources Research* 25, 655-677.

Sanz, E., Voss C., 2006. Inverse modeling for seawater intrusion in coastal aquifers: insights about parameter sensitivities, variances, correlations and estimation procedures derived from the Henry problem, *Advances in Water Resources* 29, 439-457.

Scheidegger, A. E., 1974. The Physics of Flow Through Porous Media, 3rd ed., 353 p.

Schincariol, R. A., Schwartz, F. W., 1990. An experimental investigation of variable density flow and mixing in homogeneous and heterogeneous media, *Water Resources Research* 26(10), 2317-2329.

Schincariol, R. A., Schwartz, F. W., Mendoza, C. A., 1994. On the generation of instabilities in variable density flow, *Water Resources Research* 30(4), 913-927.

Schincariol, R. A., Schwartz, F. W., Mendoza, C. A., 1997. Instabilities in variable density flows: stability and sensitivity analysis for homogeneous and heterogeneous media, *Water Resources Research* 33(1), 31-41.

Schnarr, M., Truax, C., Farquhar, G. Hood, E., Gonullu, T., Stickney, B., 1998. Laboratory and controlled field experiments using potassium permanganate to remediate trichloroethylene and perchloroethylene DNAPLs in porous media, *Journal of Contaminant Hydrology* 29, 205-224.

Schotting, R. J., Moser, H., Hassanizadeh, S. M., 1999. High-concentration gradient dispersion in porous media: experiments, analysis and approximations, *Advances in Water Resources* 22, 665-680.

Schroth, M. H, Oostrom, M., Wietsma, T. W., Istok, J. D., 2001. In-situ oxidation of trichloroethene by permanganate: effects on porous medium hydraulic properties, *Journal of Contaminant Hydrology* 50, 79-98.

Schwarzenbach, R. P., Gschwend, P. M., Imboden, D. M., 1993. Environmental Organic Chemistry, Wiley-Interscience, 681 p.

Segol, G., Pinder, G. F., Gray, W. G., 1975. A Galerkin-finite element technique for calculating the transient position of the saltwater front, *Water Resources Research* 11(2), 343-7.

Segol, G., Pinder, G. F., 1976. Transient simulation of saltwater intrusion into southeast Florida, *Water Resources Research* 12(1), 65-70.

Senger, R. K., Fogg, G. E., 1990. Stream functions and equivalent freshwater heads for modeling regional flow of variable-density groundwater 1. Review of theory and verification, *Water Resources Research* 26(9), 2089-2096.

Shoemaker, W. B., 2004. Important observations and parameters for a salt water intrusion model, *Ground Water* 42(6), 829-40.

Siegrist, R. L., Urynowicz, M. L., West, O. R., Crimi, M. L., Lowe, K. S., 2001. Principles and Practices of In Situ Chemical Oxidation Using Permanganate, Battelle Press, 348 p.

Simmons, C.T., Narayan, K. A., Wooding, R. A., 1999. On a test case for density-dependent groundwater flow and solute transport models: the salt lake problem, *Water Resources Research* 35(12), 3607-3620.

Simmons, C. T., Fenstemaker, T. R., Sharp, J. M., 2001. Variable-density groundwater flow and solute transport in heterogeneous porous media: approaches, resolutions and future challenges, *Journal of Contaminant Hydrology* 52, 245-275.

Simmons, C. T., Pierini, M. L., Hutson, J. L., 2002. Laboratory investigation of variable density flow and solute transport in unsaturated–saturated porous media, *Transport in Porous Media* 47, 215-244.

Simpson, M. J., Clement, T. P., 2003. Theoretical analysis of the worthiness of Henry and Elder problems as benchmarks of density-dependent groundwater flow models, *Advances in Water Resources* 26, 17-31.

Simpson, M. J., Clement, T. P., 2004. Improving the worthiness of the Henry problem as a benchmark for density-dependent groundwater flow models, *Water Resources Research* 40, W01504, doi:10.1029/2003WR002199.

Squillance, P. J., Moran, M. J., Lapham, W. W., Price, C. V., Clawges, R. M., Zogorski, J. S., 1999. Volatile organic compounds in untreated groundwater of the United States, 1985-1995, *Environmental Science & Technology* 33(23), 4176-4187.

Steefel, C. I., Lasaga, A. C., 1994. A coupled model for transport of multiple chemical species and kinetic precipitation/dissolution reactions with application to reactive flow in single phase hydrothermal systems, *American Journal of Science* 294, 529-592.

Stewart, R., 1965. Oxidation by permanganate. In: K.B. Wiberg, Oxidation in Organic Chemistry, Part A., Academic Press.

Stewart, C., 2002. Density-driven permanganate solution delivery and chemical oxidation of a thin trichloroethene DNAPL pool in a sandy aquifer. MSc Thesis, University of Waterloo.

Stumm, W., Morgan, J. J., 1996. Aquatic Chemistry, John Wiley.

Sun, N. -Z., 1994. Inverse Problems in Groundwater Modeling, Kluwer Academic.

Swartz, C. H., Schwartz, F. W., 1998. An experimental study of mixing and instability development in variable-density systems, *Journal of Contaminant Hydrology* 34, 169-189.

Theis, C. V., 1935. The relation between the lowering of the piezometric surface and the rate and duration of discharge of a well using ground-water storage, *Transactions, American Geophysical Union* 16, 519–524.

Tonkin, M. J., Doherty, J., 2005. A hybrid regularized inversion methodology for highly parameterized environmental models, *Water Resources Research* 41, W10412, doi:10.1029/2005WR003995.

Thomson, D., 2004. Influence of grain size variability and sedimentology on solvent DNAPL distribution in the Borden Aquifer, MSc thesis, University of Waterloo.

U. S. Environmental Protection Agency, 1998. Field applications of in situ remediation technologies: chemical oxidation; EPA542-R-98-008.

U. S. Environmental Protection Agency, 1999. A review of contaminant occurrence in public drinking water systems: Office of Water Quality, USEPA 816-R-99-006.

U. S. Environmental Protection Agency, 1999. Alternative Disinfectants and Oxidants Guidance Manual, Office of Water, EPA 815-R-99-014.

Urynowicz, M.A., 2000. Reaction kinetics and mass transfer during in situ oxidation of dissolved and DNAPL trichloroethene with permanganate, Ph.D. dissertation, Environmental Science & Engineering Division, Colorado School of Mines.

Urynowicz, M. A., Siegrist, R. L., 2005. Interphase mass transfer during chemical oxidation of TCE DNAPL in an aqueous system, *Journal of Contaminant Hydrology* 80(3-4), 93-106.

Urynowicz, M. A., Balu, B., Udayasankar, U., 2008. Kinetics of natural oxidant demand by permanganate in aquifer solids, *Journal of Contaminant Hydrology* 96, 187-194.

van Genuchten, M. Th., 1980. A closed-form equation for predicting the hydraulic conductivity of unsaturated soils, *Soil Science Society of America Journal* 44, 892 - 898.

van Leer, B., 1974. Towards the ultimate conservative scheme. II Monotonicity and conservation combined in a second order scheme, *Journal of Computational Physics* 14, 361-370.

Van Rooy, D., Keidser, A., Rosbjerg, D., 1989. Inverse modelling of flow and transport in groundwater contamination (Proceedings of the symposium held during the Third IAHS scientific assembly, Baltimore, MD, May 1989), Linda Abriola ed., IAHS Publ. no. 185, p. 11-23.

Vauclin, M., Khanji, D., Vachaud, G., 1979. Experimental and numerical study of a transient, two-dimensional unsaturated-saturated water table recharge problem, *Water Resources Research* 15 (5), 1089-1101.

Voss, C. I., 1984. A finite-element simulation model for saturated-unsaturated, fluid-density-dependent ground-water flow with energy transport or chemically-reactive single-species solute transport: U.S. Geological Survey Water-Resources Investigation Report 84-4369.

Voss, C. I., Souza, W. R., 1987. Variable density flow and solute transport simulation of regional aquifers containing a narrow freshwater-saltwater transition zone, *Water Resources Research* 23(10), 1851-1866.

Voss, C. I., Souza, W. R., 1998. Dynamics of a regional fresh water-salt water transition zone in an anisotropic coastal aquifer system. U.S. Geological Survey Open-File Report 98-398.

Wagner, B. J., Gorelick, S. M., 1987. Optimal groundwater quality management under parameter uncertainty, *Water Resources Research* 23(7), 1162-1174.

Weatherill, D., Simmons, C. T., Voss, C. I., Robinson, N. I., 2004. Testing density-dependent groundwater models: two-dimensional steady state unstable convection in infinite, finite and inclined porous layers, *Advances in Water Resources* 27, 547–562.

Weiss, R., Smith, L., 1998. Parameter space methods in joint parameter estimation for groundwater flow models, *Water Resources Research* 34(4), 647-661.

Weiss, R., Smith, L., 1998. Efficient and responsible use of prior information in inverse models, *Ground Water* 36(1), 151-163.

West, O. R., Cline, S. R., Holden, W. L., Gardner, F. G., Schlosser, B. M., Thate, J. E., Pickering, D.A., 1997. A full-scale demonstration of in situ chemical oxidation through recirculation at the X-701B site, Oak Ridge National Laboratory, ORNL/TM 13556.

West, M. R., Grant, G. P., Gerhard, J. I., Kueper, B. H., 2007. The influence of precipitate formation on the chemical oxidation of TCE DNAPL with potassium permanganate, *Advances in Water Resources* 31, 324-338.

White, M. D., Oostrom, M., 2000. STOMP subsurface transport over multiple phases: theory guide PNNL-11216 (UC-2010), Pacific Northwest National Laboratory, Richland, Washington.

Wise, W. R., 1992. A new insight on pore structure and permeability, *Water Resources Research* 28(1), 189-198.

Wooding, R. A., Tyler, S. W., White, I., Anderson, P. A., 1997. Convection in groundwater below an evaporating salt lake, 2, Evolution of fingers or plumes, *Water Resources Research* 33(6), 1219-1228.

Xu, T., Sonnenthal, E. L., Spycher, N., Pruess, K., 2004. TOUGHREACT user's guide: a simulation program for non-isothermal multiphase reactive geochemical transport in variably saturated geologic media, Lawrence Berkeley National Laboratory Report LBNL-55460.

Yan, Y. E., Schwartz, F. W., 1999. Oxidative degradation and kinetics of chlorinated ethylenes by potassium permanganate, *Journal of Contaminant Hydrology* 37, 343-365.

Yan, Y. E., Schwartz, F. W., 2000. Kinetics and mechanisms for TCE oxidation by permanganate, *Environmental Science & Technology* 34, 2535-2541.

Yeh, W. W-G., 1986. Review of parameter identification procedures in groundwater hydrology: the inverse problem, *Water Resources Research* 22(2), 95-108.

Zhang, H., Schwartz, F. W., 1995. Multispecies contaminant plumes in variable density flow systems, *Water Resources Research* 31(4), 837-847.

Zhang, H., Schwartz, F. W., Wood, W. W., Garabedian,S. P., LeBlanc, D. R., 1998. Simulation of variable-density flow and transport of reactive and nonreactive solutes during a tracer test at Cape Cod, Massachusetts, *Water Resources Research* 34, 67-82.

Zhang, H., Schwartz, F. W., 2000. Simulating the in situ oxidative treatment of chlorinated ethylenes by potassium permanganate, *Water Resources Research* 36, 3031-3042.

Zheng, C., Bennett, G. D., 2002. Applied Contaminant Transport Modeling, Wiley-Interscience, 621 p.